www.czasopisma.pan.pl PAN POLSKA AKADEMIA NAUK www.journals.pan.pl

Vol. 38 • No. 2 • 2017

Chemical and Process Engineering

Inżynieria Chemiczna i Procesowa

Polish Academy of Sciences
Committee of Chemical and Process Engineering

The Journal is supported by the Ministry of Science and Higher Education

Address

ul. Waryńskiego 1
00-645 Warszawa
cpe.czasopisma.pan.pl; degruyter.com/view/j/cpe

Printed in Poland
Print run: 100 copies

Printing/binding:
Centrum Poligrafii Sp. z o.o.
ul. Łopuszańska 53
02-232 Warszawa

www.czasopisma.pan.pl www.journals.pan.pl
Chemical and Process Engineering 2017, 38 (2), 195-207
DOI: 10.1515/cpe-2017-0015

INFLUENCE OF LOW-TEMPERATURE PLASMA TREATMENT ON THE LIQUID FILTRATION EFFICIENCY OF MELT-BLOWN PP NONWOVENS IN THE CONDITIONS OF SIMULATED USE OF RESPIRATORY PROTECTIVE EQUIPMENT

Katarzyna Majchrzycka*[1], Małgorzata Okrasa[1], Agnieszka Brochocka[1], Wiesława Urbaniak-Domagała[2]

[1]Central Institute for Labour Protection – National Research Institute (CIOP-PIB), Department of Personal Protective Equipment, Wierzbowa 48, 90-133 Łódź, Poland

[2]Lodz University of Technology, Department of Material and Commodity Sciences and Textile Metrology, Żeromskiego 116, 90-924 Lodz, Poland

Dedicated to Prof. Leon Gradoń on the occasion of his 70th birthday

Filtering nonwovens produced with melt-blown technology are one of the most basic materials used in the construction of respiratory protective equipment (RPE) against harmful aerosols, including bio- and nanoaerosols. The improvement of their filtering properties can be achieved by the development of quasi-permanent electric charge on the fibres. Usually corona discharge method is utilized for this purpose. In the presented study, it was assumed that the low-temperature plasma treatment could be applied as an alternative method for the manufacturing of conventional electret nonwovens for the RPE construction.

Low temperature plasma treatment of polypropylene nonwovens was carried out with various process gases (argon, nitrogen, oxygen or air) in a wide range of process parameters (gas flow velocity, time of treatment and power supplied to the reactor electrodes). After the modification, nonwovens were evaluated in terms of filtration efficiency of paraffin oil mist. The stability of the modification results was tested after 12 months of storage and after conditioning at elevated temperature and relative humidity conditions. Moreover, scanning electron microscopy and ATR-IR spectroscopy were used to assess changes in surface topography and chemical composition of the fibres. The modification of melt-blown nonwovens with nitrogen, oxygen and air plasma did not result in a satisfactory improvement of the filtration efficiency. In case of argon plasma treatment, up to 82% increase of filtration efficiency of paraffin oil mist was observed in relation to untreated samples. This effect was stable after 12 months of storage in normal conditions and after thermal conditioning in (70 ± 3)°C for 24 h. The use of low-temperature plasma treatment was proven to be a promising improvement direction of filtering properties of nonwovens used for the protection of respiratory tract against harmful aerosols.

Keywords: low-temperature plasma treatment, melt-blown nonwovens, respiratory protective devices

1. INTRODUCTION

The basic materials used for the construction of respiratory protective equipment (RPE) against harmful aerosols are filtering nonwovens produced with melt-blown technology (Brochocka, 2001). The

*Corresponding author, e-mail: kamaj@ciop.lodz.pl

technique of blowing molten polymer makes it possible to obtain a product of greater degree of compaction than it is in the case of traditional needle-punched nonwovens. Additionally, it ensures a possibility of spatial changes of porosity along the flow of the filtered aerosol. Fibres creating a filtering layer are arranged anisotropically in the layer plane of the nonwoven structure and often have diameters of less than 1μm. This guarantees high filtering efficiency but also causes greater airflow resistance. Higher filtering efficiency of melt-blown nonwovens can be also obtained without increasing airflow resistance by introducing electrostatic charges into a fibre during the process of corona discharge. During this process, a point electrode with a higher potential, emits ions of a specific character. They move in electric field towards the lower or opposite potential. The electrodes are mounted on a collector of the melt-blowing production line in the fibre forming area. Ions of greater density are trapped in the fibres and become semi-permanently bonded with the polymer material. Different arrangements of electrodes ensure obtaining electrets of different electrostatic charges per unit of fibre length.

When discussing the efficiency of electret nonwovens, it is important to realise the main mechanisms influencing the movement of a particle in the close proximity of a fibre, which translates directly into the probability of its capture by the filter (Barrett and Rousseau, 1998; Brown, 1993; Gougeon, Boulaud and Renoux, 1996; Kanaoka et al., 1987; Pich et al., 1987). In case of penetration of fine particles that are particularly harmful for respiratory system, it is precisely the Coulomb's interaction that is of particular significance (Martin and Moyer, 2000). The power of attraction between an aerosol particle and a fibre depends inter alia on the value of their electric charges. Thus, the neutralization of electric charges, which is often observed for RPE, causes a rapid decrease in filtration efficiency (Brown and Wake, 1999; Brown et al., 1988; Chen et al., 1993; Huang, 2013; Li and Jo, 2010; Yang et al., 2007).

In order to reduce the negative effects related to neutralization of electrets produced by corona discharge, works aimed at developing highly effective filtering materials with the use of other methods were carried out (Angadjivand, 1996; Carter et al., 1988; Jones et al., 2002; Nguyen 2005; Yang and Lee, 2005). Interesting results were obtained in case of low-temperature plasma treatment of polypropylene filtering nonwovens (Urbaniak-Domagała et al., 2010). This technique seemed to provide interesting results in the area of improving the efficiency of non-electret filtering materials towards solid aerosol particles. Brochocka et al. (2014) continued these works in relation to liquid aerosol particles. In their study low-pressure low-temperature plasma treatment was applied to polycarbonate nonwovens using process gases such as argon and oxygen. The effectiveness of treatment was assessed on the basis of the results of the penetration of nonwovens by paraffin oil mist and airflow resistance at linear velocity of 0.15 m/s. The effects of plasma modification on polycarbonate nonwovens, especially on their surface morphology and chemical structure, were evaluated by SEM microscopy and FTIR spectroscopy. The results indicated that argon plasma treatment is a good tool for improving the filtration properties of polycarbonate filtering materials. Majchrzycka (2013) also showed that the process of low-temperature argon plasma treatment results in a significant increase in the filtration efficiency of melt-blown nonwovens and that these materials present low tendency to losing their acquired filtering efficiency during the time they are treated with paraffin oil mist.

To-date there have been few studies devoted to the use of low-temperature plasma in the improvement of efficiency of filtering nonwovens towards liquid aerosols with use of gases that are not chemically neutral. In this case, it should be noted that while modifying a surface layer of polymers using low-temperature plasma, four basic phenomena may occur: purification of the material surface, etching (leading to removal of some material that is loosely connected with the surface), cross-linking of the particles (causing cohesion) and creation of new chemical structures (mainly under the influence of free radical, oxygen and steam). Due to synergy, interaction of these phenomena in shaping an appropriate adhesion between the surface of a solid matter and a particle of liquid aerosol is a complex process. The

influence of individual phenomena depends mainly on the type of material, type of gas filling the discharge chamber, construction of this chamber, temperature and pressure in the chamber, individual charge energy and the time of interaction of plasma with the material (Matsuo, 2008). That is why, each time when new application of low-temperature plasma modifications of polymer surface are considered, it is necessary to evaluate the influence of individual parameters of this treatment on the predicted effects.

Therefore, the aim of this paper is to analyse the influence of low-temperature plasma treatment conditions (i.e. gas type, gas flow velocity, time of treatment and electric power required for the initiation and continuation of the plasma treatment) on the improvement of efficiency of filtering nonwovens towards liquid aerosols and to evaluate the stability of the obtained effects in the conditions of simulated use of RPE.

2. MATERIALS AND METHODS

2.1. Materials

Filtering nonwovens were produced in the Laboratory of Respiratory Protective Devices of the Central Institute for Labour Protection – National Research Institute, at the experimental line for melt-blown nonwovens production. Manufacturer's characteristics of Malen P F401 polypropylene (PP), used in the tests are presented in Table 1, while the properties of filtering nonwovens are shown in Table 2.

Table 1. Properties of PP granulate

Parameter	Values
Density, g/cm^3	0.905 – 0.917
Flow speed, g/10min	2.4 – 3.2
Water content, %	max. 0.01
Softening point,°C	145 – 155
Melting point, °C	160 – 170
Intrinsic viscosity, cm^3/g	190

Table 2. Properties of PP nonwovens used for modification

Parameter	Values
[1)] nonwoven thickness, mm	1.66
[2)] average diameter of fibres, μm	1.5
[2)] max diameter of fibres, μm	4.4
[2)] min diameter of fibres, μm	0.6
[3)] surface weight of nonwovens, g/m^2	90

[1)] test according to ISO 9073-2 standard (ISO 9073-2:1995, 1995); [2)] using SEM scanning electron microscopy method based on n = 300 measurements; [3)] test according to EN 29073-1 standard (EN 29073-1:1992, 1992)

2.2. Plasma modification

The low-temperature plasma treatment process was carried out at the Department of Material and Commodity Sciences and Textile Metrology, Lodz University of Technology. The treatment was

performed with a commercial low-temperature, radio-frequency (13.56 MHz) plasma generator (CD 400 PLC Roll Cassette, Europlasma, Belgium) equipped with two parallel rectangular electrodes connected to an alternative voltage. The conditions in which the treatment was carried out (gas type, gas flow velocity, time of treatment and electric power required for the initiation and continuation of the plasma treatment) were controlled automatically and varied depending on the chosen modification variant (Table 3).

Table 3. The range of the plasma treatment conditions

Parameter	Value
Gas type	argon, atmospheric air, oxygen, nitrogen
Gas flow velocity [cssm]	50 – 700
Time of treatment [s]	30 – 600
Power supplied to the electrodes [W]	30 – 200

The neutral gas (argon) was chosen based on the assumption that the etching of the fibres' surface (physical modification) will result in the increased filtration efficiency of the filtering nonwoven, while in case of air, nitrogen and oxygen, the improvement of the filtration efficiency should be achieved due to increased free energy of fibres' surface (chemical modification) (Morent et al., 2008; Takemura et al., 2008; Verschuren et al., 2007). The selection of parameters of low-temperature plasma treatment was performed on the basis of literature data (Buyle, 2009; Gotoh and Yasukawa, 2010; Morent et al., 2008; Takemura et al., 2008; Verschuren et al., 2007) and previous experiences of the Authors.

Prior to the modification, samples of filtering nonwovens were placed between the electrodes. A three-stage treatment procedure was established:

- evacuation of the vacuum chamber for 30 minutes,
- surface modification with argon, atmospheric air, nitrogen or oxygen plasma (depending on the selected modification variant),
- conditioning of the sample after the treatment for 30 min.

In order to assess the influence of storage on the effect of plasma treatment samples of nonwovens were stored for 12 months in horizontal non-compressed state in stable climatic conditions (23°C ± 5% and 50% ± 10%). To assess changes in nonwoven properties due to elevated temperature, part of the plasma treated samples was placed in a dryer in horizontal non-compressed state at a temperature of 70°C and relative humidity of 20% (climatic conditions according to the EN 13274-5 standard (EN 13274-5:2001, 2001)). Samples of nonwovens to be tested for the influence of elevated humidity on the effect of plasma treatment were stored in the desiccator, under the saturation conditions (relative humidity of 100%) for 24 h (climatic conditions according to the EN 13274-5 standard (EN 13274-5:2001, 2001)).

2.3. Test methods

According to the requirements of European standards harmonized with Directive 89/686/EEC (89/686/EEC, 1989), the assessment of the effectiveness of filtering RPE should include, among others, testing of the penetration of solid (sodium chloride aerosol) and liquid particles (paraffin oil mist). In this case the use of paraffin oil mist as a challenge aerosol represents the worst-case scenario in terms of collection efficiency. Thus, the filtering material that meets the requirements for paraffin oil mist penetration should always meet the requirements for sodium chloride aerosol penetration. Therefore, in order to assess the effect of low-temperature plasma treatment on the efficiency of filtering nonwovens after storage as well as temperature and humidity conditioning nonwoven samples were tested in terms of penetration of a paraffin oil mist using a test stand presented in Fig. 1.

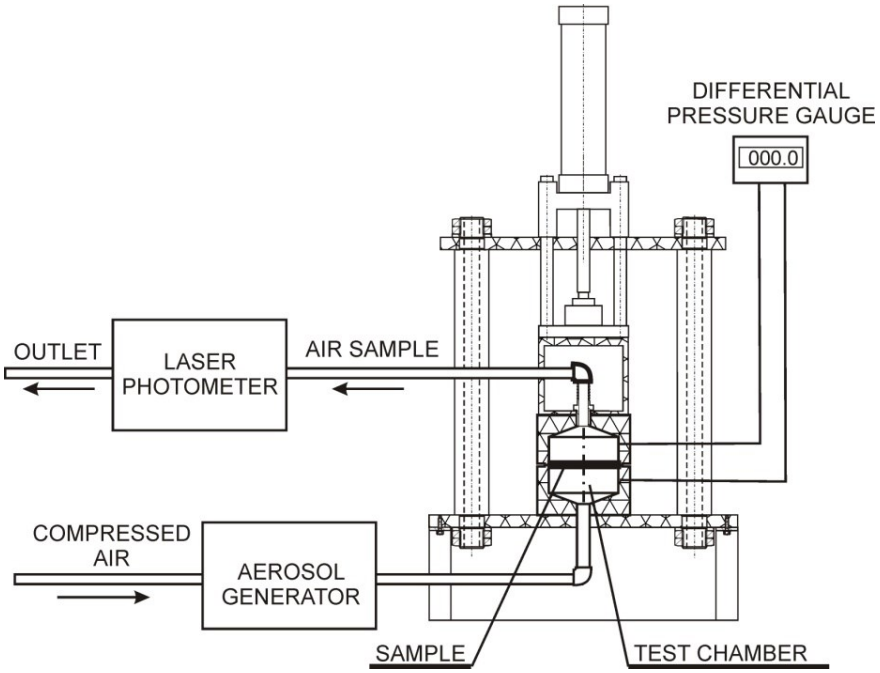

Fig. 1. The scheme of experimental set-up for testing filtration parameters of nonwoven materials

During tests the challenge aerosol was passed at a predetermined linear velocity through a nonwoven sample mounted in a sample holder of 100 mm diameter. Particle size distribution was log-normal with a median of Stokes diameter of 0.4 μm and geometric standard deviation of 1.82. Concentration of paraffin oil mist was measured with laser photometer AP2E (Lorenz, Germany) upstream and downstream of the sample. Results were collected in the initial stage of filtration, after 3 min from the beginning of each test. Penetration was calculated from the following equation:

$$P = \frac{l_2 - l_0}{l_1 - l_0} \cdot 100\% \tag{1}$$

Additionally, airflow resistance through the filtering material was measured by establishing pressure drop on a filter according to methodology described in the EN 13274-3 standard (EN 13274-3:2001, 2001).

In order to evaluate the influence of the factor j (where j = T, RH, S for thermal conditioning, humidity influence or storage, respectively) on the properties of nonwovens, which underwent plasma modification, the relative change in penetration ΔP_j resulting from this factor was calculated from the following equation:

$$\Delta P_j = \frac{\left(P_j - P\right)}{P} \cdot 100\% \tag{2}$$

Analogically, the relative change in airflow resistance ΔO_j through the filtering nonwovens was established.

Scanning electron microscope (SEM) images were obtained by Nova NanoSEM 230, (FEI, USA) microscope. The images were taken in order to assess changes in the surface morphology of nonwoven fibres as a result of plasma treatment.

The chemical properties of the surface of samples exposed to different treatments were examined with use of Fourier-transformed infrared spectroscopy on a double-beam spectrophotometer FTIR–Nicolet 6700 (Thermo Fisher Scientific Inc., USA) equipped with a reflective adaptor type ITR. The obtained spectra were analyzed using OMNIC 8.0.380 software.

3. RESULTS AND DISCUSSION

The influence of plasma treatment on the filtration efficiency of nonwovens was established by determining changes in penetration and in airflow resistance through the filtering nonwovens after modification with various process gases and also with the use of various treatment parameters. The test results were presented in Table 4.

Table 4. Changes in the filtering parameters of nonwovens as a result of plasma treatment

Treatment variant	Gas flow velocity [cssm]	Power [W]	Time [s]	P_R [%]	P [%]	O_R [Pa]	O [Pa]	ΔP [%]*	ΔO [%]*
Nitrogen									
1	500	100	30	3.7	3.2	306	284	-14	-8
2	500	100	60	3.7	2.9	306	308	-22	1
3	500	100	120	3.7	3.6	306	365	-3	16
4	700	50	30	5.5	4.8	255	323	-13	21
5	700	50	60	5.5	5.3	255	226	-4	-13
6	700	50	120	5.5	5.0	255	278	-9	8
7	700	100	30	6.4	4.8	245	339	-25	28
8	700	100	60	6.4	5.1	245	242	-20	-1
9	700	100	120	6.4	6.3	245	215	-2	-14
Oxygen									
1	500	100	30	3.2	3.6	376	339	13	-11
2	500	100	60	3.2	4.9	376	323	53	-16
3	500	100	120	3.2	5.8	376	273	81	-38
4	700	50	30	4.6	3.6	340	401	-22	15
5	700	50	60	5.5	4.2	285	324	-24	12
6	700	50	120	5.5	3.6	285	342	-35	17
7	700	100	30	3.8	3.8	350	313	0	-12
8	700	100	60	3.8	3.9	350	273	3	-28
9	700	100	120	9.0	8.7	300	255	-3	-18
Air									
1	500	100	30	5.0	4.9	348	249	-2	-40
2	500	100	60	5.0	4.1	348	368	-18	5
3	500	100	120	4.5	3.1	340	402	-31	15
4	700	50	30	4.5	2.9	373	438	-36	15
5	700	50	60	4.5	2.6	399	480	-42	17
6	700	50	120	3.2	3.1	315	328	-3	4
7	700	100	30	3.2	3.5	343	388	9	12
8	700	100	60	3.2	4.3	307	373	34	18
9	700	100	120	3.5	5.3	337	337	51	0
Argon									
1	50	30	300	3.5	1.8	332	388	-50	14
2	50	30	600	2.8	2.4	339	237	-14	-43
3	50	100	300	2.7	0.9	345	378	-69	9
4	50	100	600	9.2	1.7	210	309	-82	32
5	50	200	300	17.0	6.6	230	209	-61	-10
6	50	200	600	16.0	6.2	228	235	-61	3
7	50	100	600	2.8	0.8	325	432	-73	25
8	50	100	600	15.0	7.2	229	224	-52	-2
9	50	100	600	12.0	6.9	196	251	-43	22

*) color code corresponding to decreasing (green) or increasing (red) values of penetration / air flow resistance was applied

In case of argon plasma treatment, a drop in penetration of paraffin oil mist was observed, reaching up to 82% of the reference value, which was in compliance with the previously published studies (Brochocka 2014). Contradictory results were obtained for the variants of nonwovens modified in plasma with the use of gases that were chemically reactive.

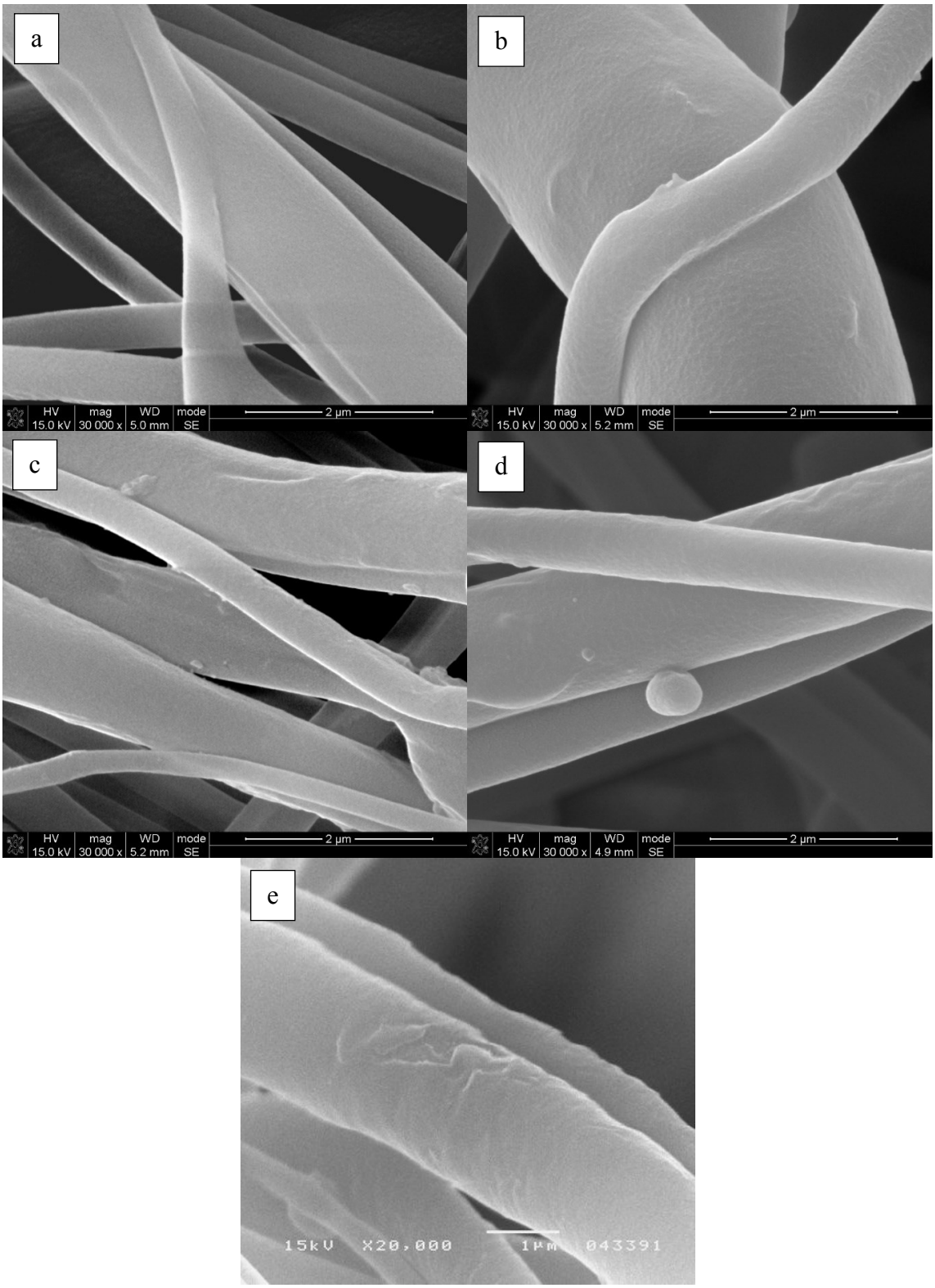

Fig. 2. SEM images of fibres of a) untreated nonwovens and nonwovens after treatment with b) nitrogen (700 cssm/100 W/60 s), c) oxygen (700 cssm/50 W/120 s), d) air (700 cssm/50 W/60 s), and e) argon (50 cssm/100 W/600 s)

The results of research on the penetration of paraffin oil mist obtained for nonwovens modified in nitrogen, oxygen and air show that in these cases interaction of low-temperature plasma influenced the efficiency of filtration in various ways. By and large, the processes of activating the surface caused both an increase in the penetration of paraffin oil mist (up to 81% for the oxygen plasma for nonwovens before modification – 500 cssm, 100 W, 120 s) or its decrease (up to -42% with reference to nonwovens before modification in case of applying air plasma – 700 cssm, 50 W, 60 s). However, it was not possible to establish a systematic dependence of relative change in penetration against their process parameters.

The results of tests concerning the airflow resistance (directly linked with the breathing resistance when used in the construction of RPE) in the majority of cases show an increasing tendency. However, it needs to be emphasized that these changes (on average around 30% of the initial value) are not an issue when applying them in RPE. They may be explained by the flattening of nonwovens during modification in a discharge chamber or by structural changes of nonwovens resulting from the movement of the loose fibres and creating compact and uneven filtering structures. The most beneficial relative changes in the airflow resistance were observed in case of oxygen plasma (decrease of the airflow resistance for the majority of modification variants).

SEM was employed to investigate the morphologies of the PP nonwovens treated with nitrogen, oxygen, air and argon plasma. The images obtained for selected modification variants are shown in Figure 2 (similar effects were obtained for other variants). For comparison, the SEM image of pristine PP nonwoven was also obtained under the identical conditions.

Modification of filtering nonwovens in argon plasma resulted in significant changes of fibre surface in relation to the untreated sample. With the lengthening of the treatment time and increasing power of discharge, a slight growth in the number deformations and non-uniformities on the fibre surface was observed due to the etching, which is consistent with the results described in the literature (Contal et al., 2004; Frising et al., 2005; Raynor and Leith, 2000; Walsh and Stenhouse, 1997). No significant differences in the morphology of fibre surface were observed for the nonwovens modified in nitrogen, oxygen or air plasma, regardless of the selected processing parameters. This conclusion is in compliance with the results described by Brochocka et al. (2014).

Figure 3 presents IR spectrograms for samples of nonwovens treated with nitrogen, oxygen, air, and argon plasma. The spectrograms show IR radiation absorption (Abs.) as a function of wavenumber.

Absorptive spectra of IR radiation of nonwoven samples for which the best improvement of filtration efficiency was achieved were performed in the range of 3500-700 cm^{-1} for argon and 1500-1000 cm^{-1} for other gases. The results show subtle changes in their chemical structure caused by interaction with the plasma environment. These changes are of varied character, depending on the type of the applied process gas.

IR spectrograms of nonwovens treated with nitrogen present absorption on a low level in a wider range of wavenumbers as opposed to the interaction with oxygen plasma: from 1300 cm^{-1} to 1510 cm^{-1}. A selective absorption of PP nonwovens in the ranges: 1320, 1340, 1390, 1420, 1488, 1506 cm^{-1} may be observed. The majority of ranges discovered are the same as those for the PP surface treated with air plasma. IR absorption of nonwovens with lower wavenumbers may be related to the presence of nitrate ions NO_2 (identified in the range of 1320 cm^{-1}, group - C –N-, identified by valence vibrations in the range of 1350-1280 cm^{-1}, group - CH_3, identified by deformation vibrations 1340-1360 cm^{-1} in groups – CO-CH_3 and group C-H identified by deformation vibrations in hydrocarbons with a branched chain.

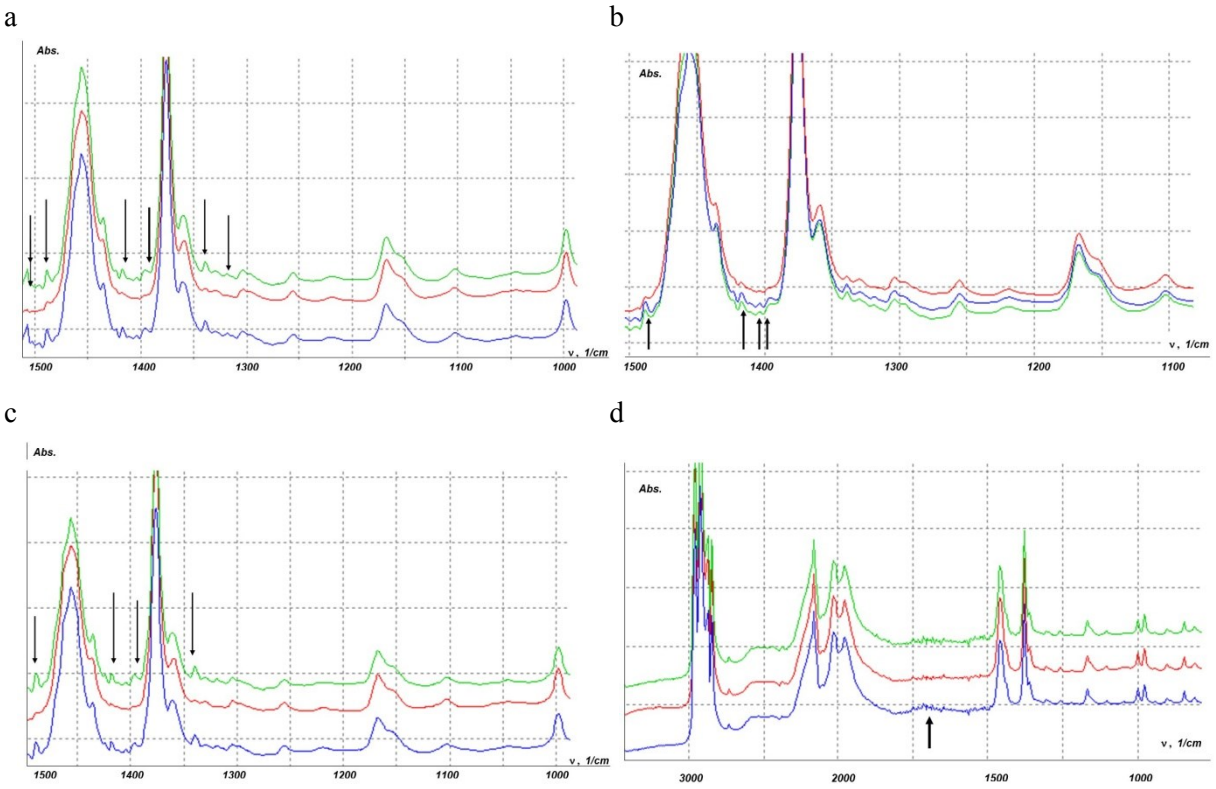

Fig. 3. IR absorption spectrum of the samples of nonwovens treated with a) nitrogen, b) oxygen, c) air and d) argon plasma; (red line – untreated sample, green and blue – plasma treated sample in two repetitions)

Nonwovens treated with oxygen plasma show absorptive ranges of low intensity, although they are well developed at the wavenumbers (1385, 1403, 1416, 1488) cm^{-1}. For nonwovens treated with air plasma selective absorption was observed at the wavenumbers (1340, 1390, 1416, 1488) cm^{-1}. Absorption may be caused by symmetric deformation vibrations of – CH_3 in isopropyl and dimethyl group (1390-1370) cm^{-1}, symmetric deformation vibrations of – CH_3 in t-butyl groups (1406-1393) cm^{-1} deformation vibrations of –O-H group (1400-1340) cm^{-1}, flat deformation vibration of C- (1410-1400) cm^{-1}, flat deformation vibration of C-H (1420-1400) cm^{-1} in compounds such as RR`C==CH_2 and RHC==CH_2 (1410-1400) cm^{-1}, scissoring vibrations of - CH_2 in linear aliphatic chains 1467 cm^{-1} or asymmetric valence vibrations of – CH_3.

Nonwovens treated with argon plasma demonstrate a new type of absorption for a range of wavenumbers (1660-1720) cm^{-1}. Absorption in this range may be caused by valence vibrations of –C=C, -C=C- groups. These groups, which are not present in non-modified PP nonwovens, may occur in chemical processes between polymer and plasma particles and in the processes of polymer crosslinking under the influence of UV radiation emitted by plasma. This type of absorption did not arise in the samples of nonwovens treated with oxygen, nitrogen and air plasma.

Analysis of IR absorption spectrograms showed that the mechanism of interaction of PP nonwovens with oxygen, nitrogen and air plasma is similar. The differences result from the efficiency of the processes. No evident relation between chemical modification of the fibres surface and the improvement of filtration efficiency was observed.

Test results related to the influence of elevated temperature and relative humidity on the effect of plasma modification of PP nonwovens is presented in Table 5.

The influence of storage on the filtering and usage properties of nonwovens was evaluated for two selected types of samples that underwent modification in air and argon plasma (Table 6).

Table 5. Results of tests on the influence of elevated temperature and humidity on samples of filtering nonwovens, which underwent the plasma treatment

No.	P [%]	P_T [%]	P_{RH} [%]	O [Pa]	O_T [Pa]	O_{RH} [Pa]	ΔP_T [%]*	ΔP_{RH} [%]*	ΔO_T [%]*	ΔO_{RH} [%]*
Nitrogen										
1	4.0	2.8	-	367	396	-	-31	-	8	-
2	5.3	5.5	-	317	331	-	4	-	4	-
3	5.0	4.2	-	338	383	-	-16	-	13	-
4	5.0	5.4	-	312	317	-	8	-	2	-
5	1.6	-	2	474	-	447	-	25	-	-6
6	6.1	-	4.8	328	-	337	-	-21	-	3
7	4.5	-	4.0	365	-	396	-	-11	-	8
8	4.1	-	5.2	344	-	324	-	27	-	-6
Oxygen										
1	5.1	4.3	-	341	364	-	-16	-	7	-
2	3.0	2.6	-	411	434	-	-13	-	6	-
3	3.0	2.3	-	430	458	-	-23	-	7	-
4	3.3	3.6	-	405	400	-	9	-	-1	-
5	4.6	-	4.3	357	-	364	-	-7	-	2
6	9.1	-	7.9	320	-	321	-	-13	-	0
7	2.4	-	2.4	436	-	438	-	0	-	1
8	3.7	-	3.3	390	-	404	-	-11	-	4
Air										
1	6.0	5.9	-	340	346	-	-1	-	2	-
2	3.2	3.3	-	435	427	-	5	-	-2	-
3	4.0	4.1	-	375	345	-	4	-	-8	-
4	2.6	2.9	-	440	417	-	14	-	-5	-
5	7.7	-	8.1	314	-	300	-	3	-	-4
6	3.0	-	3.3	435	-	418	-	12	-	-4
7	4.2	-	4.5	358	-	338	-	7	-	-6
8	2.6	-	3.2	407	-	377	-	25	-	-7
Argon										
1	3.6	5.0	-	366	369	-	39	-	1	-
2	3.7	4.6	-	370	377	-	24	-	2	-
3	1.5	2.8	-	490	463	-	83	-	-5	-
4	9.0	5.9	-	345	348	-	-35	-	1	-
5	1.6	-	1.5	459	-	501	-	-6	-	9
6	2.7	-	3.9	382	-	404	-	44	-	6
7	5.6	-	5.0	340	-	347	-	-11	-	2
8	2.6	-	2.9	371	-	381	-	12	-	3

*) color code corresponding to decreasing (green) or increasing (red) values of penetration / air flow resistance was applied

In all the tested variants of filtering nonwovens no significant influence of the time of storage (12 months) or of elevated temperature and relative humidity on durability of the obtained results of plasma modification were observed. The modification of filtering nonwovens in argon plasma caused permanent changes on the surface of fibres, which in turn resulted in the improvement of filtration efficiency. Therefore, it may be concluded that the technique of low-temperature plasma treatment is a promising direction of further studies so as to improve the filtering properties of nonwovens used in the construction of RPE against harmful aerosols.

Table 6. Test results of paraffin oil mist penetration and airflow resistance before and after storage

No.	P [%]	P_S [%]	O [Pa]	O_S [Pa]	ΔP_S [%]	ΔO_S [%]
Air						
1	3.4	2.04	319	295	-40	-8
2	3.4	2.94	319	247	-14	-29
3	7.3	5.44	259	232	-25	-12
4	7.3	5.42	259	224	-26	-15
5	5.9	4.20	263	217	-29	-21
6	5.9	4.09	263	229	-31	-15
Argon						
1	2.4	1.55	373	345	-35	-8
2	3.5	1.75	332	388	-50	14
3	2.8	2.4	339	237	-14	-43
4	2.7	1.25	343	378	-54	9
5	2.7	0.85	345	378	-69	9
7	2.5	0.66	315	397	-74	21
8	2.8	0.76	325	432	-73	25

4. CONCLUSIONS

In the paper we investigated a possibility of applying low-temperature plasma treatment to improve the filtration efficiency of melt-blown nonwovens. We also checked whether the effect of plasma modification changes after storage and conditioning in elevated temperature and increased relative humidity.

The results of the study show that in terms of an improvement of filtration efficiency low-temperature argon plasma treatment is superior to the processing with other gases. In case of argon plasma treatment up to 82% improvement of penetration of paraffin oil mist in relation to the untreated sample was achieved (for 50 cssm/100 W/600 s). For other gases relative improvement of penetration caused by plasma treatment was 25% for nitrogen (700 cssm/100 W/300 s), 35% for oxygen (700 cssm/50 W/120 s), and 42% for air (700 cssm/50 W/60 s).

The results presented in the paper indicate that argon plasma treatment could be used to improve the properties of filtering melt-blown nonwovens used in the construction of RPE along with more commonly used corona discharge.

The publication is based on the results of Phase I of the National Programme "Safety and working conditions improvement", funded in the years 2008-2010 in the area of research and development works by the Ministry of Science and Higher Education / The National Centre for Research and Development. The Programme coordinator: Central Institute for Labour Protection – National Research Institute.

SYMBOLS

j designation of a factor, which influences filtering parameters of nonwovens, it can be either thermal conditioning (T), humidity influence (RH) or storage (S)

l_1 the photometer reading in front of the filter

l_2 the photometer reading behind the filter
l_0 the photometer reading for clean air
O airflow resistance of the nonwoven before the factor j has been applied, Pa
O_j airflow resistance of the nonwoven after the factor j has been applied, Pa
ΔO_j relative change in airflow resistance of the nonwoven resulting from the factor j, Pa
O_R airflow resistance of the nonwoven prior to the plasma treatment, prior to the plasma treatment, Pa
P aerosol penetration through the plasma treated nonwoven before the factor j has been applied, %
P_j aerosol penetration through the plasma treated nonwoven after the factor j has been applied, %
ΔP_j relative change in penetration of aerosol through the nonwoven resulting from the factor j, %
P_R aerosol penetration through the nonwoven prior to the plasma treatment, %

REFERENCES

Angadjivand S.A., Jones M.E., Meyer D.E., 1996. Method of charging electret filter media. Patent no. WO 1995005501 A2.

Barrett L.W., Rousseau A.D., 1998. Aerosol loading performance of electret filter media. *Am. Ind. Hyg. Assoc. J.*, 59, 532–9. DOI: 10.1080/15428119891010703.

Brochocka A., Mian I., Majchrzycka K., Sielski J., Tyczkowski J., 2014. Plasma modified polycarbonate nonwovens as filtering material for liquid aerosols. *Fibres Text. East. Eur.*, 22, 76–80.

Brochocka A., 2001. Characteristics of melt-blown filter materials produced by simultaneous blowing of polymer melt from two extruders. *Fibres Text. East. Eur.*, 4, 66–9.

Brown R., Wake D., 1999. Loading filters with monodisperse aerosols. *J. Aerosol Sci.,* 30, 227–34. DOI: 10.1016/s0021-8502(98)00042-1.

Brown R.C., Wake D., Gray R., Blackford D.B., Bostock G.J., 1988. Effect of industrial aerosols on the performance of electrically charged filter material. *Ann. Occup. Hyg.*, 32, 271–94. DOI: 10.1093/annhyg/32.3.271.

Brown R.C., 1993. *Air filtration: An integrated approach to the theory and applications of fibrous filters*. Pergamon Press, Oxford.

Buyle G., 2009. Nanoscale finishing of textiles via plasma treatment. *Mater. Technol.*, 24, 46–51. DOI: 10.1179/175355509x417954.

Carter D.H., Howells R.D., Stern R.M., Temperante J.A., 1988. Fluorochemical oxazolidinones. Patent no. EP 0260011 A2.

Chen C.C., Lehtimäki M., Willeke K., 1993. Loading and filtration characteristics of filtering facepieces. *Am. Ind. Hyg. Assoc. J.*, 54, 51–60. DOI: 10.1080/15298669391354324.

Contal P., Simao J., Thomas D., Frising T., Callé S., Appert-Collin J.C., Bémer D., 2004. Clogging of fibre filters by submicron droplets. Phenomena and influence of operating conditions. *J. Aerosol. Sci.*, 35, 263–78. DOI: 10.1016/j.jaerosci.2003.07.003.

Council Directive 89/686/EEC of 21 December 1989 on the approximation of the laws of the Member States relating to personal protective equipment.

EN 13274-3:2001. Respiratory protective devices. Methods of test. Determination of breathing resistance. 2001.

EN 13274-5:2001. Respiratory protective devices. Methods of test. Climatic conditions. 2001.

EN 29073-1:1992. Methods of test for nonwovens. Methods of test for nonwovens. Determination of mass per unit area. 1992.

Frising T., Thomas D., Bémer D., Contal P., 2005. Clogging of fibrous filters by liquid aerosol particles: Experimental and phenomenological modelling study. *Chem. Eng. Sci.*, 60, 2751–2762. DOI: 10.1016/j.ces.2004.12.026.

Gotoh K., Yasukawa A., 2010. Atmospheric pressure plasma modification of polyester fabric for improvement of textile-specific properties. *Text. Res. J.*, 81, 368–78. DOI: 10.1177/0040517510387207.

Gougeon R., Boulaud D., Renoux A., 1996. Comparison of data from model fibre filters with diffusion, interception and inertial deposition models. *Chem. Eng. Commun.*, 151, 19–39. DOI: 10.1080/00986449608936539.

Huang S.-H., Chen C.-W., Kuo Y.-M., Lai C.-Y., McKay R., Chen C.-C., 2013. Factors Affecting filter penetration and quality factor of particulate respirators. *Aerosol Air Qual. Res.*, 13, 162–71. DOI: 10.4209/aaqr.2012.07.0179.

ISO 9073-2:1995. Textiles. Test methods for nonwovens. Part 2: Determination of thickness. 1995.

Jones M.E., Lyons C.S., Redmond D.B., Solomon J.L., Angadjivand S.A., 2002. Fluorinated electret. Patent no. US 2002/0152892 A1.

Kanaoka C., Emi H., Otani Y., Iiyama T., 1987. Effect of charging state of particles on electret filtration. *Aerosol Sci. Technol.*, 7, 1–13. DOI: 10.1080/02786828708959142.

Li K., Jo Y.M., 2010. Dust collection by a fibre bundle electret filter in an MVAC system. *Aerosol Sci. Technol.*, 44, 578–87. DOI: 10.1080/02786826.2010.481227.

Majchrzycka K., 2013. Modification of polymeric filtration nonwovens by treatment with low-temperature plasma as a method for improvement of aerosol removal efficiency. *Przem. Chem.*, 92, 1750–4.

Martin S.B., Moyer E.S., 2000. Electrostatic respirator filter media: filter efficiency and most penetrating particle size effects. *Appl. Occup. Environ. Hyg.*, 15, 609–17. DOI: 10.1080/10473220050075617.

Matsuo T., 2008. Fibre materials for advanced technical textiles. *Text. Prog.*, 40, 87–121. DOI: 10.1080/00405160802133028.

Morent R., De Geyter N., Verschuren J., De Clerck K., Kiekens P., Leys C., 2008. Non-thermal plasma treatment of textiles. *Surf. Coatings Technol.*, 202, 3427–49. DOI: 10.1016/j.surfcoat.2007.12.027.

Nguyen L.Q., 2005. Method of making a melt-blown filter medium for use in air filters in internal combustion engines and product. Patent no. US 20040172930 A1.

Pich J., Emi H., Kanaoka C., 1987. Coulombic deposition mechanism in electret filters. *J. Aerosol Sci.*, 18, 29–35. DOI: 10.1016/0021-8502(87)90006-1.

Raynor P.C., Leith D., 2000. The influence of accumulated liquid on fibrous filter performance. *J. Aerosol Sci.*, 31, 19–34. DOI: 10.1016/s0021-8502(99)00029-4.

Takemura Y., Yamaguchi N., Hara T., 2008. Study on surface modification of polymer films by using atmospheric plasma jet source. *Jpn. J. Appl. Phys.*, 5644–7. DOI: 10.1143/jjap.47.5644.

Urbaniak-Domagała W., Henryk W., Szymanowski H., Majchrzycka K., Brochocka A., 2010. Plasma modification of filter nonwovens used for the protection of respiratory tracts. *Fibres Text. East. Eur.*, 18, 94–9.

Verschuren J., Kiekens P., Leys C., 2007. Textile-specific properties that influence plasma treatment effect creation and effect characterization. *Text. Res. J.*, 77, 727–33. DOI: 10.1177/0040517507078820.

Walsh D.C., Stenhouse J.I.T., 1997. The effect of particle size, charge, and composition on the loading characteristics of an electrically active fibrous filter material. *J. Aerosol Sci.*, 28, 307–21. DOI: 10.1016/s0021-8502(96)00434-x.

Yang S., Lee G.W.M., 2005. Filtration characteristics of a fibrous filter pretreated with anionic surfactants for monodisperse solid aerosols. *J. Aerosol Sci*., 36, 419–37. DOI: 10.1016/j.jaerosci.2004.10.002.

Yang S., Lee W.-M.G., Huang H.-L., Huang Y.-C., Luo C.-H., Wu C.-C., Yu K.-P., 2007. Aerosol penetration properties of an electret filter with submicron aerosols with various operating factors. *J. Environ. Sci. Health A. Tox. Hazard Subst. Environ. Eng.*, 42, 51–7. DOI: 10.1080/10934520601015651.

Received 21 June 2016
Received in revised form 13 March 2017
Accepted 20 March 2017

www.czasopisma.pan.pl www.journals.pan.pl
Chemical and Process Engineering 2017, 38 (2), 209-215
DOI: 10.1515/cpe-2017-0016

KINETICS OF ENANTIOMERICALLY ENRICHED SYNTHESIS OF SOLKETAL ESTERS USING NATIVE AND SBA-15 SUPPORTED *P. FLUORESCENS* LIPASE

Aurelia Zniszczoł*[1], Katarzyna Szymańska[1], Jacek Kocurek[1], Jolanta Bryjak[2], Krzysztof Walczak[1], Andrzej Jarzębski*[1,2]

[1]Department of Chemical Engineering and Process Design, Silesian University of Technology, 44-100 Gliwice, Ks. M. Strzody 7, Poland

[2]Department of Bioroganic Chemistry, Faculty of Chemistry, Wrocław University of Technology, 50-370 Wrocław, Wybrzeże Wyspiańskiego 27, Poland

[3]Institute of Chemical Engineering, Polish Academy of Sciences, 44-100 Gliwice, Bałtycka 5, Poland

Dedicated to Prof. Leon Gradoń on the occasion of his 70th birthday

The studies showed that alkaline lipase from Pseudomonas fluorescens enables an irreversible transesterification of vinyl esters to give enantiomeric excess (eeR) of about 80% using vinyl butyrate as acyl donor and diisopropyl ether as a solvent, at partially optimized conditions. For the native lipase the process was adequately described by a five-parameter Ping-Pong Bi Bi model for both enantiomers plus expression accounting for the formation of enzyme-acyl donor complex, but for the same lipase supported on mesoporous materials of SBA-15-Oc type, R-product inhibition also had to be taken into account. The use of hydrophobic support increased by more than two-fold the rate of the S-solketal conversion but even more that of R-solketal. Thus the immobilization of lipase had very positive effect on the process kinetics but decreased its enantioselectivity.

Keywords: bioenantioselectivity, solketal, ping-pong kinetics, transesterification

1. INTRODUCTION

Racemic solketal (isopropylidine glycerol, IPG) is an inexpensive reagent accessible from glycerine and acetone, also as a by-product in biofuels manufacturing, whereas enentiomerically pure (R)- and (S)-solketal esters are in high demand, despite high price due to their wide application as precursors of important biologically active compounds such as glycerylphospholipids, β-blockers, e.g. (S)-propranolol, prostaglandin or leucotrienes (Boncel et al., 2013; Hanson, 1991; Hof and Kellog, 1996; Zniszczoł, et al., 2016).

Thus a rational solution would be a resolution of racemic mixtures of IPG using enantioselective catalysts, e.g. enzymes (Majewska et al., 2006). In this light a development of a method affording high enantiomeric purity as well as formulation of a mathematical model of the reaction kinetics emerges as an important goal. The model itself may also foster development of more effective catalysts, for this and related reactions.

*Corresponding author, e-mail: Andrzej.Jarzebski@polsl.pl, Aurelia.Zniszczol@gmail.com

The performed studies (Zniszczoł, 2015) revealed that among three possible synthesis pathways for enentiomerically enriched IPG esters: i) enantioselective esterification involving carboxylic acids, ii) enantioselective transesterification of vinyl esters, and iii) enentioselective hydrolysis of solketal esters, only the second one offered promising results. These studies also showed that alkaline lipase from *Pseudomonas fluorescens* enables an irreversible transesterification of vinyl esters (acyl donors) to give enantiomeric excess (ee_R) of about 80% using vinyl butyrate as acyl donor and diisopropyl ether as a solvent. Experiments with the immobilized enzyme were also performed to demonstrate that the use of carriers with hydrophobic surface: multiwall carbon nanotubes - MWCNT or mesoporous silica of SBA-15 type, the surface of which was modified with n-octyl groups (SBA-15-Oc), significantly increased biocatalysts activity, although internal diffusion limitation of activity was also observed (Boncel et al., 2013; Zniszczoł et al., 2016).

While representative experimental results and details of biocatalysts preparation have already been published (Boncel et al., 2013; Zniszczoł et al., 2016), the kinetics of IPG enrichment has not been reported, and a model capable of describing it can be of major importance for both process engineers and for the development of even more effective biocatalysts. Therefore, the kinetics of racemic IPG resolution was studied in more detail, not only using the native enzyme but also that attached to SBA-15 silicates owing to their widespread application as enzyme carriers.

2. RESULTS AND DISCUSSION

2.1. Base kinetic model

Scores of studies demonstrated that the Ping-Pong Bi Bi family of mechanisms describe lipase-mediated transesterifications and that inhibitory effects usually need to be taken into account (Barros et al., 2010; Pavia et al., 2000; Pilarek and Szewczyk, 2007). Yet, in the reaction system under study the situation is more complex since *P. fluorescence* lipase is not fully (100%) enantioselective to racemic IPG, and in addition to conversion preference for *S* enantiomer, also *R* compound is increasingly involved. Therefore, the conversion of both solketal enantiomers had to be considered, and clearly, the formation of enzyme-acyl complex also had to be taken into account. In effect the base model of the process was described by the scheme:

$$E + DAc \underset{k_{-1}}{\overset{k_1}{\rightleftarrows}} EAc + P_U \tag{1}$$

$$EAc + S_{Alc} \underset{k_{-2}}{\overset{k_2}{\rightleftarrows}} (EAcS_{Alc}) \xrightarrow{k_3} E + R_P \tag{2}$$

$$EAc + R_{Alc} \underset{k_{-4}}{\overset{k_4}{\rightleftarrows}} (EAcR_{Alc}) \xrightarrow{k_5} E + S_P \tag{3}$$

where DAc is acyl donor, S_{Alc} and R_{Alc} designate alcohols of *S* and *R* configuration, S_P and R_P are reaction products of *S* and *R* configuration, respectively and P_U is product of a side reaction. However, as vinyl alcohol produced in the first reaction is unstable and quickly tautomerizes to vinyl acetate, thus this reaction may be considered irreversible and hence k_{-1} can be assumed to be equal zero, which simplifies the model. Taking this into account and assuming that the reactions have simple order kinetics and also no loss of species to ambient temperature (e.g. by evaporation), the mass balances for each of the species (intermediates included) and the batch process can be written as:

$$\frac{d[E]}{dt} = -k_1[E][DAc] + k_3[EAcS_{Alc}] + k_5[EAcR_{Alc}] \tag{4}$$

$$\frac{d[DAc]}{dt} = -k_1[E][DAc] \tag{5}$$

$$\frac{d[EAc]}{dt} = k_1[E][DAc] - k_2[EAc][S_{Alc}] + k_{-2}[EAcS_{Alc}] - k_4[EAc][R_{Alc}] + k_{-4}[EAcR_{Alc}] \quad (6)$$

$$\frac{d[P_U]}{dt} = k_1[E][DAc] \quad (7)$$

$$\frac{d[S_{Alc}]}{dt} = -k_2[EAc][S_{Alc}] + k_{-2}[EAcS_{Alc}] \quad (8)$$

$$\frac{d[R_{Alc}]}{dt} = -k_4[EAc][R_{Alc}] + k_{-4}[EAcR_{Alc}] \quad (9)$$

$$\frac{d[EAcS_{Alc}]}{dt} = k_2[EAc][S_{Alc}] - k_{-2}[EAcS_{Alc}] - k_3[EAcS_{Alc}] \quad (10)$$

$$\frac{d[EAcR_{Alc}]}{dt} = k_4[EAc][R_{Alc}] - k_{-4}[EAcR_{Alc}] - k_5[EAcR_{Alc}] \quad (11)$$

$$\frac{d[R_p]}{dt} = k_3[EAcS_{Alc}] \quad (12)$$

$$\frac{d[S_P]}{dt} = k_5[EAcR_{Alc}] \quad (13)$$

With all reservations in mind, yet aiming at practical reasons to obtain global expressions for reaction rates, it was additionally assumed that the system attains a quasi steady state, which stipulates that derivatives of all the species are equal to zero.

Bearing in mind the mass balance for the enzyme

$$E_t = E + EAc + EAcS_{Alc} + EAcR_{Alc} \quad (14)$$

and performing a series of transformations, we finally obtained:

$$r_{(R_P)} = \frac{k_1 k_3 [E_t][DAc][S_{Alc}]}{K_{M_2}\{[S_{Alc}]\frac{k_3}{K_{M_2}} + [R_{Alc}]\frac{k_5}{K_{M_4}} + k_1[DAc](1 + \frac{[S_{Alc}]}{K_{M_2}} + \frac{[R_{Alc}]}{K_{M_4}})\}} \quad (15)$$

$$r_{(S_P)} = \frac{k_1 k_5 [E_t][DAc][R_{Alc}]}{K_{M_4}\{[S_{Alc}]\frac{k_3}{K_{M_2}} + [R_{Alc}]\frac{k_5}{K_{M_4}} + k_1[DAc](1 + \frac{[S_{Alc}]}{K_{M_2}} + \frac{[R_{Alc}]}{K_{M_4}})\}} \quad (16)$$

$$[EAcS_{Alc}] = \frac{[EAc][S_{Alc}]}{K_{M_2}} \quad (17)$$

$$K_{M_2} = \frac{k_{-2} + k_3}{k_2} \quad (18)$$

$$[EAcR_{Alc}] = \frac{[EAc][R_{Alc}]}{K_{M_4}} \quad (19)$$

$$K_{M_4} = \frac{k_{-4} + k_5}{k_4} \quad (20)$$

$$[EAc] = \frac{k_1[E][DAc]}{B} \quad (21)$$

$$B = [S_{Alc}]\frac{k_3}{K_{M_2}} + [R_{Alc}]\frac{k_5}{K_{M_4}} \tag{22}$$

$$E = \frac{E_t B}{B + k_1[DAc](1 + \frac{[S_{Alc}]}{K_{M_2}} + \frac{[R_{Alc}]}{K_{M_4}})} \tag{23}$$

Determination of the model parameters, given in Table 1, performed by fitting them to the experimental data showed that it is capable to represent (R^2=0.992) the results obtained for the native enzyme in a broad range of solketal concentrations, Figs. 1 and 2.

Table 1. Kinetic parameters of the base kinetic model evaluated for the native *P. fluorescence* lipase

k_1	$5.49 \cdot 10^{-4}$	ml·µmol^{-1}·s^{-1}
k_3	5.00	s^{-1}
k_5	$4.92 \cdot 10^{-2}$	s^{-1}
K_{M2}	$3.43 \cdot 10^{-4}$	µmol·ml^{-1}
K_{M4}	$2.88 \cdot 10^{-5}$	µmol·ml^{-1}

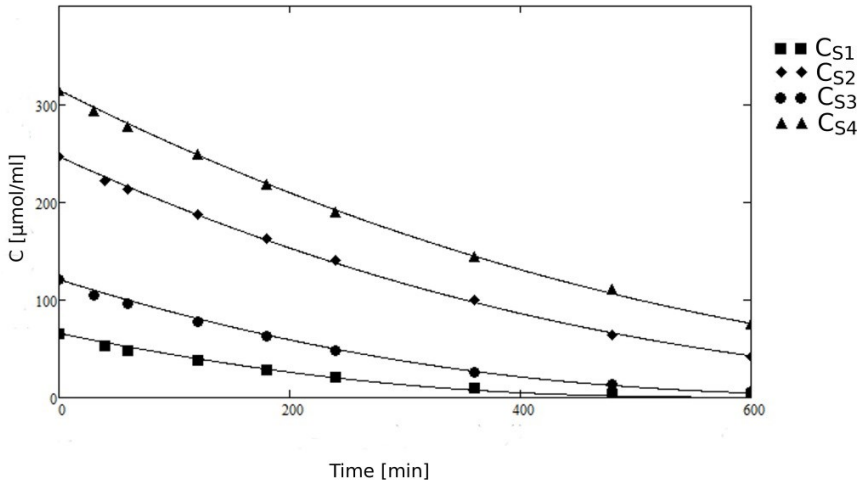

Fig. 1. Progress of S-solketal conversion in time catalyzed by the native enzyme. Solid lines represent the base kinetic model.

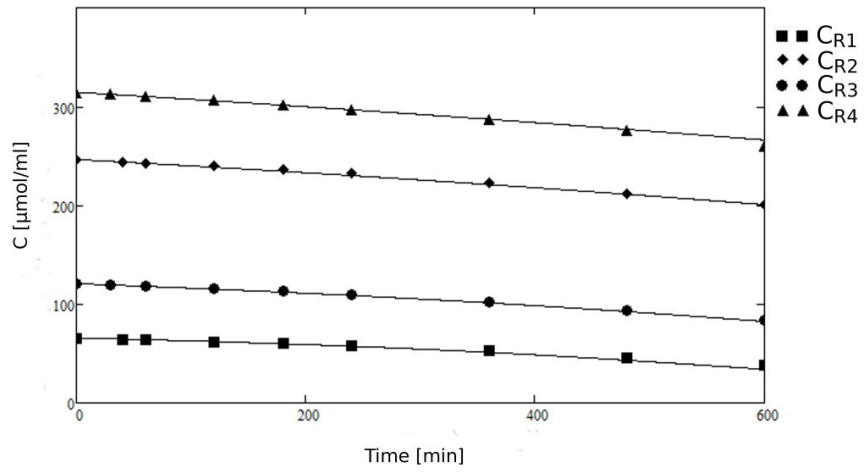

Fig. 2. Progress of R-solketal conversion in time catalyzed by the native enzyme. Solid lines represent the base kinetic model

However, for SBA-15-Oc-supported lipase applied as a slurry catalyst, more notable discrepancies were observed for large solketal concentrations (Majewska et al., 2006) (results not shown here). The use of the same model (pseudo-homogeneity assumption) could be rationalized by the very small sizes (20-40 μm dia.) of the catalysts which made a fine slurry system.

2.2. Extended kinetic model

A number of different modifications of the base kinetic model, which accounted for different inhibitory effects or even adsorption on the carrier, have been tested in order to improve its accuracy for the SBA-15 biocatalysts, but they gave only a moderate improvement. Finally, we tested the effect of the enzyme-acyl complex inhibition by R-product, governed by the equation:

$$R_P + EAc \underset{k_{-6}}{\overset{k_6}{\rightleftarrows}} EAc \tag{24}$$

Taking it into account and adopting similar assumptions as before, after numerous transformations the expressions for global reaction rates were determined:

$$r_{(R_P)} = \frac{k_1 k_3 [E_t][DAc][S_{Alc}]}{K_{M_2}\{[S_{Alc}]\frac{k_3}{K_{M_2}} + [R_{Alc}]\frac{k_5}{K_{M_4}} + k_1[DAc](1 + \frac{[S_{Alc}]}{K_{M_2}} + \frac{[R_{Alc}]}{K_{M_4}} + \frac{R_P}{K_{6R}})\}} \tag{25}$$

$$r_{(S_P)} = \frac{k_1 k_5 [E_t][DAc][R_{Alc}]}{K_{M_4}\{[S_{Alc}]\frac{k_3}{K_{M_2}} + [R_{Alc}]\frac{k_5}{K_{M_4}} + k_1[DAc](1 + \frac{[S_{Alc}]}{K_{M_2}} + \frac{[R_{Alc}]}{K_{M_4}} + \frac{R_P}{K_{6R}})\}} \tag{26}$$

For the native lipase they appeared to reproduce the experimental data more precisely ($R^2 = 0.996$, data not displayed here) than the base model, but more importantly the extended model proved capable of portraying quite well ($R^2 = 0.984$) also the data from the SBA-15-Oc-supported lipase (Figs. 3 and 4) using the parameters given in Table 2.

Table 2. Kinetic parameters of the extended kinetic model evaluated for the native and immobilized *P. fluorescence* lipase

	Native enzyme	Enzyme immobilized on SBA-15-Oc	
k_1	$5.56 \cdot 10^{-4}$	$11.8 \cdot 10^{-4}$	ml·μmol^{-1}·s^{-1}
k_3	1.91	3.65	s^{-1}
k_5	$6.16 \cdot 10^{-2}$	$92.6 \cdot 10^{-2}$	s^{-1}
K_{M2}	$2.15 \cdot 10^{-5}$	$19.7 \cdot 10^{-5}$	μmol·ml^{-1}
K_{M4}	$2.53 \cdot 10^{-5}$	$23.9 \cdot 10^{-5}$	μmol·ml^{-1}
K_{6R}	$6.81 \cdot 10^{-6}$	$386 \cdot 10^{-6}$	μmol·ml^{-1}

From the biocatalyst engineering standpoint of interest may be a significant difference in the values of K_{6R} for the native lipase (Table 2) and that attached on to SBA-15-Oc (Table 2). It can be attributed to a large adsorption potential of the applied support, i.e. highly porous silica of SBA-15 type. But even more important are very significant differences in the values of the corresponding kinetic parameters (effective values for heterogeneous catalysts), very much in favor of the SBA-15-based biocatalysts. They clearly demonstrate that specific activity of the lipase attached to SBA-15silicates, the surface of which was modified with octyl groups to impart hydrophobic properties, was over two times more active than the native lipase, which may be of practical significance. Yet, this activation occurred at the expense of increase in R-solketal conversion, and hence enantioselectivity. The former trend does not

come as a surprise and has been reported before by many authors, c.f. critical overviews more recently published (Adlercreutz, 2013; Hrydziuszko et al., 2014). The decrease in enantioselectivity with increase in conversion is also typically observed, and it poses a limit on the useful, economically justified values of conversion coefficients.

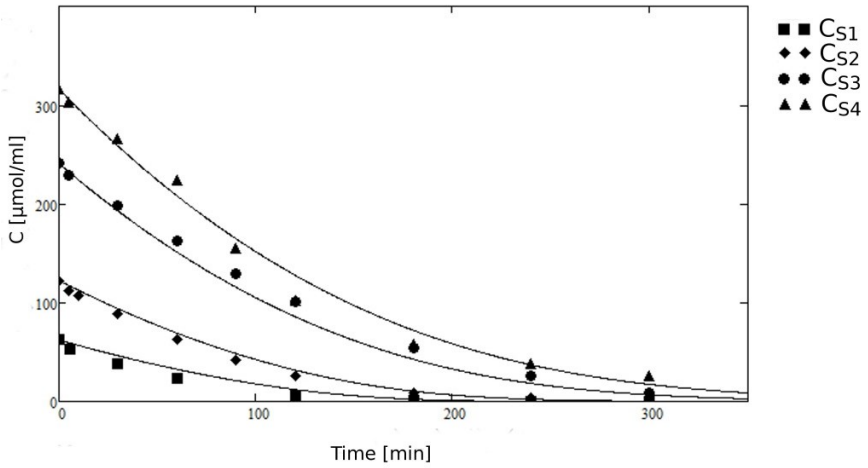

Fig. 3. Progress of S-solketal conversion in time catalyzed by SBA-15-Oc immobilized lipase. Solid lines represent predictions from the extended kinetic model.

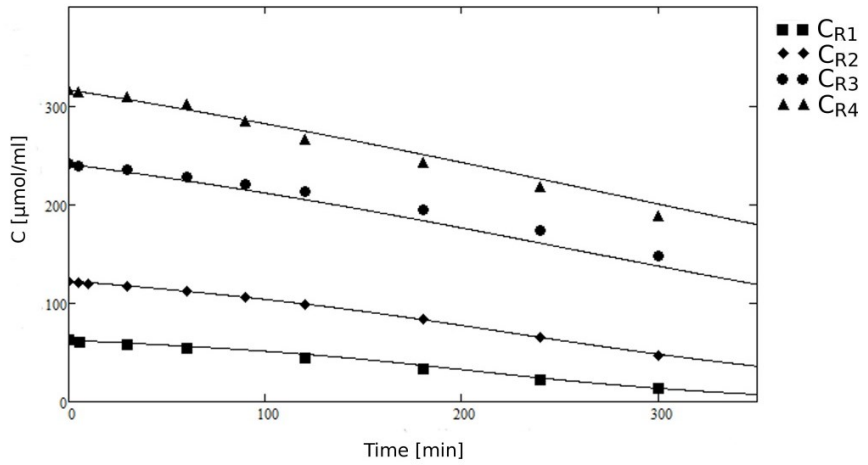

Fig. 4. Progress of R-solketal conversion in time catalyzed by SBA-15-Oc immobilized lipase. Solid lines represent predictions from the extended kinetic model.

3. CONCLUDING REMARKS

The performed studies showed that *P. fluorescence* lipase is an effective catalyst in partial separation of racemic solketal mixtures and that the process can be adequately described by the Ping-Pong Bi Bi model plus an expression accounting for the formation of an enzyme-acyl donor complex. Studies of the biocatalysts made of the same lipase but supported on siliceous mesoporous powders of SBA-15-Oc type, carried out in a batch slurry system, showed that they can be over two times more active than the native enzyme in S-solketal conversion but even more for R-solketal, and the process kinetics can be modeled using the same set of equations, but R-product inhibition needs to be taken into account.

The authors would like to thank the National Science Center (NCN) of Poland for the financial support for this work under Grant No: UMO-2013/09/B/ST8/02420.

SYMBOLS

ee_R	enantiomeric excess,
DAc	acyl donor,
S_{Alc}, R_{Alc}	alcohols of S and R configuration,
S_P, R_P	reaction products of S and R configuration,
P_U	product of a side reaction,
k_1, k_{-1},*etc.*	reaction rate constant
K_M	Michaelis-Menten constant

REFERENCES

Adlercreutz P., 2013. Immobilization and application of lipases in organic media. *Chem. Soc. Rev*., 42, 6406-6436. DOI: 10.1039/c3cs35446f.

Barros D.P.C., Lemos F., Fonseca L.P., Cabral J.M.S., 2010. Kinetic cutinase-catalyzed esterification of caproic acid in organic solvent system. *J. Mol. Catal. B: Enzym*., 66, 285-293. DOI: 10.1016/j.molcatb.2010.06.005.

Boncel S., Zniszczoł A., Szymańska K., Mrowiec-Białoń J., Jarzębski A., Walczak K., 2013. Alkaline lipase from *Pseudomonas fluorescens* non-covalently immobilised on pristine versus oxidised multi-wall carbon nanotubes as efficient and recyclable catalytic systems in the synthesis of Solketal esters. *Enzyme Microb. Technol*., 53, 263-270. DOI: 10.1016/j.enzmictec.2013.05.003.

Hanson R.M., 1991. The synthetic methodology of nonracemic glycidol and related 2,3-epoxy alcohols. *Chem. Rev.,* 91, 437-475. DOI: 10.1021/cr00004a001.

Hof R.P., Kellog R.M., 1996. Synthesis and lipase-catalyzed resolution of 5-(hydroxymethyl)-1,3-dioxolan-4-ones: Masked glycerol analogs as potential building blocks for pharmaceuticals. *J. Org. Chem*., 61, 3423-3427. DOI: 10.1021/jo952021v.

Hydziuszko Z., Dmytryk A., Majewska P., Szymańska K., Liesiena J., Jarzębski A., Bryjak J., 2014. Screening of lipase carriers for reactions in water, biphasic and pure organic solvent systems. *Acta Biochim. Polonica*, 61(1), 1-6.

Majewska P., Kafarski P., Lejczak B., 2006. Simple and effective method for the deracemization of ethyl-1-hydroxyphosphinate using biocatalysts with lipolitic activity. *Tetrahedron Asymmetry*, 17, 2870-2875. DOI: 10.1016/j.tetasy.2006.10.041.

Paiva A.L., Balcao V.M., Malcata F.X., 2000. Kinetics and mechanisms of reactions catalyzed by immobilized lipases. *Enzyme Microb. Technol.,* 27, 187-204. DOI: 10.1016/S0141-0229(00)00206-4.

Pilarek M., Szewczyk K.W., 2007. Kinetic model of 1,3-specific triacylglycerols alcoholysis catalyzed by lipases. *J. Biotechnol.,* 127, 736-744. DOI: 10.1016/j.jbiotec.2006.08.012.

Zniszczoł A., 2015. *Otrzymywanie estrów solketalu wobec lipaz natywnych oraz immobilizowanych na nośnikach stałych*. Ph.D. thesis, Silesian University of Technology, Gliwice.

Zniszczoł A., Herman A.P., Szymańska K., Mrowiec-Białoń J., Walczak K., Jarzębski A., Boncel S., 2016. Covalently immobilized lipase on aminoalkyl-, carboxy- and hydroxy-multi-wall carbon nanotubes in the enantioselective synthesis of solketal esters. *Enzyme Microb. Technol*., 87, 61-69. DOI: 10.1016/j.enzmictec.2016.02.015.

Received 27 November 2016
Received in revised form 30 March 2017
Accepted 23 April 2017

www.czasopisma.pan.pl www.journals.pan.pl
Chemical and Process Engineering 2017, 38 (2), 217-229
DOI: 10.1515/cpe-2017-0017

BRONCHIAL MUCUS AS A COMPLEX FLUID: MOLECULAR INTERACTIONS AND INFLUENCE OF NANOSTRUCTURED PARTICLES ON RHEOLOGICAL AND TRANSPORT PROPERTIES

Marcin Odziomek*, Martyna Kalinowska, Aleksandra Płuzińska, Antoni Rożeń, Tomasz R. Sosnowski

Warsaw University of Technology, Faculty of Chemical and Process Engineering,
ul. Waryńskiego 1, 00-645 Warsaw, Poland

Dedicated to Prof. Leon Gradoń on the occasion of his 70th birthday

Transport properties of bronchial mucus are investigated by two-stage experimental approach focused on: (a) rheological properties and (b) mass transfer rate through the stagnant layer of solutions of mucus components (mucine, DNA, proteins) and simulated multi-component mucus. Studies were done using thermostated horizontal diffusion cells with sodium cromoglycate and carminic acid as transferred solutes. Rheological properties of tested liquids was studied by a rotational viscometer and a cone-plate rheometer (dynamic method). First part of the studies demonstrated that inter-molecular interactions in these complex liquids influence both rheological and permeability characteristics. Transfer rate is governed not only by mucus composition and concentration but also by hydrophobic/hydrophilic properties of transported molecules. Second part was focused on the properties of such a layer in presence of selected nanostructured particles (different nanoclays and graphene oxide) which may be present in lungs after inhalation. It was shown that most of such particles increase visco-elasticity of the mucus and reduce the rate of mass transfer of model drugs. Measured effects may have adverse impact on health, since they will reduce mucociliary clearance in vivo and slow down drug penetration to the bronchial epithelium during inhalation therapy.

Keywords: mucus, biopolymers, interactions, diffusion, rheology, nanostructured particles

1. INTRODUCTION

Understanding of transport phenomena of small molecules in polymer and biopolymer solutions has a considerable practical value in many areas. In medicine, the pharmacokinetics of drugs administrated by inhalation or gastrointestinal route highly depends on their transport rate through the mucus layer covering the surface of epithelium. In the respiratory tract the mucus forms a protective layer against pathogens and pollutants inhaled with air (Cone, 2009). Foreign particles deposited on the mucus surface are removed from the respiratory tract by means of two mechanisms: mucociliary clearance (i.e. transport due to flow of the mucus induced by beating of the cilia) and cough, both being dependent on mucus composition which determines its rheological properties. If viscosity is too low, gravitational forces will overcome the mucociliary transport, so the mucus can seep down to the lungs which favors bacterial growth and increases the risk of infections. A similar risk occurs when too viscous mucus hinders cilia activity and their beating becomes ineffective. It can be observed in pulmonary diseases which are also associated with the increased thickness of mucus layer, e.g. cystic fibrosis (Rubin, 2009). Bronchial mucus is a non-Newtonian fluid with viscoelastic and thixotropic properties.

*Corresponding author, e-mail: marcin.odziomek@pw.edu.pl

Appropriate degree of elasticity is necessary for efficient transmission of energy from moving cilia to the liquid with minimal dissipation (Cone, 2009), therefore abnormal elasticity of this secretion has adverse impact on respiratory defense/protective mechanisms. Proper functioning of the second defense mechanism, i.e. cough clearance, is strictly related to thixotropy of the mucus, i.e. to time-dependent changes in mucus rheology after imposing high shear rates generated by forceful air flow during coughing. The shearing stresses result both in temporal and permanent changes of the mucus internal structure and - consequently - its rheological properties (Lai et al. 2009).

The strongest influence on mucus structure is imposed by mucins, which are high-molecular- weight glycoproteins, capable of forming physically entangled gel structures by cross-linking. The degree of entanglements depends mainly on the molecular weight of mucin subunits (which is in the range of 0.5-40 MDa), and mucin concentration, which typically does not exceed 5% w/w, but may significantly increase during a disease. According to King (2005), a common mucin molecule with the molecular weight of 2-3 MDa is randomly coiled in aqueous medium, forming a 400-600 nm sphere. At 1% (w/w) concentration, centers of mucin molecules are separated by a distance of 70-75 nm. Hence, mucins at physiologic concentration exist as highly interpenetrating polymer coils, and the main form of crosslinking is through dynamic intermolecular entanglements (King, 2005). Except for that, mucins present also a multitude of potential non-covalent (electrostatic, hydrophobic, hydrogen, van der Waals) interaction sites for binding themselves but also with other molecules and particles present in the liquid. In the mucus, mucins are present in a slightly basic (pH 7.4) aqueous environment which contains small amounts (up to 1% w/w/) of ions (Na^+, K^+, Ca^{2+} and Cl^-) and macromolecules like proteins (approximately 1% w/w), DNA (approximately 0.02 – 1.5% w/w) and lipids (approximately 1-2% w/w) (Lai et al., 2009). Due to mutual interactions, all these components have their input to rheological properties of mucus.

As an example, most of the lipid content is associated with hydrophobic domains of mucin glycoproteins. On the other hand, hydrophobic amino acids of the free proteins are frequently bound to the molecule's interior, whereas polar (hydrophilic) amino acids are bound outwards, allowing dipole-dipole interactions with the solvent (Cone, 2009). Components of mucus are also responsible for specific interactions with foreign particles or molecules which can appear in the mucus. Such interactions are often of van der Waals type which are low-affinity bonds with short half-lives, often broken within milliseconds due to thermal energy, although their multitude makes their cumulative effect be significant (Cone, 2009; Woodley, 2001).

In summary, mucus ensures protection of the organism by a few different ways due to composition, structure and rheology. Mucus is a steric barrier (Muhr and Blanshard, 1982), and its continuous secretion requires that surface of underlying epithelium may be reached by arriving molecules or particles (e.g. drugs) only after their migration against an outward current. The polymeric network physically obstructs the mass transfer through this liquid layer. The crosslink density of this network depends mainly on the length of mucin subunits, as mucin molecules are bound together by covalent disulphide bonds between the cysteine-rich, carboxyl- and amino- terminal sites of the protein backbone. Crosslink density in mucin solutions can be decreased by mucolytics (e.g. N-acetylcystine: NAC) which reduce di-sulphur bonds between mucin molecules, lowering the effective viscosity of these solutions and facilitating the diffusive mass transfer. It was demonstrated that NAC at concentration of 1.5% (w/w) lowered the apparent viscosity of dense mucus (mucin concentrations: 20% w/w, which reflects a pulmonary disease) by more than 40%, simultaneously increasing diffusion rate of small molecules by 2.2-fold (Odziomek et al. 2012; Odziomek et al., 2015). Such increase of mucus permeability can be explained by shortening the diffusion path in the complex gel-like liquid structure (Muhr and Blanshard, 1982).

The current paper is focused on the basic analysis of transport properties of the bronchial mucus and it was divided into two parts. The first part investigates the influence of main mucus components on the apparent viscosity and the mass transfer rate of selected low-molecular weight substances (acting as a

model of inhalable drugs). Obtained data are discussed on the basis of inter-molecular interactions providing the way of evaluating the role of each component in mucus rheology and permeability.

The second part of the paper extends the experimental studies to the influence of selected nanostructured particles, NPs - which may be present in bronchial fluid after inhalation - on rheological properties and permeability of the bronchial mucus simulant. These issues are of special importance for understanding the physicochemical reasons of health effects caused by inhaled nanoparticulate air contaminants. It is well known that such particles easily penetrate the respiratory tract and deposit on the lung surface (Marijnissen and Gradoń, 2010; Sosnowski, 2015; Yang et al., 2008). It was also demonstrated that NPs are capable (in a material- and dose-dependent manner) of modifying physicochemical properties of lung surfactant which is present in the alveolar region of lungs (Kondej and Sosnowski, 2013; Sosnowski et al., 2011). Similarly, it may be expected that NPs interaction with the affect natural mass transport processes in the bronchial tree: the clearance but also penetration of drugs administered by inhalation. The aim of this research is to identify the physical phenomena responsible for these effects.

2. MATERIALS AND METHODS

2.1. Structure of the experimental studies

As mentioned above, the studies were divided into two parts. Part I investigates transport properties in solutions of individual mucus constituents by viscometry and analysis of the diffusive mass transfer of two low-molecular mass solutes. Part II which is focused on effects caused by nanostructured particles on transport properties of artificial mucus. It involves more sophisticated rheological analysis of the mucus in presence of NPs and the measurements of diffusive transport. The data regarding experiments done in both parts is presented in Table 1.

Table 1. Types of experiments done within the study. Materials and experimental methods are characterized in the subsequent sections.

Type of experiment → Sample type ↓	Viscometry at constant shear rate	Mass transfer in horizontal diffusion cell (HDC)	Concentration measurements method	Dynamic rheological characteristics
Part I - measurements done for solutions of individual mucus components				
ALB–water (15 mg/ml)	+	+	Spectrophotometry	-
DNA- water (15 mg/ml)	+	+	Spectrophotometry	-
MUC-water (15 mg/ml)	+	+	Spectrophotometry	-
ALB+DNA+MUC (15+15+15 mg/ml)	+	+	Spectrophotometry	-
Part II - measurements done for mucin solutions in presence of NPs				
MUC + water (50 mg/ml) + (200 mg/ml)	-	+	HPLC	+
MUC + water + BT	-	+	HPLC	+
MUC + water + MM	-	+	HPLC	+
MUC + water + GOx	-	+	HPLC	+

ALB - albumin, MUC - mucin, BT - bentonite NPs, MM - hydrophobic montmorillonite, NPs, GOx - graphene oxide NPs.

2.2. Materials

Mucin - MUC (type II, M2378), albumin – ALB (A5253), deoxyribonucleic acid - DNA (74782), trizma base (T4661), carminic acid – CA (29253) were purchased from Sigma Aldrich, phosphate buffer and sodium azide were purchased from POCH (Poland). Disodium cromoglycate (DC) was donated by GlaxoSmithKline Pharmaceuticals S.A. (Poland). Nanostructured particles of bentonite - BT ($H_2Al_2O_6Si$) and hydrophobized montmorillonite - MM (I.28E), were purchased from Sigma-Aldrich. These NPs were characterized in detail in the paper by (Kondej and Sosnowski, 2013) where they were denoted as PGV and MM1 particles. Graphene oxide (GOx) nanoparticles were fabricated in Graphene Laboratory at the Faculty of Chemical and Process Engineering, Warsaw University of Technology. Water used for the preparation of all solutions and for other analytical purposes were obtained from the reverse osmosis purification system (Puricom, USA).

2.3. Sample preparation

Liquid samples used for rheological and mass transfer studies were prepared by dissolution of mucin, albumin, DNA in phosphate buffer (pH 7.4) to achieve the desired final concentration (15 mg/ml). Overall concentration of dissolved substances in the sample imitating the natural mucus (MUC + ALB + DNA) was equal to 45 mg/ml. The concentration of mucin in samples used for studies with NPs (Part II of the study) was 50 mg/ml and 200 mg/ml, whereas the ratio of NPs to MUC was 1:50 and 1:20, respectively. NPs were first dispersed in phosphate buffer using ultrasounds. Then mucin was added gradually to the gently stirred solutions. The pH of all prepared samples was precisely controlled and, if necessary, adjusted with trizma base. A small amount (0.02% w/w) of sodium azide was added to protect the samples from microbial contamination. After setting the pH and adding all components, mucus samples were gently stirred for the time necessary for them to complete dissolution.

2.4. Rheological measurements

The apparent viscosity of samples containing different mucus components (Part I of the study) was measured with rotational rheometer (Smart - Fungilab, Spain). In this case, for a straightforward comparison of the results, all measurements were done at the similar shear rate $\dot{\gamma} \approx 8\ s^{-1}$, which lies within the range found in bronchial mucus at normal physiological conditions (Cone, 2009). All viscosity measurements were taken at constant temperature (20 ± 0.5°C). In Part II of the studies, which were done for mucin solutions in presence of NPs, more extensive rheological measurements were conducted with Anton Paar Rheometer (model MCR 302, Austria), working with cone and plate geometry and Peltier temperature controller. The applied dynamic oscillatory shear measurements are suited for studies of complex liquids since they do not rupture the internal structure of the fluid (Schramm, 2000). Tested liquid is subjected only to small oscillations of fixed amplitude (strain) at different shear frequencies (Lai et al., 2009). These measurements were done at physiological temperature (37 ± 0.2°C).

2.5. Mass transfer studies

Permeability of tested solutions (Part I) or suspensions (Part II) was measured out using thermostated glass horizontal diffusion cells, HDC (PermeGear, Germany) as described in detail elsewhere (Odziomek et al., 2015). In brief, the donor and receiver compartments of HDC were filled with 5 ml of the aqueous solution of diffusing substance (DC or CA, 0.1 mg/ml) and pure phosphate buffer (pH 7.4), respectively. Liquids in both compartments were agitated by a magnetic microstirrer in order to assure

uniform concentration and to reduce the local mass transfer resistance at the surface of the supporting membranes. The 3-mm stagnant layer (300 µl) of the tested liquid was placed between the compartments, and it was supported from both sides by PVDF (polyvinyl difluoride) Durapore® porous membranes (pore size 0.1 µm, thickness 0.125 mm - Millipore, USA). The membranes, which were selected according to literature data (Norris and Sinko 1996), guarantee low intrinsic resistance for diffusing solutes, and they simultaneously assure no leakage of the inner sample. Diffusion cells were thermostated (20 ± 0.5°C in Part I, and 37 ± 0.5°C in Part II). Concentration of diffusing substances in each compartment was periodically measured either by UV-VIS spectrophotometry (Thermo Scientific, USA - in Part I of the studies), or by HPLC (model Infinity 1220, Agilent Technologies, USA, equipped with UV-VIS detector and 100 mm ZORBAX Eclipse Plus C18 column - in Part II of the studies). DC and CA were analyzed at 325 nm and 540 nm wavelength, respectively. During each experiment (typically: 6 hours) samples from each compartment were taken for analysis at 30 min intervals (25 µl for HPLC or 0.5 ml for spectrophometry - these samples were returned to the compartments after quick absorbance reading).

The effective diffusion coefficient in the stagnant layer, D_{eff}, was calculated from the appropriate solution of the Fick's law, assuming the steady-state process in the layer (Desai and Vadgama, 1992; Odziomek et al., 2015). This assumption is true when the time necessary for solute transport through the layer, t_d, is significantly shorter than the time necessary to change its concentration in the HDC compartments, t_c. It is correct only if the volume of the stagnant layer is significantly smaller than cell volume (Truskey et al., 2009), which is true for our system (0.3 vs. 5 ml). It was also assumed that the main resistance of the mass transfer from donor phase to acceptor phase is located in the stagnant layer. It means that membrane resistance is negligible and the mass transfer resistance at the membrane surface in both diffusion chambers is eliminated by stirring inside each cell. Another simplification is the assumption of constant concentration difference between both diffusion chambers. As the measurements were conducted in a closed system, the concentration of analyzed substances in both diffusion chambers would equalize at sufficiently long time. However, because of limited time of measurement (6 hours), the solute concentration in the donor chamber was always much higher than that in the acceptor chamber which justifies the above assumption (Brodin et al., 2010).

3. RESULTS AND DISCUSSION

3.1. Part I – influence of individual mucus constituents on transport properties

The first part of the study was focused on determination of the permeability (i.e. effective diffusivity: D_{eff}, for DC and CA) and the apparent viscosity (measured at the fixed shear rate: μ_a) of aqueous systems which contained different components of the mucus: albumin, DNA, mucin (each at concentration of 15 mg/ml). Comparison of D_{eff} for DC and CA is shown in Fig. 1.

As expected, mass transfer of DC and CA through a 3-mm liquid layer in HDC is fastest in water (D_{eff} = $8.35 \cdot 10^{-10}$ m^2/s for DC and $9.24 \cdot 10^{-10}$ m^2/s for CA). Presence of any mucus constituents noticeably reduces diffusive transport through the layer. For both transported compounds (DC and CA), the effective diffusion coefficient is reduced by 17%-25% in ALB or DNA solutions, by approximately 30% in MUC solution, and by more than 40% in the reconstituted mucus containing a mixture of all three constituents (MIX = MUC+ALB+DNA).

Measured apparent viscosity μ_a of ALB or DNA solutions was similar and almost twice higher than that of water (1.79-1.85 mPa s). Mucin solution was more viscous (2.64 mPa s), and the highest μ_a was found for MIX (5 mPas), although in this system the total content of the components was also higher (45 mg/ml). It can be stated therefore, that liquid viscosity somehow correlates with the permeability of

the stagnant layer. However, a more detailed explanation of the mass transfer in these complex fluids can be derived from further analysis of molecular interactions presented herewith.

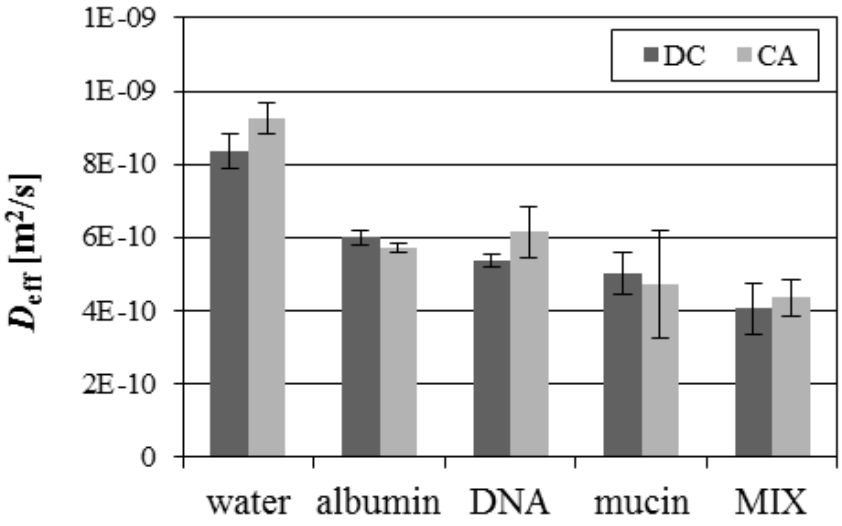

Fig. 1. The effective diffusion coefficient, D_{eff}, of DC and CA in examined samples. Average ± SD, number of replicates = 3

Insignificant differences in mass transfer rate, which were found for both studied compounds (DC and CA) of similar molecular mass (468.4 Da and 492.4 Da, respectively) may be explained by their different physiochemical properties. DC has a more hydrophilic character as suggested by partition coefficient (Log*P* = - 4.80) which refers to the equilibrium of the compound (in the ionized and unionized form) between aqueous and organic phases at physiological pH. For carminic acid, Log*P* = 1.53 which means that CA molecules are more hydrophobic. This explains the minor differences in their transport rate through the complex liquids tested in this work.

It is known that MUC - as biopolymer - allows to create a spatial network by crosslinking through intermolecular entanglements, although smaller molecules such as ALB or DNA do not demonstrate sufficient interactions. As a consequence, transport of solutes cannot be hindered for ALB or DNA by 'obstruction effect', but it is possibly reduced by specific interactions between diffusing molecules and the components of the solution. For all forms of DNA, the global structure has an overall negative charge and the total electrostatic potential is negative. This is largely due to the phosphate groups of DNA which bear an overall negative charge due to the negatively charged oxygen atoms they have. However, DNA has both positive and negative charges covering its outer structure (Rohs et al., 2010) which may be responsible for stronger interactions of DNA molecules with more polar molecules of DC. This explains slightly slower diffusion of DC as compared to CA through DNA solution.

The difference also might be expected for DC and CA transport in ALB solution. In solutions of globular proteins (like albumin), hydrophobic amino acids are frequently bound to the molecule's interior whereas polar hydrophilic amino acids are bound outwards, allowing dipole-dipole interactions with the solvent (Cone, 2009). Such a structure should result in greater hindering of DC molecules (more hydropophilic) than CA molecules (more hydrophobic). However, results presented in Fig. 2 show practically no difference in the rate of diffusive mass transport of both solutes, which may suggest that such interactions are not critical for mass transfer rate under tested conditions.

For MUC, the reduction of transport rate can be explained by mucin's structure. Protein backbone of mucin has PTS regions – regions with high content of amino acids like proline, threonine and serine (Cone, 2009). Hydroxyl groups of these amino acids are bound through O-glycosylation linkages with carbohydrate molecules which are partly responsible for expansion of the mucus gel. This is the result of the negative charge of sialic acid (pKa ~ 2.6) which is bound to these side chains. Generally,

oligosaccharide side chains of mucins are responsible for electrostatic interactions and non-specific hydrogen bonding, while the protein backbone allows for hydrophobic interactions. Such a structure allows them to bind substances with different properties, and therefore to hinder their transport rate through the gel (Bansil and Turner, 2006; Bhat et al., 1995; Sanders et al., 2000; Widdicombe, 1997).

The lowest values of D_{eff} were obtained for DC (4.04×10^{-10} m^2/s) and CA (4.35×10^{-10} m^2/s) in the sample MIX which mimics natural bronchial mucus. These results can be explained by 'obstruction effect' in the liquid mixture with high (although physiologically-relevant) total concentration of dissolved substances. These findings also demonstrate good barrier properties of the mucus layer in protecting tracheobronchial tree and the whole organism against penetration of inhaled particles.

Presented results show that due to varied display of interaction modes, the mucus is well adapted to trap molecules that have either hydrophobic or hydrophilic properties. In Part II of this paper, we do the next step in this analysis by identifying interactions of mucin with nanostructured particles.

3.2. Part II. Influence of nanostructure particles (NPs) on transport properties of mucin solutions

Investigations focused on relations between NPs and rheological and transport properties of mucin solutions were done for two MUC concentrations: 50 and 200 mg/ml. The lower concentration value lies within physiological range for bronchial mucus, which can be expected only at conditions of a lung disease (Boucher, 1988). For 'physiological' concentration, the content of NPs was adjusted to 1 mg/ml (NPs/mucin = 1:50), while for the 'disaese' - to 10 mg/ml (NPs/mucin = 1:20). NP concentration of 1 mg/ml corresponds to the deposited dose which may be expected after a few-hour breathing with air contaminated by NP dust (Kondej and Sosnowski, 2013). The higher NPs concentration (10 mg/ml) was chosen to test the sensitivity of the already impaired system ('disease') to dust overloading, which is known to occur in occupational or accidental exposures (Oberdörster, 1995).

The rheological measurements have been carried out with strain amplitude 3% which kept the system inside linear viscoelasticity region. Concentrated MUC samples show both an elastic and viscous response when subjected to sinusoidal strain. The storage (G') and loss (G'') moduli of each sample for angular frequency range $\omega = 0.1 – 100$ rad/each are shown in Fig. 2. The values of phase shift angles: $\phi = \arctan(G''/G')$, measured at strain amplitude 3%, are compared in Fig. 3.

Loss modulus G'' is higher in the whole range of angular frequencies for solutions with pure MUC and MUC + bentonite NPs. For the other two samples (with MM and GOx) the viscous component (G'') of the dynamic response exceeds the elastic component (storage modulus G') only at low frequencies. In this range both samples react more like a viscous liquid than elastic solid. It can be understood as dashpot-like response of their internal structure which gives enough time to react to a given strain (i.e. to relax). At high frequencies the relation between G' and G'' is reversed, so both samples react more like solids ('spring') since there is not sufficient time for the 'dashpot' to react in line with the assigned strain (Schramm, 2000). It is known that curves of the two moduli cross-over at a particular value of the angular frequency which is characteristic for the given polymer structure. Generally, when mean molecular weight of polymers increases, the crossing point of the $G'(\omega)$ and $G''(\omega)$ curves is shifted to the lower frequencies. Simultaneously, a decrease of molecular weight distribution moves this point to higher values of moduli (Schramm, 2000). This means that samples with MM and - to a lesser extent - with GOx, show properties which are characteristic for solutions of polymers with higher molecular weight. This may suggest that addition of NPs of montmorillonite or graphene oxide enhances mutual interactions between mucin molecules, increasing the crosslink density. Montmorillonite NPs probably interact with protein backbone whereas graphene oxide NPs - with side chains of mucin. This is not the case for BT NPs, since no crossing of $G'(\omega)$ and $G''(\omega)$ is observed. In fact, these relationships are almost indistinguishable from pure MUC solutions. It must be stressed that results shown in Fig. 3 were obtained for extremely concentrated MUC solution where mutual interactions between mucin

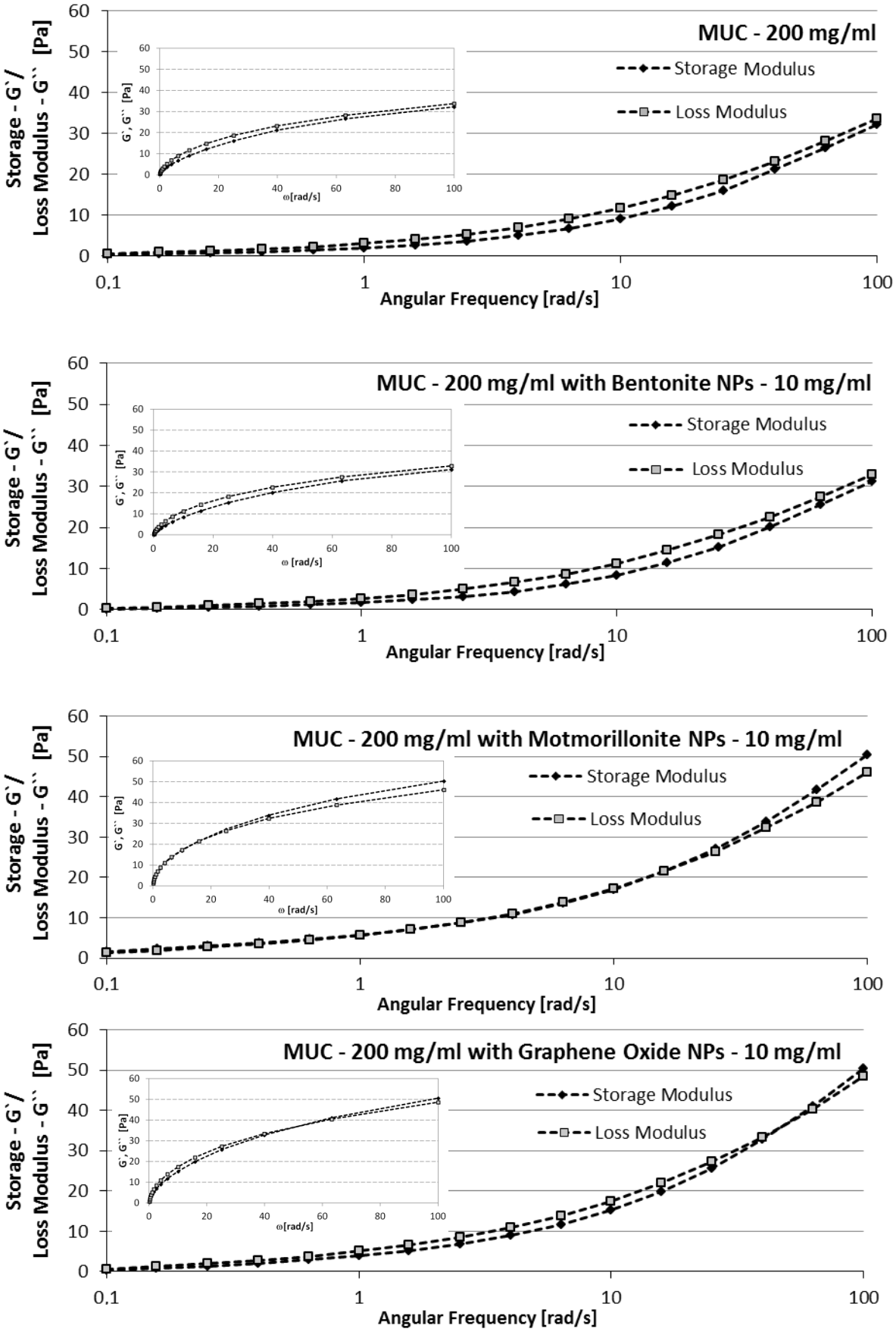

Fig. 2. Storage and loss moduli of 200 mg/ml MUC and MUC+NPs samples (strain amplitude 3%). Inserts show the same relationships with linear scale of the frequency

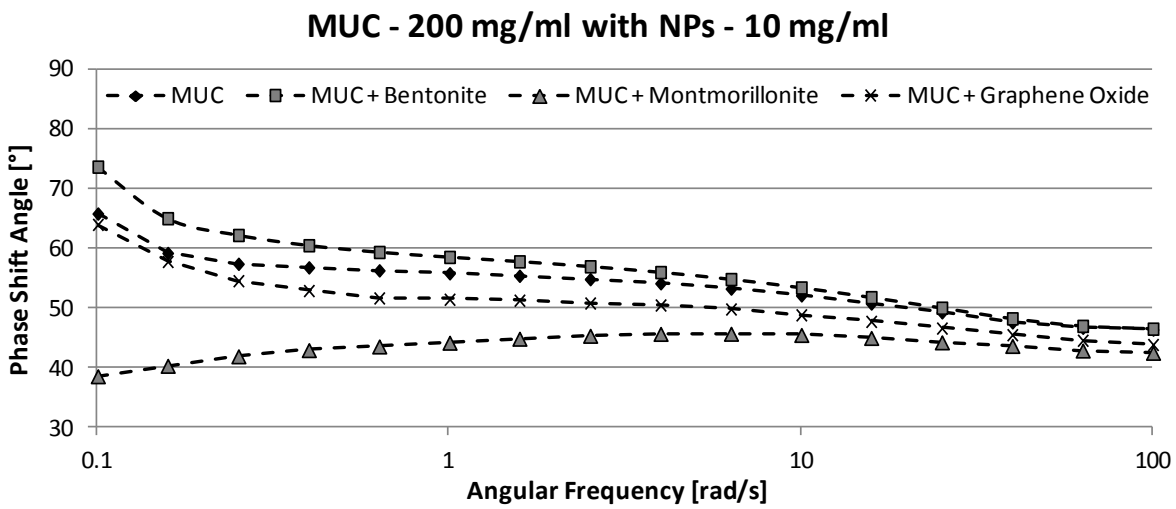

Fig. 3. Phase shift angle for 200 mg/ml MUC samples for strain amplitude 3%

molecules were originally strong. Therefore, addition of NPs may modify these interactions only if particles have special properties. Hydrophobized MM probably forms aggregates in the aqueous phase which can stiffen the internal structure of MUC solution, and this explains the increase of both G' and G''. On the contrary, GOx is hydrophilic but has very high surface area (~ 150 m^2/g - Stobinski et al., 2014), which allows effective binding to polar moieties of MUC molecules, increasing the crosslinking interactions. BT, which is also hydrophilic, does not have such a large surface area (~ 67 m^2/g - Kondej and Sosnowski, 2013) so cannot bind to MUC so efficiently. In case of samples with pure mucin and mucin with bentonite NPs, the viscous response suppresses the elastic one in the whole range of angular frequencies. One of the possible explanations is polydispersion of mucin in the solution, which may be considered as a blend containing both very high- and very low-molecular weight molecules. Small molecules may act as a kind of low viscosity lubricants for the rest of the polymer while larger molecules may show up as an additional elasticity parameter (Schramm, 2000).

Figure 4 shows rheometric results obtained for 50 mg/ml MUC with tested NPs (1 mg/ml). The values of both moduli were much lower than those for samples with higher mucin concentration. Moreover, the results show that only samples with MM and GOx were visco-elastic, and in this case elastic reaction on stress exceeded viscous reaction. In solution of pure mucin and in solution with addition of bentonite NPs storage modulus ($G`$) is close to 0 in all range of angular frequencies, so the liquid is purely viscous. The values of phase shift angles for those solutions are shown in Fig. 5. They confirm that elastic effects in both 50 mg/ml MUC solution and in this solution with BT can be detected only for very low angular frequencies ($\omega < 10$ - 15 rad/s). On the contrary, MUC solutions with MM and GOx are visco-elastic in full range of angular frequencies, although the dissipative (viscous) part becomes dominant for higher values of ω.

Results of mass transport experiments in all samples obtained for DC as a diffusing solute are shown in Fig. 6. It is evident that permeability of the layers of more concentrated MUC solutions is lower, independently of NP presence. In analogy to variations of rheological properties (Fig. 4), MM and GOx reduce the permeability of the layer of 200 mg/ml mucin solutions. D_{eff} calculated for samples with MM and GOx ($D_{eff} \approx 2.6\times10^{-10}$ m^2/s) is more than 10% lower than that of the control sample (pure mucin, $D_{eff} = 2.95\times10^{-10}$ m^2/s). No effect on mass transfer rate was found for BT particles.

For samples with low mucin concentration (50 mg/ml), D_{eff} in a control sample is relatively high (~4.5×10^{-10} m^2/s) and always decreases when any NPs are present. The strongest effect is observed for GOx where D_{eff} is reduced by almost 35%. In case of BT and MM particles, mass transfer hindrance is smaller and quite similar (by 10 and 15%, respectively), although rheometric parameters obtained for

these systems are significantly different. It confirms the observation that overall rheological properties of the complex fluid only partially can explain mass transfer phenomena, and material-dependent molecular interactions are also of relevance.

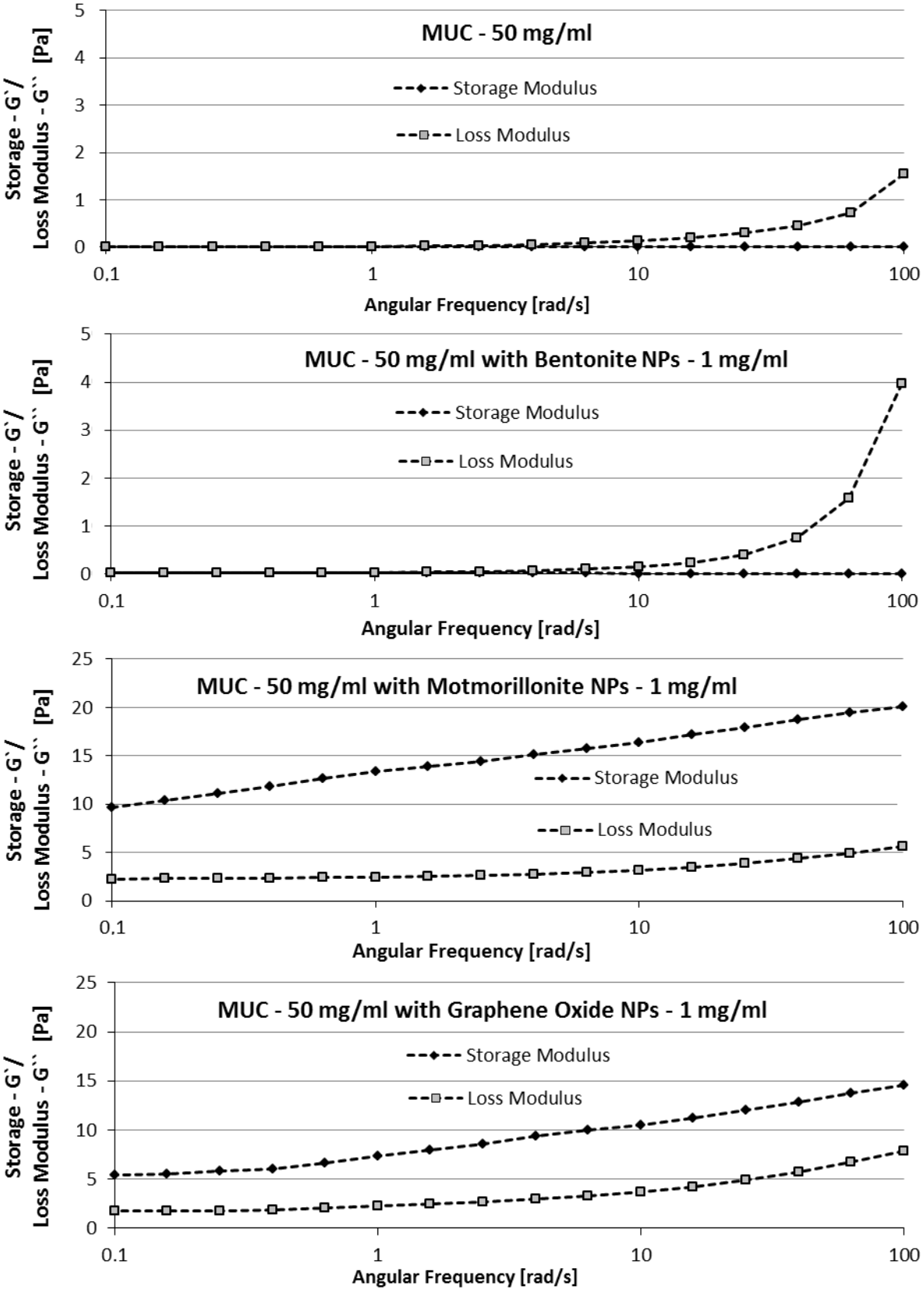

Fig. 4. Storage and loss moduli of 50 mg/ml MUC and MUC/NPs samples (strain amplitude 3%)

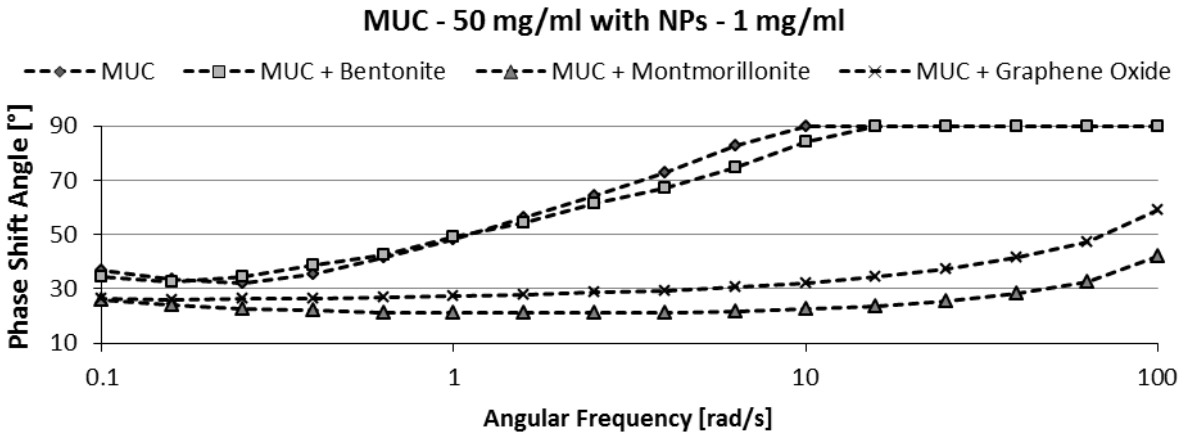

Fig. 5. Phase shift angle for 50 mg/ml MUC samples for strain amplitude 3%

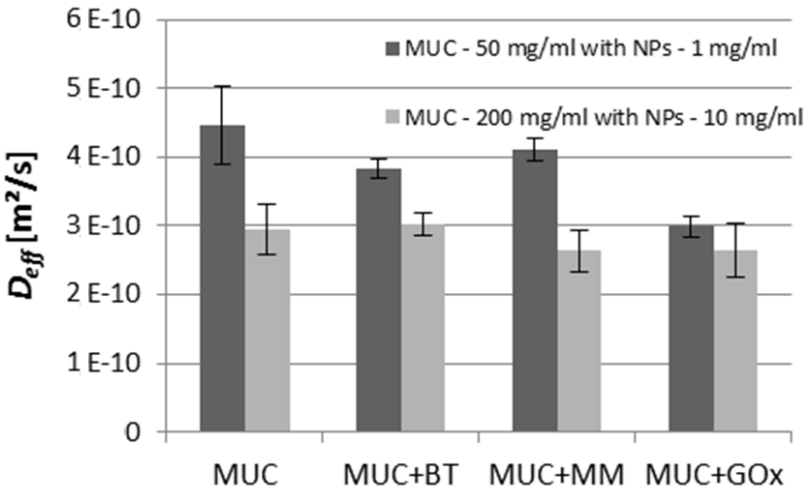

Fig. 6. The effective diffusion coefficient, D_{eff} of DC in examined samples. Average ± SD, number of replicates = 3

4. CONCLUSIONS

Two-stage research reported in this paper confirms that transport properties of bronchial mucus are influenced by many interfering factors. In Part I it was shown that the peculiar chemical composition determines inter-molecular interactions in this complex liquid, which are reflected by variable rheological and permeability characteristics. Each of the essential mucus components (mucin, DNA, proteins) has its own input to the mass transfer resistance for solutes permeating through the mucus layer. Cooperative interactions of the mucus constituents allow to form a complex gel-like visco-elastic barrier which plays an essential role in the respiratory system. It is important for organism protection against inhaled pollutants. On the other hand, this barrier must be overcome by drugs delivered via inhalation, and this can be achieved by applying special drug carriers (Odziomek et al., 2012).

Part II of this study was focused on the properties of this protective layer in presence of nanostructured particles arriving to the mucus with inhaled contaminated air. The results confirmed that most of such particles increase visco-elastic properties of the mucus. This effect should be considered undesirable since it can lessen the rate of mucociliary clearance in vivo, so particles may remain for longer time and accumulate in the bronchial tree. Increased particle retention may be dangerous for health, especially if NPs carry toxic chemicals (such as carcinogenic volatile organics in case of combustion particles)

which will have a longer time for washing-out from particulate carriers. Mucus accumulation in the airways also induces increased airway resistance and susceptibility to infection or inflammation, all being potentially dangerous for health. As shown by results of thes studies, drug penetration through a modified mucus layer may be noticeably slowed down, which calls for new strategies in medical treatment using inhaled drugs.

This work was supported by National Science Centre, projects No. 2011/03/N/ST8/04912 and 2014/13/ST8/00808.

SYMBOLS

D_{eff}	effective diffusion coefficient in a stagnant liquid layer, m^2/s
G'	storage modulus, Pa
G''	loss modulus, Pa

Greek symbols

ϕ	phase shift angle: $\phi = \arctan(G''/G')$
μ_a	apparent viscosity (measured at constant shear rate), Pa s
ω	angular frequency range of strain, rad/s

Abbreviations

ALB	albumin
BT	bentonite (nanoclay)
CA	carminic acid
DC	disodium cromoglycate
DNA	deoxyribonucleic acid
HDC	horizontal diffusion cell
GOx	graphene oxide
HPLC	high performance liquid chromatography
MIX	mixed system: MUC + DNA + ALB
MM	hydrophobic montmorillonite (nanoclay)
MUC	mucin
NAC	N-acetylcysteine
NP	nanostructured particle
PTS	mucin domains with high content of proline, threonine, and serine
SD	standard deviation

REFERENCES

Bansil R., Turner B. S., 2006. Mucin structure, aggregation, physiological functions and biomedical applications. *Curr. Opin. Colloid Interface Sci.,* 11, 164–170. DOI: 10.1016/ j.cocis.2005.11.001.

Bhat P. G., Flanagan D. R., Donovan M. D., 1995. The limiting role of mucus in drug absorption: drug permeation through mucus solution. *Int. J. Pharm.,* 126, 179–187. DOI: 10.1016/0378-5173(95)04120-6.

Brodin B., Steffansen B., Nielsen C. U., 2010. *Molecular biopharmaceutics.* Pharmaceutical Press, London.

Cone R. A., 2009. Barrier properties of mucus. *Adv. Drug Deliv. Rev*., 61, 75–85. DOI: 10.1016/j.addr.2008.09.008.

Desai M. A., Vadgama P., 1992. Estimation of effective diffusion coefficients of model solutes through gastric mucus: assessment of a diffusion chamber technique based on spectrophotometric analysis. *Analyst,* 116, 1113-1116. DOI: 10.1039/AN9911601113.

King M., 2005. *Physiologic basis of respiratory disease.* BC Decker Inc., Hamilton, 409–416.

Kondej D., Sosnowski T. R., 2013. Alteration of biophysical activity of pulmonary surfactant by aluminosilicate nanoparticles. *Inhal. Toxicol.,* 25, 77–83. DOI: 10.3109/08958378.2012. 756087.

Lai S. K., Wang Y., Wirtz D., Hanes J., 2009. Micro- and macrorheology of mucus. *Adv. Drug Deliv. Rev.,* 61, 86–100. DOI:10.1016/j.addr.2008.09.012.

Muhr A. H., Blanshard J. M. V., 1982. Diffusion in gels. *Polymer*, 23, 1012–1026. DOI: 10.1016/0032-3861(82)90402-5.

Marijnissen J., Gradoń L. (Eds.), 2010. *Nanoparticles in medicine and environment. Inhalation and health effects.* Springer, Dordrecht.

Norris D. A., Sinko P. J., 1997. Effect of size, surface charge, and hydrophobicity on the translocation of polystyrene microspheres through gastrointestinal mucin. *J Appl. Polym. Sci.* 63, 1481–1492. DOI: 10.1002/(SICI)1097-4628(19970314)63.

Oberdörster G., 1995. Lung particle overload: implications for occupational exposures to particles. *Regul. Toxicol. Pharmacol.,* 21, 123-135. DOI: 10.1006/rtph.1995.1017.

Odziomek M., Sosnowski T. R., Gradoń L., 2012. Conception, preparation and properties of functional carrier particles for pulmonary drug delivery. *Int. J. Pharm.*, 433, 51–59. DOI: 10.1016/j.ijpharm.2012.04.067.

Odziomek M., Sosnowski T. R., Gradoń L., 2015. The Influence of Functional Carrier Particles (FCPs) on the molecular transport rate through the reconstructed bronchial mucus: In vitro studies. *Transp. Porous Media*, 106, 439–454. DOI: 10.1007/s11242-014-0409-1.

Rohs R., Jin X., West S. M., Joshi R., Honig B., Mann R. S., 2010. Origins of specificity in protein-DNA recognition. *Annu. Rev. Biochem.*, 79, 233–269. DOI: 10.1146/annurev-biochem -060408-091030.

Rubin B. K., 2009. Mucus, phlegm, and sputum in cystic fibrosis. *Respir. Care*. 54, 726-732.

Sanders N. N., De Smedt S. C., Van Rompaey E., Simoens P., De Baets F., Demeester J., 2000. Cystic fibrosis sputum: a barrier to the transport of nanospheres. *Am. J. Respir. Crit. Care Med.*, 162, 1905–11. DOI: 10.1164/ajrccm.162.5.9909009.

Schramm G., 2000. *A practical approach to rheology and rheometry.* 2nd edition, Gebrueded HAAKE GmbH, Karlsruhe.

Sosnowski T.R., 2015. Nanosized and nanostructured particles in pulmonary drug delivery. *J. Nanosci. Nanotechnol.* 15, 3476-3487. DOI: 10.1166/jnn.2015.9863.

Sosnowski TR., Koliński M., Gradoń L., 2011. Interactions of benzo[a]pyrene and diesel exhaust particulate matter with the lung surfactant system. *Ann. Occup. Hyg.*, 55, 329–338. DOI: 10.1093/annhyg/mer007.

Stobinski L., Lesiak B., Malolepszy A. Mazurkiewicz M., Mierzwa B., Zemek J., Jiricek P. Bieloshapka I., 2014. Graphene oxide and reduced graphene oxide studied by the XRD, TEM and electron spectroscopy methods. *J. Electron. Spectrosc. Relat. Phenom.,* 195, 145–154. DOI: 10.1016/j.elspec.2014.07.003.

Truskey G., Yuan F., Katz D., 2009. *Transport phenomena in biological system.* 2nd edition, Pearson Prenticee Hall.

Widdicombe J. G., 1997. Airway liquid: A barrier to drug diffusion? *Eur. Respir. J.*, 10, 2194–2197. DOI: 10.1183/09031936.97.10102194.

Woodley J., 2001. Bioadhesion: New possibilities for drug administration? *Clin. Pharmacokinet.*, 40, 77-84. DOI: 10.2165/00003088-200140020-00001.

Yang W., Peters J. I., Williams R. O., 2008. Inhaled nanoparticles-a current review. *Int. J. Pharm.*, 356, 239–47. DOI: 10.1016/j.ijpharm.2008.02.011.

Received 30 November 2016
Received in revised form 14 February 2017
Accepted 15 March 2017

www.czasopisma.pan.pl PAN POLSKA AKADEMIA NAUK www.journals.pan.pl
Chemical and Process Engineering 2017, 38 (2), 231-239
DOI: 10.1515/cpe-2017-0022

A NEW METHOD FOR ASSESSING HAEMOLYSIS IN A ROTARY BLOOD PUMP USING LARGE EDDY SIMULATIONS (LES)

Maciej Szwast*, Arkadiusz Moskal, Wojciech Piątkiewicz

Warsaw University of Technology, Faculty of Chemical and Process Engineering, Waryńskiego 1, 00-645 Warsaw, Poland

Dedicated to Prof. Leon Gradoń on the occasion of his 70th birthday

The opportunity to assess haemolysis in a designed artificial heart seems to be one of the most important stages in construction. We propose a new method for assessing haemolysis level in a rotary blood pump. This method is based on CFD calculations using large eddy simulations (LES). This paper presents an approach to haemolysis estimation and shows examples of numerical simulation. Our method does not determine the value of haemolysis but allows for comparison of haemolysis levels between different artificial heart constructions.

Keywords: rotary blood pump, large eddy simulations, haemolysis

1. INTRODUCTION

Over the decades pulsatile pumps have been used to assist a diseased heart. Their pulsatile operation resembles the work of the natural heart. The most popular pulsatile pump in the world has been a membrane pump with pneumatic drive, which was used for the first time in 1982 by Jarvik (Leprince et al., 2003). In clinical practice, it has been used to this day.

Currently, one can note a growing interest in centrifugal pumps. Such pumps provide a continuous flow of blood. It is noted that the pulsating flow, despite its physiological nature, is not so important when using artificial ventricles (Garatti et al., 2008; Saito and Nishinaka, 2005). The advantage of centrifugal pumps is their small size, which in the future may lead to their total implantation. Another advantage of these pumps is the lack of the diaphragm and valves, failure of which may lead to a sudden death of the patient.

There are two main types of rotary pumps: axial and centrifugal. In the first type of pumps, blood flows along the axis of the pump. An impeller rotating around the axis of the pump causes the flow. In the second type, i.e. centrifugal pumps, the impeller blades move blood, and thus the blood ejection is caused by the centrifugal force. The efficiency of rotary pumps depends on the rotor speed, which for this type of pumps, is several thousand revolutions per minute.

There are many aspects that must be considered while designing an artificial heart. The constructor should have in mind problems such as reliability, material haemocompatibility, chamber's size, heat exchange and many others. But one of the most important issues is whether the artificial heart will not damage blood cells. It is known that in rotary blood pumps high mechanical stress may occur inside the chamber.

*Corresponding author, e-mail: m.szwast@ichip.pw.edu.pl

In the artificial heart ventricle a centrifugal pump with the rotating impeller creates areas of high values of hydrodynamic stress. This physical stress may affect blood cells and can result in blood cell deformation and damage. The literature presents many hypotheses of the destruction of Red Blood Cells (erythrocytes) in the blood flow. The literature also gives different, often very divergent, values of stress that cause cell damage.

A Red Blood Cell (erythrocyte) is a specific cell. It does not contain a cell nucleus. Its task is to transfer oxygen between the alveoli and all the cells of the body. Gas transport is possible thanks to the protein haemoglobin which is dissolved in the cytoplasm of red blood. The destruction or leakage of the erythrocyte membrane causes the release of haemoglobin into the circulating blood plasma. High concentrations of free haemoglobin and in particular of its degradation products, such as bilirubin, are strong poisons for the body. Therefore, there is a need to prevent the destruction of red blood cells, i.e. haemolysis during the application of artificial organs and in particular of blood pumps.

Inside a centrifugal pump, one can expect mostly physical stresses affecting the red blood cells. These stresses are caused by hemodynamic effects, such as the collision of cells with the impeller blades or with the pump housing. Such stresses can also be a result of a mutual cell collision or because of cell - flow interactions (Pohorecki et al., 2001).

As a result of this stress, the cells may be destroyed. Threshold values for such a stress that erythrocytes can resist, are not clearly defined. The literature gives a number of figures for these stresses - from 10^2 to up to 10^4 Pa. These values were determined using different measurement methods. In addition, the exposure of erythrocytes to these stresses was different when assessed by different methods (Leverett et al., 1972; Rooney, 1970; Szwast et al., 2012; Williams et al., 1970).

It is also important that there is a large variation in the erythrocyte stamina depending on the donor (Nevaril et al., 1968), which means that all considerations carried out on responses of biological material refer only to the average values of the selected property.

Many scientific publications describe blood damage as a consequence of physical stress over years, i.e. (Bludszuweit, 1995; Gregoriades et al., 2000; Jones, 1995; Leverett et al., 1972; Nevaril et al., 1968; Pohorecki et al., 2001; Sutera and Mehrjardi, 1975). In these papers, one can find considerations that are not directly related to the artificial heart.

However, one can find papers in the literature concerning haemolysis inside the artificial heart. Song et al. (2003) assessed haemolysis by tracking a set of particles and their stress history. They used Computational Fluid Dynamics (CFD) for this purpose. Also Arvand et al. (2001) and Apel at al. (2001) have used CFD for haemolysis in their evaluation of artificial hearts.

Computational Fluid Dynamics (CFD) is a method used in medical device technology in particular when modelling the operation of artificial hearts (Bluestein, 2017). Pulsatile blood pumps have been modelled by e.g., Kim et al. (1992) and Okamoto et al. (2003). Nonpulsatile rotary blood pumps have been modelled by e.g. Medvitz et al. (2011), Mitamura et al. (2011) and Wang et al. (2008). CFD calculations refer to blood velocity distribution, mechanical stress distribution in different sites inside the artificial heart and heat exchange with external environment. The aforementioned papers of Arvand et al. (2001) and Song et al. (2003) also concern haemolysis assessment inside the artificial heart. However, their approach differs from the approach presented in this paper.

2. NEW METHOD FOR HAEMOLYSIS ASSESSMENT

Inside a rotary blood pump one can expect that the stress that acts on erythrocytes is induced in several ways. Such stress occurs as a result of collisions between erythrocytes and impeller blades and between two erythrocytes, and as well as an effect of cell-flow interactions (Pohorecki et al., 2001).

The best way to evaluate haemolysis could be a direct calculation of hydrodynamic stresses inside the artificial heart (Apel et al., 2001; Bluestein and Mockros, 1969; Gregoriades et al., 2000). This is impossible by exclusively using CFD. But it is possible by an indirect approach because a relationship between energy dissipation (ε) and hydrodynamic stresses exist. Bluestein and Mockros (1969) showed that there is a linear relationship in a log-log plot between haemolysis and energy dissipation rate. One can deduce it by analyzing the equations (1) and (2), which concern viscous and inertial subrange of turbulent spectrum, respectively (Bałdyga and Bourne, 1995):

$$\tau = \rho \cdot \sqrt{\varepsilon \cdot \nu} \quad \text{for} \quad d < \lambda_k \tag{1}$$

$$p = C \cdot \rho \cdot (\varepsilon \cdot d)^{\frac{2}{3}} \quad \text{for} \quad d > \lambda_k \tag{2}$$

where

$$\lambda_k = \frac{\nu^{0.75}}{\varepsilon^{0.25}} \tag{3}$$

Having in mind relations given by Eqs. (1) - (3), our method of haemolysis assessment is reduced to calculations of energy dissipation which occurs in the artificial heart.

To obtain energy dissipation values, the Large Eddy Simulations (LES) method has been used. Tavoularis et al. (2003) and Yoganathan et al. (2005) recognized LES as a very promising tool in modeling phenomena inside the artificial heart.

3. LARGE EDDY SIMULATIONS (LES)

A new promising approach to solve equations related to turbulent flow is known as "Large Eddy Simulations techniques (LES)". In LES, a set of equations is derived from the Navier - Stokes equations by performing a spatial averaging. It is different when compared to time averaging in RANS (Reynolds-averaged Navier-Stokes equations) technique. The averaged equations contain stress terms that must be evaluated through modeling to achieve closure. The equations solved in LES are developed by "filtering" Navier - Stokes equations. This process removes small spatial scales. The resulting equations describe the evolution of large eddies and contain the subgrid-scale stress tensor that represents the effects of the unresolved small scales. Leonard (1974) proposed to decompose, flow variables into large (filtered, resolved) and sub-grid (residual) scales, as follows:

$$v_i = \overline{v_i} + v_i^{`} \tag{4}$$

The filtered variable is defined in the general case by the convolution integral:

$$\overline{v_i}(x_1, x_2, x_3) = \iiint \left[\prod_{j=1}^{3} G_j\left(x_j, x_j^{`}\right)\right] v_i\left(x_1^{`}, x_2^{`}, x_3^{`}\right) dx_1^{`} dx_2^{`} dx_3^{`} \tag{5}$$

over the entire flow domain, where x_i and $x_i^{`}$ are position vectors and G is the general filter function. The function G is normalized by requiring that:

$$\iiint \left[\prod_{j=1}^{3} G_j\left(x_j, x_j^{`}\right)\right] dx_1^{`} dx_2^{`} dx_3^{`} = 1 \tag{6}$$

Several filter functions G, have already been examined (Aldama, 1990), but the volume-averaged "box" filter is most frequently used with finite-difference and finite-volume methods. The box filter function is given by:

$$G_j\left(x_j - x_j^{`}\right) = \begin{cases} \frac{1}{\Delta_j} & \left|x_j - x_j^{`}\right| \le \frac{\Delta_j}{2} \\ 0 & otherwise \end{cases} \tag{7}$$

using this filtering function we obtain

$$\overline{v_i}(\mathbf{x},t) = \frac{1}{\Delta^3}\int_{x_1-\frac{1}{2}\Delta x_1}^{x_1+\frac{1}{2}\Delta x_1}\int_{x_2-\frac{1}{2}\Delta x_2}^{x_2+\frac{1}{2}\Delta x_2}\int_{x_3-\frac{1}{2}\Delta x_3}^{x_3+\frac{1}{2}\Delta x_3} v\left(x_1-\grave{x_1},x_2-\grave{x_2},x_3-\grave{x_3}\right)d\grave{x_1}d\grave{x_2}d\grave{x_3} \quad (8)$$

where

$$\Delta = \sqrt[3]{\Delta_1\Delta_2\Delta_3} \quad (9)$$

and Δ_1, Δ_2, Δ_3 are increments in x_1, x_2, x_3, respectively. Filtering the Navier – Stokes and the continuity equation gives:

$$\frac{\partial \overline{v_j}}{\partial x_j} = 0 \quad (10)$$

$$\frac{\partial \overline{v_i}}{\partial t} + \frac{\partial \overline{v_i v_j}}{\partial x_j} = -\frac{\partial \bar{p}}{\partial x_i} + \frac{\mu}{\rho}\frac{\partial^2 \overline{v_i}}{\partial x_k^2} \quad (11)$$

The system cannot be solved for both $\overline{v_i}$ and $\overline{v_i v_j}$, so that the convective flux should be represented by decomposed variables, as follows:

$$\overline{v_i v_j} = \overline{v_i}\,\overline{v_j} + \tau_{ij} \quad (12)$$

Introducing Eq. (12) into (11), the following equation can be obtained:

$$\frac{\partial \overline{v_i}}{\partial t} + \frac{\partial \overline{v_i}\,\overline{v_j}}{\partial x_j} = -\frac{\partial \bar{p}}{\partial x_i} + \frac{\mu}{\rho}\frac{\partial^2 \overline{v_i}}{\partial x_k^2} - \frac{\partial \tau_{ij}}{\partial x_j} \quad (13)$$

where τ_{ij} is the sub-grid–scale (SGS) stress tensor:

$$\tau_{ij} = \left(\overline{\overline{v_i}\,\overline{v_j}} - \overline{v_i}\,\overline{v_j}\right) + \left(\overline{\grave{v_i}\,\overline{v_j}} + \overline{\overline{v_i}\grave{v_j}}\right) + \left(\overline{\grave{v_i}\grave{v_j}}\right) \quad (14)$$

The first term in parentheses on the right-hand side of the Eq. (14) is known as “Leonard stress”, the second term as “cross-term stress”, and the third term as “Reynolds stress”. Note, that if time averaging has been employed instead of filtering, the first two terms would be zero leaving only the Reynolds stress. To get the solution of Eq. (13), the effect of the sub-grid-scale (SGS) stresses must be modeled. The earliest and simplest model was proposed by Smagorinski (1963). It takes the form of mixing-length or gradient diffusion model with the length proportional to the filter width. Thus, the SGS stress tensor is represented by:

$$\tau_{ij} = 2\mu_T S_{ij} \quad (15)$$

where S_{ij} is the rate of strain tensor and

$$\mu_T = \rho(C_s\Delta)^2\sqrt{2S_{ij}S_{ij}} \quad (16)$$

where C_s is a well-known Smagorinsky constant which has to be prescribed as a fixed value in the entire integration domain with value from 0.1 to 0.24, or can be determined as a function of time and space by a dynamic procedure originally proposed by Germano et al. (1991) and later improved by several authors, e.g. by Lilly (1992). For models with a constant value of C_s, Van Driest – type exponential damping function results in a form such as (Moin and Kim, 1982):

$$l = C_s\Delta\sqrt{\left[1-e^{\left(\frac{-y^+}{A^+}\right)^3}\right]} \quad (17)$$

It is required in order to take into account the reduction of the sub-grid length l near solid walls. y^+ from Eq. (17) is defined by

$$y^+ = \frac{y\rho}{\mu}\sqrt{\frac{\tau_s}{\rho}} \quad (18)$$

With A^+ = 25. Recently, in many published investigations, the fixed parameter version of the Smagorinsky model has been applied. A theoretical value for the C_s = 0.165 can be derived for homogeneous isotropic flows (Lilly, 1967). For practically anisotropic shear flows, smaller values of C_s were found to be more appropriate. The well-established standard constant C_s = 0.1 is implemented in standard version of the LES model into CFD package FLUENT. The solution of the filtered Navier – Stokes equations gives the time-dependent solution for the resolved variables. In applications that operate nominally at a steady state, we are usually interested in the time–mean motion of flow in a steady sense. The time averaging of filtered equations is needed to obtain the time-averaged values of the variables.

In the literature, there is no paper where LES is used for haemolysis assessment in the artificial heart. However, this method has already been used for modeling of non-Newtonian blood flows through blood vessels (Molla and Paul, 2009).

5. RESULTS AND DISCUSSION

Using FLUENT package 6.13 and LES method, computational results for different centrifugal pump impeller geometries have been obtained. In view of Eqs. (1) and (2), we have focused on the analysis of energy dissipation inside the modeled artificial heart. On the basis of computational results, we concluded that haemolysis will be greater where areas of higher values of energy dissipation are noticed or where the average value of energy dissipation inside the artificial heart is higher than that of other geometries. In calculation, blood rheological properties have been approximated by Newtonian fluid with a density of 1 g/cm^3 and a viscosity of 3.26 mPas.

Figures 1–3 present computational results of energy dissipation obtained for 3 different impeller geometries and for 2 different rotation speeds.

We have analysed an impeller with curved blades (Fig.1) and impellers with curved channels (Fig. 2 and Fig. 3). A common analysis of the results obtained for all impellers allows one to note the following observations. The average value of energy dissipation in the artificial heart for all impeller geometries is always less for the lower rotation speed. This statement is rather obvious.

For the impeller with curved blades (Fig.1), the highest values of energy dissipation are observed at the end of blades. Thus, according to the authors' proposed method, haemolysis will take place in particular in these areas. To reduce destruction of blood elements, the geometry at the end of the blades should be optimised and corrected.

For impellers with curved channels, the highest values of energy dissipation are noted inside the channels and around the periphery of the impeller, in particular at the blood outflow from the channels. This is obviously related to the high speed of blood flowing through a narrow channel. To reduce the destruction of blood elements, the geometry of the end of the channels should be corrected.

From comparing the results shown in Fig. 2 and Fig.3, it can be concluded that the average value of energy dissipation in the pumps with such impellers is lower for the impeller whose channels are bent in the opposite direction to the rotation of the impeller (Fig. 3). It is clearly seen when comparing Fig. 2b and Fig.3b. The difference in the values of energy dissipation is 10 times.

The exemplary calculation results, which are given in this paper, indicate that the lowest haemolysis should be expected for the impeller with curved channels that are bent in the opposite direction to the rotation of the impeller. The results of these calculations confirm the results of the experimental studies of one of the authors conducted on prototype pumps using human blood (Szwast, 2009).

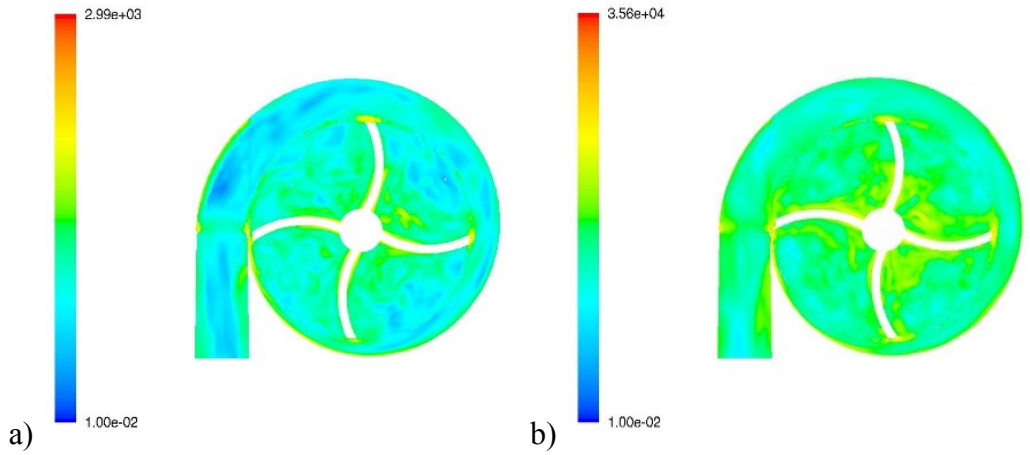

Fig. 1. Energy dissipation [m^2/s^3] in artificial heart, geometry 1: a) 1000 rpm, b) 3000 rpm. Open impeller with left-curved blades

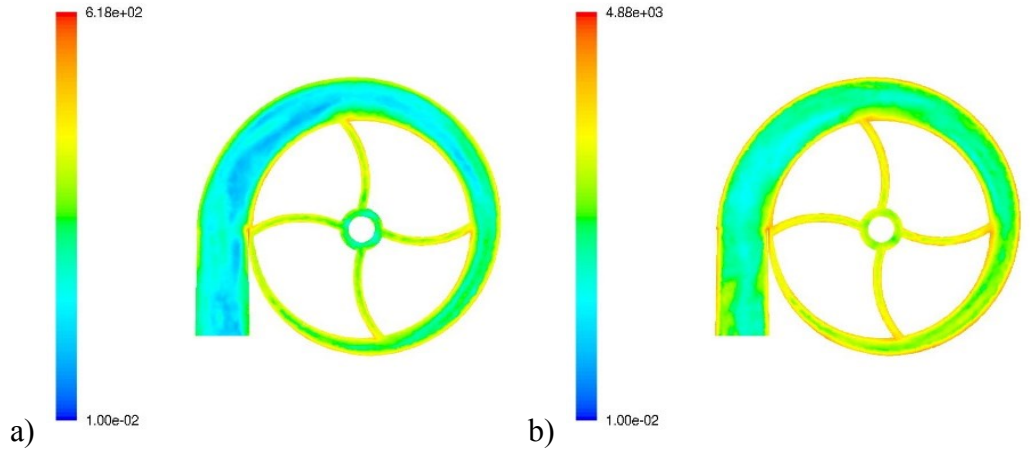

Fig. 2. Energy dissipation [m^2/s^3] in artificial heart, geometry 2: a) 1000 rpm, b) 3000 rpm. Closed impeller with left-curved channels

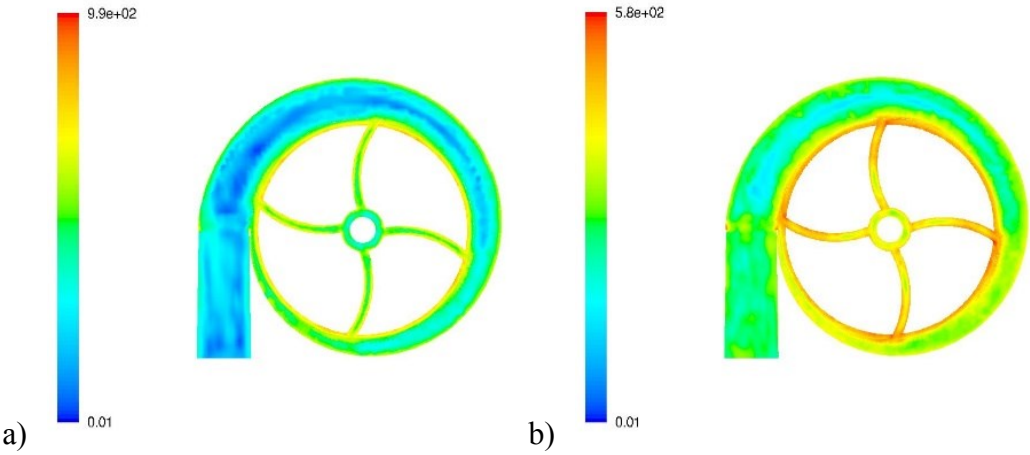

Fig. 3. Energy dissipation [m^2/s^3] in artificial heart, geometry 3: a) 1000 rpm, b) 3000 rpm. Closed impeller with right-curved channels

5. CONCLUSIONS

This paper presents a new method for assessing blood cell haemolysis based on stress analysis that has been caused by the impeller of a centrifugal pump in an artificial heart. CFD modeling using the LES model allows one to obtain reliable results of the value of energy dissipation inside the artificial heart. These results may be directly associated with the destruction of blood elements inside the pump. The haemolysis assessment tool proposed in this paper can be used for optimisation of new geometries of impellers for pumps, which will be used as heart assist devices.

SYMBOLS

A^+	damping constant
C	constant
C_S	Smagorinski constant
d	particle diameter, m
G_j	box filter function
p	stress in inertial subrange, Pa
$\bar{p}$	filtered value of pressure , Pa
S_{ij}	strain tensor
v_i'	sub-grid scale velocity, m/s
$\bar{v}_j$	jth component of velocity, m/s
$\bar{v}_l$	filtered value of velocity, m/s
x_j	position vector
x_j'	position vector
y^+	dimensionless parameter defined by Eq. (18)
Δ	increment in space, m
Δ_j	increment in x_j, m
ε	turbulent energy dissipation rate per mass unit, $m^2 \cdot s^{-3}$
λ_k	Kolmogorov scale, m
μ	dynamic viscosity, Pa·s
μ_T	turbulent viscosity, Pa·s
ν	kinematic viscosity, $m^2 \cdot s^{-1}$
ρ	density, $kg \cdot m^{-3}$
τ	stress in viscous subrange, Pa
τ_{ij}	viscous stress tensor
τ_S	viscous stress on wall

REFERENCES

Aldama A.A., 1990. Filtering techniques for turbulent flow simulation. *Lecture Notes in Engineering*. Vol. 56, Springer-Verlag, Berlin.

Apel J., Paul R., Klaus S., Siess T., Reul H., 2001. Assessment of hemolysis related quantities in a microaxial blood pump by computational fluid dynamics. *Artif. Organs*, 25, 341-347. DOI: 10.1046/j.1525-1594.2001.025005341.x.

Arvand A., Hormes M., Reul H., 2005. A validated computational fluid dynamics model to estimate hemolysis in a rotary blood pump. *Artif. Organs*, 29, 531-540. DOI: 10.1111/j.1525-1594.2005.29089.x.

Bałdyga J., Bourne J.R., 1995. Interpretation of turbulent mixing using fractals and multifractals. *Chem Eng Sci.*, 50, 381-400. DOI:10.1016/0009-2509(94)00217-F.

Bludszuweit C., 1995. Model for a general mechanical blood damage prediction. *Artif. Organs*, 19, 583-589. DOI: 10.1111/j.1525-1594.1995.tb02385.x.

Bluestein D., 2017. Utilizing Computational Fluid Dynamics in cardiovascular engineering and medicine—What you need to know. Its translation to the clinic/bedside. *Artif. organs*, 41, 117-121. DOI: 10.1111/aor.12914.

Bluestein M., Mockros, L.F., 1969. Hemolytic effects of energy dissipation in flowing blood. *Med. Biol. Eng. Comput.*, 7, 1-16. DOI: 10.1007/BF02474665.

Garatti A., Bruschi G., Colombo T., Russo C., Lanfranconi M., Milazzo F., Vitali E., 2008. Clinical outcome and bridge to transplant rate of left ventricular assist device recipient patients: comparison between continuous-flow and pulsatile-flow devices. *Eur. J. Cardiothorac. Surg.*, 34, 275-280. DOI: 10.1016/j.ejcts.2008.02.019.

Germano M., Piomelli U., Moin P., Cabot W.H., 1991. A dynamic subgrid-scale eddy viscosity model. *Phys. Fluids A: Fluid Dyn.*, 3, 1760-1765. DOI: 10.1063/1.857955.

Gregoriades N., Clay J., Ma N., Koelling K., Chalmers J.J., 2000. Cell damage of microcarrier cultures as a function of local energy dissipation created by a rapid extensional flow. *Biotech. Bioeng.*, 69, 171-182. DOI: 10.1002/(SICI)1097-0290(20000720)69:2.

Jones S.A., 1995. A relationship between Reynolds stresses and viscous dissipation: Implications to red cell damage. *Ann Biomed Eng*, 23, 21-28. DOI: 10.1007/BF02368297.

Kim S.H., Chandran K.B., Chen C.J., 1992. Numerical simulation of steady flow in a two-dimensional total artificial heart model. *J. Biomech. Eng.*, 114, 497-503. DOI: 10.1115/1.2894101.

Leonard A., 1975. Energy cascade in large-eddy simulations of turbulent fluid flows. *Adv. Geophys.*, 18, 237-248. DOI: 10.1016/S0065-2687(08)60464-1.

Leprince P., Bonnet N., Rama A., Leger P., Bors V., Levasseur J.P., Gandjbakhch I., 2003. Bridge to transplantation with the Jarvik-7 (CardioWest) total artificial heart: A single-center 15-year experience. *J. Heart Lung Transplant.*, 22, 1296-1303. DOI: 10.1016/S1053-2498(03)00036-6.

Leverett L.B., Hellums J.D., Alfrey C.P., Lynch E.C., 1972. Red blood cell damage by shear stress. *Biophys J.*, 12, 257. DOI: 10.1016/S0006-3495(72)86085-5.

Lilly D.K., 1967. The representation of small-scale turbulence in numerical simulation experiments, In: Goldstine H.H. (Ed.), *Proceedings of the IBM Scientific Computing Symposium on Environmental Sciences*. IBM Forum No. 320 – 1951, 195 - 210.

Lilly D.K., 1992. A proposed modification of the Germano subgrid-scale closure method. *Phys. Fluids A: Fluid Dyn.*, 4, 633-635. DOI: 10.1063/1.858280.

Medvitz R.B., Boger D.A., Izraelev V., Rosenberg G., Paterson E.G., 2011. Computational fluid dynamics design and analysis of a passively suspended Tesla pump left ventricular assist device. *Artif. Organs*, 35, 522-533. DOI: 10.1111/j.1525-1594.2010.01087.x.

Mitamura Y., Takahashi S., Amari S., Okamoto E., Murabayashi S., Nishimura I., 2011. A magnetic fluid seal for rotary blood pumps: effects of seal structure on long-term performance in liquid. *J Artif. Organs*, *14*(1), 23-30. DOI: 10.1007/s10047-010-0526-8.

Moin P., Kim J., 1982. Numerical investigation of turbulent channel flow. *J. Fluid Mech.*, 118, 341-377. DOI: 10.1017/S0022112082001116.

Molla M.M., Paul M.C., 2009. LES of non-newtonian physiological blood flow. *1st International Conference on Mathematical and Computational Biomedical Engineering* - CMBE2009. June 29 - July 1, 2009, Swansea, UK.

Nevaril C.G., Lynch E.G., Alfrey C.P., Hellums J.D., 1968. Erythrocyte damage and destruction induced by shearing stress. *J. Lab. Clin. Med.*, 71(5), 784-790.

Okamoto E., Hashimoto T., Inoue T., Mitamura Y., 2003. Blood compatible design of a pulsatile blood pump using computational fluid dynamics and computer-aided design and manufacturing technology. *Artif. Organs*, 27, 61-67. DOI: 10.1046/j.1525-1594.2003.07183.x.

Pohorecki R., Bałdyga J., Ryszczuk A., Motyl T., 2001. Erythrocyte destruction during turbulent mixing. *Biochem. Eng. J.*, 9, 147-154. DOI: 10.1016/S1369-703X(01)00135-8.

Rooney J.A., 1970. Hemolysis near an ultrasonically pulsating gas bubble. *Science*, 169(3948), 869-871. DOI: 10.1126/science.169.3948.869.

Saito S., Nishinaka T., 2005. Chronic nonpulsatile blood flow is compatible with normal end-organ function: Implications for LVAD development. *J Artif. Organs*, 8, 143-148. DOI: 10.1007/s10047-005-0295-y.

Smagorinsky J., 1963. General circulation experiments with the primitive equations: I. The basic experiment. *Mon. Weather Rev.*, 91, 99-164. DOI: 10.1175/1520-0493(1963)091.

Song X., Throckmorton A.L., Wood H.G., Antaki J.F., Olsen D.B., 2003. Computational fluid dynamics prediction of blood damage in a centrifugal pump. *Artif. Organs*, 27, 938-941. DOI: 10.1046/j.1525-1594.2003.00026.x.

Sutera S.P., Mehrjardi M.H., 1975. Deformation and fragmentation of human red blood cells in turbulent shear flow. *Biophys. J.*, 15, 1-10. DOI: 10.1016/S0006-3495(75)85787-0.

Szwast M., 2009. *Selected experimental and computational aspects of artificial heart acting as a centrifugal pump*. PhD Thesis.

Szwast M., Suchecka T., Piątkiewicz W., 2012. Mathematical model for biological cell deformation in a cylindrical pore. *Chem. Process Eng.*, 33, 385-396. DOI: 10.2478/v10176-012-0034-x.

Tavoularis S., Sahrapour A., Ahmed N.U., Madrane A., Vaillancourt R., 2003. Towards optimal control of blood flow in artificial hearts. *Cardiovascular Eng.*, 8, 20-31. DOI: 10.1046/j.1525-1594.2003.00026.x.

Wang Y., Song X., Ying C., 2008. Applications of traditional pump design theory to artificial heart and CFD simulation. *Front. Energy Power Eng. China*, 2, 504-507. DOI: 10.1007/s11708-008-0059-5.

Williams A.R., Hughes D.E., Nyborg W.L., 1970. Hemolysis near a transversely oscillating wire. *Science*, 169(3948), 871-873. DOI: 10.1126/science.169.3948.871.

Yoganathan A.P., Chandran K.B., Sotiropoulos F., 2005. Flow in prosthetic heart valves: state-of-the-art and future directions. *Ann. Biomed. Eng.*, 33, 1689-1694. DOI: 10.1007/s10439-005-8759-z.

Received 29 November 2016
Received in revised form 15 May 2017
Accepted 16 May 2017

DE GRUYTER OPEN
www.czasopisma.pan.pl PAN POLSKA AKADEMIA NAUK www.journals.pan.pl
Chemical and Process Engineering 2017, 38 (2), 241-248
DOI: 10.1515/cpe-2017-0018
PAN

MEASUREMENTS OF HYDROGEN SOLUBILITY IN NITROBENZENE/ANILINE MIXTURES

Aleksandra Srebniak[1], Manfred Kraut[*2], Oliver Görke[2], Paweł Sobieszuk[*1]

[1]Warsaw University of Technology, Faculty of Chemical and Process Engineering, Warynskiego1, 00-645 Warsaw, Poland

[2]Institute for Micro Process Engineering/Karlsruhe Institute of Technology/Hermann-von-Helmholtz-Platz 1, 76344 Eggenstein-Leopoldshafen, Germany

Measurements of hydrogen solubility in various nitrobenzene-aniline mixtures were conducted in an autoclave reactor with a stirrer and control of temperature. The solubility of hydrogen was measured at 7 different values of temperature (30 °C, 40 °C, 50 °C, 90 °C, 130 °C, 170 °C, 210 °C, respectively), 3 values of stirrer rotation speed (1200 rpm, 1600 rpm, 2000 rpm, respectively) and a range of pressure of 20 – 30 bar. Moreover, pure aniline, pure nitrobenzene and their mixtures with different concentrations were used. In the next step, values of Henry's constant were calculated. Based on experimental data a dependence of Henry's constant on temperature for pure aniline and pure nitrobenzene was proposed. Additionally, for each temperature correlations between Henry's constant and aniline's concentration in mixture of nitrobenzene-aniline were found.

Keywords: solubility, Henry's constant, hydrogenation

1. INTRODUCTION

The annual world production of aniline amounts to 3.8 million tones and increases from year to year (Kahl et al., 2011). Originally, aniline was produced in the process of reduction of nitrobenzene by cheap reagents, for instance, sulphuric and nitric acid in the presence of an iron catalyst (Morrison and Boyd, 2002). This process generated large quantities of waste reagents and was finally replaced by catalytic hydrogenation of nitrobenzene (Machado, 2007). The amount of hydrogen dissolved in the liquid mixture directly affects and limits this process. Three-phase-hydrogenation processes seem to be a promising way of enhancing the space-time yield (Ramachardan and Chaudhari, 1983; Tatterson, 1991), especially in microreactors such as microfall film reactors (Yeong et al., 2003), therefore, it is of high interest to know the solubility and also the solution rate of hydrogen in nitrobenzene/aniline mixtures. With thermodynamic solubility and kinetic solution rate data, it would be possible to build up a computer-aided model of a nitrobenzene hydrogenation reactor. However, there is a lack of experimental data concerning the solubility of hydrogen in mixtures of nitrobenzene/aniline. Therefore, the aim of this work is to measure hydrogen solubility in nitrobenzene/aniline mixtures under different process conditions (influence of temperature, mixing intensity and liquid phase composition). The experimental data obtained is essential for nitrobenzene hydrogenation with a catalyst in further microreactors' investigation.

*Corresponding authors, e-mail: Pawel.Sobieszuk@pw.edu.pl, manfred.kraut@kit.edu

2. EXPERIMENTAL SETUP

The experiments were carried out in an autoclave reactor with a stirrer. The autoclave was filled with a mixture of nitrobenzene and aniline to half of its volume (85 ml) and sealed up (Fig. 1). Before the first experiment, on each day and after every following one, the reactor was purged with nitrogen for half an hour when the inlet and outlet valves were open and the stirrer was slowly rotating. The experiments were conducted for five mixtures: 100% nitrobenzene volume content, 75% nitrobenzene + 25% aniline, 50% nitrobenzene + 50% aniline, 25% nitrobenzene + 75% aniline and 100% aniline, respectively. Each mixture was investigated at 7 temperatures: 30 °C, 40 °C, 50 °C, 90 °C, 130 °C, 170 °C and 210 °C, respectively. For 25% nitrobenzene + 75% aniline mixture and 100% aniline the results for 210 °C were omitted. This temperature is higher than the boiling point (184 °C) of aniline and under atmospheric pressure at the beginning of the experiments these liquids were boiling, which led to incorrect results. To perform the experiments, the inlet and outlet gas nozzles were tightly closed and hydrogen was dosed with the mass flow controller into the autoclave reactor. Gas pressure in the pipe before the inlet valve was recorded. When the pipe filled up with sufficient amount of hydrogen, its flow was switched off. Next the inlet valve to the autoclave was opened. The moment the pressure inside the autoclave had the desired value, the inlet valve was quickly closed and the stirrer was set on the desired speed of rotation. The first value of pressure (for zero time) was written down. For each temperature the experiments were carried out at three stirrer rotation speeds: 1200 rpm, 1600 rpm and 2000 rpm, respectively (for pure nitrobenzene only under 1200 and 1600 rpm). Finally, each experiment was replicated three times for each stirrer rotation speed, filling the reactor with such an amount of hydrogen that the initial pressure at time zero was in the range of 20 – 30 bar. The pressure of gas in reactor was measured. Hydrogen absorption by the liquid was accompanied by a pressure decrease until a steady-state has been reached. Based on the final value of gas pressure, the solubility of hydrogen in the mixture was determined.

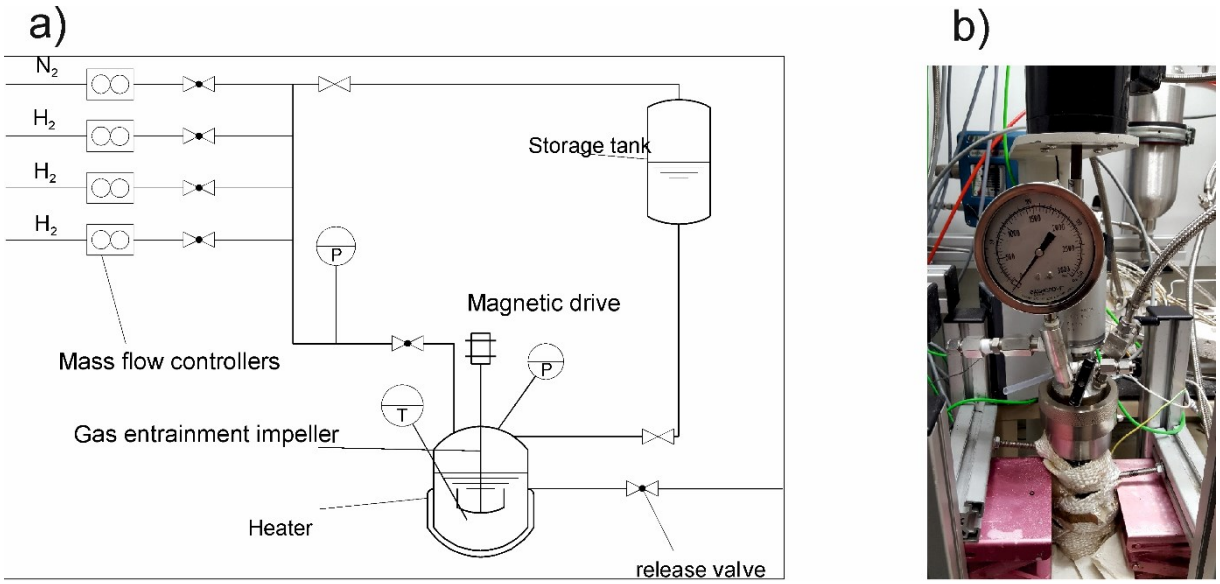

Fig. 1. Experimental set-up: a) flow scheme , b) image of stirred autoclave

3. METHODOLOGY

Pressure drop, p, observed in the course of experiments (a difference between the initial pressure and that at the moment of its stabilization) is a sum of hydrogen pressure p_{H2} and the vapour pressure of liquid p_L. The values of p_L were calculated according to the Antoine's equation for pure nitrobenzene and pure aniline. In the case of nitrobenzene/aniline mixtures, vapour pressure was calculated from the

Raoult law. In this way, the pressure drop observed as a result of hydrogen absorption Δp was found and used to count the number of moles of absorbed hydrogen. Under the experimental conditions the compressibility factor equals 1 and for the number of moles of absorbed gas the ideal gas law is applicable:

$$n = \frac{\Delta p\, V_G}{T\, R} \tag{1}$$

The amount of absorbed hydrogen per liquid volume L [mol/m^3] was found from the equation:

$$L = \frac{n}{V_L} \tag{2}$$

In the next step the Henry' constant H [bar m^3/mol] was determined as:

$$H = \frac{p_{H2}}{L} \tag{3}$$

In Eq. (3) hydrogen pressure p_{H2} is exactly what has been measured at each measurement point. For aniline Henry's constant was described as H_{AN}, for pure nitrobenzene as H_{NB} and for mixture as H_M, respectively. Values L are dependent on pressure, while Henry's constant H calculated from Eq. (3) is independent of pressure within the range of pressure used.

4. RESULTS AND DISCCUSION

In all experiments the changes of pressure in time were measured. As an example, the pressure drops are shown in Fig. 2 at 1200 rpm, 1600 rpm and 2000 rpm, respectively for 50% nitrobenzene + 50% aniline mixture at 130 ℃. The pressure at the start of the experiment was similar for this mixture at all three stirrer rotation speeds. It can be deduced that the duration time of experiment was shorter for higher stirrer rotation speeds and in all cases the steady-states conditions were achieved.

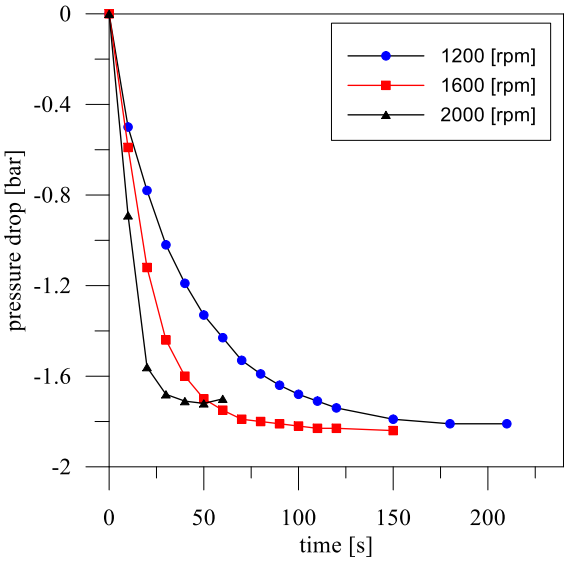

Fig. 2. Pressure drop for 50 % volumetric concentration of aniline at 130℃

Based on the steady-state conditions in all experiments, the values of Δp were determined. Using Eq. (2) the amount of absorbed hydrogen was calculated and presented in Fig. 3. As can be seen in Fig. 3, an increase in the amount of hydrogen in nitrobenzene/aniline mixtures was observed with the increasing temperature. Similar results for hydrogen were found for other organic substances. Brunner

(1985) investigated solubility of hydrogen in *n*-hexane, *n*-octane, toluene, acetonitrile, 1,4-dioxane, N,N-dimethylformamide, *n*-decane, tetrahydrofuran, 1- methylpyrrolidone-2, acetone at 298.15 K, 323.15 K and 373.15 K, respectively, and partially at pressures up to 14 MPa. He found that the solubility of hydrogen increases with the increasing temperature.

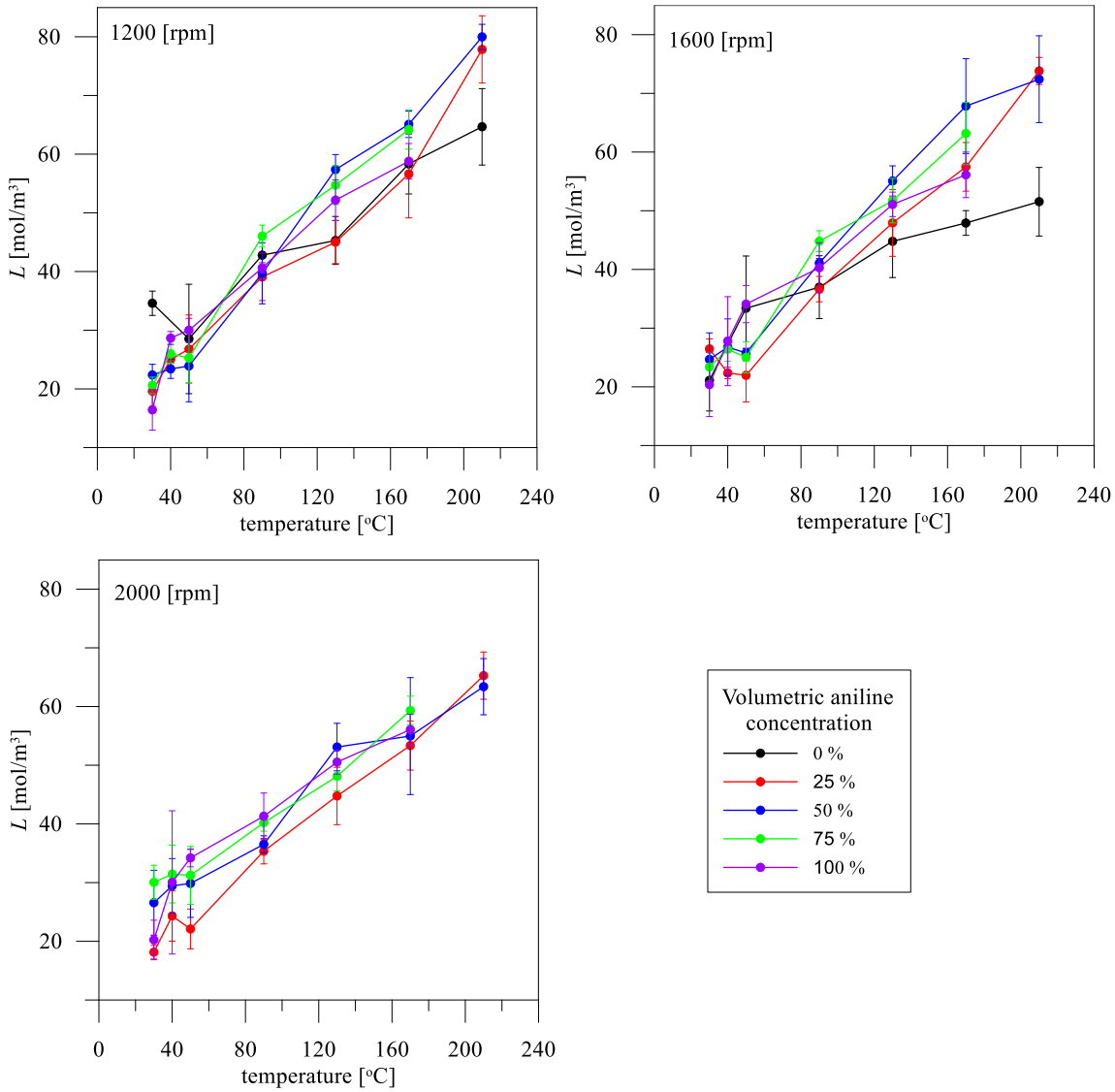

Fig. 3. Amount of absorbed hydrogen per liquid volume in nitrobenzene/aniline mixtures at 1200, 1600 and 2000 rpm

D'Angelo and Francesconi (2001) investigated solubility of hydrogen in liquid alcohols: methanol, ethanol, 1-propanol and 1-butanol within the range of temperatures between 298.15 K and 525.15 K and at pressures between 3.6 MPa and 10 MPa. They concluded that the solubility of hydrogen in all studied alcohols increased with increasing temperature and pressure. An exemplary influence of the stirrer rotation speed on solubility of hydrogen is shown in Figs. 4 – 5. *L* is practically independent of the stirrer rotation speed, when error bars of experimental data are in the limit of experimental scatters.

In order to present results as pressure, independent *H* values are calculated. For pure liquids, the Henry's constants were calculated based on the results of experiments and Eq. (3). The average values of these constants were calculated for the experiment temperatures and for three stirrer rotation speeds. The *H* values are presented in Fig. 6.

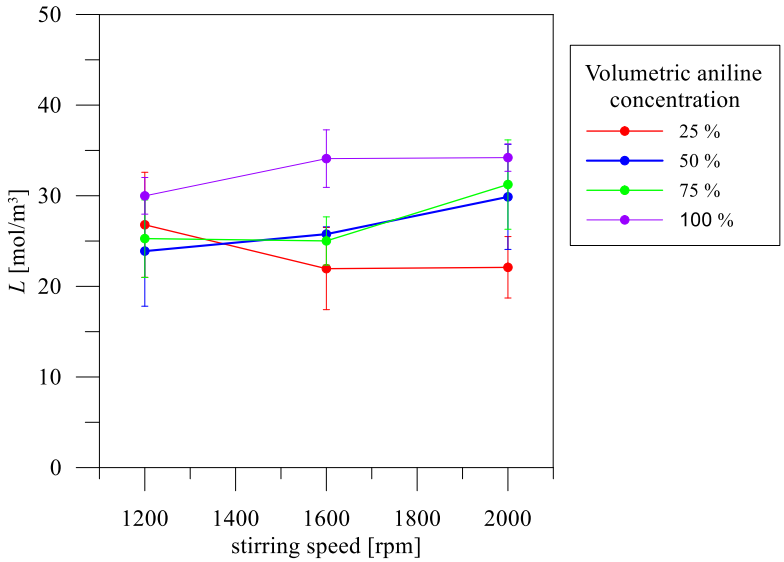

Fig. 4. Amount of absorbed hydrogen per liquid volume in nitrobenzene/aniline mixtures at 50 °C

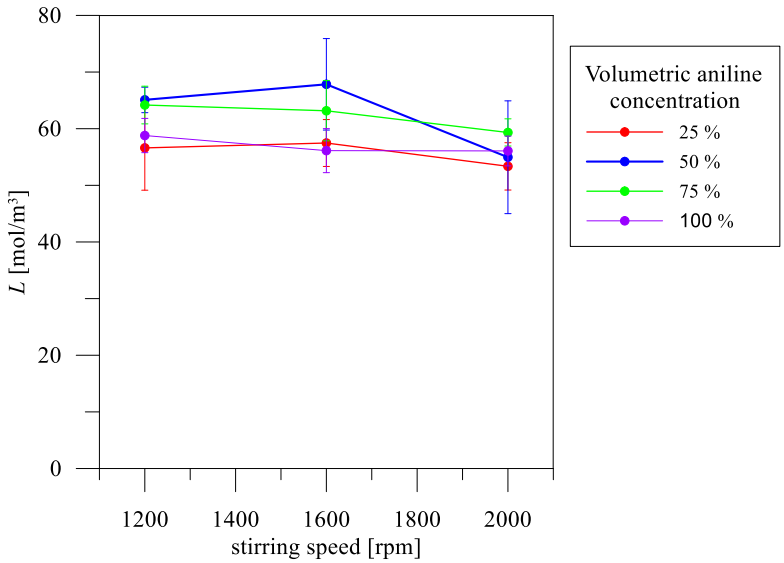

Fig. 5. Amount of absorbed hydrogen per liquid volume in nitrobenzene/aniline mixtures at 170 °C

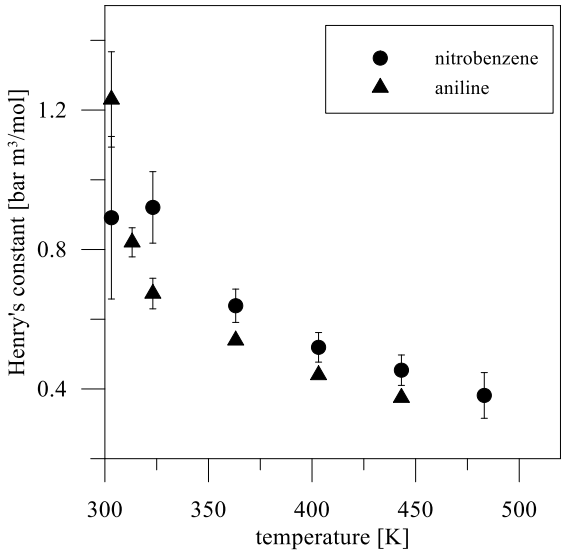

Fig. 6. Henry's constants for pure nitrobenzene and aniline

In the next step, the dependences of Henry's constants in function of temperature for pure nitrobenzene (H_{NB}) and pure aniline (H_{AN}) were determined:

$$\log H_{NB} = 1.2268 - 0.0053 \cdot T + 4.06 \cdot 10^{-6} \cdot T^2 \tag{4}$$

$$\log H_{AN} = 2.4105 - 0.0108 \cdot T + 10^{-5} \cdot T^2 \tag{5}$$

The form of correlations (4) and (5) is widely cited based on the publications of Barret (1966) and Danckwerts (1970), who investigated the influence of temperature on gas solubility in liquids.

To compare the experimental values of Henry's constants with those calculated from Eqs. (4, 5), parity plots were presented in Fig. 7 for nitrobenzene and in Fig. 8 for aniline, respectively. As can be seen Eq. (4) is accurate with an error of ±10%, while Eq. (5) with an error of ±16%.

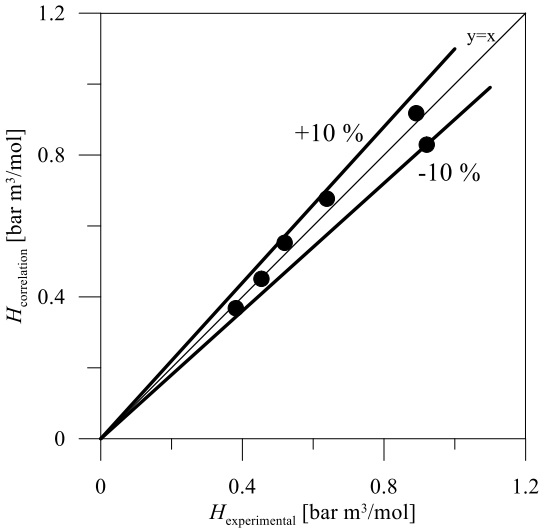

Fig. 7. Parity plot of Eq. (4)

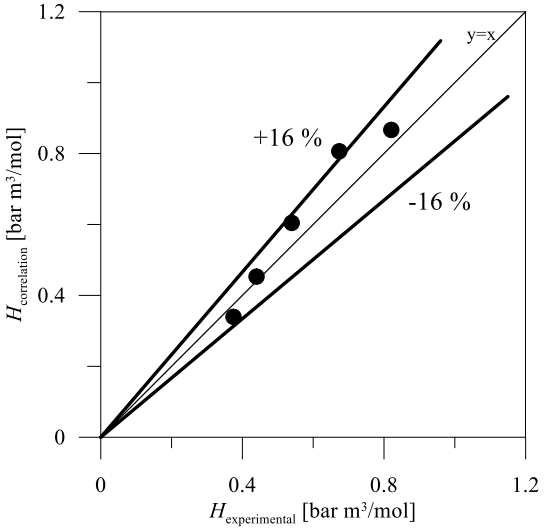

Fig. 8. Parity plot of Eq. (5)

Finally, for temperature in the range of 40 °C – 170 °C, the values of the Henry's constant for nitrobenzene/aniline mixtures are presented in Fig. 9. As can be seen, H_M slightly decreases with increase of aniline concentration, which is in agreement with data in Fig. 6.

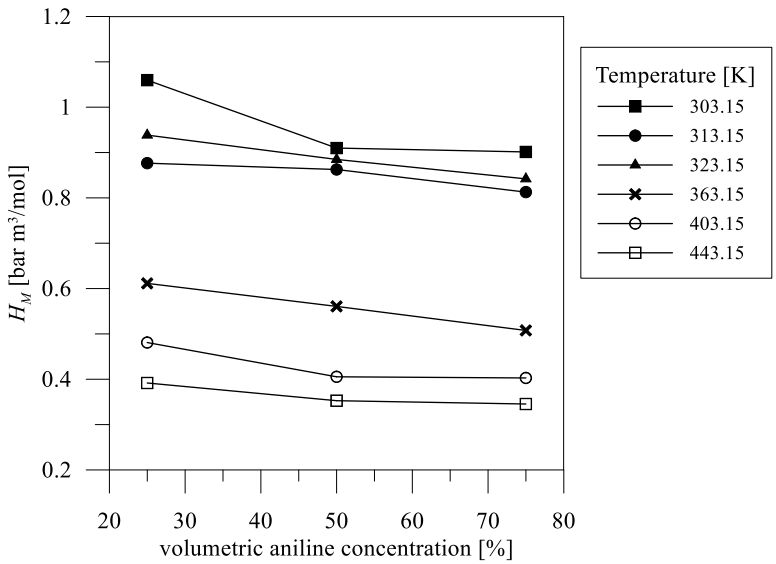

Fig. 9. Henry's constant values for aniline/nitrobenzene mixtures

5. CONCLUSIONS

The measurements of hydrogen absorption in nitrobenzene/aniline mixtures were carried out in an autoclave reactor equipped with a stirrer for a wide range of temperature, concentration of aniline and stirrer rotation speed. It was found that the amount of absorbed hydrogen in these mixtures decreases with decreasing temperature in the range of 30 °C – 210 °C, and under pressure between 20 and 30 bar. Similar effect for other organic liquids is reported in literature. Based on the results of experiments, the Henry's constants as a function of temperature for pure nitrobenzene and aniline were experimentally determined and adequate correlations were proposed. Finally, values of the Henry's constant for nitrobenzene/aniline mixtures at different temperatures were presented.

The data determined represent an important extension of thermodynamic solubility for such a basic reaction mixture system of nitrobenzene, aniline and hydrogen. As the next step, it should further be extended by including water as reaction product in the system. The data obtained can be implemented to establish a better computational model of a three-phase hydrogenation reactor.

SYMBOLS

H	Henry's constant, bar·m^3/mol
L	amount of hydrogen absorbed per liquid volume, mol/m^3
n	number of mole of absorbed hydrogen
p	pressure, Pa
R	gas constant, J/(mol·K)
T	temperature, K
V	volume, m^3
Δp	pressure drop, Pa

Subscripts

AN	aniline
G	gas
H2	hydrogen
NB	nitrobenzene

L liquid
M mixture

REFERENCES

Barret P.V.L., 1966. *Gas absorption on a sieve plate*. Ph.D. Thesis, University of Cambridge.

Brunner E., 1985. Solubility of hydrogen in 10 organic solvents at 298.15, 323.15, and 372.15 K. *J. Chem. Eng. Data*, 30, 269-273. DOI: 10.1021/je00041a010.

Danckwerts P.V., 1970. *Gas-Liquid Reaction.* Mc Graw-Hill, New York.

d'Angelo J.V.H., Francesconi A.Z., 2001. Gas-liquid solubility of hydrogen in *n*-alcohols ($1 \leq n \leq 4$) at pressures from 3.6 MPa to 10 MPa and temperatures from 298.15 K to 525.15 K. *J. Chem. Eng. Data*, 46, 671-674. DOI: 10.1021/je000189u.

Kahl T., Schroeder K.W., Lawrence F.R., Marshall W.J., Hoeke H., Jackh R., 2011. *Ullmann's encyclopedia of industrial chemistry*. Wiley-VCH.

Machado R., 2007. Fundamentals of mass transfer and kinetics for the hydrogenation of nitrobenzene to aniline. *Air Products and Chemicals,* 1, 1-14.

Morisson R.T., Boyd R.N., 1992. *Organic chemistry*. Prentice Hall, New Jersey.

Ramachandran P.A., Chaudhari R.V., 1983. Three-phase catalytic reactors. *Topics in Chemical Engineering*, Vol. 2, Chapters 9, Gordon and Breach Science Publishers, Philadelphia.

Tatterson G.B., 1991. *Fluid mixing and gas dispersion in agitated tanks.* McGraw-Hill, New York.

Yeong K.K., Gavrilidis A., Zapf R., Hessel V., 2003. Catalyst preparation and deactivation issues for nitrobenzene hydrogenation in a microstructured falling film reactor. *Catalysis Today*, 81, 641–651. DOI: 10.1016/S0920-5861(03)00162-7.

Received 25 September 2016
Received in revised form 3 April 2017
Accepted 12 April 2017

DE GRUYTER OPEN www.czasopisma.pan.pl PAN POLSKA AKADEMIA NAUK www.journals.pan.pl
Chemical and Process Engineering 2017, 38 (2), 249-264
DOI: 10.1515/cpe-2017-0019
PAN

SEPARATION OF CONTAMINANTS IN THE FREEZE/THAW PROCESS

Janusz A. Szpaczyński*[1], Jeffrey A. White[2], Caroline L. Côté[2,3]

[1]Wrocław University of Science and Technology, ul. Wybrzeże Wyspiańskiego 27, 50-370 Wrocław, Poland

[2]Northern Watertek Corporation, 1796 Courtwood Crescent, Ottawa, Ontario, K2C 2B5, Canada

[3]Laval University, 1030 avenue de la Médecine, Québec, G1V 0A6, Canada

These studies examined the concept of concentration and purification of several types of wastewater by freezing and thawing. The experiments demonstrated that freezing of contaminated liquid contributed to concentration of contaminants in solution as well as significant concentration and agglomeration of solid particles.

A high degree of purification was achieved for many parameters. The results of comparative laboratory tests for single and multiple freezing are presented. It was found that there was a higher degree of concentration of pollutants in wastewater frozen as man-made snow than in bulk ice. Furthermore, the hypothesis that long storage time of liquid as snow and sufficient temperature gradient metamorphism allows for high efficiency of the concentration process was confirmed.

It was reported that the first 30% of the melted liquid volume contained over 90% of all impurities. It gives great opportunities to use this method to concentrate pollutants. The results revealed that the application of this process in full scale is possible. Significant agglomeration of solid particles was also noted. Tests with clay slurry showed that repeated freezing and thawing processes significantly improve the characteristics of slurry for sedimentation and filtration.

Keywords: freeze crystallization, snow metamorphism, landfill leachate, wastewater, sludge dewatering

1. INTRODUCTION

Conventional methods for treatment of municipal and industrial fluid waste are costly, particularly if large volumes have to be processed. Professional engineers and scientists are looking for economical alternatives for methods that are currently in use. In recent decades, with particular emphasis, the process of freezing of wastewater has been investigated. Several different approaches have been studied and the process has gained new interest for industrial and municipal wastewaters.

In the 1960's, research studies were intensified at the two-phase concentration process. In such an approach, ice grows in solution by adding to its structure water molecules. If ice incorporates to its structure impurities, internal stresses appear. Therefore, ice crystals try to collect only molecules of water and reject dissolved and solid compounds. In this approach, impurities are concentrated in the remaining unfrozen liquid. Such method was studied by Baker (1967; 1967a; 1969), Taft (1965) and recently by Wakisaka et al. (2001) and Gay et al. (2003). Researchers focused on issues of trapping and rejection of solid particles during freezing of contaminated water and migration of particles in front of a growing ice plane (Cisse and Bolling, 1971; Corte, 1962; Halde, 1979). The authors reported that the best particle migrations as well as the best concentration effect were obtained at a low freezing rate.

*Corresponding authors, e-mail: janusz.szpaczynski@pwr.edu.pl

This fact was also noted by Chian et al. (2002). However, Parker (1999), for higher concentration of solids, noted satisfactory results after experiments with ultra-rapid freezing of alum sludge.

Muller and Sekoulov (1992) used a falling film reactor to examine the potential of freeze concentration to reuse municipal wastewater. Pure water was removed from the solution as ice. Impurities were concentrated in the remaining water. The authors noted efficiencies of up to 99% of conductivity, TOC, DOC and NH_4-N in a single stage freezing of municipal wastewater. For wastewater with higher concentration of impurities the efficiency was about 91%.

Cragin (1995) studied an exclusion of sodium chloride from ice during freezing. He reported that for a given freezing rate, the salt incorporation mechanism depends upon the solution concentration. Later, Geo et al. (2009) noted that mixing of the freezing liquid reduces the influence of the initial feed water impurity concentration on the efficiency of separation.

Various attempts have been made to apply, in full scale, the beneficial effect of the freeze crystallization process. For example, the process has been successful in food industry for concentration of fruit juices and pre-concentration of wine (Kyprianidou-Leodidou and Botsaris,1990). Recently Montusiewicz et al. (2010) examined the effect of freezing and thawing effects on anaerobic digestion of mixed sewage sludge from municipal WWTP. For treatment of industrial or municipal wastewater, in most cases, the traditional freeze and thaw process with application of the refrigeration system has not been accepted for full scale application because of its high energy consumption. The concept of freezing wastewater in natural weather conditions, with ambient temperature below zero, dramatically changes the situation and creates favourable circumstances for industrial applications.

Large volumes of wastewater, such as mine tailings, create serious environmental problems. The wastewater, from Canadian Athabasca Oil Sands, is a well known example. Treatment of fine tailings from Athabasca Basin has been the subject of many theoretical and experimental studies in the last several decades. Many different methods and technologies, including freezing, were tested (FTFC, 1995). Sego (1996) used freezing for impurity removal from recycle water from the extraction of bitumen from oil sands. The author reported achieving separation of over 95% of original chloride and sodium concentration in field tests. Gao et al. (2004) used spray freezing for concentration of oil sands tailings pond water and the pulp mill wastewater. In the experiments, the wastewater froze partially with run off production or completely during the operation. The authors concluded that to achieve higher efficiency of impurity removal, the wastewater should be only partially frozen. It could be assumed that the method of partially frozen spray is similar to conventional two phase concentration process. Most probably, part of wastewater in the form of droplets was frozen as a bulk ice on the ground and the concentrated run off was created. Beier et al. (2007) as well investigated the feasibility of using freeze separation process for reducing salinity of oil sands process water from Athabasca Basin in Northern Alberta. Experiments revealed that during freeze-thaw cycle, the majority of salts were concentrated into less than one quarter of the original frozen volume. Moreover, Gao and Shao (2009) used progressive freeze concentration process for removal of five commonly used pharmaceuticals (ibuprofen, gemfibrozil, acetylsalicylic acid, metoprolol and sulfamethoxazole). By freezing only 80% of feed water and without washing the ice, about 84-92% of the drug content reduction in ice was achieved in single unidirectional downward freezing (UDF). In two stage UDF about 99% reduction was achieved. With a few exceptions, which will be discussed later in this paper, freeze-thaw concept has been applied for treatment of several different industrial wastewaters but only in small scale experimental studies.

At the same time, parallel to research of wastewater freezing, independent studies were carried out in the field of separation of impurities present in the natural snow. Johannessen et al. (1975; 1978) reported that 20 to 30 % of the first run off from a natural snow pack contained up to 80% of dissolved compounds absorbed to snowflakes and deposited on the ground. This phenomenon, called “ionic pulse” or “first flash”, is partially responsible for acidification of surface water during spring. The

process of ion elution from natural snowpack still remains of particular concerns of scientists (Bales, 1989; Brimblecombe et al., 1985, 1987; Tranter, 1992). Recently, Meyer et al. (2006; 2009), based on experiments, reported that even though conductivity of melt indicated a preferential early elution of ions, in the first meltwater fraction, no "first flash" phenomenon was observed for soluble PAHs. Furthermore, the authors noted that water soluble organic chemicals, such as atrazine, are preferentially released at an early stage of melting. Authors concluded that such chemicals were accumulated at the surface of snow particles and dissolved in downward percolating meltwater. Therefore, they were released with first meltwater. Furthermore, the author stated that hydrophobic substances attached to particles such as larger polycyclic aromatic hydrocarbons, are often released at the end of melting because of particle coagulation and its trapping in pores of the snow pack. Recently, Meyer and Wania (2011) developed a snowmelt model to simulate and predict the elution of organic substances from melting snow.

The process responsible for segregation of chemical compounds in the natural snow pack, as well as its concentration is different than the standard processes in freeze and thaw operations. Segregation of impurities in natural snowpack and ion elution as well as ionic pulse are created by the snow metamorphism phenomenon (Sommerfeld, LaChapelle, 1970). The effect of metamorphism in natural snow is known but the mechanism of this segregation is still investigated by many researchers (Christon et al. 1994; Colbeck, 1980; Marbouty, 1980; Pinzer et al. 2012). Brimblecombe et al. (1985; 1987) revealed that some compounds are released earlier and with higher concentration than others. The authors established the following sequence of ion elution from the natural snowpack:

$$SO_4^{2-} > NO_3^- > NH_4^+ > K^+ > Ca^{2+} > Mg^{2+} > Na^+ > Cl^-$$

Sulphate and nitrate are removed in preference to chloride and the cations such as sodium, magnesium, calcium as well as potassium. Preferential chemical elution was also noted by Cragin et al. (1993). The authors noted that preferential chemical elution during snow melting is influenced by preferential rejection of ions during snow crystal growth. The author also stated that less soluble chemical impurities, such as sulphates, are rejected more efficiently and therefore appear sooner and in higher concentrations in the meltwater than more soluble species, such as chloride. Droste and Johnson (1993) analysed various pollutants in snow and snowmelt from four snow dumpsites in the Ottawa-Carleton Region. They also noted a high concentration of contaminants in the first meltwater coming from the snow pack. Tatarniuk et al. (2009) also reported "ionic pulse" in the first melt from snow at municipal storage facilities. The salt concentration in the first meltwater was 10 times higher than average concentration in the bulk snow. The authors reported that about 90% of the chloride and sodium was released from experimental cores within the first 19% of meltwater.

Several studies were done to use man-made snowmaking techniques and freeze/thaw process for treatment of wastewater. The first trial was done in 1974. The Upper Yampa Water Conservation District of Colorado and Wright-McLaughlin Engineers performed trials of sewage effluent storage as snow. The purpose of the study was to evaluate the use of sewage for snowmaking on ski slopes. A limited monitoring program was conducted. Pollutants in effluent, snow and snow melt were examined. Significant reduction of BOD_5 in the snowpack was noted. Huber and Palmateer in a joint project with White of Delta Engineering (1985) performed extensive studies on properties of secondary treated effluent converted to man-made snow. Particular emphasis was placed on the bacteriological aspects of atomizing freeze crystallization (AFC) and chemical properties of snowpack and meltwater. The results were very promising. The authors stated that ponded meltwater was of better quality than the tertiary effluents. Similar studies of freeze crystallization, done by Zapf-Gilje et al. (1985) also referred to municipal wastewater. The phenomenon of chemical compound segregation in man-made snow pack profile was reported. In 1995, Delta Engineering built the first full scale AFC plant for treatment of secondary effluent in Carrabassett Valley, Maine, USA. Shortly after, the second AFC plant, also for secondary effluent from wastewater treatment plant, was built in Westport, Ontario, Canada.

Numerous research projects were conducted to investigate possible application of AFC for treatment of municipal and industrial fluid waste (White, 1998). White and Lefebvre (1997) presented pilot scale field experiment with treatment of agricultural and hog manure wastes. Szpaczynski and White (2000a) presented results from experiments with freeze/thaw treatment of boiler and cooling water system from a fertilizer plant. The wastewater was converted into ice crystals (man-made snow) by atomizing wastewater in cold ambient temperature. To simulate the natural condition of temperature fluctuations and the temperature gradient metamorphism - TGM, the container with ice crystals was kept outdoors and buried in natural snowpack. In March, when the ambient temperature in the snowpack reached melting point, the snow gradually melted (48 hours) and samples of discharged meltwater were analysed for selected contaminants. The calculated efficiency of nitrate concentration was 94%. High concentration was also reported for nitrite – 89.7 % and phosphorous – 87 %. About 80% by weight of sodium, chloride and sulphate were concentrated in the first 30% of melt. Additionally, the authors presented the results of experiments with acid mine drainage. The samples originated from a drainage pond at the Inco Copper Cliff Mill Site in Sudbury, Ontario. The experiment was done by White in 1989. The wastewater was converted to snow by two-phase atomization. The snow was made in February and deposited in several insulated containers (about 100 l. each), then stored for five weeks outdoors, and melted at room temperature in 48 hours. Progressively during the melting, the samples of meltwater were collected and analyzed in the professional laboratory. Preferential elution of ions was noted. However, the results for SO_4 did not support results of research work done by Brimblecombe et al. (1985) for natural snowpack. In White's project, elution of sulphate ions was less efficient than other measured parameters (Fig. 8, Szpaczynski and White, 2000a). Nevertheless, the concentration of metals in the first melt was very impressive. Application of freeze and thaw processes and phenomenon of ice crystal metamorphism for treatment of landfill leachate in small scale experiments were investigated in late 1990's and presented by Szpaczynski and White (2000b). The leachate samples were converted into ice crystals (snow). As expected, leachate was highly contaminated with organic and inorganic compounds. During the storage of leachate in the form of man-made snow, the temperature gradient metamorphism took place. After several weeks of storage and simulating the presence of temperature gradient, the samples of meltwater were collected and the volume of each sample was measured. Significant concentration of organic and inorganic contaminants took place during the metamorphosis of snow. Most of the pollutants were concentrated and removed in the first 30% of the melt. Compared to raw leachate, the first samples of meltwater were darker in colour. This illustrated the efficacy of the concentration by freeze and thaw process.

Several more studies were done by different authors. Recently, spray freezing technology has been promoted. In fact, the base of action of spray freezing is similar to regular two phase freezing with falling film reactor. The authors (Gao et al., 2004) stated that to achieve higher efficiency of impurity removal, the wastewater should be only partially frozen. In our opinion, temperature gradient metamorphism (TGM) of ice crystals can assure very high efficiency of impurity concentration in the first part of melt and the complete freeze out by atomization of fluid waste in cold ambient temperature guarantee a high efficiency of treatment. Furthermore, it creates favourable condition for precipitation of dissolved compounds inside the droplet. These precipitates are later released because of TGM actions. However, sufficient time of snow storage is required to insure proper condition for metamorphism. Periodical thawing and refreezing in warm days and cold nights in spring can significantly improve efficiency of concentration of contaminants in the first "ionic pulse".

2. EXPERIMENTS OF FREEZE/THAW OF FLUID WASTE

2.1. Materials and methods

In the following experiment, the authors of this work present the comparison of two different freeze and thaw processes for treatment of landfill leachate. The first one is based on TGM of ice crystals. The

second one, the decantation test, concerns complete freeze out of the same volume of leachate sample but frozen as a bulk ice. For the best results, to simulate melting and refreezing in natural condition, the second sample (B) was frozen and thawed 5 times. Schematic of the experimental setup used in the snowmelt experiments is presented in Fig. 1.

For the first container (A), the sample of landfill leachate was frozen in small droplets (dia. ~5 mm). Then, the droplets were crushed in a laboratory ice crusher to make man-made snow (dia. < 1 mm). The column was filled with about 9 litres of snow for further processing by TGM. The "A" container was located outdoors and buried in the natural snow pack. Variations of ambient temperature created favourable conditions for TGM and concentration of contaminants at the surface of ice grains. The snow was kept outdoors for a period of about 4 weeks in temperatures ranging from -15 °C to -1 °C. The temperature of the snowpack was controlled by thermocouples. When the temperature in the snowpack warmed up to the melting point, the container was temporarily placed in the laboratory freezer. The TGM was further simulated for about 4 weeks by changing the temperature of the container from -15 °C to -1 °C. Although the temperature was kept below 0 °C some liquid and soluble compounds were present at boundaries and in pores of snow particles and could gradually flow down because of freezing point depression. Therefore, some dissolved compounds (salts), with a low eutectic point, accumulated at the bottom of the container. Before melting, the container was placed in the second, larger container with ice cubes that insured slow melting of snow. The samples were collected from the bottom.

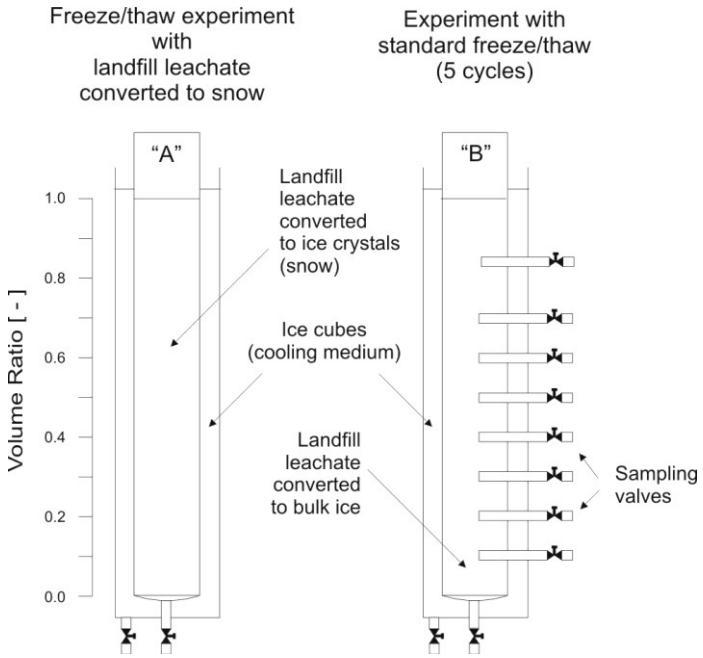

Fig. 1. Schematic of the experimental setup for snowmelt experiment

The second column "B" was filled out with raw landfill leachate. The container was placed in a vertical position in a large size freezer, where leachate was completely frozen at a temperature of about -25 °C. Then, the container was removed from the freezer and the ice was slowly melted at room temperature. To simulate the natural conditions of freeze, melt and refreeze during winter the process of freeze and melt was repeated 5 times. Because small particles of colloids that precipitate during freezing were noticed, care was taken not to disturb the meltwater in the container before the next cycle of freezing. As soon as five cycles of freeze/thaw were finished, when all ice melted, the meltwater was discharged by the special valves.

The first volume of sample was withdrawn from the top valve, the last one at the bottom. Although, there were several sampling valves, for comparison purposes, the melt water was collected only from

4 valves. Four composite samples were prepared from it. The top sample represents the cleanest water - the effluent. The closer to the bottom, the more pollutants were found in the samples. The bottom one, with some colloids and particles that precipitated during freezing and were suspended in leachate or settled, represents the most contaminated part of melt - the concentrate.

The results are presented in Figs. 2 – 5 and in Tables 1 and 2. The chemical composition of the samples from containers was analysed, accordingly to the standard method for the examination of water and wastewater, at the professional laboratory with accreditation.

3. RESULTS AND DISCUSSIONS

3.1. Landfill leachate

The efficiency of the process was different for different elements. Not like with tests with acid mine drainage (Szpaczynski and White, 2000a), the efficiency of concentration of sulphate in the first flash of 30 % of meltwater was very high (93.2%), and after that, in the rest of meltwater, was generally not detectable. Very high efficiency of the treatment with presence of TGM was also noted for chloride (92.3%) and such compounds as boron (93.8%), potassium (92.9%) and sodium (93.7%). An increase in BOD_5, COD, DOC and TOC in the first melt was also very high and reached values of 90.2%, 90.5%, 92.2% and 93.3%, respectively. Other elements such as chromium, nickel, zinc and iron were concentrated to 86.9%, 90.9%, 88% and 91.2%, respectively. The concentration efficiency of copper was at the range of 73%. Very low efficiency of concentration was reported for fluoride. Fluoride is easily incorporated into the ice structure and thus its efficiency of concentration was limited. Over 90% of analysed elements were removed from the snow sample of container "A" in the first 30% of meltwater. In the graphs (Figs. 2 – 5), continuous lines represent concentration of compounds in meltwater from this container. The area under each curve represents the mass ratio of a compound in a sample. For example, if we assume that the first 30% of melt is the concentrate, the mass ratio of a compound in this concentrate is represented by the area under the curve in the range of V/V_0 from 0 to 0.3. Dashed lines represent meltwater from the decantation test, where the landfill leachate was frozen as bulk ice.

It is clear, that the concentration efficiency of contaminants in the first melt is higher if the dominant process of separation is snow metamorphism (container "A"). Moreover, the concentration curve of TGM is steeper. Therefore, the sharpness of the TGM separation is higher.

The separation of contaminants in complete freeze out of leachate, even with five cycles of freeze and thaw does not give the same quality of treatment as for snow samples with the presence of TGM. The efficiency of concentration in decantation test is noticeably lower.

Based on these small scale experiments, it was established that the relative concentration of a compound in meltwater can be described very well by the following exponential equation:

$$\overline{C} = a + b \cdot \exp\left(-c \cdot \overline{V}\right) \tag{1}$$

where: $\overline{C} = \dfrac{C}{C_0}$; $\overline{V} = \dfrac{V}{V_0}$.

Efficiency of concentration E_{30} was defined as the relative mass of compound in the first 30% of meltwater. Results for selected parameters are presented in Tables 1 and 2.

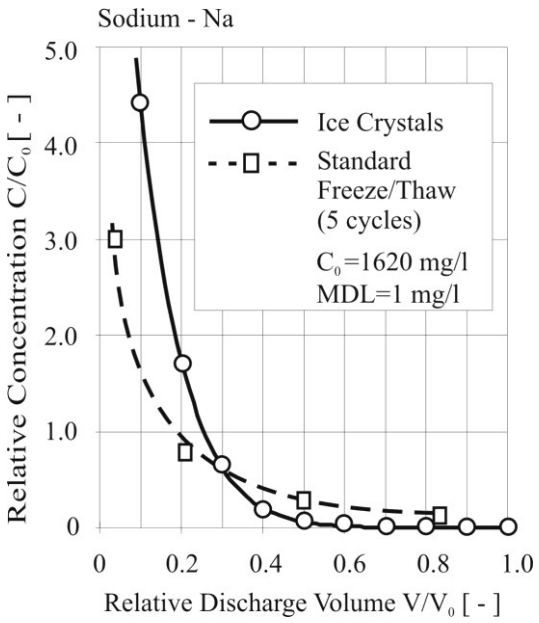

Fig. 2. Concentration of Na in meltwater of landfill leachate

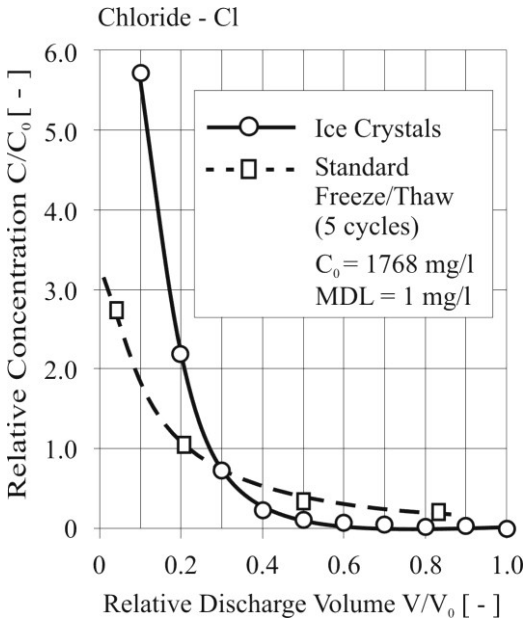

Fig. 3. Concentration of Cl in meltwater of landfill leachate

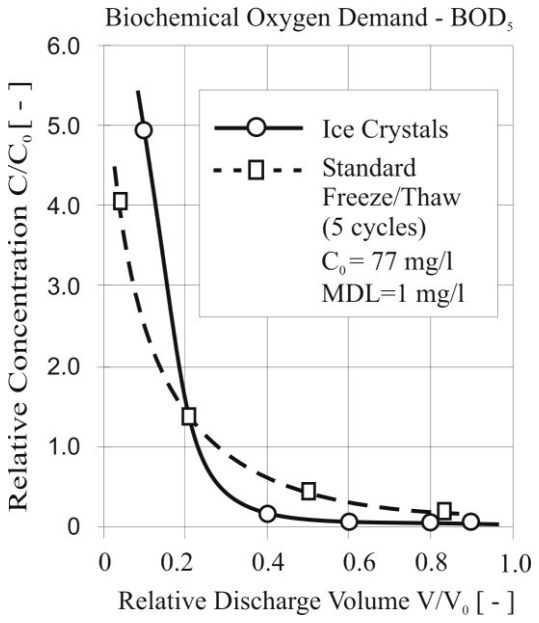

Fig. 4. Concentration of BOD_5 in meltwater of landfill leachate

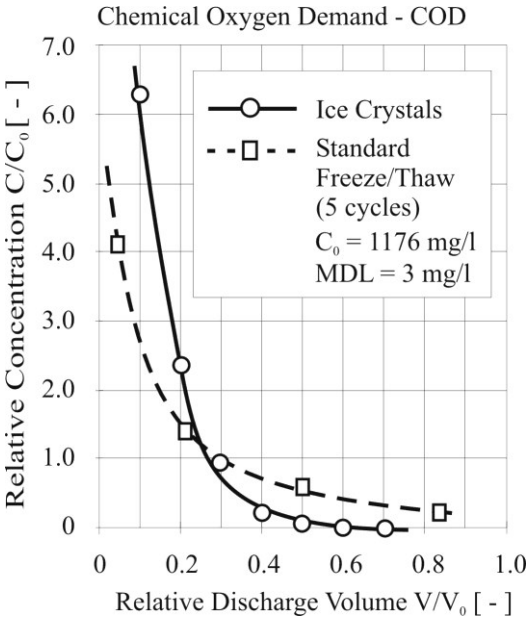

Fig. 5. Concentration of COD in meltwater of landfill leachate

Because of relatively a small volume of sample that was collected for the analysis, it was not possible to describe the concentration of compounds in the first few percent of meltwater. In order to eliminate the influence of the concentration peak at the beginning of melting on the calculation result, the efficiency of the concentration was determined based on Equation (2).

$$E_{30} = 1 - \int_{0.3}^{1} a + b \cdot \exp\left(-c \cdot \overline{V}\right) d\overline{V} \tag{2}$$

Table 1. Coefficients of Eq. (1) and efficiency of landfill leachate concentration with ice crystal metamorphism (container A)

Parameter	C_0 [mg/l]	MDL [mg/l]	*a*	*b*	*c*	Adj R^2	E_{30} [%]	$C_{e,70}$ [mg/l]
Na	1620	1	-0.0051	11.5668	9.6199	0.999	93.7	145.8
Cl	1768	1	-0.0034	15.4280	9.9228	0.999	92.3	194.5
Cr	0.07	0.01	0.0659	21.0392	10.5402	0.994	86.9	0.01
Ni	0.27	0.01	0.0265	12.7652	9.6625	0.999	90.9	0.04
K	758	1	0.0011	10.8516	9.3489	0.998	92.9	76.9
Fe	3.77	0.01	0.0721	9.0564	10.4370	0.996	91.2	0.47
Zn	0.21	0.01	0.0772	10.8381	9.4969	0.994	88.0	0.04
BOD_5	77	1	0.0609	14.2007	10.6092	0.999	90.2	10.8
COD	1176	3	-0.0017	16.5535	9.6196	0.998	90.5	159.6
B	9.91	0.01	0.0110	16.7219	11.0928	0.999	93.8	0.88
Cu	0.07	0.01	0.2512	16.0806	9.5871	0.994	73.0	0.03
SO4	12	3	0.0502	12.6729	11.6736	0.998	93.2	1.2
TOC	520	1	-0.0353	11.8871	8.9139	0.998	93.3	49.8
DOC	470	1	0.0015	13.8701	9.7342	0.999	92.2	52.4

Table 2. Coefficients of Equation (1) and the efficiency of landfill leachate concentration with standard freeze-thaw (container B)

Parameter	C_0 [mg/l]	MDL [mg/l]	*a*	*b*	*c*	Adj R^2	E_{30} [%]	$C_{e,70}$ [mg/l]
Na	1620	1	0.1966	4.1157	9.0174	0.997	83.9	372.6
Cl	1768	1	0.2109	3.3545	6.4016	0.998	83.5	416.7
Cr	0.07	0.01	0.3002	3.0230	6.8979	0.998	77.8	0.02
Ni	0.27	0.01	0.2244	3.3173	7.3389	0.995	82.4	0.07
K	758	1	0.2018	3.4414	7.2959	0.996	83.7	176.5
Fe	3.77	0.01	0.2045	2.3043	8.3421	0.999	84.7	0.82
Zn	0.21	0.01	0.6704	3.9514	6.6350	0.993	50.7	0.15
BOD_5	77	1	0.2752	5.0638	6.8153	0.998	78.8	23.3
COD	1176	3	0.3255	5.1231	7.0827	0.988	74.2	433.4

3.2. Tannery effluents

Unit operations at tannery factory include the use of a number of chemicals such as surfactants, acids, dyes, tanning agents, salts etc. (Di Iaconi et al., 2002). Because of low biodegradability of such chemicals, effluents from tannery wastewater treatment plants create a serious problem. Moreover, in many cases effluents after conventional biological treatment do not meet the required limits for parameters such as COD, salinity, ammonia and surfactants.

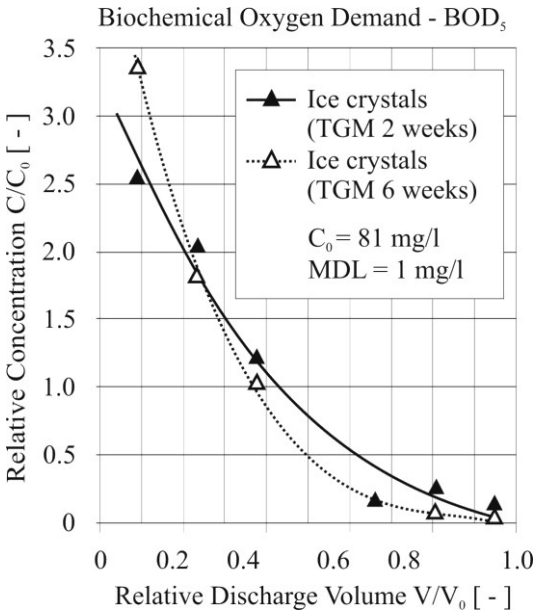

Fig. 6. Concentration of BOD_5 in meltwater (wastewater from tanneries)

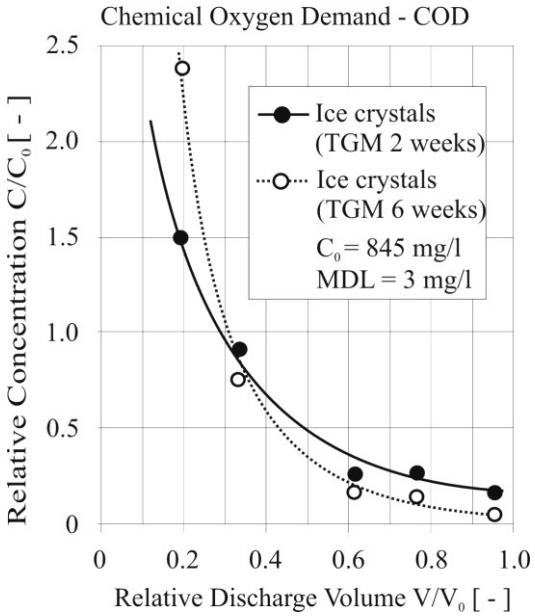

Fig. 7. Concentration of COD in meltwater (wastewater from tanneries)

The authors of this work performed preliminary research into the possibility of application of freeze/thaw process for treatment of effluents from tanneries. The effluent samples used in this study were collected from the plant after partial treatment. In Figs. 6 and 7, examples of concentration curves for BOD_5 and COD for freeze/thaw experiment with effluents from tanneries are illustrated. The effluent was converted to man-made snow and divided into two equal volumes. The first was placed in a container and kept for 2 weeks at temperature from about –15 °C to –1 °C and then slowly melted. The samples of melt were analysed for concentration of several compounds. The second part of man-made snow was placed in the same container but kept for 6 weeks at temperature from –15 °C to –1 °C. The temperature in the freezer was controlled and the TGM was simulated and intensified by changing the temperature inside the freezer. Examples of experimental data, for BOD_5 and COD are presented in Figs. 6 and 7 and in Table 3.

Table 3. Coefficients of Equation (1) and the efficiency of tannery effluent concentration with ice crystal metamorphism

Parameter	C_0 [mg/l]	MDL [mg/l]	a	b	c	Adj R^2	E_{30} [%]	$C_{e,70}$ [mg/l]	TGM [weeks]
BOD_5	81	1	-0.5026	3.6832	1.9897	0.902	58.6	47.9	2
			-0.1269	4.7696	3.8198	0.996	71.9	32.5	6
COD	845	3	0.15694	3.2148	4.5583	0.975	71.8	340.4	2
			0.13433	12.5251	9.0022	0.994	81.3	225.7	6

Higher impurity removal from the first 30% of meltwater was observed for the snow with longer storage time (6 weeks) when the TGM had time to "process" the whole volume of the snow sample. Efficiency of contaminants concentration E_{30} after 2 weeks of ice crystals metamorphism for BOD_5 was only 58.6 %. However, after increasing time of metamorphism to 6 weeks, the efficiency increased to 71.9 %. A similar situation was noted for the efficiency of concentration of COD. It was reported that the efficiency was as high as 71.8 % and 81.3 % for 2 weeks and 6 weeks of TGM, respectively. This confirms hypothesis that long storage time and sufficient TGM allows for high efficiency of the concentration process.

3.3. Full-scale treatment of municipal wastewater

An additional test was done at the full scale AFC plant in Westport, Ontario, Canada. At the beginning of melting season, the conductivity of ponded meltwater in close range from the main snowpack was measured. The results are shown in Fig. 8.

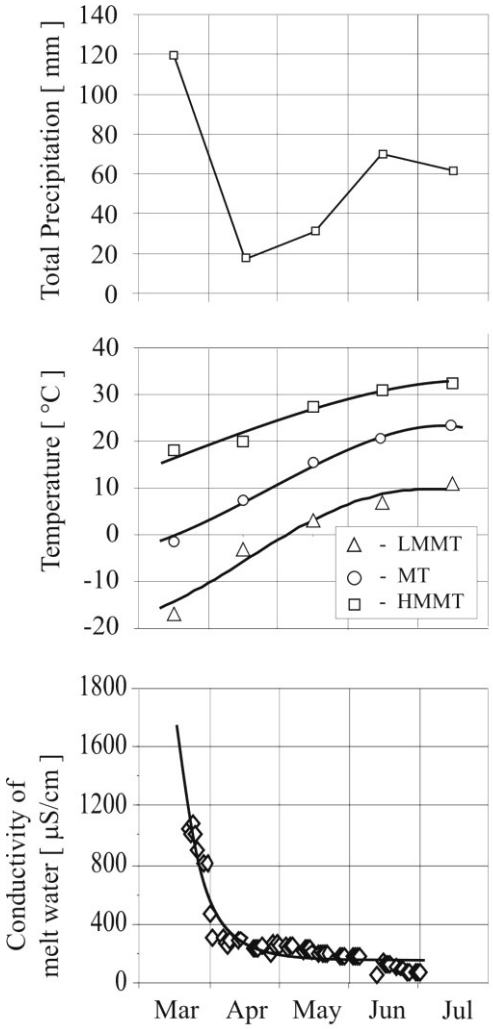

LMMT - Lowest Monthly Min. Temp. [°C]
TM - Mean Temperature [°C]
HMMT - Highest Monthly Max. Temp.[°C]

Fig. 8. Conductivity of meltwater, precipitation and temperatures during the melting season

The average conductivity of the wastewater was about 800 µS/cm. The graph also presents total precipitation as well as the lowest and the highest monthly temperatures and the mean temperature for each month of melting season. Because of the size of the snowpack (height ~ 10 m, length ~ 50m) the volume of meltwater discharge was not recorded. However, based on the graph presented in Fig. 8, it can be noticed that fast melting started in March after a significant precipitation event. Ionic pulse took place at the beginning of March but, unfortunately, it was recorded only in part.

The first fraction of the meltwater is observed to have significantly higher conductivity than later fractions. Elevated concentration of salts (high conductivity) was reported in the second half of March and dropped at the turn of March and April. After that, until the beginning of June, conductivity was dropping slowly and ranged from about 300 µS/cm to about 200 µS/cm. The next substantial drop was noticed in June after heavy rain.

The full scale experimental data for conductivity, revealed that concentration of compounds in meltwater can also be described by an exponential function (1) with adj $R^2 = 0.91$. However, it should be noted that the rate of melting of man-made snow in natural condition is influenced by a number of factors, including: precipitation, solar radiation, ambient temperature, the size and the shape of snowpack etc. Therefore, minor inaccuracies of the predicted concentration curve may occur in practice.

3.4. Agglomeration of solid particles in freeze and thaw process

If the rate of freezing is sufficiently small, most of fine solid particles are rejected by ice and push in front of growing crystals. It is well known fact that freeze/thaw process can improve efficiency of agglomeration of particles and dewatering. Significant work in the field of freezing of solid-liquid mixture was done by Corte (1962); Dawson et al. (1999); Halde (1979); Martel et al. (1998); Nakamura and Okada (1976); Reed et al. (1986); Vesilind et al. (1990); Volkhin and Ponomarev (1965) and recently by Gao (2011); Tao et al. (2006 a, b).

Agglomeration of solid particles in man-made snow crystals made from municipal sludge or mineral suspension is more complex. It starts from liquid droplets that have to be super-cooled and nucleated to freeze out in cold ambient air. At the first moment, after nucleation, the development of ice is fast. The surface of droplet is covered with a thin shell of ice but inside there is liquid and its temperature rises to about 0 °C. Then, because the droplet is still exposed to low ambient temperature, the liquid inside the droplet cools down. At this stage, ice crystals grow inside the droplet. It is a slow process and depends on the ambient temperature. The volume of liquid within the drop is reduced and the pressure increases. Because ice absorbs only pure water molecules, the concentration of dissolved compounds increases. Some of them, such as dissolved salts exceed the limits of its solubility and precipitate. If gases exceed its solubility range, it nucleates and inside the droplet bubbles of gas are created. That gas is later released during the TGM. If the temperature is sufficiently low, the droplet can freeze out completely in the air and hits the ground entirely frozen. Solid particles that are inside the droplet, such as colloids, undergo natural agglomeration and are easily separated in the next step. Particles are pushed to each other and create clusters that are dehydrated because water molecules can diffuse in the direction of ice. These clusters are also released if the TGM take place in the snowpack or are released during melting and refreezing processes in spring. Meltwater percolates down and the particles remain in the pores of snow and further agglomerate to form relatively large granules. At the end, most solids remain on the surface. In Fig. 9, the photograph of the full scale snowpack surface from atomizing freeze crystallization plant in Westport, Ontario is presented. These precipitated solids can be easily removed if liner is installed under the snowpack and/or it can be used as fertilizer. The freeze and thaw cycles significantly enhance the process of separation during the storage period. At a time when there is a high TGM in the snowpack, the majority of the snow volume is transferred to a vapour state and back into a solid state. Longer storage time and more frequent and higher variations in temperature during winter give a higher efficiency of concentration and more efficient process of agglomeration. Most contaminants are deposited on the surface of the ice grains in the pores of the snow pack. Moreover, fluctuations in the ambient temperature around freezing point repeatedly thaw and freeze the ice crystals and the solid particles are rejected from the ice structure.

The authors of this work carried out an experiment to see the difference in the characteristics of the clay slurry that was once and five times frozen. In order not to distort the characteristics of the sludge, the sample of sludge was not filtered, but freeze-dried. Frozen water in the pores of the sludge sublimated and the undisturbed structure of sludge was revealed.

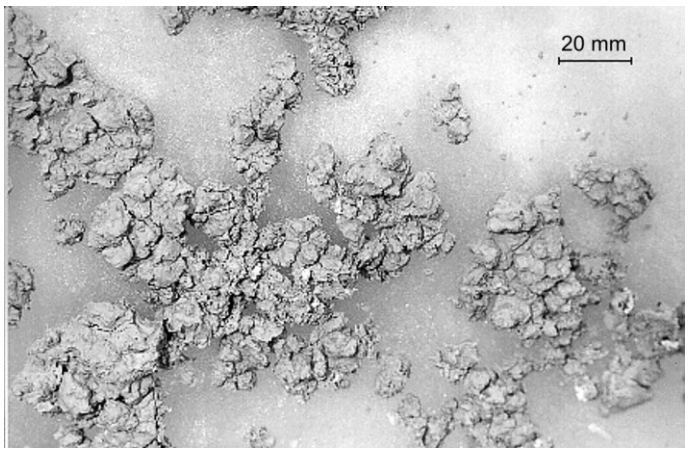

Fig. 9. The surface of the full scale of man-made snow-pack from secondary effluent of municipal wastewater processed by atomizing freeze crystallization (AFC). End of melting season in June, Westport, Ontario, Canada

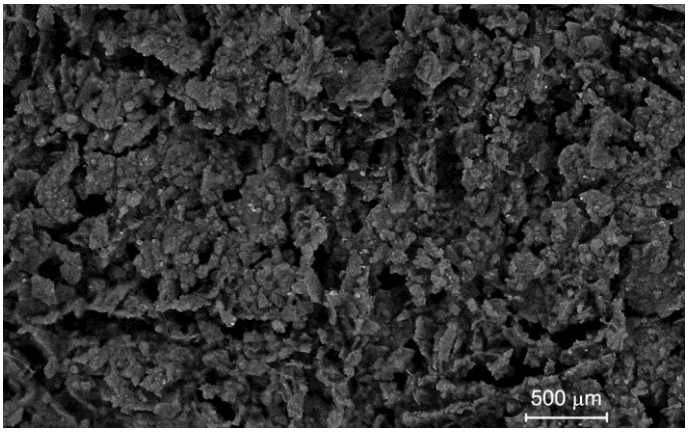

Fig. 10. Microscopic view of the surface of clay slurry with one cycle of freeze and thaw process

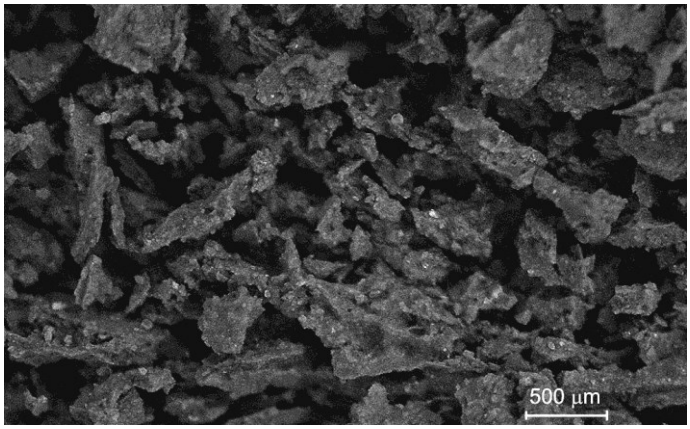

Fig. 11. Microscopic view of the surface of clay slurry with five cycles of freeze and thaw process

Clay slurry such as, for example, mine tailings from Athabasca Oil Sands cannot be filtered because the resistance of filtration is very high and filtration is not economical. After freezing one time, the agglomerates of clay particles are created (Fig. 10) and solid-liquid separation is enhanced. Even better results can be achieved if the slurry is frozen five times (Fig. 11). It can be hypothesised that during the TGM the snow particle volume is transferred to a vapour state and back into a solid state several times. Therefore, the efficiency of agglomeration and subsequent separation of solid particles is so high in atomising freeze crystallization plant (Fig. 9).

4. CONCLUSIONS

Very high efficiency of the freeze/thaw leachate treatment with presence of TGM was noted for chloride and such compounds as boron, potassium and sodium. It was reported that about 93 % of these elements were removed in concentrate from the snow sample. An increase in BOD_5, COD, DOC and TOC, in the first melt was also very high. The efficiency of concentration reached values of 90.2, 90.5%, 92.2 % and 93.3 %, respectively. Chromium, nickel, zinc and iron were concentrated in the first 30% of melt to 86.9 %, 90.9%, 88% and 91.2 %, respectively. The concentration efficiency of copper was in the range of 73 %. Generally, more than about 90 % of all contaminants were concentrated and discharged in the first 30 % of the melt water volume.

The effluent concentrations of Na, Cl, Cr, Ni, K, Fe and Zn in the last 70% of melt water from container "A", where TGM was present, were: 145.8 mg/l, 194.5 mg/l, 0.01 mg/l, 0.04 mg/l, 76.9 mg/l, 0.47 mg/l and 0.04 mg/l, respectively. The concentrations of the same compounds after five cycles of standard freeze/thaw were higher and reached the following values: 372.6 mg/l, 416.7 mg/l, 0.02 mg/l, 0.07 mg/l, 176.5 mg/l, 0.82 mg/l and 0.15, respectively.

Freezing of landfill leachate by converting it to man-made snow and its storage with presence of TGM before melting, resulting in an improved efficiency of concentration of pollutants. For such compounds as sodium, chloride, chromium, nickel, potassium, iron and zinc, the application of TGM gives, from 6.5 % for Fe to 37.3% for Zn, higher efficiency of concentration than that in five cycles of the standard freeze-thaw process. The method of freeze/thaw with presence of TGM proved to be better than the standard freeze-thaw and decantation option also for BOD_5 and COD. Increase in BOD_5 efficiency of concentration was by about 11.4% higher for TGM than that for five cycles of standard freeze/thaw. Even better results of increase, in the range of 16.3% were achieved for COD. The average concentrations of BOD_5 and COD in effluent for TGM option were as low as 10.8 mg/l and 159.6 mg/l, respectively. With the application of five cycles of standard freeze/thaw the average concentrations of these compounds in effluent were higher and reached the values of: 23.3 mg/l and 433.4 mg/l, respectively.

A significant concentration effect of BOD_5 and COD was also reported for tannery effluent. Higher impurity removal from meltwater was observed for the snow with longer storage time (6 weeks) – longer exposer to TGM. The results show about 13% and 10 % higher efficiency of concentration of BOD_5 and COD, respectively. This proves the hypothesis that TGM has influence on the efficiency of the freeze crystallization process. Moreover, TGM and spring melting and refreezing improve agglomeration of particles and the characteristics of the sludge.

The effect of the freeze/thaw process as well as TGM can be observed in full scale operations. The measurements of conductivity of melt water that was discharged from the full size operation, where about 70,000 m^3 of wastewater were converted to man-made snow, revealed a significant decrease of salt concentration with the passage of time during the melting process of a large snowpack.

SYMBOLS

a, b, c	constants in both, equations (1) and (2)
$\overline{C}$	relative concentration
C	current concentration of compound in a sample, kg/m^3
$C_{e,70}$	average concentration of compound in the last 70% of melt water, kg/m^3
C_0	concentration of the feed water, kg/m^3
E_{30}	efficiency of concentration in 30% of meltwater volume, %
$\overline{V}$	relative discharged volume

V discharged volume of meltwater, m^3
V_0 total volume of meltwater, m^3

Abbreviations

AFC Atomizing freeze crystallization
BOD_5 Biochemical oxygen demand, mg/l
COD Chemical oxygen demand, mg/l
DOC Dissolved organic carbon, mg/l
MDL Method detection limit, mg/l
PAH Polycyclic aromatic hydrocarbons
TGM Temperature gradient metamorphism
TOC Total organic carbon, mg/l
UDF Unidirectional downward freezing

REFERENCES

Baker R.A., 1967. Trace organic contaminant concentration by freezing – I; Low inorganic aqueous solutions. *Water Res.*, 1, 61-77. DOI: 10.1016/0043-1354(67)90064-4.

Baker R.A., 1967a. Trace organic contaminant concentration by freezing – II; Inorganic aqueous solutions. *Water Res.*, 1, 97-113. DOI: 10.1016/0043-1354(67)90078-4.

Baker R.A., 1969. Trace organic contaminant concentration by freezing – III; Ice washing. *Water Res.*, 3, 717-730. DOI:10.1016/0043-1354(69)90013-X.

Beier N., Sego D., Donahue R., Biggar K., 2007. Trickle-freeze separation of contaminants from saline wastewater. *Int. J. Min. Reclam. Environ.,* 21, 144-155. DOI: 10.1080/17480930701197643.

Bales R.C., 1989. Ion elution through shallow homogeneous snow. *Water Resour. Res.,* 25, 1869-1877. DOI: 10.1029/WR025i008p01869.

Brimblecombe P., Tranter M., Abrahams P. W., Blackwood I., Davies T.D., Vincent C.E., 1985. Relocation and preferential elution of acidic solute through the snowpack of a small, remote, high-altitude Scottish catchment. *Ann. Glaciol.,* 7, 141–147.

Brimblecombe P., Clegg S.L., Davies T.D., Shooter D., Tranter M., 1987. Observations of the preferential loss of major ions from melting snow and laboratory ice. *Water Res.*, 21, 1279–1286. DOI: 10.1016/0043-1354(87)90181-3.

Chen L.C., Chian C.Y., Chen L.C., Yen P.S., Chu C.P., Lee J.C., Lee S.F., 2001. High-speed sludge freezing. *Water Res.*, 35, 3502-3507. DOI: 10.1016/S0043-1354(01)00048-3.

Chian C.Y., Chen L.C., Yen P.S., Chu C.P., Lee J.C., Lee S.F., Chen T.H., 2002. Sludge freezing at high speed. *Drying Technol.*, 20, 1019-1033. DOI: 10.1081/DRT-120003775.

Christon M., Burns P.J., Sommerfeld R.A., 1994. Quasi-steady temperature gradient metamorphism in idealized, dry snow. *Numer. Heat Transfer*, *Part A*, 25, 259-278. DOI: 10.1080/10407789408955948.

Cisse J., Bolling G.F., 1971. A study of the trapping and rejection of insoluble particles during the freezing of water. *J. Cryst. Growth*, 10, 67-76. DOI: 10.1016/0022-0248(71)90047-9.

Colbeck S.C., 1980. Thermodynamics of snow metamorphism due to variations in curvature. *J. Glaciol.*, 26(94), 291-301.

Corte A.E., 1962. Vertical migration of particles in front of a moving freezing plane. *J. Geophys. Res.*, 67, 1085-1090. DOI: 10.1029/JZ067i003p01085.

Cragin J.H., 1993. *Elution of ions from melting snow*. Army Cold Regions Research and Engineering Laboratory. CRREL Report, 93-8.

Cragin J.H., 1995. Exclusion of sodium chloride from ice during freezing. *52nd Eastern Snow Conference.* Toronto, Ontario, Canada.

Dawson R..F., Sego D.C., Pollock G.W., 1999. Freeze-thaw dewatering of oil sands fine tails. *Can. Geotech. J.,* 36, 587-598. DOI: 10.1139/t99-028.

Di Iaconi C., Lopez A., Ramadori R., Di Pinto A.C., Passino R., 2002. Combined chemical and biological degradation of tannery wastewater by a periodic submerged filter (SBBR). *Water Res.*, 36, 2205-2214. DOI: 10.1016/S0043-1354(01)00445-6.

Geo W., Smith D.W., Sego D.C., 2004. Treatment of pulp mill and oil sands industrial wastewaters by the partial spray freezing process. *Water Res.*, 38, 579-584. DOI: 10.1016/j.watres.2003.10.053.

Gao W., Shao Y., 2009. Freeze concentration for removal of pharmaceutically active compounds in water. *Desalin.*, 249, 398-402. DOI: 10.1016/j.desal.2008.12.065.

Gao W., 2011. Freezing as a combined wastewater sludge pretreatment and conditioning method. *Desalin.*, 268, 170-173. DOI: 10.1016/j.desal.2008.12.065.

Gay G., Lorain O., Aouni A., Aurelle Y., 2003. Wastewater treatment by radial freezing with stirring effects. *Water Res.*, 37, 2520-2524. DOI: 10.1016/S0043-1354(03)00020-4.

FTFC (Fine Tailings Fundamentals Consortium), 1995. *Advances in Oil Sands Tailings Research.* Alberta Department of Energy. Oil Sands and Research Division. III-29.

Halde R., 1979. Concentration of impurities by progressive freezing. *Water Res.*, 14, 575-580. DOI: 10.1016/0043-1354(80)90115-3.

Huber D., Palmateer G., 1985. *Snowfluent - A join experimental project between Southwest Region of the Ministry of the Environment and Delta Engineering in the storage and renovation of sewage effluent by conversion to snow*. MOE Report. Ontario, Canada.

Johannessen M., Dale T., Gjessing E.T., Henriksen A., Wright R.F., 1975. Acid precipitation in Norway: The regional distribution of contaminants in snow and the concentration processes during snowmelt. *Proceedings of the Isotopes and impurities in snow and ice symposium*. Grenoble, 1975. Int. Ass. Hydrol. Sci. Publ. 118, 116-120.

Johannessen M., Henriksen A., 1978. Chemistry of snow meltwater: Changes in concentration during melting. *Water Resour. Res.*, 14, 615-619. DOI: 10.1029/WR014i004p00615.

Kyprianidou-Leodidou T.C., Botsaris G.D., 1990. Freeze concentration of aqueous solutions, In: Myerson A.S., Toyokura K. (Eds.), *Crystallization as a separation process.* 438, Chapter 27, ACS Symposium Ser.

Marbouty D., 1980. An experimental study of temperature gradient metamorphism in snow. *J. Glaciol.*, 26, 303-311.

Meyer T., Wania F., 2011. Modelling the elution of organic chemicals from a melting homogeneous snow pack. *Water Res.*, 45, 3627-3637. DOI: 10.1016/j.watres.2011.04.011.

Meyer T., Lei D.Y., Wania F., 2006. Measuring the release of organic contaminants from melting snow under controlled conditions. *Environ. Sci. Technol.*, 40, 3320-3326. DOI: 10.1021/es060049q.

Meyer T., Lei D.Y., Muradi I., Wania F., 2009. Organic contaminant release from melting snow. 1. Influence of chemical partitioning. *Environ. Sci. Technol.,* 43, 657-662. DOI: 10.1021/es8020217.

Montusiewicz A. , Lebiocka M., Rożej A., Zacharska E., Pawłowski L., 2010. Freezing/thawing effects on anaerobic digestion of mixed sewage sludge. *Bioresour. Technol.*, 101, 3466-3473. DOI: 10.1016/j.biortech.2009.12.125.

Muller M., Sekoulov I., 1992. Wastewater reuse by freeze concentration with falling film reactor. *Water Sci. Technol.*, 26, 1475-1482.

Nakamura A., Okada R., 1976. The coagulation of particles in suspension by freezing-thawing. *Colloid. Polym. Sci.*, 254, 718-725.

Parker P.J., Collins A.G., 1999. Ultra-rapid freezing of water treatment residuals. *Water Res.*, 33, 2239-2246. DOI: 10.1016/S0043-1354(98)00449-7.

Pinzer B.R., Schnebeli M., Kaempfer T.U., 2012. Vapor flux and recrystallization during dry snow metamorphism under a steady temperature gradient as observed by time-lapse micro-tomography. *Cryosphere*, 6, 1141-1155. DOI: 10.5194/tc-6-1141-2012.

Reed S., Bouzoun J., Medding W., 1986. A rational method for sludge dewatering via freezing. *Journal (Water Pollution Control Federation)*, 58(9), 911-916. Available at: http://www.jstor.org/stable/25043077/.

Sego, D.C., 1996. Use of Natural freeze-thaw processes to separate and treat mine wastewater. *Proceedings from IWC-96.*

Sommerfeld R. A., LaChapelle E., 1970. The classification of snow metamorphism. *J. Glaciol.*, 9, 3-17. DOI: 10.3198/1970JoG9-55-3-18.

Szpaczynski J.A., White J.A., 2000a. Experimental studies on the application of natural process of snow metamorphism for concentration and purification of liquid wastes. *WEF & Purdue University, Industrial Wastes Technical Conference*. May 21, 2000, St. Louis, Missouri, USA.

Szpaczynski J.A., White J.A., 2000b. Efficiency of landfill leachate treatment by freeze crystallization and natural process of snow metamorphism. *1st Intercontinental Landfill Research Symposium.* Luleå, December 11-13, 2000.

Taft R.A., 1965. *The advanced waste treatment research program*. U.S. Department of Health, Education, and Welfare.

Tao T., Peng X.F., Lee D.J., 2006a. Interaction between wastewater-sludge floc and moving ice front. *Chem. Eng. Sci.*, 61, 5369–5376. DOI: 10.1016/j.ces.2006.04.019.

Tao T., Peng X.F., Lee D.J., Hsu J.P., 2006b. Micromechanics of wastewater sludge floc: Force-deformation relationship at cyclic freezing and thawing. *J. Colloid Interface Sci.,* 298, 860-868. DOI: 10.1016/j.jcis.2006.01.002.

Tatarniuk Ch., Donahue R., Sego D., 2009. Freeze separation of salt contaminated melt water and sand wash water at snow storage and sand recycling facilities. *Cold Reg. Sci. Technol.,* 57, 61-66. DOI: 10.1016/j.coldregions.2009.03.001.

Tranter M., Tsiouris S., Davies T. D., Jones G. H., 1992. A laboratory investigation of the leachating of solute from snow pack by rainfall. *Hydrol. Processes*, 6, 169-178. DOI: 10.1002/hyp.3360060205.

Vesilind P.A., Martel J.C., 1990. Freezing of water and wastewater sludge. *J. Environ. Eng.,* 116, 854-862. DOI: 10.1061/(ASCE)0733-9372(1990)116:5(854).

Vol'khin V.V., Ponomarev E.I., 1965. Effect of freezing on the properties of coagulated metal hydroxides. *Kolloidnyi Zhurnal*, 27(1), 14-18.

Wakisaka M., Shirai Y., Sakashita S., 2001. Ice crystallization in a pilot-scale freeze wastewater treatment system. *Chem. Eng. Process.*, 40, 201-208. DOI: 10.1016/S0255-2701(00)00112-4.

White J.A., 1998. USA, Patent #5,726,405.

White J.A., Lefebvre P., 1997. Snowfluent® - the use of atomizing freeze crystallization on municipal, agricultural and hog manure wastes. *Conference, World-Wise'97*, Selkirk, Manitoba.

Wright K.R., 1976. Sewage effluent turned to snow: Provides storage, removes pollutants. *J. Civil Eng. – ASCE*, 88-89.

Zapf-Gilje, S., Russell, D.S., Mavinic, D.S., 1986. Concentration of impurities during melting of snow made from secondary sewage effluent. *Water Sci. Technol.*, 18(2), 151-156.

Received 04 October 2016
Received in revised form 10 May 2017
Accepted 12 May 2017

www.czasopisma.pan.pl www.journals.pan.pl
Chemical and Process Engineering 2017, 38 (2), 265-281
DOI: 10.1515/cpe-2017-0020

NUMERICAL ANALYSIS OF THE EFFECT OF HYDRODYNAMICS AND OPERATING CONDITIONS ON BIODIESEL SYNTHESIS IN A ROTOR-STATOR SPINNING DISK REACTOR

Zhuqing Wen, Jerzy Petera*

Lodz University of Technology, Faculty of Process and Environmental Engineering, 90-924 Łódź, Wólczańska 213, Poland

A rotor-stator spinning disk reactor for intensified biodiesel synthesis is described and numerically simulated in the present research. The reactor consists of two flat disks, located coaxially and parallel to each other with a gap ranging from 0.1 mm to 0.2 mm between the disks. The upper disk is located on a rotating shaft while the lower disk is stationary. The feed liquids, triglycerides (TG) and methanol are injected into the reactor from centres of rotating disk and stationary disk, respectively. Fluid hydrodynamics in the reactor for synthesis of biodiesel from TG and methanol in the presence of a sodium hydroxide catalyst are simulated, using convection-diffusion-reaction multicomponent transport model with the CFD software ANSYS©Fluent v. 13.0. Effect of operating conditions on TG conversion is particularly investigated. Simulation results indicate that there is occurrence of back flow close to the stator at the outlet zone. Small gap size and fast rotational speed generally help to intensify mixing among reagents, and consequently enhance TG conversion. However, increasing rotational speed of spinning disk leads to more backflow, which decreases TG conversion. Large flow rate of TG at inlet is not recommended as well because of the short mean residence time of reactants inside the reactor.

Keywords: biodiesel synthesis, ANSYS©Fluent, rotor-stator reactor, backflow, operating conditions

1. INTRODUCTION

The widely used method for biodiesel production is transesterification of oil or fat feedstock with methyl alcohol under alkaline conditions in a liquid-liquid environment. Transesterification is a liquid-liquid two phase reaction. Reaction rate can be limited by mass transfer between the oil and alcohol phases. Therefore, the efficiency of mass transfer is of importance for improving production capacity, reducing process cost and equipment size. Many intensification technologies have been explored to enhance contact and contact area between the two liquid phases and decrease resistance to mass transfer in the reactor. SDR (short for spinning disk reactor), which includes spinning disks (also known as rotors) and stationary disks (also known as stators), is one of the process intensification technologies employing high gravity-centrifugal force fields caused by the rotation of rotors. Extensive studies using this technology have shown that process time, reactant inventories, and impurity levels can be reduced by up to 99% (Brechtelsbaueret al., 2001; Cafieroet al., 2002; Clifford et al., 2009).

The hydrodynamics inside the rotor-stator gap are mostly important to quantify the performance (such as conversion of reactants, mass transfer rate) of the SDR. Researchers have investigated the fluid flow inside rotor-stator gap with and without superposed through flow. The boundary layers of fluid flow inside rotor-stator gap without superposed through flow are supposed to be a combination of Von

*Corresponding authors, e-mail: jerzy.petera@p.lodz.pl

Kármán layer along the rotating disk (Von Kármán, 1921) and Bodewadt layer along the stationary disk (Bodewadt, 1940).The Von Kármán layer is characterized by a net centrifugal radial velocity and a net negative axial (towards the disk) fluid velocity; analogously, the Bodewadt layer has a net centripetal velocity and a net positive axial (away from the disk) velocity. The Von Kármán layer and Bodewadt layer form the basis for depicting the flow structures inside the rotor-stator gap.

Investigations indicate that either a Von Kármán layer develops on the rotor alone, or Von Kármán layer and Bodewadt layer develop on both the rotor and the stator depending on the boundary conditions of the disk (Brady and Durlofsky, 1987; Lopez, 1998). In the former case, the bulk fluid is at rest and only a Von Kármán layer is formed along the spinning disk (Stewartson, 1953). In the latter case, the exact flow structure is mainly determined by the rotational Reynolds number (also known as channel Reynolds number) and the gap ratio of the system (Batchelor, 1951; Daily and Nece, 1960).

The present research simulated the fluid flow inside SDR gap with feedstocks injected from inlets. Introducing an externally applied through flow into SDR gap alters the flow structures depicted above. Studies show that in the case of a superposed centrifugal through flow, at low radial positions, the tangential velocity (swirl velocity) decreases to zero outside the Von Kármán layer, and the radial velocity is positive (radially outward) for all axial positions (Haddadi and Poncet, 2008; Phadke and Owen, 1988; Poncet et al., 2005a; Poncet et al., 2005b; Soo, 1958). At higher radial positions, the flow structure depends on the gap ratio employed (Haddadi and Poncet, 2008; Poncet et al., 2005b), the radial velocity is centrifugal along the spinning disk and centripetal along the stationary disk.

An engineering model of the fluid flow patterns inside the inter-disk space of rotor-stator was proposed, previously depicted by De Beer et al. (2014). The flow through a rotor–stator cavity can be described as a combination of radial plug flow and ideally mixed region. The radius where flow pattern changes from plug flow to ideally mixed flow decreases with increasing rotational Reynolds number and gap ratio, and increases with increasing superposed through flow rate. In the present research, the SDR developed to explore the possibility of improving the efficiency of biodiesel production is described and used, as shown in Fig.1. ANSYS©Fluent 13.0 is chosen to simulate and analyse fluid hydrodynamics in this reactor for the synthesis of biodiesel using convection-diffusion-reaction multicomponent transport model. Simulation results show similarity to the study carried out by De Beer et al. (2014), and details are described below. There is an obvious occurrence of back flow near the stator from the outlet. The size of the backflow zone increases with the rotational speed increase; it decreases with the gap size reduction and with the flowrate increase. It is also demonstrated that backflow is undesirable in the present study by analysing the reactant conversion in SDR.

2. EXPERIMENTAL SETUP AND MECHANISM OF ALKALI-CATALYSED TRANSESTERIFICATION REACTION

The experimental setup was built and described by Qiu and Weatherley (Qiu et al., 2012), who are our collaborative partners from Department of Chemical and Petroleum Engineering, Kansas University, USA. We use their experiment data to verify our simulation results. The SDR system consists of two parallel coaxial disks: one stationary and the other rotational with controllable rotational speed. The disks in the present research are separated by an adjustable gap. The two immiscible liquid feed stocks, oil and alcohol, are pumped axially into the reactor from the centres of the spinning disk and the stationary disk, respectively. The model reaction system chosen for study is methyl-esterification of canola oil in the presence of a sodium hydroxide catalyst to form biodiesel and glycerol. Before being pumped into SDR, sodium methoxide is prepared by dissolving sodium hydroxide in methanol. The experimental setup is shown in Fig. 1.

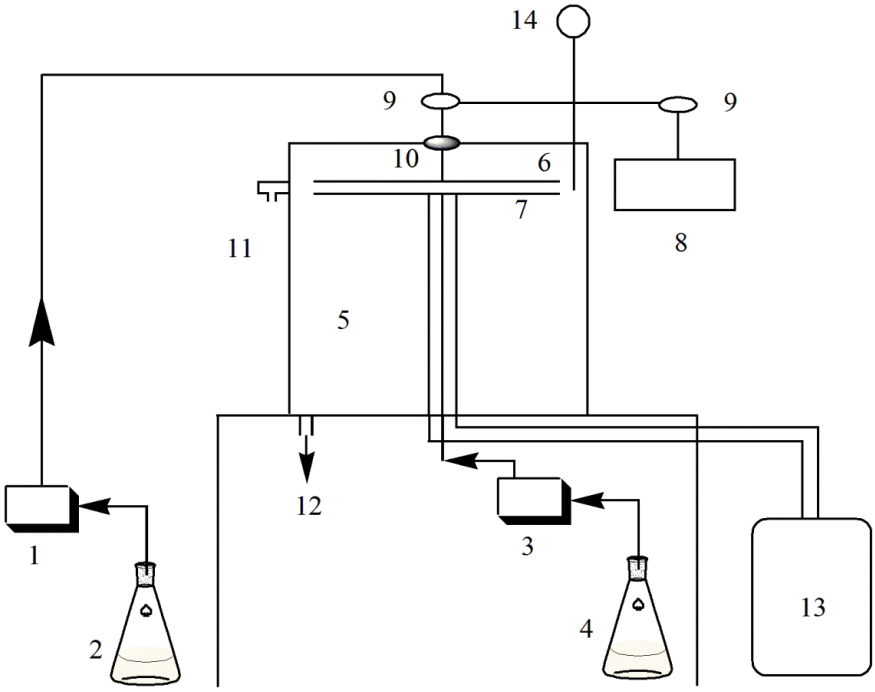

Fig. 1. Experimental setup of the intensive SDR for biodiesel synthesis;
1 - peristaltic pump; 2 - canola oil vessel; 3 - digital piston pump; 4 - sodium methoxide vessel; 5 - cylinder; 6 - rotating disk; 7 - stationary disk; 8 - variable-speed DC motor; 9 - pulley; 10 - bearing; 11 - sampling point; 12 - products drainage; 13 - heating circulator; 14 - thermometer

As mentioned above, biodiesel is mainly made by transesterification of vegetable oils and animal fats with alcohol in the presence of catalysts. Vegetable oils and animal fats typically consist of triglycerides (TG) which are esters of free fatty acids with the trihydric alcohol, glycerol.

During the transesterification of TG, there are three stepwise and reversible reactions with intermediate formation of diglycerides (DG) and monoglycerides (MG) resulting in the production of methyl esters ($RCOOCH_3$, biodiesel) and glycerol (GL) as shown in chemical equations I-III (Freedmanet al., 1986; Noureddini and Zhu, 1997). The alcohol to TG molar ratio, catalyst type, reaction time and reaction temperature can affect the transesterification at different levels (Freedmanet al., 1984).

$$TG + CH_3OH \underset{k_2}{\overset{k_1}{\leftrightarrow}} DG + RCOOCH_3 \quad \text{(I)}$$

$$DG + CH_3OH \underset{k_4}{\overset{k_3}{\leftrightarrow}} MG + RCOOCH_3 \quad \text{(II)}$$

$$MG + CH_3OH \underset{k_6}{\overset{k_5}{\leftrightarrow}} GL + RCOOCH_3 \quad \text{(III)}$$

In order to describe the chemical kinetics of the transesterification reaction, the following equations are used.

$$\begin{aligned} -r_I &= k_1 \cdot C_{TG} \cdot C_{CH3OH} - k_2 \cdot C_{DG} \cdot C_{RCOOCH3} \\ -r_{II} &= k_3 \cdot C_{DG} \cdot C_{CH3OH} - k_4 \cdot C_{MG} \cdot C_{RCOOCH3} \\ -r_{III} &= k_5 \cdot C_{MG} \cdot C_{CH3OH} - k_6 \cdot C_{GL} \cdot C_{RCOOCH3} \end{aligned} \quad (1)$$

where k_i (i = 1, ..., 6) represents the respective kinetic constant that follows the Arrhenius equation:

$$k_i = A_i \, e^{-E_i/(RT)} \qquad i = 1, 2, \ldots, 6 \quad (2)$$

3. SIMULATION METHODOLOGY

3.1. Mesh information and boundary conditions

The CFD software, ANSYS©Fluent v.13.0 was chosen to simulate and analyse the hydrodynamics performance of SDR. The effects of gap size between spinning disk and stationary disk, rotational speed of spinning disk, and TG flow rate at inlet are investigated.

It is important to appropriately mesh the computational domain to get accurate simulation results. To obtain satisfactory mesh, it is necessary to simplify the real construction of SDR. As can be seen from Fig. 1, the region of interest in the experimental setup is the space between spinning disk and stationary disk. Besides, this construction is axisymmetric, hence, only half of it is simulated. The magnification of the reaction part and the computational domain are shown in Figs. 2 and 3.

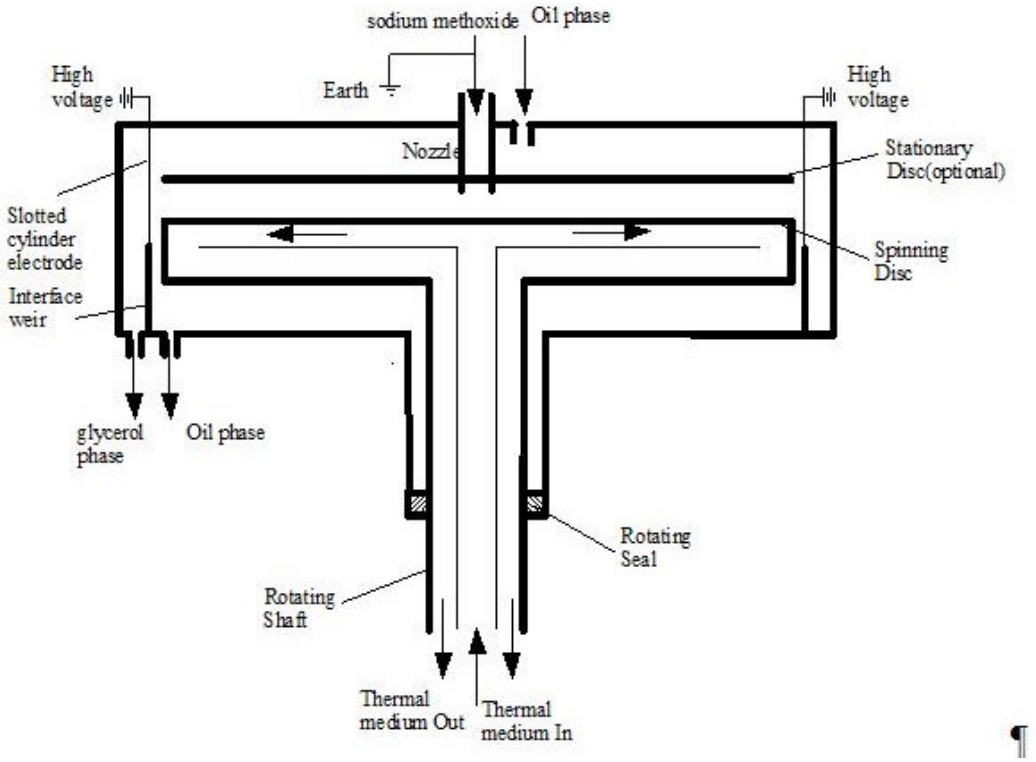

Fig. 2. Magnification of the reaction part

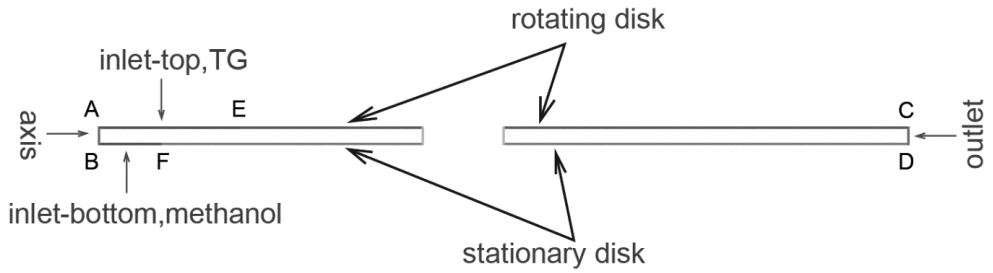

Fig. 3. Simplified computational domain of SDR

Dimensions of the domain, based on the SDR construction and after simplification, are as follows. Domain radius AC: 50 mm. Gap size between rotor and stator is adjustable, applied gap size AB: 0.1 mm, 0.15 mm, 0.2 mm. Radius of inlet-top AE and inlet-bottom BF are 1.75 mm and 0.77 mm. As

introduced before, TG and sodium methoxide (methanol in the simulation) are pumped into the reactor through the centres of spinning disk and stationary disk, respectively. When the volume flow rate of TG and methanol at inlet-top and inlet-bottom are 5.77×10^{-8} m^3s^{-1} (3.84 ml/min) and 1.3×10^{-8} m^3s^{-1}, the injecting velocities of TG and methanol are 0.006 ms^{-1} and 0.007 ms^{-1}; when the volume flow rate of TG and methanol at the inlet-top and the inlet-bottom are $1.12\times10^{-7}m^3s^{-1}$ (6.69 ml/min) and 2.9×10^{-8} m^3s^{-1}, the injecting velocities of TG and methanol are 0.0116 ms^{-1} and 0.0156 ms^{-1}, respectively. The boundary conditions will be introduced in detail below.

The computational domains are meshed with ANSYS meshing tool in Workbench 13. The mesh information for different gap size is shown in Table 1. Three different gap sizes between rotor and stator are investigated in the present simulation. Six cases are simulated for each gap size, differing from the rotational speed of spinning disk. Moreover, two flow rates of TG at inlet are studied when gap size is 0.2 mm. The overall boundary conditions are summarised in Tables 2 and 3.

Table 1. Mesh information for different gap sizes

Gap size, mm	Cells	Faces	Nodes
0.1	50000	105010	55011
0.15	94444	194460	100017
0.2	100035	205088	105054

Table 2. Overall boundary conditions in the simulation

	AB	AE	BF	EC	FD	CD
Boundary type	Axis	Velocity-inlet	Velocity-inlet	Wall	Wall	Outflow
Length, mm	0.1, 0.15, 0.2	1.75	0.77	48.25	49.23	0.1, 0.15, 0.2
Temperature, K	-	298.15	298.15	298.15	298.15	-
Velocity, ms^{-1}	-	0.006 or 0.0116	0.007 or 0.0156	-	-	-
Rotational speed of spinning disk, rpm	-	-	-	1000 - 2000	-	-

Table 3. Rotational speed of spinning disk for each case

	case 1	case 2	case 3	case 4	case 5	case 6
Rotational speed of spinning disk, rpm	1000	1200	1400	1600	1800	2000

3.2. Equations solved in the simulation

The computational domain is simplified to a 2D axisymmetric geometry as described above, and the external body forces are not considered in the present research, hence conservation equations solved in the simulation are shown as follows (ANSYS©Fluent v.13.0 Theory Guide, 2010).

The continuity equation is given as

$$\frac{\partial\rho}{\partial t}+\frac{\partial}{\partial x}(\rho v_x)+\frac{\partial}{\partial r}(\rho v_r)=0 \tag{3}$$

The axial momentum conservation equation is given by

$$\frac{\partial \rho}{\partial t}(\rho v_x)+\frac{1}{r}\frac{\partial}{\partial x}(r\rho v_x v_x)+\frac{1}{r}\frac{\partial}{\partial r}(r\rho v_r v_x)=-\frac{\partial p}{\partial x}+\frac{1}{r}\frac{\partial}{\partial x}\left[r\mu\, 2\frac{\partial v_x}{\partial x}-\frac{2}{3}(\nabla\cdot v)\right]+\frac{1}{r}\frac{\partial}{\partial r}\left[r\mu\left(\frac{\partial v_x}{\partial r}+\frac{\partial v_r}{\partial x}\right)\right] \quad (4)$$

where

$$\nabla\cdot v=\frac{\partial v_x}{\partial x}+\frac{\partial v_r}{\partial r}+\frac{v_r}{r} \quad (5)$$

The radial momentum conservation equation is given by

$$\frac{\partial}{\partial t}(\rho v_r)+\frac{1}{r}\frac{\partial}{\partial x}(r\rho v_x v_r)+\frac{1}{r}\frac{\partial}{\partial r}(r\rho v_r v_r)=-\frac{\partial p}{\partial r}+\frac{1}{r}\frac{\partial}{\partial x}\left[r\mu\left(\frac{\partial v_x}{\partial r}+\frac{\partial v_r}{\partial x}\right)\right]+\frac{1}{r}\frac{\partial}{\partial r}\left[r\mu\, 2\frac{\partial v_r}{\partial r}-\frac{2}{3}(\nabla\cdot v)\right]+ \quad (6)$$
$$-2\mu\frac{v_r}{r^2}+\frac{2}{3}\frac{\mu}{r}(\nabla\cdot v)+\rho\frac{v_w^2}{r}$$

$$\frac{\partial}{\partial t}(\rho v_w)+\frac{1}{r}\frac{\partial}{\partial x}(r\rho v_x v_w)+\frac{1}{r}\frac{\partial}{\partial r}(r\rho v_r v_w)=\frac{1}{r}\frac{\partial}{\partial x}\left[r\mu\frac{\partial v_w}{\partial x}\right]+\frac{1}{r^2}\frac{\partial}{\partial r}\left[r^3\mu\frac{\partial}{\partial r}\left(\frac{v_w}{r}\right)\right]-\rho\frac{v_r v_w}{r} \quad (7)$$

There is no additional source for species in the present study. ANSYS©Fluent predicts the local mass fractions of each species through the solution of convection-diffusion-reaction equation for each species. The general form of this equation is shown as follows (ANSYS©Fluent v.13.0 Theory Guide, 2010):

$$\frac{\partial}{\partial t}(\rho Y_i)+\nabla\cdot(\rho v Y_i)=-\nabla\cdot J_i+R_i \quad (8)$$

The channel Reynolds number (also known as rotational Reynolds number) inside SDR cavity in the present research can be calculated using equation given by Sinnott (2005) and modified here to the following form

$$\mathrm{Re}=\frac{\rho N D d}{\mu} \quad (9)$$

All the channel Reynolds numbers used in the present research imply that the flow in this SDR is laminar flow. This can be demonstrated by the previous studies (Daily and Nece, 1960; Djaouiet al., 2001; de Beer et al., 2014). Hence, the diffusion flux of species i, J_i, which arises due to concentration gradients, can be written as

$$J_i=-\rho D_{m,i}\nabla Y_i \quad (10)$$

As generally known, the two feed stocks TG and methanol are immiscible and they form a two-phase liquid-liquid system after being injected into the SDR, thus the reactions are limited by mass transfer among reagents. The gap sizes between the spinning disk and the stationary disk which are used in the current SDR vary in the range of 0.1 mm to 0.2 mm. As a result, a high velocity gradient is present between the spinning disk and the stationary disk, creating a high shear force occurring in the gap. Fast rotation of spinning disk amplifies further the effect of shearing in the gap thus reducing the mass transfer resistance by shortening the diffusive micro-distance transport.

We apply the homogeneous model describing the reacting mixture as a Newtonian suspension of droplets with viscosity depending on local volumetric fraction of dispersed phase. We want to obtain a qualitative but possibly rigorous explanation of experimentally observed increase of the conversion at higher shear inside the gap. We think that including “ad hoc” the explicit two-phase model facilities

(like velocity field for each phase, droplet break up, etc.) could obscure the main phenomena in our case. Similar conclusions were drawn by Rudniak et al. (2004).

We assume that droplets do not disappear during the whole process, in agreement with Qiu (2010) who mentioned that the reaction mixture passes from a biphasic (methanol and oil) system to a biphasic (methyl ester-rich and glycerol-rich) system during transesterification. The reaction generally preserves volume and in the dispersed phase the methanol substrate is at least partially replaced by glycerol product. Zhou and Boocock (2006) investigated phase distribution of methanol, glycerol, and catalyst in the transesterification of soybean oil. Investigation revealed that 42.0% of the alcohol, 2.3% of the glycerol, and only 5.9% of the catalyst were present in the ester-rich phase at steady state starting with an initial condition of 6:1 alcohol/oil molar ratio and catalyst concentration (1.0 wt% sodium methoxide). The reaction conditions used in Zhou and Boocock's investigation are similar to those utilized in the present research, and the investigation further demonstrated the existence of the droplet mainly consisting of methanol, glycerol and catalyst during the whole transesterification process. Thus we propose that the enhanced conversion at higher rotational speeds is caused by faster mass transport in the interface diffusional layer, the thickness of which decreases at higher shear in the gap between the disks. The diameter distribution is also expected to tend towards smaller droplets, which at approximately the same total volume of dispersed phase means a development of the interface area. Figure 4 below illustrates the process.

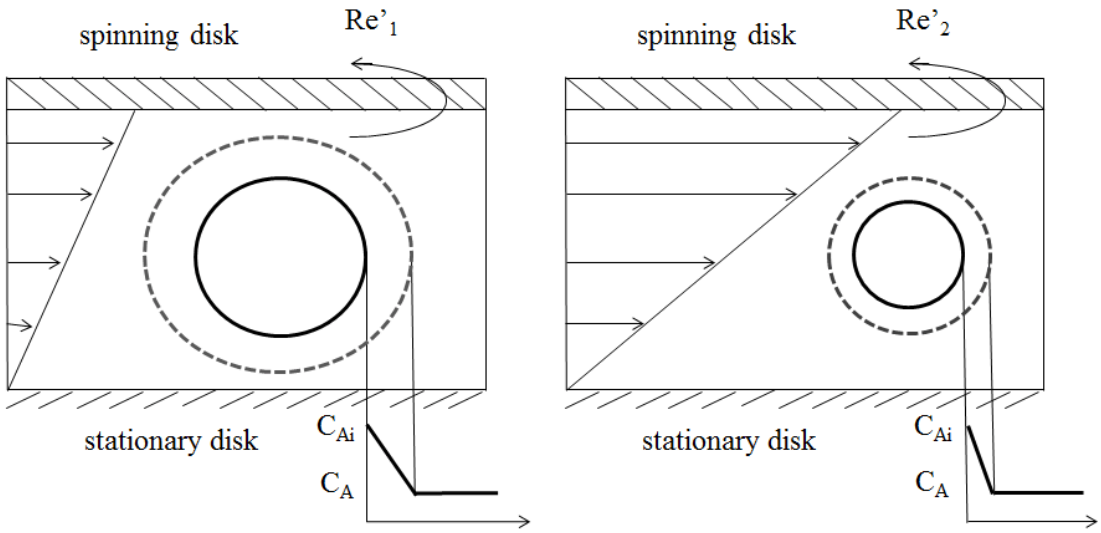

Fig. 4. Illustration of the effect of shear force on effective diffusivity; C_{Ai} - concentration of product at the interface, C_A - concentration of product in the continuous phase

In the model approach this is equivalent to an increase of the mixture effective diffusivities $D_{m,i}$ controlled by the gap size and rotational speed. In the present research we propose the following formula for modification of the mixture diffusivities to account for the shearing influence, which means effective diffusivity:

$$D_{m,i} = D_{m,io}\left[1 + A\left(Re'\right)^a\right] \tag{11}$$

where $D_{m,io}$ are understood as pure diffusivities for individual components.

The value of A defines the magnitude of D_m under different operating conditions and is set as 0.022. The value of a is deduced from the exponent on Reynolds number in empirical correlations among Sherwood number, Reynolds number and Schmidt number, which describe mass transfer in the continuous phase around drops. Sandoval-Robles et al. (1980) have shown how the exponent on Reynolds number changes with the value of Reynolds number from 1/3 for Stokes regime to 1/2 for

boundary-layer theory, and to 2/3 for a surface renewal mechanism or turbulent conditions (Richardson, 1963).

The particle diffusion Reynolds number, *Re'*, is modified from the particle Reynolds number proposed by Rusconi and Stone (2008).

$$Re' = \frac{\rho N D d}{\mu}\left(\frac{D}{d}\right)^2 \tag{12}$$

For the calculation of chemical reactions, the laminar finite-rate model is used. The net source of chemical species i due to reaction R_i is computed as the sum of the Arrhenius reaction sources over the N_R reactions that the species participate in:

$$R_i = M_{w,i}\sum_{r=1}^{N_R} R''_{i,r} \tag{13}$$

The molar rate of creation/destruction of species i in reaction r($R'_{i,r}$) in Eq. (13)) is given by

$$R'_{i,r} = \left(\vartheta''_{i,r} - \vartheta'_{i,r}\right)\left(k_{f,r}\prod_{j=1}^{N_R}\left[C_{j,r}\right]^{\eta'_{j,r}} - k_{b,r}\prod_{j=1}^{N_R}\left[C_{j,r}\right]^{\eta''_{j,r}}\right) \tag{14}$$

The forward rate constant for reaction r, $k_{f,r}$, is computed using the Arrhenius expression.

$$k_{f,r} = A_r e^{-E_r/RT} \tag{15}$$

In this research, the kinetic rate constant and activation energy data are obtained and modified on the basis of data in Table 4.

Table 4. Chemical kinetics data for all reactions (Noureddini and Zhu, 1997)

Parameter	Reaction I *(TG → DG)*	Reaction II *(DG → MG)*	Reaction III *(MG → GL)*
Kinetic rate constant, k_i	8.333×10^{-4}	3.583×10^{-3}	4.033×10^{-3}
Activation energy, E_i	5.5×10^{7}	8.309×10^{7}	2.687×10^{7}

For reversible reaction the backward rate constant $k_{b,r}$ for reaction r is determined by following expression:

$$k_{b,r} = \frac{k_{f,r}}{K_r} \tag{16}$$

where K_r is the equilibrium constant for the reaction r, determined by the expression:

$$K_r = \exp\left(\frac{\Delta S_r^0}{R} - \frac{\Delta H_r^0}{RT}\right)\cdot\left(\frac{P_{atm}}{RT}\right)^{\sum_{i=1}^{N}\left(\vartheta''_{i,r}-\vartheta'_{i,r}\right)} \tag{17}$$

$$\frac{\Delta S_r^0}{R} = \sum_{i=1}^{N}\left(\vartheta''_{i,r} - \vartheta'_{i,r}\right)\frac{S_i^0}{R} \tag{18}$$

$$\frac{\Delta H_r^0}{RT} = \sum_{i=1}^{N}\left(\vartheta''_{i,r} - \vartheta'_{i,r}\right)\frac{H_i^0}{RT} \tag{19}$$

3.3. Modelling assumptions

For the purpose of modelling and in order to simplify the calculation, initial assumptions are made as follows:

- Due to the fact that canola oil, as a mixture of fatty acids, consists mainly of oleic acid, triolein ($C_{57}H_{104}O_6$) is chosen as a representation of TG, accordingly, diolein ($C_{39}H_{72}O_5$) is chosen as a representation of DG, monoolein ($C_{21}H_{40}O_4$) is chosen as a representation of MG, and methyl oleate ($C_{19}H_{36}O_2$) is chosen as a representation of the resulting methyl ester (biodiesel).
- Feed stocks from inlet-top and inlet-bottom are TG and methanol, respectively. Molar ratio of methanol to TG is 6:1, and concentration of NaOH is 1.0 wt%. There is no explicit occurrence of a catalyst; although the presence of the catalyst is taken into account by modification of the rate constants in the kinetic equations.
- The problem is nearly isothermal because the thermal boundary conditions assume perfect thermal control, thus all physicochemical properties are nearly constant. In the present research, the reaction temperature is chosen as 25 °C for all cases.
- At the start the whole domain (the gap) is filled with TG at rest and from this point the process starts by injecting substrates TG and methanol.
- The order of magnitude for diffusion coefficients for vegetable oils is 10^{-9} m^2s^{-1} (Cussler, 1997). Egbuna et al. (2013) investigated diffusivities for the diffusion of palm oil into different solvents, the values ranged from 6.47 to 7×10^{-9} m^2s^{-1}. Based on this, a pure diffusivity value for each component in the reacting mixture, Dm,i0, is assumed to be 7×10^{-9} m^2s^{-1} in the present research.
- The feedstock for inlet-top is canola oil (ConAgra Foods, USA) in experiments (Qiu, 2010). Generally the content of free fatty acids in canola oil is 0.4 - 1.2%, which can result in saponification reaction (Przybylski, 2007). Owing to the low level of free fatty acids content in canola oil and relatively small amount of catalyst used in the experiments, saponification side reaction is ignored in the present research.

4. SIMULATION RESULTS

4.1. Simulation results of hydrodynamics inside SDR gap

Figure 5(a) shows the flow field in the SDR gap, Fig. 5(b) is the magnification of the flow field near the inlet, as marked in square in Fig. 5(a), Fig. 5(c) is the magnification of the flow field near the outlet, as marked in oval in Fig. 5(a). In the present research, the liquids injected into SDR flow outwards at low radial positions as shown in Fig. 5(b), while at high radial positions, there are two situations. The liquid accelerates near the rotor outwards because of centrifugal force caused by the spinning disk rotation, while a backflow near the stator is created as a result of the continuity conservation, which prevents the liquid from breakage as shown in Fig. 5 (c), the inwards flow is identified as backflow in the present study.

The simulation of the flow pattern inside the SDR gap is consistent with the research conducted by De Beer et al. (2014). They proposed and depicted an engineering model of the fluid flow patterns inside the inter-disk space of rotor-stator. The flow through a rotor–stator cavity can be described as a combination of radial plug flow and ideally mixed region, the radial liquid velocity profile between the rotor and the stator which is dominated by plug flow has a parabolic shape over the height between the rotor and the stator. In the mixed region, the radial velocity profile of the liquids dominated by boundary layer formation. The centrifugal Von Kármán boundary layer is present at the rotor, and the centripetal Bodewadt boundary layer is present at the stator.

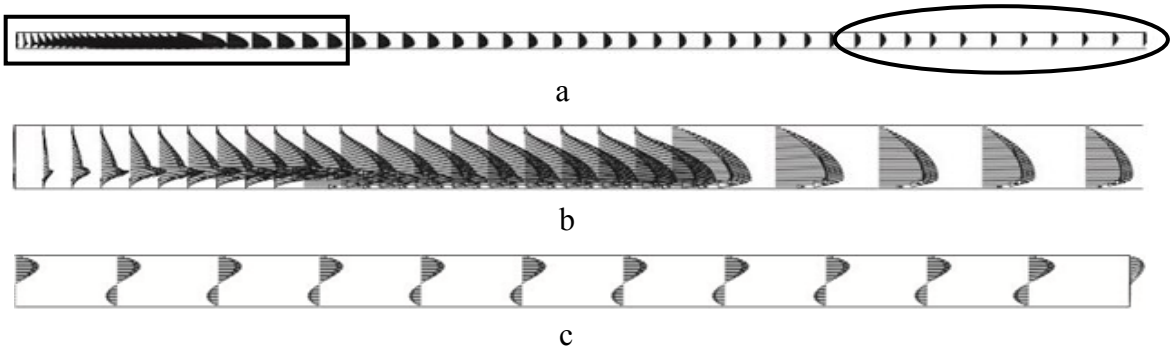

Fig. 5. The flow field in the SDR gap (a), the inlet (b) and the outlet (c)

Figure 6 presents the backflow zone inside SDR gap showing a characteristic pattern. The vertical position of the picture is justified by the ANSYS©Fluent technicality. When the axisymmetric geometry is modelled, the direction of swirl axis is assumed to be the X axis and the computational domain is situated above the X axis. A pattern such as the one marked in purple indicates where the backflow meets with the predominant outward stream, the mixed liquids flow together outwards outlet after meeting. The boarder of this backflow zone may move with varying rotational speed of spinning disk, gap size between rotor and stator, and flow rate of TG at the inlet.

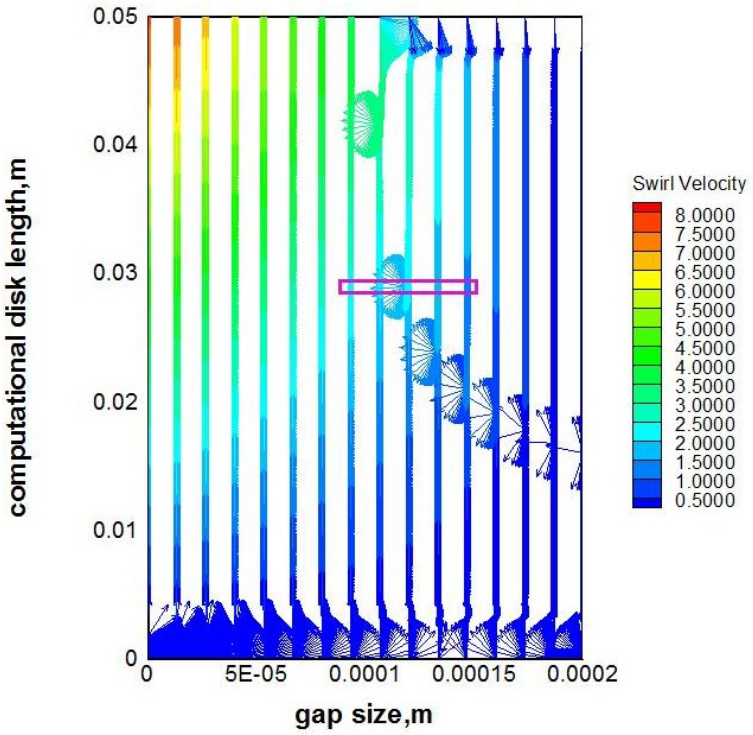

Fig. 6. Overall backflow zone within SDR gap in form of velocity vectors (The geometry proportions are intentionally changed.)

To investigate how operating conditions affect the size of backflow zone, three gap sizes of SDR are simulated. For each gap size, six rotational speeds of spinning disk are studied. For the gap size 0.2 mm, two flow rates of TG at inlet are simulated. The sizes of backflow zones under different operating conditions are shown in Figs.7 and 8.

Figure 7 demonstrates that the size of backflow zone increases as the rotational speed of spinning disk increases, and decreases with decreasing gap size between rotor and stator. In other words, faster

rotational speed of spinning disk and bigger gap size between spinning disk and stationary disk lead to more backflow in SDR gap. On the other hand, as is evident in Fig. 8, the size of backflow zone decreases with increasing flow rate of TG at the inlet. It indicates that larger flow rate of TG at inlet leads to less backflow in SDR gap.

The simulation results reflected in Figs.7 and 8 are also consistent with the research carried out by De Beer et al. (2014). The authors concluded that the radius where flow pattern changes from plug flow to ideally mixed flow decreases with increasing rotational Reynolds number and gap ratio, and increases with increasing superposed through flow rate.

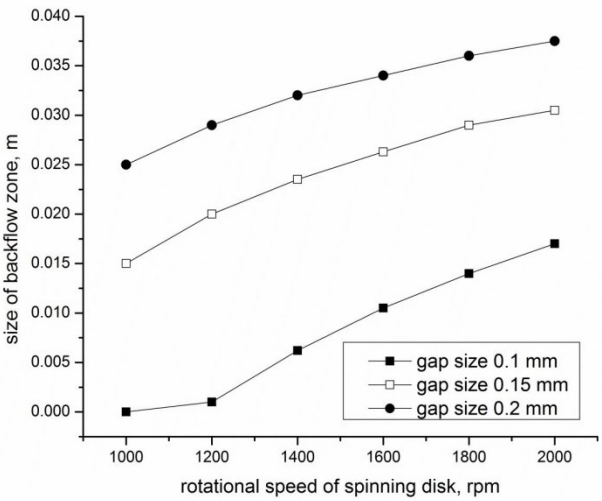

Fig. 7.Changes of backflow zone size with varying rotational speed and gap size

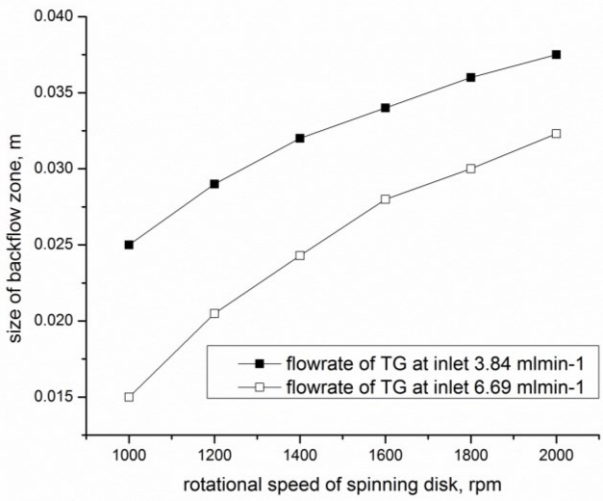

Fig. 8. Changes of backflow zone size with varying flow rate of TG at inlet

4.2. Analysis of effect of operating conditions on TG conversion in SDR

SDR, identified as having small gap size and fast rotational speed, is an efficient intensification technology for liquid-liquid two-phase reaction. The small gap sizes induce a high shear force to act on the reactants in the gap, leading to better mass transfer. Fast rotational speed of spinning disk is also of importance to intensify mixing and helps to eliminate the mass transfer resistance in the SDR gap. Since the rate of TG transesterification is limited by mass transfer between oil and alcohol phases due to their immiscibility, small gap size and fast rotational speed apparently result in higher TG conversion.

To determine values of TG conversion κ, the following equation is used:

$$\kappa = \frac{C_0 \cdot Q_{v0} - C_k \cdot Q_{vk}}{C_0 \cdot Q_{v0}} \cdot 100\% \tag{20}$$

All of the above variables C_0, C_k, Q_{v0}, Q_{vk}, can be discerned with ANSYS©Fluent Reports.

The verification experiments conducted by Qiu and Weatherley using the experimental setup are shown in Fig. 1. The Feed stocks are TG and methanol, molar ratio of methanol to TG is 6:1, and concentration of catalyst NaOH is 1.0 wt%. The experiment conditions are the same as those used in the simulation, as shown in Table 5. Simulation results and experimental data of TG conversion varying with different gap size and rotational speed are displayed in Figs. 9, 10 and 11.

Table 5. Verification experiment conditions

	Temperature, K	Gap size, mm	Flow rate of TG, ml/min	Rotational speed of spinning disk, rpm
Value	298.15	0.1 / 0.15 / 0.2	3.84 / 6.69	1000 / 1200 / 1400 / 1600 / 1800 / 2000

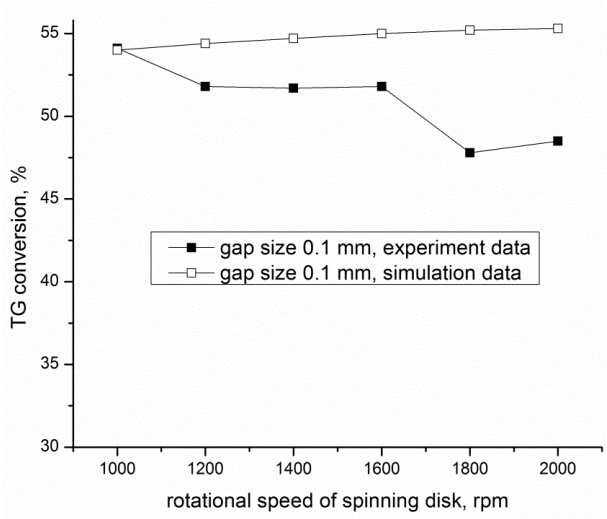

Fig. 9. Effect of rotational speed of spinning disk on TG conversion when gap size is 0.1 mm

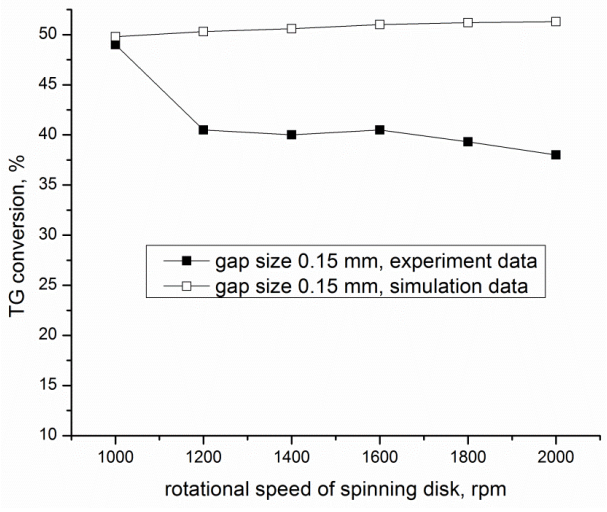

Fig. 10. Effect of rotational speed of spinning disk on TG conversion when gap size is 0.15 mm

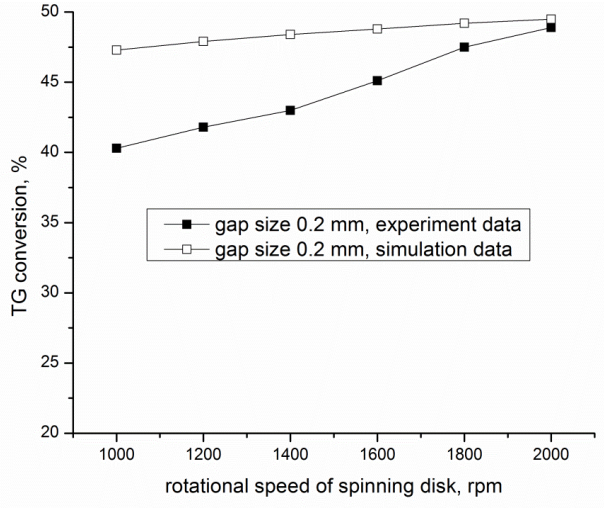

Fig. 11. Effect of rotational speed of spinning disk on TG conversion when gap size is 0.2 mm

From Fig.9, Fig.10 and Fig.11 we can state that TG conversion increases as gap size decreases, simulation results show good agreement with experiment data. The simulation results indicate that TG conversion increases slightly with increasing rotational speed. While the experimental data show that when gap sizes are 0.1mm and 0.15mm, TG conversion decreases as rotational speed of spinning disk increases. Fig. 7 reveals that faster rotational speed of spinning disk and bigger gap size between spinning disk and stationary disk lead to more backflow in SDR gap, we conclude that TG conversion decreases as size of backflow zone increases, i.e., backflow is undesirable in biodiesel synthesis in SDR.

We give below a rigorous original explanation of the observed negative effect of increasing backflow zone on the conversion (which is enhanced either with increasing gap size or increasing rotational speed).

First, let us recall that the overall chemical equation for transesterification of TG and methanol producing biodiesel and glycerol can be written as

$$\mathrm{TG} + 3\,\mathrm{CH_3OH} \xleftrightarrow{catalyst} 3\,\mathrm{RCOOCH_3} + \mathrm{GL} \qquad \text{(IV)}$$

The reaction rate for the overall chemical equation of the transesterification, r_t, can be calculated by Eq. (21)

$$r_t = k_f \cdot C_{TG} \cdot C_{methanol}^3 - k_b \cdot C_{RCOOCH3}^3 \cdot C_{GL} \qquad (21)$$

Although it is a reversible reaction, the forward reaction is dominant under the present operating conditions thus the overall reaction rate depends mainly on concentrations of TG and methanol.

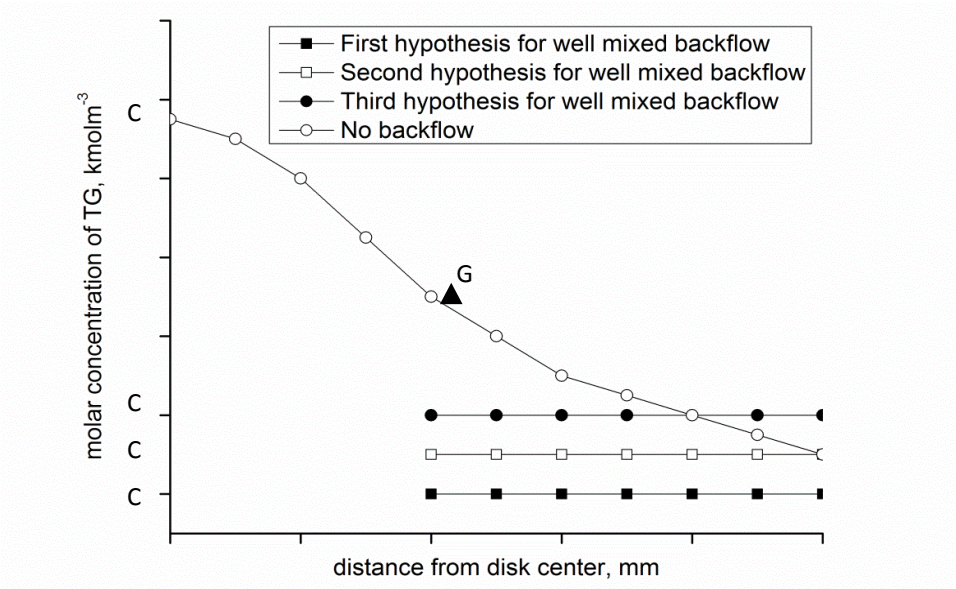

Fig. 12. Molar concentration of TG changes along SDR gap under different hypothesis

The reactants TG and methanol are injected into the SDR from centres of rotor and stator respectively, and without any backflow the concentration of TG will decrease along the SDR gap. This is illustrated in Fig. 12 by the hollow circles connecting points of concentrations C_1 to C_3.

Naturally, back mixing results in a tendency to level off all the concentrations in the backflow zone, including TG concentration. Suppose a back mixing starts at a distance marked by the point G in Fig. 12, which implies a constant concentration of TG as illustrated by one of the three horizontal lines in this figure.

Suppose now hypothetically that TG concentration in the back-mixing zone is equal or less than C_3 in Fig. 12. This would mean that the conversion is better than in case of no back-mixing described by the hollow circles. On the other hand, however, according to Eq. (21), rate of reaction would be smaller in the back-mixing zone which obviously contradicts the initial hypothesis as the final lower substrate concentration, such as C_4 cannot be achieved with lower reaction rate. Subsequently the final substrate concentration must be bigger than C_3, such as C_2 in Fig. 12 which means that the conversion is worse in case when the back-mixing occurs.

There is an exception when the gap size is equal to 0.2 mm, for which TG conversion increases with the rotational speed increase, even though size of the backflow zone increases. Probably the larger gap size produces smaller shear force and the reaction rate of transesterification is still limited by the mass transfer between the two phases. In this situation growing rotational speed enhances the interface of mixing between reactants and consequently the TG conversion increases. The effect of flow rate of TG at inlet is also investigated in the present research. Fig. 8 shows that size of backflow zone is smaller when bigger flow rate of TG at inlet (6.69 ml/min) is utilized. Theoretically, TG conversion is supposed to be higher when flow rate of TG at inlet is bigger than that obtained when smaller flow rate of TG at inlet (3.84 ml/min) is used. However, both simulation results and experimental data show that TG conversion is smaller when bigger flow rate of TG at inlet is used, as shown in Fig.13. This can be explained by the fact that the mean residence time of the reactants in SDR when flow rate of TG at inlet is 6.69 ml/min is much shorter than that when flow rate of TG at inlet is 3.84 ml/min. The mean residence time is too short for the reactants to react when flow rate is 6.69 ml/min, that is why bigger flow rate of TG at inlet leads to smaller TG conversion.

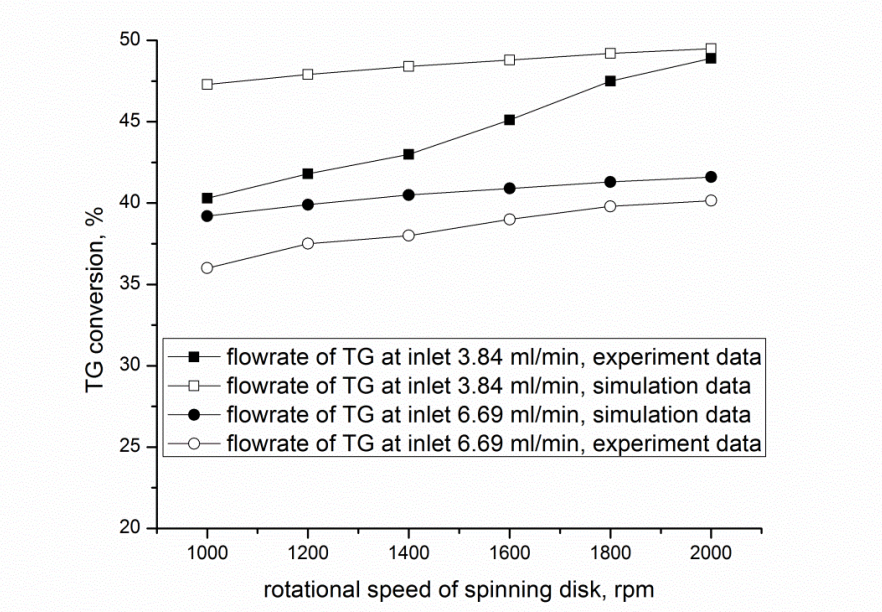

Fig. 13. Effect of TG flow rate at the inlet on TG conversion when gap size is 0.2 mm

5. CONCLUSIONS

The CFD software ANSYS©Fluent v.13.0 was successfully used to investigate the hydrodynamics inside SDR gap for biodiesel synthesis from canola oil and methanol in the presence of a sodium hydroxide catalyst. To accomplish this task, an adequate model was formulated and expressed in terms of facilities available within ANSYS©Fluent. The simulating results were compared with corresponding experiment data obtained from a setup built by our collaborating partner from Kansas University. The modelling provides useful information on the reactor performance.

In the present research, liquids are injected into SDR and flow outwards at low radial positions, while at high radial positions there are two phenomena. The liquid accelerates near the rotor outwards because of centrifugal force caused by the spinning disk rotation, while a backflow near the stator is created as a result of the continuity conservation, which prevents the liquid from breakage.

In order to investigate effects of operating conditions on size of backflow zone, three gap sizes were simulated and for each gap size six rotational speeds of spinning disk were studied. For gap size 0.2mm, two flow rates of TG at inlet were simulated. The present study research well simulates the

backflow phenomenon and explains why backflow is undesirable (resulting in lower TG conversion). Results show that the size of backflow zone increases as the rotational speed increases, and decreases with decreasing gap size between rotor and stator. Likewise size of backflow zone reduces with increasing flow rate of substrates at inlet.

The simulation also reveals that small gap size and fast rotational speed induce large shear force inside SDR, intensifying micro-mixing among reagents, consequently enhancing TG conversion. However, too fast rotational speed of the spinning disk leads to more backflow decreasing TG conversion, which is confirmed by experimental data. Hence, excessive rotational speeds are not recommended in practice.

What is more, large flow rate of TG at inlet is not recommended either. The mean residence time of the reactants in SDR is shorter than that when flow rate of TG at inlet is small. The mean residence time is too short for the reactants to react with large TG flow rate at inlet, consequently leads to smaller TG conversion.

Nevertheless spinning disk reactors are very effective devices intensifying the transesterification process for biodiesel synthesis. With the use of SDR, shorter process time and smaller equipment size is needed, which is very important for industrial production. We discussed the process time issue in our previous paper (Wen and Petera, 2015) confirming higher efficiency of SDR compared to the conventional apparatus. However, it is necessary to optimise the operating conditions in order to attain better biodiesel production efficiency as recommended above.

SYMBOLS

A	correction factor
A_i	pre-exponential factor, $m^3 \cdot kmol^{-1} \cdot s^{-1}$
a	correction factor
C_0	volume flow rate-average TG molar concentration at inlet, $kmol \cdot m^{-3}$
$C_{j,r}$	molar concentration of species j in reaction r, $kmol \cdot m^{-3}$
C_k	volume flow rate-average TG molar concentration at outlet, $kmol \cdot m^{-3}$
$C_{methanol}$	methanol concentration in the SDR gap, $kmol \cdot m^{-3}$
C_{Ai}	concentration of product at the interface, $kmol \cdot m^{-3}$
C_A	concentration of product in the continuous phase, $kmol \cdot m^{-3}$
C_{TG}	TG concentration in the SDR gap, $kmol \cdot m^{-3}$
D	diameter of the reactor, m
$D_{m,i0}$	pure diffusivities for individual components, $m^2 s^{-1}$
$D_{m,i}$	effective diffusion coefficients for species i in the mixture, $m^2 s^{-1}$
d	gap size of the reactor, m
E_i	activation energy, $J \cdot kmol^{-1}$
H_i^0	standard state enthalpy of species i, $J \cdot kmol^{-1}$
J_i	diffusion flux of species i, $kg \cdot m^{-2} \cdot s^{-1}$
k_b	backward rate constant, $m^3 \cdot kmol^{-1} \cdot s^{-1}$
k_f	forward rate constant, $m^3 \cdot kmol^{-1} \cdot s^{-1}$
$k_{b,r}$	backward rate constant for the reaction r, $m^3 \cdot kmol^{-1} \cdot s^{-1}$
$k_{f,r}$	forward rate constant for the reaction r, $m^3 \cdot kmol^{-1} \cdot s^{-1}$
k_i	respective kinetic constant, $m^3 \cdot kmol^{-1} \cdot s^{-1}$
$M_{w,i}$	the molecular weight of species i, kg $kmol^{-1}$
N	rotational speed of spinning disk, rps
N_R	total number of reactions that species i participate in
n	number of species

P_{atm}	atmospheric pressure (101325 Pa)
Q_{v0}	volume flow rate at inlet, m^3s^{-1}
Q_{vk}	volume flow rate at outlet, m^3s^{-1}
R	ideal gas constant, J $kmol^{-1}K^{-1}$
R_i	net rate of production of species i by chemical reaction, $m^3 \cdot kmol^{-1} \cdot s^{-1}$
Re	channel Reynolds number or rotational Reynolds number
$R'_{i,r}$	the Arrhenius molar rate of creation (or destruction) of species i in reaction r, $m^3 \cdot kmol^{-1} \cdot s^{-1}$
Re'	particle diffusion Reynolds number
r	the radial coordinate, m
r_I, r_{II}, r_{III}	reaction rate, kmol $m^{-3}s^{-1}$
r_t	the reaction rate for the overall chemical equation of transesterification, $m^3 \cdot kmol^{-1} \cdot s^{-1}$
S_i^0	standard state entropy of species i, J $kmol^{-1}K^{-1}$
v	species velocity, ms^{-1}
v_i	velocity of species i, ms^{-1}
v_x	the axial velocity, ms^{-1}
v_r	the radial velocity, ms^{-1}
v_w	the swirl velocity, ms^{-1}
x	the axial coordinate, m
Y_i	mass fraction of species i

Greek symbols

$\eta'_{j,r}$	rate exponent for reactant species j in reaction r
$\eta''_{j,r}$	rate exponent for product species j in reaction r
$\vartheta'_{i,r}$	stoichiometric coefficient for reactant i in reaction r
$\vartheta''_{i,r}$	stoichiometric coefficient for product i in reaction r
κ	TG conversion
μ	viscosity, $kgm^{-1}s^{-1}$
ρ_i	density of species i, kgm^{-3}

REFERENCES

Batchelor G., 1951. Note on a class of solutions of the Navier–Stokes equations representing steady rotationally-symmetric flow. *Mech. Appl. Math*., 4, 29–41. DOI: 10.1093/qjmam/4.1.29.

Bodewadt U.T., 1940. Die Drehströmung über dem festem Gründe. *Z. Angew. Math. Mech*., 20, 241–253.DOI: 10.1002/zamm.19400200502.

Brady J., Durlofsky L., 1987. On rotating disk flow. *Fluid Mech*., 175, 363–394. DOI: 10.1017/S0022112087000430.

Brechtelsbauer C., Lewis N., Oxley P., Ricard F., Ramshaw C., 2001. Evaluation of a spinning disc reactor for continuous processing. *Org. Process Res. Dev*., 5, 65-68. DOI: 10.1021/op0000834.

Cafiero L.M., Baffi G., Chianese A., Jachuck R.J., 2002. Process intensification: precipitation of barium sulphate using a spinning disc reactor. *Ind. Eng. Chem. Res*., 41, 5240-5246. DOI: 10.1021/ie010654w.

Clifford Y.T, Wang Y.H., Tai C.T., Liu H.S., 2009. Preparation of silver nanoparticles using a spinning disk reactor in a continuous mode. *Ind. Eng. Chem. Res*., 48, 10104–10109. DOI: 10.1021/ie9005645.

Cussler E.L., 1997. *Diffusion: Mass transfer in fluid systems*. 2nd edition. Cambridge University Press, NewYork, 111-120.

Daily J.W., Nece R.E., 1960. Chamber dimension effects on induced flow and frictional resistance of enclosed rotating disks. *Basic Eng*., 82, 217–232. DOI: 10.1115/1.3662532.

De Beer M.M., Keurentjes J.T.F., Schouten J.C., van der Schaaf J., 2014. Engineering model for single-phase flow in a multi-stage rotor–stator spinning disc reactor. *Chem. Eng. J*., 242, 53–61. DOI: 10.1016/j.cej.2013.12.052.

Djaoui M., Dyment A., Debuchy R., 2001. Heat transfer in a rotor–stator system with a radial inflow. *Eur. J. Mech. – B/Fluids*, 20, 371–398. DOI: 10.1016/S0997-7546(01)01133-5.

Egbuna S.O, Ozonoh M, Aniokete T.C., 2013. Diffusion rate analysis in palm kernel oil extraction using differentextraction solvents. *IJRET*, 02, 639-648. DOI: 10.15623/ijret.2013.0211098.

Freedman B., Pryde E.H., Mounts T.L., 1984. Variables affecting the yields of fatty esters from transesterified vegetable oils. *J. Am. Oil Chem. Soc.*, 61, 1638-1643. DOI: 10.1007/BF02541649.

Freedman B., Butterfield R.O., Pryde E.H., 1986. Transesterification kinetics of soybean oil. *J. Am. Oil Chem. Soc.*, 63, 1375-1380. DOI: 10.1007/BF02679606.

Haddadi S., Poncet S., 2008. Turbulence modelling of torsional Couette flows. *Int. J. Rotating Mach*., 2008, 635138. DOI: 10.1155/2008/635138.

Lopez J., 1998. Characteristics of endwall and sidewall boundary layers in a rotating cylinder with a differentially rotating endwall. *Fluid Mech*., 359, 49–79.DOI: 10.1017/S002211209700829X.

Noureddini H., Zhu D., 1997. Kinetics of transesterification of soybean oil. *J. Am. Oil Chem. Soc.*, 74, 1457-1463. DOI: 10.1007/s11746-997-0254-2.

Phadke U., Owen J.M., 1988. Aerodynamic aspects of the sealing of gas-turbine rotor–stator systems. Part 1: The behavior of simple shrouded rotating-disk systems in a quiescent environment. *Int. J. Heat Fluid Flow*, 9, 98–105. DOI: 10.1016/0142-727X(88)90060-4.

Poncet S., Chauve M.P., Le Gal P., 2005a. Turbulent rotating disk flow with inward throughflow. *Fluid Mech*., 522, 253–262. DOI: 10.1017/S0022112004002046.

Poncet S., Chauve M.P., Schiestel R., 2005b. Batchelor versus Stewartson flow structures in a rotor–stator cavity with throughflow. *Phys. Fluids*, 17, 075110. DOI: 10.1063/1.1964791.

Przybylski R., 2007. *Canola oil: Physical and chemical properties*. Canola council of Canada. Available at: http://www.canolacouncil.org/media/515239/canola_oil_physical_chemical_properties_1.pdf.

Qiu Z.Y., 2010. *Intensification of liquid-liquid contacting processes*. PhD Thesis, University of Kansas.

Qiu Z.Y., Petera J., Weatherley L.R., 2012. Biodiesel synthesis in an intensified spinning disc reactor. *Chem. Eng.J*., 210, 597-609. DOI: 10.1016/j.cej.2012.08.058.

Richardson, P. D., 1963. Heat and mass transfer in turbulent separated flows. *Chem. Eng. Sci.*, 18: 149 –155.

Rudniak L., Machniewski P.M., Milewska A., Molga E., 2004. CFD modelling of stirred tank chemical reactors: homogeneous and heterogeneous reaction systems. *Chem. Eng. Sci.,* 59, 5233–5239.

Rusconi R., Stone H.A., 2008. Shear-induced diffusion of platelike particles in microchannels. *Phys. Rev. Lett.,* 101, 254502. DOI: 10.1103/PhysRevLett.101.254502.

Sandoval-Robles J.G., Riba J.P., Couderc J. P., 1980. Mass transfer around a sphere. *Trans IChemE*, 58, 132–134.

SAS IP, Inc., 2010. ANSYS©Fluent v.13.0 Theory Guide.

Soo S.L., 1958. Laminar flow over an enclosed rotating disk. *Trans. ASME*, 80, 287–296.

Stewartson K., 1953. On the flow between two rotating coaxial disks. *Math. Proc. Camb. Phil. Soc*. 49, 333–341. DOI: 10.1017/S0305004100028437.

Von Kármán T., 1921. Über laminare und turbulente Reibung. *Z. Angew. Math. Mech*., 1(4), 233–252. DOI: 10.1002/zamm.19210010401.

Wen Z., Petera J., 2015. CFD Numerical simulation of biodiesel synthesis in a spinning disc reactor. *Chem. Process Eng.*, 36, 21–37. DOI: 10.1515/cpe-2015-0002.

Zhou W., Bookcock D.G.B., 2006. Phase distributions of alcohol, glycerol, and catalyst in the transesterification of soybean oil. *J. Am. Oil Chem. Soc.*, 83, 1047-1052. DOI: 10.1007/s11746-006-5161-4.

Received 01 December 2015
Received in revised form 02 February 2017
Accepted 19 February 2017

www.czasopisma.pan.pl www.journals.pan.pl
Chemical and Process Engineering 2017, 38 (2), 283-294
DOI: 10.1515/cpe-2017-0021

WASTE PLANT MATERIAL AS A POTENTIAL ADSORBENT OF A SELECTED AZO DYE

Elwira Tomczak*, Paweł Tosik

Lodz University of Technology, Faculty of Process and Environmental Engineering, 90-924 Łódź, Wólczańska 213, Poland

This paper discusses the adsorption of Direct Orange 26 azo dye on sunflower husk – an agricultural waste product. During the study, sorption kinetics and equilibrium as well as sorption capacity of the husk were investigated. The adsorption kinetics was analyzed using pseudo-first and pseudo-second order equations, which indicated a chemical sorption mechanism. The sorption equilibrium was approximated with the two-parameter Freundlich and Langmuir equations and the three-parameter Redlich-Peterson equation. The main experiments were carried out in a laboratory adsorption column under different process conditions. Experimental data were interpreted with the Thomas model, based on the volumetric flow rate, initial composition of the feed solution and mass of the adsorbent. The results of modeling the adsorption equilibrium, adsorption kinetics and adsorption dynamics were evaluated statistically.

Keywords: sunflower husk, Direct Orange 26, adsorption equilibrium, adsorption kinetics, adsorption dynamics

1. INTRODUCTION

Textile industry wastewater, usually having a complex chemical composition with a significant share of dye substances, can negatively affect water resources as even small concentrations of dyes become discernible. Many dyes and compounds coming from their chemical transformation can possess carcinogenic and/or mutagenic properties and accumulate in living organisms. Dyes in natural waters reduce their transparency, impede photosynthesis, impair plant and animal growth, affect the solubility of oxygen and the self-cleaning process. There are many conventional (chemical and physical) methods of wastewater treatment reducing the concentration of dye contaminants (Avdicevic et al., 2017; Borges et al., 2016). They are often expensive and cause waste disposal problems. Among many available methods including coagulation, chemical deposition, ion exchange and membrane processes, adsorption gives the most promising results in terms of its economics and efficiency (Allen and Koumanova, 2003; Priya et al., 2014).

Activated carbons, zeolites and silica gels are the most popular adsorbents due to their high sorption capacity. Currently, however, there is also a demand for other efficient, but simultaneously cheap and easily available materials. These properties are characteristic of plant sorbents, whose lignocellulosic structure enables adsorption of many contaminants from water. To a great extent, plant sorbents are waste materials that do not generate additional costs and thus are becoming attractive substitutes for synthetic sorbents.

The available studies indicate an interest in new and inexpensive materials of plant origin to be used in biosorption processes. Biosorbents should effectively remove various contaminants from aqueous

*Corresponding authors, e-mail: elwira.tomczak@p.lodz.pl

media, be non-toxic to the environment and easily recyclable. It is also important that the sorbent material be cheap and available in a given region (Hameed and Ahmad, 2009; Muthamilselvi et al., 2016; Nassar and El-Geundi, 1991; Soldatkina et al., 2009; Sud et al., 2008). The studies employing new biosorbents usually deal with sorption of heavy metal ions and dyes. Interestingly, some researchers use algae, bacteria, fungi, yeast as well as industrial and agricultural waste in order to sorb metal ions (Kotrba et al., 2011). Sorption capacities of selected biosorbents and wastes from food, wood and agricultural industries are presented in the work of Gala and Sanak-Rydlewska (2010). Also, similar natural sorbents of plant origin are used to adsorb dyes (Jain et al., 2009; Osma et al., 2007; Srinivasan and Viraraghavan, 2010; Tomczak et al., 2015). The experiments employing sunflower husk to remove dyes from the textile industry wastewater were described by Oguntimein and Duwane (2014) and Oguntimein (2016). The authors also proposed optimal conditions for the process and modification of the sorbent material increasing its adsorption capacity. In another study, sunflower husk was used to adsorb Cu^{+2} ions. The maximum sorption capacity of 57.14 mg/g was achieved at 30 °C and a pH of 5.0 (Witek-Krowiak, 2012). The optimization of known sorbent materials consists in searching for appropriate process parameters as well as possible modifications allowing the enhancement of their sorption capacity.

Another review (Crini, 2006) presents a critical analysis of low-cost materials, describes their characteristics, advantages and limitations, and discusses various mechanisms involved. The literature presents different values of sorption capacity for the same sorbent – sorbate systems. It depends on the origin, physical and chemical processing of the sorbent and the pH and temperature of the process. Some examples are summarized in Table 1.

Table 1. Sorption capacity of plant biosorbent with respect to certain dyes (Tomczak and Tosik, 2014)

Dyes	Sorbent	Maximum sorption capacity, mg/g
Direct Red 80 Direct Red 81 Acid Blue 92 Acid Red 14	Soy meal hulls	178.57 120.48 114.94 109.89
Methylene Blue	Duckweed (*Spirodela polyrhiza*)	112.36
Methylene Blue	Palm kernel fibre	671.59
Methylene Blue	Wheat shells	21.50
Methylene Blue	Neem leaf powder (*Azadirachta indica*)	8.76
Methylene Blue	Rice husk	40.58
Methylene Blue	Jute waste	22.47
Methylene Blue	Banana peel	20.80
Methylene Blue	Orange peel	18.60
Direct Red 23	Orange peel	10.72
Direct Red 80	Orange peel	21.05
Reactive Orange 16	Corn cob	25.25
Acid Yellow 36	Rice husk	86.90
Direct Orange 26	Rye straw	22.00
Reactive Blue 81	Rye straw	14.00

This work examines the possibility of removing Direct Orange 26 azo dye from water with the help of waste sunflower husk, which had been previously modified to improve the process performance. Sorption kinetics and equilibrium were investigated in batch experiments, and dynamics in a laboratory adsorption column via adjusting process parameters such as the initial dye concentration, volumetric flow rate of the feed solution and bed height. The resulting breakthrough curves were used to model the process mathematically with the Thomas equation.

2. EXPERIMENTAL MATERIALS

The adsorption of Direct Orange 26 was performed using sunflower husk obtained from domestic sunflower harvest (*Helianthus annus L.)* in 2015. Sunflower husk is a waste material produced through decorticating sunflower seeds (the price of 100 kg of husk is roughly 100 PLN). Due to its chemical composition and lignocellulosic structure, sunflower husk is not used by the food industry but can be used as a feed additive. It is built from cellulose (48%), hemicellulose (35%) and lignin (17%) (Piyo, 2014). Cellulose and hemicellulose are polymers composed of sugars, while lignin is a biopolymer made up of phenol derivatives. Chemical structure of sunflower husk indicates its good sorption ability (Fig. 1).

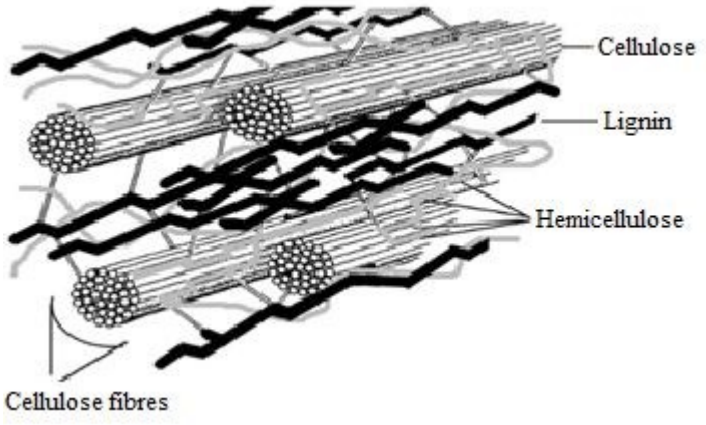

Fig. 1. Lignocellulosic complex (Leja et al., 2009)

The cell wall of a biosorbent is built mostly from polysaccharides, lipids and proteins containing numerous functional groups allowing the creation of a new bond, e.g. sorbent-dye bond. The functional groups responsible for bonding a substance include carboxyl, hydroxyl, sulfonyl, phosphate and amine groups (Volesky, 2007). Bonding between the sorbent and the solute can result from the weak van der Waals forces and strong interactions between the charged sulfonyl groups of the dye and the sorbent surface represented by the hydroxyl groups, according to the following mechanism (Sateu et al., 2011):

$$\text{Husk - OH} + \text{H}^+ + {}^-\text{O}_3\text{S - Dye} = \text{Husk - OH}_2^+ + {}^-\text{O}_3\text{S - Dye}$$

At first, the sunflower husk used in the experiments was washed and boiled for 2 h in a pressure cooker at 130 °C. Then, for the purpose of enhancing its adsorption capacity the husk was modified by wet etching with 10% H_2SO_4 performed for 6 h at 60 °C. After the chemical treatment, the husk was dried for 2 h at 105 °C. The treatment procedure was developed after previous studies, in which the husk had only been washed. The investigations of sorption kinetics, dynamics and equilibrium were carried out at 25 °C and a pH of 5 to 6.

Direct Orange 26 of standardized purity, molecular formula $C_{33}H_{22}N_6Na_2O_9S_2$ and a molecular mass of 756.67 g/mol was purchased from Boruta-Zachem Kolor company (Poland). The dye is widely used by

the textile industry but also as a colour additive permitted for use in cosmetics and household products by the Minister of Health Regulation of 30 March 2005.

3. SORPTION KINETICS

Determination of sorption kinetics is a fundamental step in the assessment of sorbent usability. For this purpose, changes in concentration of the solute in both the feed solution and the adsorbent are measured as a function of time.

The sorption kinetics and sorption equilibrium experiments were performed simultaneously using the same laboratory setup. 5 g dry weight of the sorbent was added to 200 cm^3 of the feed solution, containing 50 – 800 mg/dm^3 of Direct Orange 26. Afterwards, the flasks were mechanically shaken in a thermostated bath at 25 °C until the adsorption equilibrium was reached. During the process, the concentration of Direct Orange 26 in the aqueous phase was measured using a UV-Vis Jasco V639 spectrophotometer at a wavelength of 494 nm.

The decreasing concentration of Direct Orange 26 in the feed during the adsorption process corresponds to the amount of the dye adsorbed by the husk (Fig. 2), which can be calculated with Eq. (1):

$$q = \frac{V}{m}(C_0 - C) \tag{1}$$

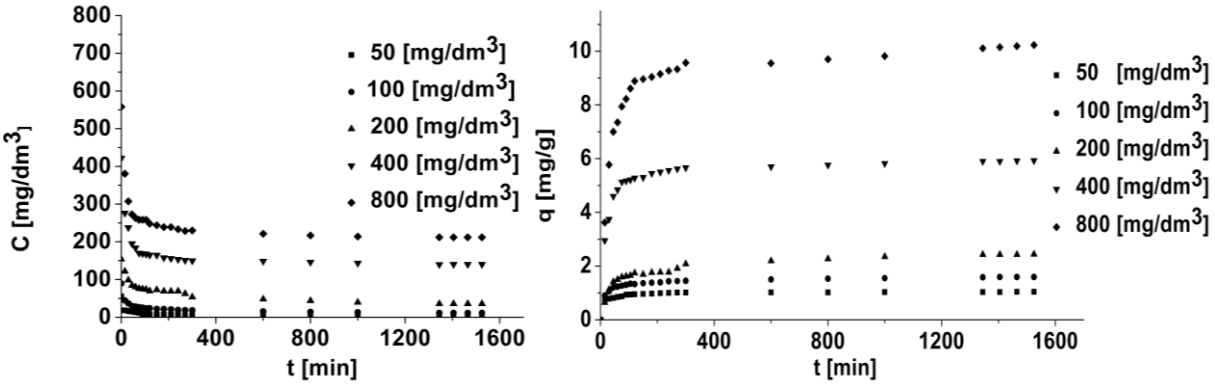

Fig. 2. Experimental data of sorption kinetics for the sunflower husk – Direct Orange 26 system

Chemical reaction kinetics allows to determine the process rate and thereby the pace of the expected concentration changes of the separated substance. The sorption kinetics is most often described using:

- the pseudo-first order Lagergren equation:

$$\frac{dq}{dt} = k_1(q_e - q) \tag{2}$$

- the pseudo-second order Ho and McKay equation:

$$\frac{dq}{dt} = k_2(q_e - q)^2 \tag{3}$$

The models given by Eqs. (2) and (3) are frequently used (Ho and Wang, 2004; Ho, 2006; Sočo and Kalembkiewicz, 2016). When the adsorption mechanism is mainly physical, the kinetics is usually described with Eq. (2), which gives perfect approximation at lower equilibrium concentrations and poor

approximation at higher concentrations. In the latter case, the psuedo-second order model given by Eq. (3) becomes preferable. This model assumes that chemisorption is the prevailing mechanism controlling the process.

Figure 3 compares the kinetic experimental data in the sunflower husk – Direct Orange 26 system at an initial feed concentration of 800 mg/dm^3 with the estimated values calculated using Eqs. (2) and (3). The points on the graph represent the experimental data while the solid lines reflect the approximations obtained with both models. The calculated R^2 values show that the psuedo-second order model provides more accurate results, which suggests that the sorption mechanism is of chemical rather than physical nature.

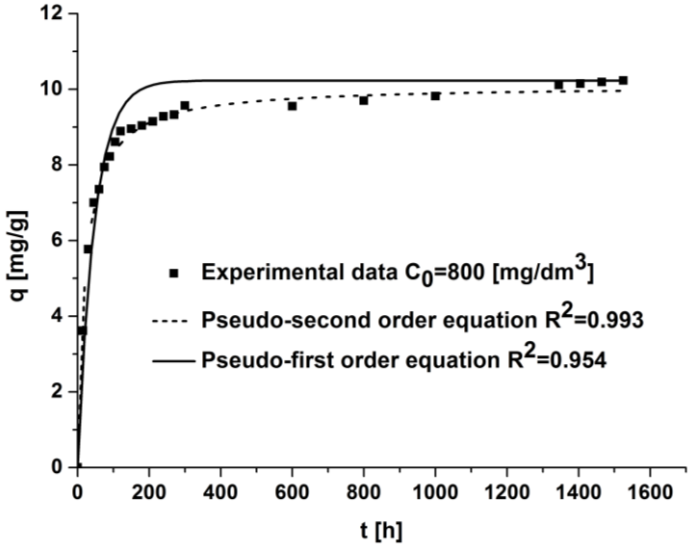

Fig. 3. Mathematical description of sorption kinetics for the sunflower husk – Direct Orange 26 system

4. SORPTION EQUILIBRIUM

Determination of the equilibrium between a sorbent and a solute at constant temperature, termed as a sorption isotherm, is of fundamental significance in sorption studies. The equilibrium is reached when the rate of adsorption is equal to the rate of desorption. As a result, a relation is obtained between the concentration of the separated substance in the sorbent material q_e [mg/g dry weight] and its concentration in the feed solution C_e [mg/dm^3]. The equilibrium study allows recognition of the sorption capacity of a given material. Commonly, the following equations are used with regard to the solid-liquid equilibrium:

- Freundlich equation

$$q_e = K_F C_e^{1/n} \tag{4}$$

- Langmuir equation

$$q_e = \frac{q_m K_L C_e}{1 + K_L C_e} \tag{5}$$

- Redlich-Peterson equation

$$q_e = \frac{q_m K_{RP} C_e}{1 + K_{RP} C_e^n} \tag{6}$$

The approximation results obtained with Eqs. (4) - (6) at C_0 = 800 mg/dm^3 are presented in Fig. 4.

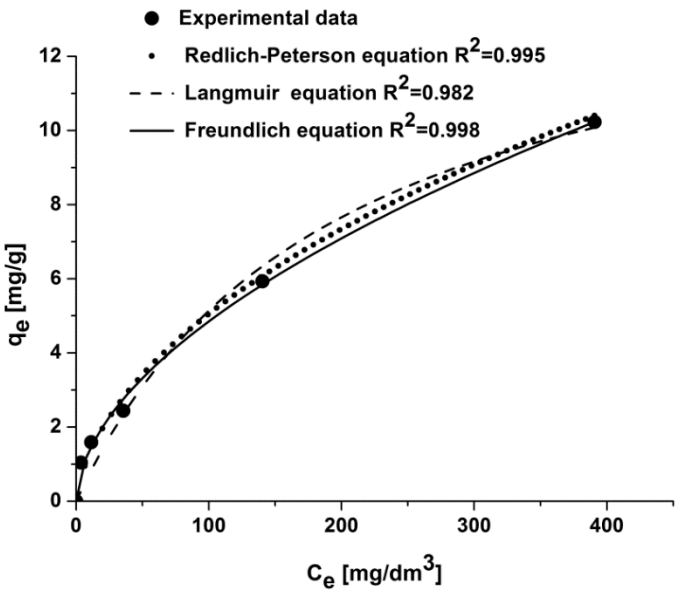

Fig. 4. Mathematical description of sorption equilibrium for the sunflower husk – Direct Orange 26 system

The respective equation parameters were determined with the simplex algorithm using Origin 7 software. In Table 2 values of coefficients for Eqs 4 - 6 are presented. Statistical analysis shows that all three equations give similar results, although the Freundlich isotherm seems to be the most accurate.

Table 2. Values of coefficients for Equations (4) ÷ (6)

Equation	Coefficients
Freuendlich	K_F = 0.389; 1/n= 0.548
Langmuir	K_L = 0.517·10^{-2}; q_m= 15.066
Redlich - Peterson	K_{RP} = 0.487; q_m = 0.682; n = 0.530

5. SORPTION DYNAMICS

Adsorption dynamics studies were performed in a glass column of 3.45·10^{-3} m diameter and 0.70 m length. The column was filled with dry sunflower husk of 453 kg/m^3 density. The feed solution was pumped upwards through the bed using a metering pump and removed from the top of the column. At specified time intervals, samples were taken at the column outlet and analyzed with the UV-Vis Jasco V630 spectrophotometer. The feed temperature and pH were stabilized at 25°C and 5.8, respectively. In order to evaluate the proposed adsorption model, experiments had to be performed varying the process parameters. For this reason, the following quantities were combined: solute concentration of 50 and 75 mg/dm^3, feed flow rate of 50, 100, 200 and 400 cm^3/h, bed height of 0.580, 0.435, 0.290 and 0.145 m corresponding to the mass of sunflower husk equal to 145, 108, 72.5 and 36.25 g, respectively.

Approximations of the experimental results were performed with the Thomas model (Garba et al., 2016; Ghribi and Chlendi, 2011; Kocadagistan and Kocadagistan, 2016; Lambrecht et al. 2015; Mahendra et al., 2015; Mustafa and Ebrahim, 2010; Xu et al., 2013), which does not rely on the internal and external mass transfer resistance and omits the axial dispersion phenomenon:

$$\ln\left(\frac{C_0}{C}-1\right)=\frac{K_T\cdot q\cdot m}{Q}-K_T\cdot C_0\cdot t \qquad (7)$$

For the purpose of finding the equation coefficients, the $\ln((C_0 / C_t) - 1)$ expression values were plotted versus time. Coefficients a and b were determined from the linear approximation of experimental data, while coefficients K_T and q_0 were estimated with the following formulas:

$$K_T = \frac{-a}{C_0} \tag{8}$$

$$q = \frac{b \cdot Q}{K_T \cdot m} \tag{9}$$

The calculated values of the coefficients are given in Table 3. The experimental results were interpreted using the breakthrough curves generated with the Thomas model in accordance with the equation:

$$C = \frac{1}{1 + \exp\left(\frac{K_T \cdot q \cdot m}{Q}\right) - K_T \cdot C_0 \cdot t} \cdot C_0 \tag{10}$$

Table 3. Values of K_T and q_0 calculated for C_0=50mg/dm^3 and 75mg/dm^3 at different feed flow rates

Flow rate	Q = 400, cm^3/h	Q = 200, cm^3/h	Q = 100, cm^3/h	Q = 50, cm^3/h
C_0 = 50 mg/dm^3				
K_T, cm^3/(mg·h)	5.2×10^{-3}	1.8×10^{-3}	1.2×10^{-3}	5.0×10^{-4}
q, mg/g	2.34	2.72	2.54	3.53
C_0 = 75 mg/dm^3				
K_T, cm^3/(mg·h)	5.2×10^{-3}	1.1×10^{-3}	1.0×10^{-3}	2.3×10^{-4}
q, mg/g	2.04	4.61	3.34	6.47

6. COLUMN ADSORPTION RESULTS

Figure 5 presents changes in the dye concentration at outlet of column versus time, recorded at different feed flow rates, i.e. Q = 400 cm^3/h, Q = 200 cm^3/h, Q = 100 cm^3/h and Q = 50 cm^3/h, different initial concentrations, i.e. C_0 = 50 mg/dm^3 and C_0 = 75 mg/dm^3, and an adsorbent bed height of 0.58 m.

Analysis of the graphs allowed determination of breakthrough and saturation time (for the dye concentrations equal to $0.05C_0$ and $0.95C_0$). The results are summarized in Table 4.

The breakthrough time and the saturation time are influenced by such process parameters as the adsorbent bed height, feed flow rate and initial dye concentration in the influent stream. Both the breakthrough time and the saturation time increase with decreasing flow rate, decreasing dye concentration and increasing bed height.

Figure 6 illustrates the changes in the outlet composition against time at Q = 50 cm^3/h measured for four different bed heights. Figure 7 shows the changes in outlet composition against time measured at constant bed height of 0.58 m and constant C_0 = 50 mg/dm^3 for four different feed flow rates. The points on the graphs correspond to the experimental values while the solid lines were generated with the Thomas model.

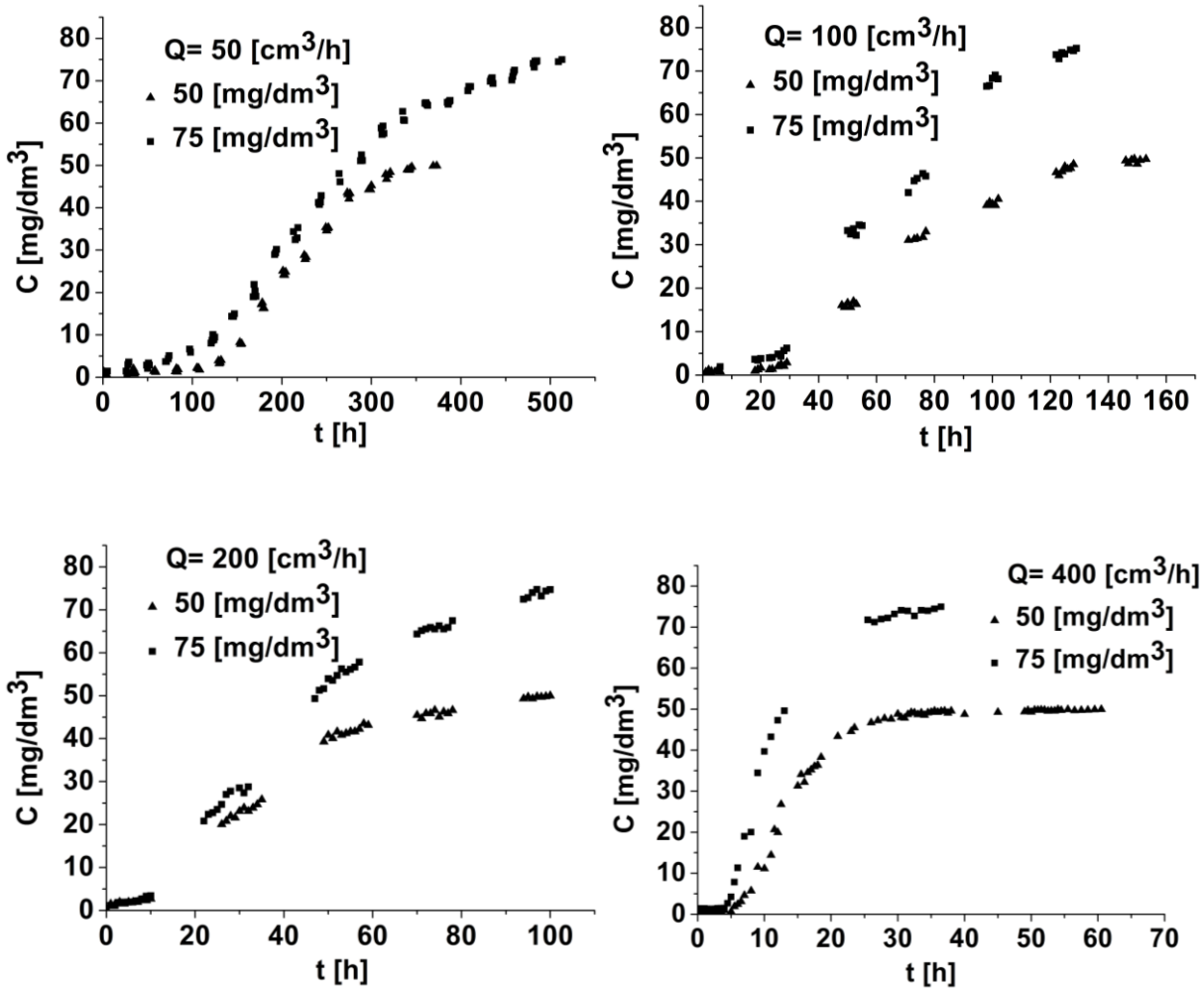

Fig. 5. The breakthrough curves - changes in the dye concentration versus time at Q = 50cm^3/h, Q = 100cm^3/h, Q = 200 cm^3/h and Q = 400 cm^3/h

Table 4. Breakthrough time and saturation time at different feed flow rates

Feed flow rate at C_0 = 50 mg/dm^3	Breakthrough time $0.05C_0$ = 2.5 mg/dm^3	Saturation time $0.95C_0$ = 47.5 mg/dm^3
Q, cm^3/h	t_B, h	t_S, h
400	6	27.5
200	9.5	80
100	27	126
50	118	310
Feed flow rate at C_0 = 75 mg/dm^3	Breakthrough time $0.05C_0$ = 3.75mg/dm^3	Saturation time $0.95C_0$ = 71.25 mg/dm^3
Q, cm^3/h	t_B, h	t_S, h
400	4.5	26.5
200	12	90
100	20	120
50	71	458

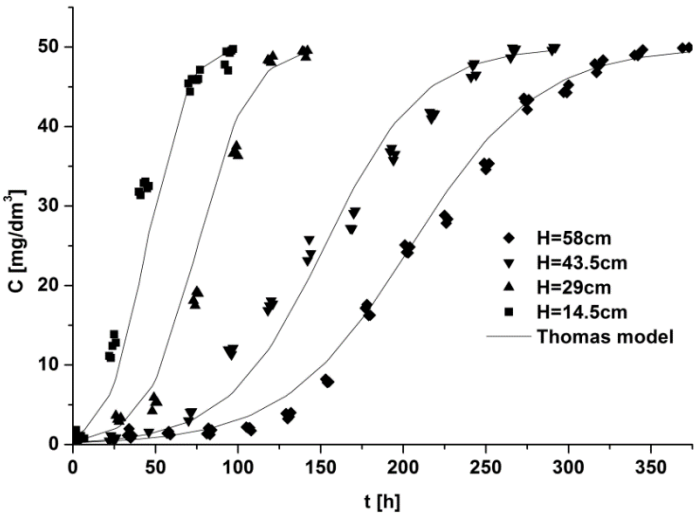

Fig. 6. The breakthrough curves - changes in the outlet dye concentration versus time at different bed heights

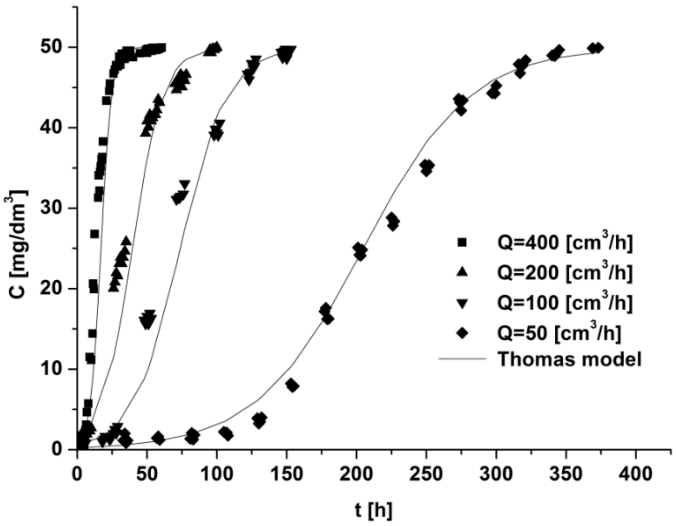

Fig. 7. The breakthrough curves - changes in the outlet dye concentration versus time at different feed flow rates

Figures 6 and 7 indicate that the Thomas model can successfully be used to estimate dye concentration at the column outlet. However, in order to characterize sorption dynamics in the adsorption column, a column mass balance is necessary, in its simple or modified form, as suggested elsewhere (Babu and Gupta, 2005; Chen et al., 2003; Tomczak, 2013).

7. SUMMARY

The paper analyzes sorption kinetics, dynamics and equilibrium in the laboratory adsorption column employed to remove Direct Orange 26 from aqueous media. To separate the dye, modified sunflower husk was used due to its availability and inexpensiveness. The aim of modification was to enhance the adsorption capacity of the husk.

In summary, sunflower husk is a useful sorption material, which can be utilized for textile wastewater treatment. A sorption capacity of 11 mg/g dry weight was achieved when the initial dye concentration in the feed was equal to 800 mg/dm^3.

The adsorption kinetics was successfully modeled using the pseudo-first order Lagergren and the pseudo-second order Ho and McKay formulas. However, better results were obtained with the latter equation, which suggests a chemisorption mechanism.

For the purpose of characterizing the sorption equilibrium, the two-parameter Freundlich and Langmuir equations as well as the three-parameter Redlich-Peterson equation were proposed. In every case, experimental data were satisfactorily approximated, which was confirmed by statistical analysis.

The obtained breakthrough curves were further used to model the results with the Thomas equation. The performance of the adsorption column turned out to be a function of the investigated process parameters. When the bed height was constant, lowering the dye concentration and the feed flow rate resulted in longer breakthrough and saturation times.

SYMBOLS

C	dye concentration in the feed, mg/dm^3
C_0	initial dye concentration in the feed, mg/dm^3
C_e	equilibrium solute concentration in the solution, mg/dm^3
k_1	kinetic constant, 1/s
k_2	kinetic constant, g/(mg min)
K_F	Freundlich constant, mg$^{1-1/n}$ dm$^{3(1/n)}$/g
$1/n$	Freundlich constant
K_L	Langmuir constant, dm^3/mg
K_{RP}	Redlich-Peterson constant, (dm^3/mg)^n
K_T	coefficient in Eq. (7), cm^3/(mg·h)
m	mass of the adsorbent, g
n	Redlich-Peterson constant
q	amount of the dye adsorbed in the adsorbent, mg/g
q_e	equilibrium amount of the dye adsorbed per unit mass of the adsorbent, mg/g
q_e	equilibrium solute concentration in the adsorbent bed, mg/g
q_m	sorption capacity, mg/g
t_B	breakthrough time, h
t_S	saturation time, h
V	solution volume, dm^3

REFERENCES

Allen S.J., Koumanova B., 2003. Decolourisation of water/wastewater using adsorption. *J. Univ. Chem. Technol. Metallurgy*. 40, 175–192.

Avdicevic M.Z., Kosutic K., Dobrovic S. 2017. Effect of operating conditions on the performances of multichannel ceramic UF membranes for textile mercerization wastewater treatment. *Environ. Technol.*, 38, 65-77. DOI: 10.1080/09593330.2016.1186225.

Babu B.V., Gupta S., 2005. Modelling and simulation of fixed bed adsorption column: effect of velocity variation. *J. Eng. Techn*., 1, 60-66. DOI: 10.1016/30923-4748(05)00044-05.

Borges G.A., Silva L.P., Penido J.A., de Lemos L.R., Mageste A.B., Rodrigues G.D. 2016. A method for dye extraction using an aqueous two-phase system: Effect of co-occurrence of contaminants in textile industry wastewater. *J. Environ. Manage*., 183, 196-203. DOI: 10.1016/*j*.jenvman.2016.08.056.

Chen J.P., Yoon J.T., Yiadoumi S., 2003. Effects of chemical and physical properties of influence on copper sorption onto activated carbon fixe-bed columns. *Carbon*, 41, 1635-1644. DOI: 10.1016/S0008-6223(03)00117-9.

Crini G., 2006. Non-conventional low-cost adsorbents for dye removal: a review. *Bioresour. Technol.* 97, 1061-85. DOI: 10.1016/j.biortech.2005.05.001.

Gala A., Sanak-Rydlewska S., 2010. Sorpcja jonów metali toksycznych z roztworów wodnych na odpadach naturalnych – przegląd literaturowy. *Górnictwo i Geoinżynieria*, 4(1), 49-59.

Garba A., Nasri N.S., Basri H., Ismail R., Majid Z.A., Hamza U.D., Mohammed J., 2016, Adsorptive removal of phenol from aqueous solution on a modified palm shell-based carbon: fixed-bed adsorption studies. *Desalin. Wat. Treat*., 57, 29488-29499. DOI: 10.1080/19443994.2016.1184187.

Ghribi A., Chlendi M., 2011. Modeling of fixed bed adsorption: Application to the adsorption of an organic dye. *Asian J. Textile*, 1, 161-171. DOI: 10.3923/ajt.2011.161.171.

Hameed B.H., Ahmad A.A., 2009. Batch adsorption of methylene blue from aqueous solution by garlic peel, an agricultural waste biomass. *J. Hazard. Mat*., 164, 870-875. DOI: 10.1016/j.jhazmat.2008.08.084.

Ho Y.S., 2006. Second-order kinetic model for the sorption of cadmium onto tree fern: A comparison of linear and non-linear methods. *Wat. Res.*, 40, 119-125. DOI:10.1016/j.watres.2005.10.040.

Ho Y.S., Wang C.C., 2004. Pseudo-isotherms for the sorption of cadmium ion onto tree fern. *Proc. Biochem.*, 39, 761-765. DOI:10.1016/S0032-9592(03)00184-5.

Jain M., Garga V.K., Kadirvelub K., 2009. Chromium(VI) removal from aqueous system using Helianthus annuus (sunflower) stem waste. *J. Haz. Mat*., 162(1), 365-372. DOI: 10.1016/j.jhazmat.2008.05.048.

Lambrecht R., Barros M.A.S.D., Arroyo P.A., Borba C.E., Silva E. A., 2015. Adsorption of the dye reactive blue 5g in retorted shale. *Braz. J. Chem. Eng*. 32, 269 - 281. DOI: 10.1590/0104-6632.20150321s00001715.

Leja K., Lewandowicz G., Grejek W., 2009. Produkcja bioetanolu z surowców celulozowych. *Biotechnologia*, 4(87), 88-101.

Kocadagistan B., Kocadagistan E., 2016. Batch and column removal of the dye blue 3R over pumice. *Desalin. Wat. Treat.*, 57, 28042-28055. DOI: 10.1080/19443994.2016.1184186.

Kotrba P., Mackova M., Urbánek V. (Eds.), 2011. *Microbial biosorption of metals*. Springer Science+Business Media B.V. DOI: 10.1007/978-94-007-0443-5.

Mahendra Ch., Anand Babu, Satyasai P.M., K.K. Rajan. 2015. Application of the Thomas model for cesium ion exchange on AMP-PAN, In: Shirish Sonawan, Y. Pyde Setty, Srinu Nayak S. (Eds.), *Chemical and Bioprocess Engineering: Trends and Developments*. Chapter: 18. CRC press - A Taylor and Francis Group. DOI: 10.13140/2.1.3833.8561.

Mustafa Y.A., Ebrahim S.E., 2010. Utilization of Thomas model to predict the breakthrough curves for adsorption and ion exchange, *J. Eng.*, 4(16), 6206-6223.

Muthamilselvi P., Karthikeyan R., Kumar B.S.M. 2016. Adsorption of phenol onto garlic peel: Optimization, kinetics, isotherm, and thermodynamic studies. *Desalin. Water Treat*., 57, 2089–2103. DOI: 10.1080/19443994.2014.979237.

Nassar M.M., El-Geundi M.S. 1991. Comparative cost of colour removal from textile effluents using natural adsorbents. *J. Chem. Technol. Biotechnol.*, 50(2), 257-264. DOI: 10.1002/jctb.280500210.

Oguntimein G.B., Duwane T., 2014. The potential use of acid treated dried sunflower seed hull as a biosorbent for the removal of textile effluent dye from aqueous solution. *Res. Inventy: Int. J. Eng. Sci.*, 4(7), 21-30.

Oguntimein G.B. 2016. Textile dye removal using dried sun flower seed hull a new low cost biosorbent: equilibrium, kinetics and thermodynamic studies. *Adv. Res. Text Eng*., 1(1), 1008-1014.

Osma J.F., Saravia V., Toca-Herrera J.L., Rodriguez Couto S., 2007. Sunflower seed shells: A novel and effective low-cost adsorbent for the removal of the diazo dye Reactive Black 5 from aqueous solutions. *J. Haz. Mat*., 147, 900-905. DOI: 10.1016/j.jhazmat.2007.01.112.

Piyo N., 2014. Liquefaction of sunflower husks for biochar production, Master degree dissertation, North-West University, South Africa.

Priya R., Nithya R., Anuradha R., Kamachi T., 2014. Removal of colour from crystal violet dye using low cost adsorbents. *Int. J. Chem. Tech. Res*., 6(9), 4346-4351.

Sateu D., Malutan T., Bilba D., 2011. Agricultural waste corn cob as a sorbent for removing reactive dye Orange 16: Equilibrium and kinetic study. *Cellulose Chem. Technol.*, 45(5-6), 413-420.

Sočo E., Kalembkiewicz J., 2016. Comparison of adsorption of Cd(II) and Pb(II) ions on pure and chemically modified fly ashes. *Chem. Proc. Eng*., 37(2), 215-234. DOI: 10.1515/cpe-2016-0018.

Soldatkina L. M. , Sagaidak E. V., Menchuk V. V., 2009. Adsorption of cationic dyes from aqueous solutions on sunflower husk. *J. Wat. Chem. Technol.,* 31, 238-243. DOI: 10.3103/S1063455X09040055.

Srinivasan A., Viraraghavan T., 2010. Oil removal from water using biomaterials. *Biores. Technol*., 101, 6594–6600. DOI: 10.1016/j.biortech.2010.03.079.

Sud D., Mahajan G., Kaur M.P., 2008. Agricultural waste material as potential adsorbent for sequestering heavy metal ions from aqueous solutions - A review. *Biores. Technol*., 99, 6017-6027. DOI: 10.1016/j.biortech.2007.11.064.

Tomczak E., 2013. Water purification from heavy metal ions in a packed column. *Sep. Sci. Technol*., 48, 2270-2276. DOI: 10.1080/01496395.2013.805224.

Tomczak E., Kamiński W., Tosik P., 2015. Adsorption dynamics studies of azo dyes removal by biosorbent. *Desalin. Wat. Treat.* 55, 2669–2674. DOI: 10.1080/19443994.2014.939490.

Tomczak E., Tosik P., 2014, Sorption equilibrium of azo dyes Direct Orange 26 and Reactive Blue 81 onto a cheap plant sorbent. *Ecol. Chem. Eng S*, 21, 435-445. DOI: 10.2478/eces-2014-0032.

Volesky B., 2007. Biosorption and me. *Wat. Res.*, 41, 4017-4029. DOI: 10.1016/j.watres.2007.05.062.

Witek-Krowiak A., 2012. Analysis of temperature-dependent biosorption of Cu^{2+} ions on sunflower hulls: Kinetics, equilibrium and mechanism of the process. *Chem. Eng. J*., 192, 13-20. DOI: 10.1016/j.cej.2012.03.075.

Xu Zhe, Cai Jian-guo, Pan Bing-cai. 2013. Mathematically modeling fixed-bed adsorption in aqueous systems. *Appl. Phys. Eng*., 14(3), 155-176. DOI: 10.1631/jzus.A1300029.

Yasmen A.M., Shahlaa E.E., 2010. Utilization of Thomas model to predict the breakthrough curves for adsorption and ion exchange. *J. Eng*., 16(4), 6206-6223.

Received 11 January 2017
Received in revised form 24 March 2017
Accepted 20 April 2017

www.czasopisma.pan.pl www.journals.pan.pl
Chemical and Process Engineering 2017, 38 (2), 295-306
DOI: 10.1515/cpe-2017-0023

THE EFFECT OF DISACCHARIDE CONCENTRATION IN A LIQUID BINDER ON THE MECHANISMS AND KINETICS OF DISC GRANULATION

Andrzej Obraniak[1], Tadeusz Gluba[2*]

[1]Lodz University of Technology, Faculty of Process and Environmental Engineering, Wolczanska 213, 90-924 Lodz

[2]Lodz University of Technology, Faculty of Biotechnology and Food Sciences, Wolczanska 173, 90-924 Lodz

Analysis of granulation kinetics was carried out using a laboratory disc granulator with a diameter *D* of 0.5 m. A liquid binder was delivered to the tumbling bed at a constant flow rate with a nozzle generating droplets with a size of approx. 4-5 mm. Fine-grained chalk was used as a model of raw material and water or disaccharide solution with concentrations of 20 – 40% as a wetting liquid. Different times of droplet delivery ranging from 2 to 6 min were utilized. Granulometric composition of the bed for selected lengths of process, bed moisture and the moisture of individual size-fractions were assessed. Mass of granulated material, which was transferred from nuclei fraction to other size fractions was determined on the basis of mass balance analysis and the assessment of liquid migration between fractions. The influence of disaccharide concentration in wetting liquid on the aforementioned phenomena was also examined.

Keywords: disc granulation, kinetics, disaccharide solution

1. INTRODUCTION

Kinetics of tumble granulation depends mainly on the prevailing mechanisms of granule formation occurring during the process. Newitt and Conway-Jones (1958) and Capes and Danckwerts (1965) analysed this process and identified the following mechanisms of granulation: wetting and nucleation, layering, coalescence, consolidation as well as crushing and abrasion. The authors assumed that these mechanisms may occur independently or jointly at a given stage of the process. The use of wetting liquid in a process was a common feature of the analysed studies. The type of capillary interactions between liquid and bulk material depends on: the ratio of liquid volume and intergranular volume. Newitt-Jones and Conway (1973) identified several states of a liquid-solid material system: pendular, funicular, capillary and droplets - on the basis of liquid content.

Nucleation, during which the delivered binding liquid wets powder forming initial aggregates (nuclei) is the first step of granulation. Previous analyses of this step focused mostly on two aspects: the wettability of a solid body by a liquid binder and the conditions of liquid phase distribution in powder material. Jaiyeoba and Spring (1980) performed the aforementioned analysis of a mixture of three powders. Gluba et al. (1990) examined the influence of conditions of selected powder material wetting on the parameters of particle size distribution of granules formed during the process of wet drum granulation. The parameters of granulometric composition of products obtained from particular materials were linked with their wettability expressed as so-called aspiration potential. Vonk (1997)

*Corresponding authors, e-mail: tadeusz.gluba.@p.lodz.pl

showed that nucleation mechanism is influenced by the quotient of droplet size and basic dimensions of powder particles. Schaefer and Mathiesen (1996) proposed two different mechanisms of nucleation, depending on the relative size of droplets and raw material particles: distribution mechanism and immersion mechanism. The aforementioned mechanisms describing granulation process have been extended to wet granulation in high-speed mixers by Scott et al. (2000). Analysis of the influence of wetting liquid properties on the granulation process shows also the impact of viscosity on nucleation kinetics. Viscous binders, despite being difficult to distribute, may modify the mechanisms of nucleation (Hoornaert et al., 1998), which in many cases improves process conditions. Schaafsma (1998) demonstrated the association between nuclei formation with the degree of bed saturation and wetting time. A similar description of nucleation mechanism was suggested by Butensky and Hyman (1971). Le et al. (2011) have investigated the granulation mechanisms on a microscopic, single granule scale, and their effect on the uniformity of granule structure, binder content, porosity, dissolution rate and granule strength. Apart from mechanisms responsible for the increase of granule size during granulation processes, also destructive processes characteristic of grinding processes, e.g. in ball mills (Olejnik, 2013) or in pearl mills (Heim and Solecki, 2000) take place.

Pearson (1998) and Ramaker (1998) carried out analysis of granulation process with the use of coloured liquid for a more detailed examination of disintegration mechanism. Similar experiments were performed by Obraniak and Gluba (2012) and Obraniak (2017) who analysed changes in absorbance of individual fractions of granulated bed. Litster and Ennis (2004) introduced the criteria of granule disintegration on the basis of Stokes deformation number.

Ramachandran et al. (2009) presented a dynamic model for granulation process, employing a three-dimensional population balance framework. They obtained a good agreement between experimental and simulation results for the granule size distribution under different operating conditions.

Previous analyses have shown that the conditions of wetting liquid delivery influence nucleation and in consequence the effect of granulation. Litster et al. (2001) defined an equipment independent parameter, dimensionless spray flux, to characterise the most important process parameters in the nucleation process: solution flow rate, powder flux, and binder drop size. Iveson et al. (2001) critically evaluated the understanding of the three key areas of wet granulation processes: wetting and nucleation, consolidation and growth, and breakage and attrition. Hapgood et al. (2003) proposed a nucleation regime map which demonstrated the interaction between drop penetration time and spray flux in nucleation. The nucleation regime map provides a rational basis for design and scale-up of nucleation and wetting in wet granulation. Hapgood et al. (2002) studied the kinetics of drop penetration by filming single drops of several different fluids as they penetrated into loosely packed beds of glass ballotini, lactose, zinc oxide and titanium dioxide powders. A new two-phase model was proposed where the total volume of macrovoids was assumed to be the difference between the bed porosity and the tap porosity. Abberger et al. (2002) used the ratio of droplet size/particle size to determine whether the mechanism of nucleation was distribution or immersion. Distribution was promoted by a low ratio, whereas immersion was promoted by a high ratio. Charles-Williams et al. (2011) carried out single drop penetration experiments into static dry and pre-wetted powder beds. They have discovered that, on porous surfaces, the infiltration rate has a greater degree of dependence, to that of spreading, on changes in viscosity. Hapgood et al. (2004) determined nuclei distribution by the dimensionless spray flux and found that the fraction of drop controlled nuclei could be calculated analytically in advance. Nguyen et al. (2009) conducted single drop nucleation experiments using a syringe and small powder bed on varying ratios of salicylic acid and lactose powders to study the kinetics of drop penetration. They stated that the drop penetration time increased as the proportion of hydrophobic component increased in the powder mixture. Smirani-Khayati et al. (2009) used a new binder liquid distribution coefficient to characterise binder liquid distribution. They discussed the relationships between binder liquid distribution coefficient and granule size distribution. Wauters et al. (2002b) examined the

influence of the nozzle pressure and the distance from the nozzle to the powder bed on the growth behaviour of granules as well as on the binder distribution.

Knight (1983) in his experiments added wetting liquid to calcium carbonate powder in a high shear mixer in three different ways. The method of binder delivery affected both the initial distribution of nucleus sizes and the subsequent growth of granules. Similar experiments with the same materials and devices were performed by Scott (2000). Schaefer and Mathiesen (1996) confirmed that the increase in binder particle size was associated with the increase in initial size of nuclei and with the subsequent growth rate of granules. The uniformity of binder distribution deteriorates with an increase in its viscosity, which results in a broad or even bimodal distribution of granule size. Wauters et al. (2002) studied the growth in drum granulation of particles which were pre-wetted by kneading in a plastic bag. Pre-wetting and uniform distribution of a binder in powder allowed to obtain a narrow distribution of agglomerate sizes. Also, the correlation between droplet size and the distribution of nucleus sizes in fluid bed granulators was demonstrated. According to Waldie (1991) one droplet usually tends to form one nucleus, and the size of formed granule is larger than droplet size. The intensity of liquid binder delivery is one of the most widely studied variable parameters influencing binder distribution. Rankell (1964) proved that the initial rate of nucleation increased along with increasing intensity of wetting.

Despite a wide range of studies on the mechanisms of granulation and the impact of liquid binder properties on the process, still there is no universal model concerning the discussed issues. These studies usually concern specific systems: liquid – raw powder material and are limited by the scope of used apparatus – process parameters. Moreover, there are no models which allow not only for qualitative analysis but also for a quantitative estimation of the prevalence of individual granulation mechanisms. An important utilitarian issue related with the obtaining of durable granules which would meet the requirement of clients is the selection of appropriate binding liquid used in the granulation process. In case of many fine-grained materials (e.g. limestone, dolomite and chalk powder) the use of water as binding liquid does not allow to obtain products with desired strength properties. For that reason, it is necessary to use other binders e.g. aqueous solutions of sugars, which increases the cost of granulate production. Therefore, the optimisation of disaccharide content in binding liquid is necessary.

This paper suggests a model that enables quantitative analysis of agglomeration mechanisms and determines the influence of disaccharide content in liquid binder on the kinetics of disc granulation of chalk.

2. PURPOSE OF THE STUDY

The aim of the study was to:

- determine the effect of disaccharide concentration in the liquid binder on granulation mechanisms and the kinetics of disc granulation,
- develop and validate methods for the quantitative assessment of nucleation and granule build-up mechanisms in disc granulation process with the method of liquid mass balance analysis in individual fractions of a semi-product,
- determine the effect of wetting liquid parameters on the size of nuclei formed during granulation,
- analyse conditions of bed moistening with monodisperse drops of liquid binder in respect to the distribution of formed nuclei size and grain composition in granulate.

3. APPARATUS AND SCOPE OF THE STUDY

Studies were carried out in a disc granulator schematically shown in Fig. 1.

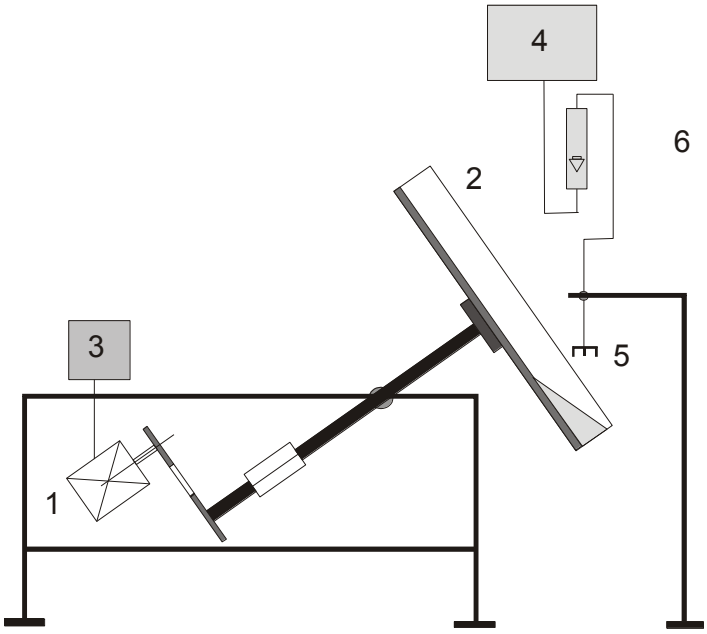

Fig. 1. The scheme of laboratory stand – disc granulator with liquid binder dosing system;
1 – electric engine, 2 – granulating disc, 3 – inverter, 4 – tank, 5 – hydraulic sprinkler, 6 – rotameter

A plate of disc granulator (2) with a diameter D = 0.5 m, and band height h = 0.08 m, mounted on a shaft connected with an electric motor (1) via belt transmission was the main part of the laboratory stand. Disc rotational speed was changed with an inverter (3). Liquid binder was delivered to a bed circulating at the plate from a reservoir (4) mounted at a height of 2.5 m through a hydraulic sprinkler (5) which provided the outflow of liquid in the form of droplets. Constant liquid pressure during the analysis was maintained by the control of its stable level in a tank.

Chalk produced by Lhoist Bukowa lime plant, with a grain size of less than 0.2 mm was used as a model material in granulation analysis. Water and aqueous solutions of disaccharide (food sugar) at a concentration of 20%, 25%, 30%, 35%, 40% were used as liquid binders.

4. METHODOLOGY AND THE SCOPE OF STUDY

Granulated bed was wetted during tumbling with water or five aqueous solutions with different concentrations of sugar. The granulation process was carried out at the time of bed wetting. The duration of each test was equal to the wetting time. After a specified time of liquid binder delivery (2, 3, 4, 5 or 6 minutes) granulometric composition of the formed bed was analysed. This method of conducting experiments allowed to compare granulation effects in subsequent tests. These comparisons concerned the course of the process, the type of bed movement, and the resulting effects for the same granulation times.

Basic apparatus and process parameters including the mass of raw material, mass flow rate of wetting liquid delivery and rotational speed of the plate were determined during preliminary analysis. The angle of plate axis inclination from the horizontal axis was set to be $\alpha = 45°$ and the rotational speed of the plate was n = 14 min^{-1}. The optimum mass of fine raw material placed on a plate was m_s = 1500 g for this setting. Mass flow rate of liquid binder delivery q = 22.5 g/min was applied, which allowed to obtain the outflow of each solution concentration from the nozzles in form of droplets. The liquid was delivered to the bed in such a way that droplets always fell on a dry material to eliminate the phenomenon of solid particle coalescence. Bed circulating in the granulator was moistened with drops of 4 – 5 mm. Droplets of such size were obtained with the gravitational liquid delivery method through

a uniform atomiser. The purpose of the method of wetting was to obtain a monodisperse fraction of granulated nuclei whose size would be closely related to the constant diameter of droplets. The size of droplets that initiated the granulation was determined on the basis of volume of a certain number of liquid droplets delivered to the measuring cylinder, assuming that their shape is spherical.

The product obtained was subjected to particle size analysis performed with a set of sieves with mesh sizes: 1.0 – 12.5 mm. Each of the obtained size fractions was weighed on a laboratory scale and then dried at 100 °C for 24 h. After drying, each fraction was re-weighed in order to determine its moisture and the mass of water accumulated in it.

5. MODEL

The assumptions used during the formulation of the model are associated with droplet manner of bed wetting and the site of liquid delivery to the bed. It was assumed that:

1. Droplets of sizes between 4 and 5 mm after falling on the dry powder material form nuclei in which the whole delivered liquid is accumulated.
2. Liquid droplets always fall on a non-granulated raw material thus eliminating the phenomenon of solid particle coalescence.
3. The migration of liquid binder to other size fractions occurs only as a result of transfer of abraded or crumbled pieces of wet material nuclei.
4. Moisture of abraded and crushed fragments of nuclei is the same as the moisture of nuclei.
5. The transfer of wet loose material to other size fractions and the accompanying migration of liquid are the result of the following granulation mechanisms:
   a) abrasion of nuclei - migration to smaller factions,
   b) crushing of nuclei - migration to smaller factions,
   c) layering of nuclei - migration to larger factions.

The following process parameters and parameters measured after the end of wetting were assumed to be known:

- Liquid concentration - c
- Mass of each wet and dry material size fraction "j" for particular times of wetting t_i : $m_j(t_i)$, $M_j(t_j)$
- Mass of water contained in each fraction "j", moisture of "j" fraction in time t_i: $M^W_j(t_i)$, $w_j(t_i)$

Ad a) The mass of dry material transferred from nuclei fraction to 0 – 1 mm size fraction as a result of abrasion can be calculated from Eq. (1) after transforming the formula defining moisture content in the abrades:

$$M_{0-1}^{abr}(t_i) = \frac{M_{0-1}^{w}(t_i)}{w_{nucl}(t_i)} \tag{1}$$

Dry mass of the abraded material calculated using Eq. (1) contains the mass of transferred bulk material and the mass of sugar contained in a liquid accumulated in (0 - 1) size fraction. Sugar mass can be computed from Eq. (2).

$$M_{0-1}^{sug.}(t_i) = \frac{c \cdot M_{0-1}^{w}(t_i)}{1-c} \tag{2}$$

Ad b) Mass of material transferred as a result of crushing from nuclei fraction to any other „j" fraction in the range of 1 – 4 mm is calculated using Eq. (3) and sugar mass is computed in the same manner from Eq. (2).

$$M_j^c(t_i) = \frac{M_j^w(t_i)}{w_{nucl}(t_i)} \tag{3}$$

Ad c) Mass transferred from nucleus fraction to granule fraction:

Mass of granule fraction determined on the basis of sieve analysis contains the mass of nuclei which after the attachment of bulk or abraded material increased their diameter as a result of layering. If the aforementioned increase in dimensions is due to the adherence of wet material from previously abraded nuclei, then the moisture of granule fraction will be approximately the same as the moisture of nuclei. If the moisture of formed granules is lower than that of nuclei it means that dry raw material was additionally attached to granules. The mass of nucleus fraction $M^o_{g.nucl}$, which after t_i time co-forms granule fraction was calculated from Eq. (4).

$$M^o_{g.nucl.}(t_i) = \frac{M_g^w(t_i)}{w_{nucl}(t_i)} \tag{4}$$

6. EXPERIMENTAL RESULTS

On the basis of the obtained results, associations reflecting changes in granulometric composition of processed bed after a specified time of wetting have been prepared. The results of a sieve analysis demonstrate the dominant portion of 6.3 – 8 mm size fraction and adjacent fractions in the formed granulate in case of all times of wetting. It is directly associated with bed wetting manner and the size of sprayed droplets of liquid (4 – 5 mm). Such a delivery of liquid to bulk material promotes, in the presented range of parameters and in case of a given material, the formation of granulation nuclei which produce 6 – 8 mm agglomerates (larger than the size of delivered droplets). This trend is consistent with the results of other studies (Schaafsma et al., 1998; Waldie, 1991).

Figures 2, 3, 5 present a comparison of mass content of individual size fractions obtained using different process parameters. The analysis of the obtained results reveals a relatively small content of 1 – 4 mm fraction which, taking into account the wetting method, does not constitute the nucleus fraction with smallest sizes.

Observations of droplet wetting phenomenon both during granulation and preliminary analysis ruled out the possibility that droplets broke into smaller pieces while falling from the height of a mounted nozzle tip and resulting in formation of nuclei of smaller diameters. These fractions are formed as a result of nucleus crushing. There is also the possibility that the raw material adheres to wet, crumbled part of nuclei. Also, the mass content of a 10 – 12.5 mm fraction is small, which can be explained by a hindered build-up of surface dry agglomerates and the lack of conditions to coalesce. This fraction, and probably also a part of 8 - 10 mm fraction composes of granules formed from nuclei which attached material from 0 – 1 mm size fraction through layering and thus enlarging their dimensions.

Figure 4 presents sample change of the mass of water accumulated in individual size fractions between various wetting times. The comparison of results which is shown in Figs. 3, 4 and 5 allows for a more comprehensive analysis of the impact of various granulation mechanisms on granulometric composition of obtained granules. Similar distribution and the nature of changes in bed properties can be observed in case of various wetting times.

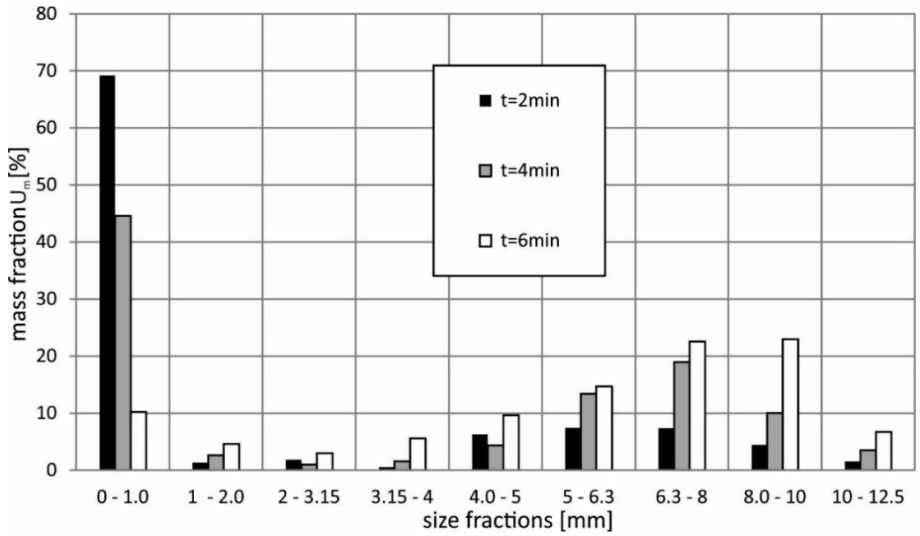

Fig. 2. The comparison of mass content of granulated bed between three various times of wetting (the concentration of wetting liquid c = 25%)

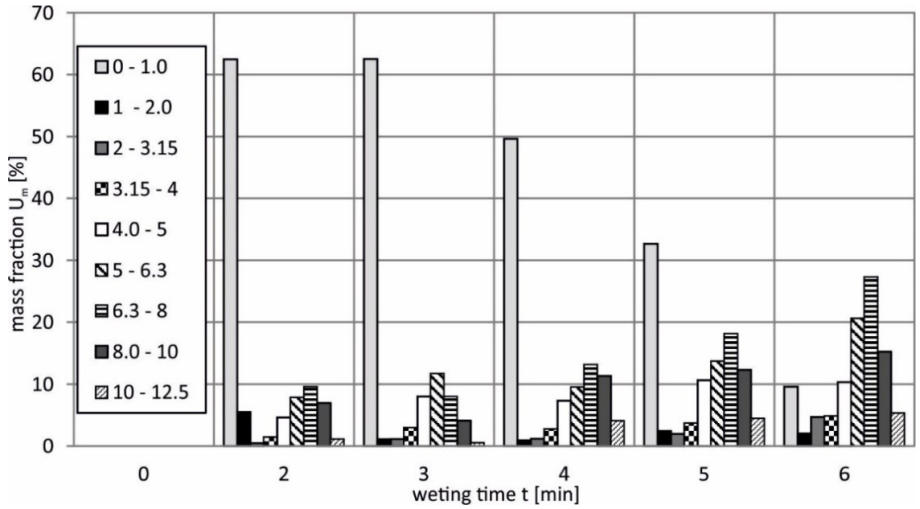

Fig. 3. Sample change in mass content of granulated bed during the process of wetting with liquid with a concentration c = 40%

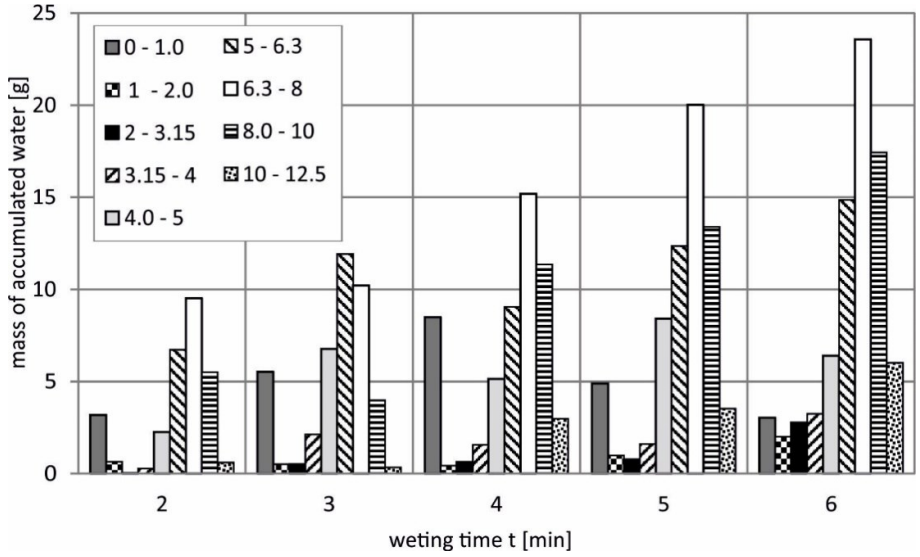

Fig. 4. Sample change in the mass of water accumulated in particular fractions of granulated bed during the process of wetting with liquid with a concentration c = 40%

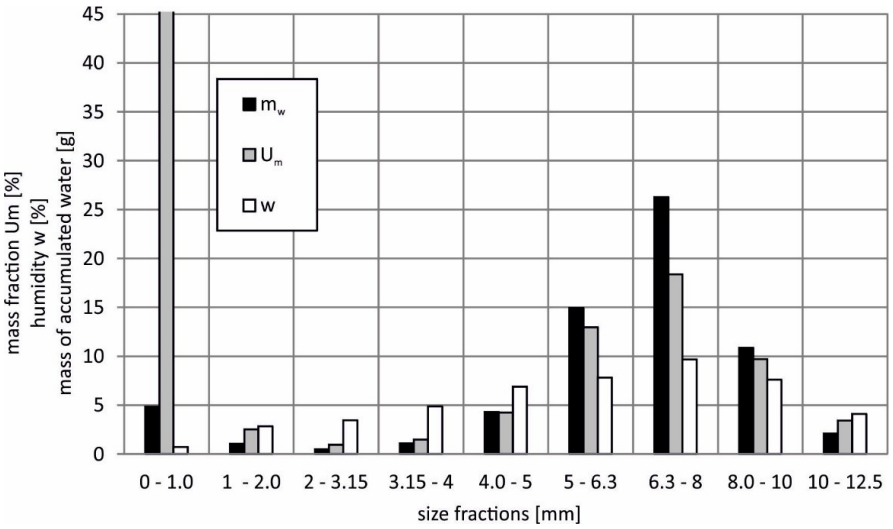

Fig. 5. The comparison of sample changes in mass content, moisture, and the mass of accumulated water in individual fractions of granulated bed during the process of wetting with liquid with the concentration $c = 25\%$, ($t = 4$ min)

The analysis of graphs confirms the assumptions made during model preparation and leads to the conclusion that changes in water mass in individual size fractions as well as changes in moisture of these fractions can be indicators for a qualitative and quantitative evaluation of granulation mechanisms responsible for the transfer of material mass between various factions of formed granulate. The obtained results allow for the assessment of the nature of changes in the content of fractions, nuclei and granules, and also for the comparison of the range of two disintegration phenomena, i.e. crushing and abrasion.

On the basis of the obtained results, it can be concluded that the extent of abrasion of the wet material from the surface of nuclei and granules may be smaller than the extent of their crushing. This suggestion is confirmed by a higher total mass of accumulated water in fractions 1 – 4 than that in fractions 0 – 1. This phenomenon is disadvantageous in the context of required product homogeneity, especially due to the fact that the probability of the attachment of wet abraded material to previously formed agglomerates is greater than the possibility of the attachment of small fragments constituting 1 – 4 mm size fraction because of their size. Moreover, agglomerates formed from small fragments (crumbs) are characterised by a lower strength.

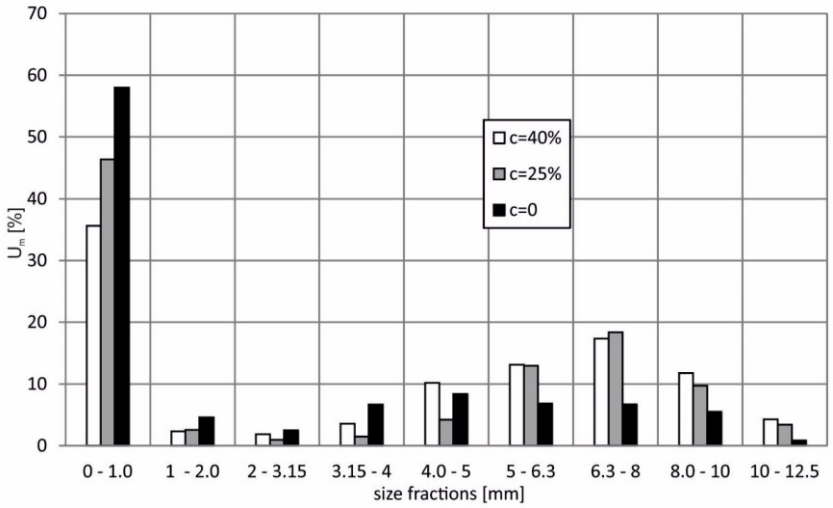

Fig. 6. The impact of the concentration of wetting liquid solution on mass content of size fractions (bed moisture $w = 4.4\%$)

Figure 6 presents the comparison of mass contents of bed fractions for selected concentrations of wetting liquid. This paper provides also analysis of impact of wetting liquid concentration on the formation and properties of nuclei. The obtained results indicate that an increase in sugar content in a solution positively affects granulation process. Figure 6 shows that for the specified moisture content ($w = 4.4\%$), the share of the finest fractions comprising non-granulated material and created abraded material decreases along with an increase in the concentration of wetting liquid. This observation confirms beneficial impact of disaccharide content in a solution on the rate of granule formation (approx. 2/3 of the total bed mass became granulated) and on the increased resistance to abrasion of formed agglomerates.

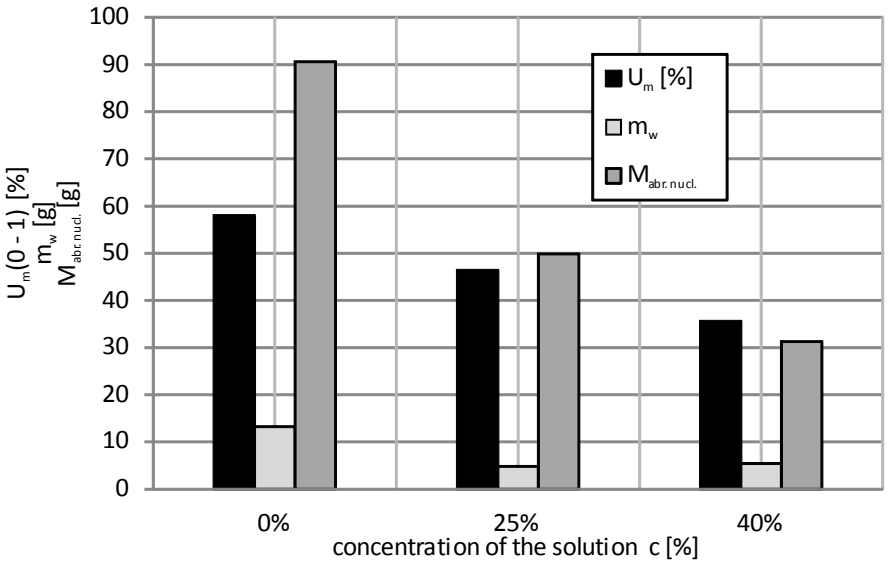

Fig. 7. The impact of wetting liquid concentration on mass content of fraction (0 – 1), mass of water accumulated in this fraction and the mass of nuclei which underwent the abrasion process

The aforementioned conclusions are confirmed by the results of sample analysis presented in Fig. 7. This graphic contain the comparison of mass content of fraction (0 – 1), the mass of liquid accumulated in this fraction and the mass of fine material which was abraded from the fraction of nuclei $M_{abr.nucl.}$ and adhered to fraction (0 – 1). This comparison was performed for different concentrations of the wetting solution. The mass of abraded nuclei was calculated from the model in Eq. (1). The obtained results show that application of disaccharide solution not only accelerates the granulation process, but also results in the formation of agglomerates that are more resistant to abrasion. This conclusion is confirmed by much smaller mass of abraded material adhered to fraction (0 – 1) in experiments carried out with disaccharide as a wetting solution in comparison to experiments when using water. Obtaining a satisfactory granulation results despite using much lower bed moisture is another benefit of the application of disaccharide as wetting solution. This allows for significant savings during drying of a product which is additionally enriched with organic ingredients.

7. CONCLUSIONS

- The use of water solution of disaccharide as wetting liquid positively influences the kinetics of disc granulation.
- Bed wetted with disaccharide solution is more resistant to abrasion and granulation process is faster and requires less moisture.
- The proposed model allows for qualitative and quantitative analysis of granulation mechanisms occurring during bed wetting.

- The course of nucleation assumed in this model was confirmed in the analysis of disc granulation.
- The obtained results confirmed the assumed mechanism of water migration from nucleus fraction towards other size fractions, which is based on the transfer of liquid to other size fractions together with wet material.
- The phenomenon of disintegration of nucleus and granule fractions is the driving force behind the formation of fractions with sizes of 1 – 4 mm.
- Agglomerates formed as a result of crushing of nuclei and granules can increase their mass by attaching the surrounding material abraded from other size fractions and dry raw material (layering).
- Bed wetting with monodisperse drops of binding liquid does not result in the formation of a monodisperse product with granular size resulting from the multiplicity of droplets although the proportion of this granule fraction is dominant for all process times.

The work was carried out under research projects no. 501/10-34-1-7015 and 501/15-30-1-9156.

SYMBOLS

c	liquid concentration, kg of sugar/kg of solution
$M_{abr.nucl}$	mass of fine material which was abraded from the fraction of nuclei, g
$M_{0\text{-}1}^{abr}(t_i)$	mass of dry material transferred from nucleus fraction to 0 – 1 mm size fraction as a result of abrasion, g
$M_{g.nucl.}^{o}(t_i)$	mass of nucleus fraction, which after t_i time co-forms granule fraction, g
$M_g^w(t_i)$	mass of water contained in granule fraction for particular times of wetting t_i, g
$m_j(t_i)$	mass of each wet material size fraction "j" for particular times of wetting t_i , g
$M_j(t_j)$	mass of each dry material size fraction "j" for particular times of wetting t_i, g
$M_j^c(t_i)$	mass of material transferred as a result of crushing from nuclei fraction to any other „j" fraction, g
$M_j^w(t_i)$	mass of water contained in each fraction "j", in time t_i, g
m_s	mass of fine raw material, g
$M_{0\text{-}1}^{sug.}(t_i)$	mass of sugar contained in a liquid accumulated in (0 – 1) size fraction, g
n	rotational speed of the plate, min^{-1}
q	mass flow rate of liquid binder delivery, g/min
t	wetting time, min
U_m	mass fraction, %
$w_j(t_i)$	moisture of "j" fraction in time t_i
$w_{nucl}(t_i)$	moisture of nuclei fraction after "i" time of wetting t_i, kg of water/kg dry material
α	the angle of plate axis inclination

REFERENCES

Abberger T., Seo A., Schaefer T., 2002. The effect of droplet size and powder particle size on the mechanisms of nucleation and growth in fluid bed melt agglomeration. *Int. J. Pharm.*, 249, 185-197. DOI: 10.1016/S0378-5173(02)00530-6.

Butensky M., Hyman D., 1971. Rotary drum granulation. An experimental study of the factors affecting granule size. *Ind. Eng. Chem. Fundam.*, 10, 212-219. DOI:10.1021/i160038a005.

Capes C.E., Danckwerts P.V., 1965. Granule formation by the agglomeration of damp powders: Part 1. The mechanism of granule growth. *Trans. Inst. Chem. Eng.*, 43, 116-124.

Charles-Williams H.R., Wengeler R., Flore K., Feise H., Hounslow M.J., Salman A.D., 2011, Granule nucleation and growth: Competing drop spreading and infiltration processes. *Powder Technol*., 206, 63-71. DOI: 10.1016/j.powtec.2010.06.013.

Gluba T., Heim A., Kochanski B. 1990. Application of the theory of moments in the estimation of powder granulation of different wettabilities. *Powder Handling and Processing*, 2, 323-326.

Hapgood K.P., Litster J.D., Biggs S.R., Howes T., 2002. Drop penetration into porous powder beds. *J. Colloid Interface Sci.*, 253, 353-366. DOI: 10.1006/jcis.2002.8527.

Hapgood K.P., Litster J.D., Smith R., 2003. Nucleation regime map for liquid bound granules. *AIChE J.*, 49, 350-361. DOI: 10.1002/aic.690490207.

Hapgood K.P., Litster J.D., White E.T., Mort P.R., Jones D.G., 2004. Dimensionless spray flux in wet granulation: Monte Carlo simulations and experimental validation. *Powder Technol*. 141, 20-30. DOI: 10.1016/j.powtec.2004.02.005.

Heim A., Solecki M., 2000. Dezintegracja komórek mikroorganizmów w przepływowych młynach mieszalnikowych. *Inż. Chem. Proces.,* 21, 311-327.

Hoornaert F., Wauters P.A.L., Meesters G.M.H., Pratsinis S.E., Scarlett B., 1998. Agglomeration behaviour of powders in a Lödige mixer granulator. *Powder Technol.*, 96, 116–128. DOI: 10.1016/S0032-5910(97)03364-0.

Iveson S.M., Litster J.D., Hapgood K.P., Ennis B.J., 2001. Nucleation, growth and breakage phenomena in agitated wet granulation processes: A review. *Powder Technol.*, 117, 3-39. DOI: 10.1016/S0032-5910(01)00313-8.

Jaiyeoba K.T.,. Spring M.S, 1980. The granulation of ternary mixtures: The effect of the wettability of the powders. *J. Pharm. Pharmacol.*, 32, 386–388. DOI: 10.1111/j.2042-7158.1980.tb12948.x.

Knight P.C., Instone T., Pearson J.M.K., Hounslow M.J., 1998. An investigation into the kinetics of liquid distribution and growth in high shear mixer agglomeration. *Powder Technol.,* 97, 246-257. DOI: 10.1016/S0032-5910(98)00031-X.

Le P.K., Avontuur P., Hounslow M.J., Salman A.D., 2011. A microscopic study of granulation mechanisms and their effect on granule properties. *Powder Technol*., 206, 18-24. DOI: 10.1016/j.powtec.2010.06.014.

Litster J.D., Hapgood K.P., Michaels J.N, Sims A., Roberts M., Kameneni T., Hsu T., 2001. Liquid distribution in wet granulation: Dimensionless spray flux. *Powder Technol*., 114, 32-39. DOI: 10.1016/S0032-5910(00)00259-X.

Litster J.D., Ennis B.J., 2004. *The science and engineering of granulation processes*. Particle Technology Series. B. Scarlett, Kluwer Academic Publishers, Dordrecht, The Netherlands.

Newitt D.M., Conway-Jones J.M., 1958. A contribution to the theory and practice of granulation. *Trans. I. Chem. Eng.*, 36, 422-441.

Nguyen T., Shen W., Hapgood K., 2009. Drop penetration time in heterogeneous powder beds. *Chem. Eng. Sci.*, 64, 5210-5221. DOI: 10.1016/j.ces.2009.08.038.

Obraniak A., Gluba T., 2012. A model of agglomerate formation during bed wetting in the process of disk granulation. *Chem. Process Eng.,* 33, 153-165. DOI: 10.2478/v10176-012-0014-1.

Obraniak A., 2017. Analysis of the phenomenon of nuclei mass transfer during the disc granulation. *Przemysł Chemiczny*, 96, 241-244. DOI: 10.15199/62.2017.1.30.

Olejnik T.P., 2013. Selected mineral materials grinding rate and its effect on product granulometric composition. *Physicochem. Probl. Miner. Process.*, 40, 407−418. DOI: 10.5277/ppmp130203.

Pearson J.M.K., Hounslow M.J., Instone T., Knight P.C., 1998. Granulation kinetics: the confounding of particle size and age. *World Congress on Particle Technology, Brighton, UK, I. Chem. E, paper 86.*

Ramachandran R., Immanuel C.D., Stepanek F., Litster J.D., Doyle F.J., 2009. A mechanistic model for breakage in population balances of granulation: Theoretical kernel development and experimental validation. *Chem. Eng. Res. Des.*, 87, 598-614. DOI: 10.1016/j.cherd.2008.11.007.

Ramaker J.S., Jelgersma M.A., Vonk P., Kossen N.W.F., 1998. Scale-down of a high shear pelletisation process: flow profile and growth kinetics. *Int. J. Pharm.*, 166, 89-97. DOI: 10.1016/S0378-5173(98)00030-1.

Rankell A.S., Scott M.W., Lieberman H.A., Chow F.S., Battista J.V., 1964. Continuous production of tablet granulations in fluidized bed II. Operation and performance of equipment. *J. Pharm. Sci.*, 53, 320–324. DOI: 10.1002/jps.2600530316.

Scott A.C., Hounslow M.J., Instone T., 2000. Direct evidence of heterogeneity during high-shear granulation. *Powder Technol.*, 113, 205-213. DOI:10.1016/s0032-5910(00)00354-5.

Schaafsma S.H., Vonk P., Segers P., Kossen N.W.F., 1998. Description of agglomerate growth. *Powder Technol.,* 97, 183-190. DOI: 10.1016/S0032-5910(97)03399-8.

Schaefer T., Wørts O., 1977. Control of fluidised bed granulation II: Estimation of droplet size of atomised binder solutions. *Arch. Pharam. Chem.*, 5, 178-193.

Schaefer T., Mathiesen C., 1996. Melt pelletization in a high shear mixer: IX. Effects of binder particle size. *Int. J. Pharm.*, 139, 139-148. DOI: 10.1016/0378-5173(96)04548-6.

Smirani-Khayati N., Falk V., Bardin-Monnier N., Marchal-Heussler L., 2009. Binder liquid distribution during granulation process and its relationship to granule size distribution. *Powder Technol*., 195, 105-112. DOI: 10.1016/j.powtec.2009.05.020.

Vonk P., Ramaker J.S., Vromans H., Kossen N.W.F., 1997. Growth mechanisms of high-shear palletisation. *Int. J. Pharm.,* 157, 93-102. DOI: 10.1016/S0378-5173(97)00232-9.

Waldie B., 1991. Growth mechanism and the dependence of granule size on drop size in fluidised bed granulation. *Chem. Eng. Sci.*, 46, 2781-2785. DOI: :10.1016/0009-2509(91)85147-P.

Wauters P.A.L., Van de Water R., Litster J.D., Meesters G.M.H., Scarlett B., 2002. Growth and compaction behavior of copper concentrate granules in rotating drum. *Powder Technol.,* 124, 230-237. DOI: 10.1016/S0032-5910(02)00029-3.

Wauters P.A.L., Jakobsen R.B., Litster J.D., Meesters G.M.H., Scarlett B., 2002b. Liquid distribution as a means to describing the granule growth mechanism. *Powder Technol.*, 123, 166-177. DOI: 10.1016/S0032-5910(01)00446-6.

Received 15 October 2016
Received in revised form 10 May 2017
Accepted 18 May 2017

www.czasopisma.pan.pl www.journals.pan.pl
Chemical and Process Engineering 2017, 38 (2), 307-319
DOI: 10.1515/cpe-2017-0024

EXTERNAL MASS TRANSFER MODEL FOR HYDROGEN PEROXIDE DECOMPOSITION BY TERMINOX ULTRA CATALASE IN A PACKED-BED REACTOR

Ireneusz Grubecki*

UTP University of Science and Technology, Faculty of Chemical Technology and Engineering,
3 Seminaryjna Street, 85-326 Bydgoszcz, Poland

It is known that external diffusional resistances are significant in immobilized enzyme packed-bed reactors, especially at large scales. Thus, the external mass transfer effects were analyzed for hydrogen peroxide decomposition by immobilized Terminox Ultra catalase in a packed-bed bioreactor. For this purpose the apparent reaction rate constants, k_P, were determined by conducting experimental works at different superficial velocities, U, and temperatures. To develop an external mass transfer model the correlation between the Colburn factor, J_D, and the Reynolds number, Re, of the type $J_D = K\,Re^{(n-1)}$ was assessed and related to the mass transfer coefficient, k_{mL}. The values of K and n were calculated from the dependence $(a_m k_p^{-1} - k_R^{-1})$ vs. Re^{-1} making use of the intrinsic reaction rate constants, k_R, determined before. Based on statistical analysis it was found that the mass transfer correlation $J_D = 0.972\,Re^{-0.368}$ predicts experimental data accurately. The proposed model would be useful for the design and optimization of industrial-scale reactors.

Keywords: hydrogen peroxide decomposition, immobilized terminox ultra catalase, packed bed reactor, external film diffusion, mass transfer coefficient

1. INTRODUCTION

Catalases (EC 1.11.1.6) are abundant enzymes in nature that decompose hydrogen peroxide to water and molecular oxygen (Zámocký and Koller, 1999). These enzymes can find many industrial applications, namely: 1) in the textile industry after textile blenching (Costa et al., 2002a), 2) in the food industry after cold pasteurization of milk (Farkye, 2004), 3) coupled with oxidases, prevention of the inactivation of the oxidases by the deleterious action of a high concentration of peroxide (Fernández-Lafuente et al., 1998) and 4) coupled with oxidases, prevention of side reactions caused by the H_2O_2 that can destroy the target product (Schoevaart and Kieboom, 2001). It is worth noting that application of catalase reduces 48% of the energy consumption, 83% of the chemical costs, 50% of the water consumption and 33% of the processing time (Eberhardt et al., 2004). However, direct application of free catalase promotes interaction between the protein and the dye which in turn reduces dye uptake by the fabric. Immobilization of catalase overcomes this constraint and concomitantly enables reuse of the enzyme. The attempts of catalase immobilization have been made by several authors by using organic and inorganic materials (Alptekin et al., 2011; Betancor et al., 2003; Vera-Avila et al., 2004;). However, when working with immobilized enzymes mass-transfer resistances are likely to occur no matter which method of immobilization is used. Two types of resistances may occur (Illanes et al., 2014): 1) external diffusional resistances (EDR) when the rate of diffusional transport through the stagnant layer surrounding the solid biocatalyst particle is the limiting one, 2) internal diffusional resistances (IDR) when the substrate will have to diffuse from the biocatalyst

*Corresponding authors, e-mail: ireneusz.grubecki@utp.edu.pl

surface inside the biocatalyst internal structure at the diffusion rate lower than that in the bulk liquid phase. Usually penetration of the substrate into the interior of the biocatalyst particle is the slowest step. Hence, the EDR are negligible compared to IDR. In many cases this assumption is often but not always valid. So, in the case of significant EDR the combined effect of EDR and IDR is described (Mudliar et al., 2008). The analysis of a combined effect of EDR and IDR can also be indicated in the case of hydrogen peroxide decomposition (HPD) by catalase (Traher and Kittrell, 1974; Greenfield et al., 1975). Hence, the reports on immobilized enzyme (especially catalase) dealing only with EDR effect are limited. In order to analyse EDR the internal diffusional resistances should be eliminated. Thus, in this paper a realistic engineering analysis of the external mass transfer combined with the reaction of the HPD by commercial Terminox Ultra catalase (TUC) immobilized on non-porous glass and correlation of experiment with theory has been carried out. Consequently, an external film diffusion model was developed to predict the behavior of the fixed-bed reactor for enzymatic decomposition of hydrogen peroxide occurring under diffusional resistances. Although film diffusion studies of immobilized catalase in a tubular reactor were taken into account by Greenfield et al. (1975) as well as Traher and Kittrell (1974) it is necessary to evaluate each immobilized enzyme system individually.

2. DEVELOPMENT OF EXTERNAL MASS TRANSFER MODEL

2.1. Apparent reaction rate

External mass transfer analysis presented in this work is developed based on the approach used by Rovito and Kittrell (1973). Thus, in a packed-bed column with ideal plug flow of hydrogen peroxide solution a single biochemical reaction takes place. Taking additionally into account that catalase deactivation is very slow or does not proceed at all, mass balance of the process can be described by the following equation

$$\left(\frac{HQ}{W}\right)\frac{dC_A}{dh} = -r_A \tag{1}$$

The process of HPD by the catalase in industrial practice undergoes at low substrate concentrations (Costa et al., 2002b; Deluca et al., 1995; Tarhan and Telefoncu, 1990; Tarhan and Uslan, 1990; Tarhan, 1995; Vasudevan and Weiland, 1990; Vasudeven and Weiland, 1993). Thus, a relationship between the reaction rate, r_A, and the substrate (hydrogen peroxide) concentration in the bioreactor (at the fixed activity of catalase) is given by

$$r_A = k_P C_A \tag{2}$$

Substitution of Eq. (2) into Eq. (1) and integration of the resulting equation subject to the boundary conditions given below

$$C_A(h=0) = C_{A,In} \tag{3a}$$

$$C_A(h=H) = C_{A,Out} \tag{3b}$$

yields

$$ln\left(\frac{1}{1-\alpha}\right) = k_P\left(\frac{W}{Q}\right) \tag{4}$$

The apparent reaction rate constant, k_P, can be found from Eq. (4) based on the experimentally measured conversion values, α, assessed at different volumetric flow rates, Q, and quantities of immobilized catalase, W.

2.2. Combined mass transfer and reaction of hydrogen peroxide decomposition

The mass transport rate of the H_2O_2 from the bulk liquid to the outer surface of the immobilized beads is proportional to the external mass transfer coefficient, k_{mL}, area of the external mass transfer, a_m, and the H_2O_2 concentration difference between the bulk, C_A, and the external surface of immobilized beads, C_{As}:

$$r_m = k_{mL} a_m (C_A - C_{As}) \tag{5}$$

The surface area per unit of weight, a_m, can be determined as

$$a_m = \frac{6(1-\varepsilon)}{d_P \rho_U} \tag{6}$$

The rate of hydrogen peroxide decomposition can be expressed by Eq. (7)

$$r_A = k_R a_m C_{As} \tag{7}$$

At a steady state process, the rate of mass transfer, r_m, is equal to the reaction rate, r_A. Thus, equating Eq. (5) with Eq. (7) and solving for the unknown surface concentration of hydrogen peroxide, Eq. (8) is obtained

$$C_{As} = \frac{k_{mL}}{k_{mL} + k_R} C_A \tag{8}$$

Equation (8) represents the H_2O_2 behaviour under EDR. A combination of Eqs. (2), (7) and (8) leads to a dependence between the pseudo first-order, k_P, and intrinsic, k_R, reaction rate constants as well as the mass transfer coefficient, k_{mL}

$$k_P = \frac{k_{mL} k_R a_m}{k_{mL} + k_R} \tag{9}$$

2.3. External mass transfer correlation model

It is known that external mass transfer coefficient, k_{mL}, changes with many parameters (Kalaga et al., 2014). Therefore, a correlation allowing to determine a mass transfer coefficient at different operating parameters is needed. Such a correlation may be obtained by defining a dimensionless group:

$$J_D = \mathrm{St_D Sc}^{2/3} \tag{10}$$

A large number of correlations describing J_D - factor as a function of Reynolds number (Re) are available as follows (Dizge and Tansel, 2010)

$$J_D = K\,\mathrm{Re}^{(n-1)} \tag{11}$$

Different values of K and n are related to different mass transfer conditions. The value of n varies from 0.1 to 1.0 depending on the flow characteristics. Equating Eq. (10) with Eq. (11) yields a dependence for the external mass transfer coefficient

$$k_{mL} = AG^n \tag{12}$$

$$A = \frac{K}{\rho}\mathrm{Sc}^{-2/3}\left(\frac{d_P}{\eta}\right)^{n-1} \tag{13}$$

Substituting Eq. (12) in Eq. (9) leads to the following correlation

$$\frac{1}{k_P} = \frac{1}{Aa_m}\left(\frac{1}{G^n}\right) + \left(\frac{1}{k_R a_m}\right) \tag{14}$$

The experimentally measured values of k_P^{-1} vs. G^{-n} for various values of K and n can be plotted. From a straight line with a slope, $(Aa_m)^{-1}$, and an intercept, $(k_R a_m)^{-1}$, a_m and k_R values can then be determined. The estimated values of a_m are compared to that calculated from Eq. (6) to determine the set of K and n values adequate for HPD in the packed-bed.

A trial-and-error procedure can be neglected, when a value of the reaction rate constant (k_R) is known and assessed independently. In such a case Eq. (14) can be expressed by

$$Y = \left(\frac{1}{Re}\right)^n \times \left[K^{-1} Sc^{2/3}\left(\frac{\rho d_P}{\eta}\right)\right] \tag{15}$$

where $Y = a_m k_P^{-1} - k_R^{-1}$. From Eq. (15) the slope of the $\ln(Y)$ - $\ln(\mathrm{Re}^{-1})$ plot should correspond to n and its intercept $\ln[K^{-1}\mathrm{Sc}^{2/3}(\rho d_P \eta^{-1})]$.

3. MATERIALS AND EXPERIMENTAL PROCEDURE

3.1. Preparation of immobilized catalase beads

Terminox Ultra catalase (E.C. 1.11.1.6; 50,000 U/g) was immobilized by glutaraldehyde-coupling to the silanised support according to the method of Vasudevan and Weiland (1990). In order to eliminate any IDR, non-porous glass beads (425-600 μm) were used as a support. Commercial TUC was purchased from Novozymes (Bagsvaerd, Denmark), (gamma-aminopropyl)triethoxysilane as well as glutaraldehyde (50% w/w aqueous solution) were purchased from Sigma-Aldrich (Steinheim, Germany). All other chemicals employed, including commercial hydrogen peroxide (30% w/w aqueous solution), were products of Avantor Performance Materials (Gliwice, Poland).

3.2. Packed bed enzyme reactor studies

The experimental set-up used in this study consisted of a vertical tubular reactor, peristaltic pump, flowmeter and feed solution container (Fig. 1). The test tubular reactor ($8 \cdot 10^{-3}$ m inner diameter and height adjusted to the bulk mass of the biocatalyst) was jacketed and water from a thermostat was circulated through the jacket. The feed flow rate of the H_2O_2 solution (concentration of about $85 \cdot 10^{-3}$ kg·m^{-3}) was forced through the packed-bed reactor by a peristaltic pump and controlled by a flowmeter.

At both ends the reactor was equipped with a screen made of stainless steel. A biocatalyst bed was set on the bottom screen while the upper screen served to prevent biocatalyst entrainment by the outflowing substrate stream. The experiments were conducted in two steps. In the first one the values of pseudo first-order rate constant, k_P, were obtained (Eq. (4)) by collecting samples at the various bed mass (from $0.5 \cdot 10^{-3}$ kg to $3.5 \cdot 10^{-3}$ kg) under different superficial velocities (from $4.0 \cdot 10^{-3}$ m·s^{-1} to $10.3 \cdot 10^{-3}$ m·s^{-1}). In each case, the plug flow condition with no axial dispersion has been satisfied (Burghardt and Bartelmus, 2001).

In the second step the intrinsic rate constants for reaction, k_R, and (at the same time) for deactivation, k_D, were determined. These kinetic parameters of the immobilized TUC represent its proper behaviour and correspond to that observed in the absence of EDR.

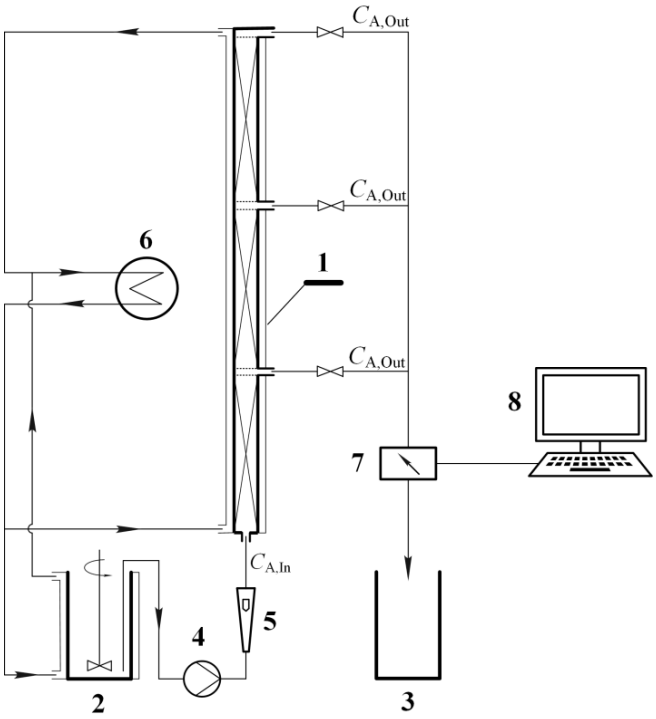

Fig. 1. Experimental set-up: 1-tubular bioreactor, 2-feed solution tank, 3-product collector, 4-peristaltic pump, 5-flowmeter, 6-thermostat, 7-spectrophotometer, 8-computer

Such conditions (feed flow rate) have been established by monitoring the H_2O_2 concentration in the outlet stream under the various superficial velocities and invariable residence time. Then, the conversion measurements were done (Altomare et al., 1974). It was accomplished by combining three reactors in series and filling each of them with biocatalyst of a mass of $11 \cdot 10^{-3}$ kg established earlier. The bulk density of biocatalyst bed equaled to 1823 kg·m^{-3} (bed porosity of $\varepsilon = 0.3$) corresponded to the bed depth of ca. 0.12 m in each segment. Such a system of three combined reactors may be considered as a single reactor enabling to control H_2O_2 conversion, α, as a function of time, t ($\tau = tQ\rho_U / W$), and position, h ($z = h/H$). From measurements a discrete function

$$\alpha(z_i, \tau_j) = 1 - C_{A,Out}(z_i, \tau_j) / C_{A,In} \quad (i = 1..M,\ j = 1..N) \tag{16}$$

was formulated.

The experimental data described by Eq. (16) were fitted to an equation derived by Altomare et al. (1974)

$$\alpha(z_i, \tau_j) = 1 - \frac{\exp[\beta_2(\tau_j - z_i)]}{\exp(\beta_1 z_i) + \exp[\beta_2(\tau_j - z_i)] - 1} \tag{17}$$

using a non-linear least squared regression method which minimizes the sum of deviation squares in a series of iterative steps. In Eq. (17) β_1 and β_2 can be expressed as

$$\beta_1 = \frac{W}{Q} k_R a_m \tag{18}$$

$$\beta_2 = \frac{W}{Q\rho_U} k_D C_{A,In} \tag{19}$$

The experiments were conducted at a superficial velocity of U =$5 \cdot 10^{-2}$ m·s^{-1} and repeated for temperature values ranging from 278K to 323K.

3.3. Analysis of hydrogen peroxide concentration

The concentration of H_2O_2 in the exit stream of reactor was monitored spectrophotometrically making use of a UV-Vis Jasco V-530 spectrophotometer (Artisan T.G., Champaign IL, USA) equipped with a quartz cuvette Q11020 (Gallab, Warsaw, Poland) with optical light path of 20 mm. The measurements were carried out at 240 nm ($\varepsilon_{240} = 39.4$ dm^3·mol^{-1}·cm^{-1}).

4. RESULTS AND DISCUSSION

4.1. Determination of the specific surface area for the mass transfer

In order to estimate a value of the mass transfer interfacial area information on the diameter of a single bed element is indispensable. It was assessed on the basis of a sieve analysis carried out using the Vibratory Sieve Shaker Analysette 3 Pro system (Fritsch GmbH, Germany). In consequence, an average particle diameter of $d_P = 5.05 \cdot 10^{-4}$ m was determined. Now, making use of Eq. (6) it is possible to calculate the specific external surface area of the biocatalyst equal to $a_m = 4.57$ m^2·kg^{-1}.

4.2. Determination of intrinsic kinetic parameters

A function, $\alpha = \alpha(z_i, \tau_j)$ describing a relationship between conversion of H_2O_2 and position in the reactor, z, and time, τ, (Eq. (17)) was fitted to the experimental data (Eq. (16)) using a non-linear least squares regression procedure with Matlab Optimization Toolbox (Mathworks Inc., Natick MA, USA). As a result, values of intrinsic rate constants for reaction, k_R, and deactivation, k_D, were obtained (Fig. 2). Based on these values the activation energy for reaction and the frequency factor in the Arrhenius equation equal to $E_R = 12.57 \pm 0.30$ kJ·mol^{-1} and $k_{R0}a_m = (26.32 \pm 2.95) \cdot 10^{-3}$ m^3·kg^{-1}·s^{-1}, respectively, were assessed.

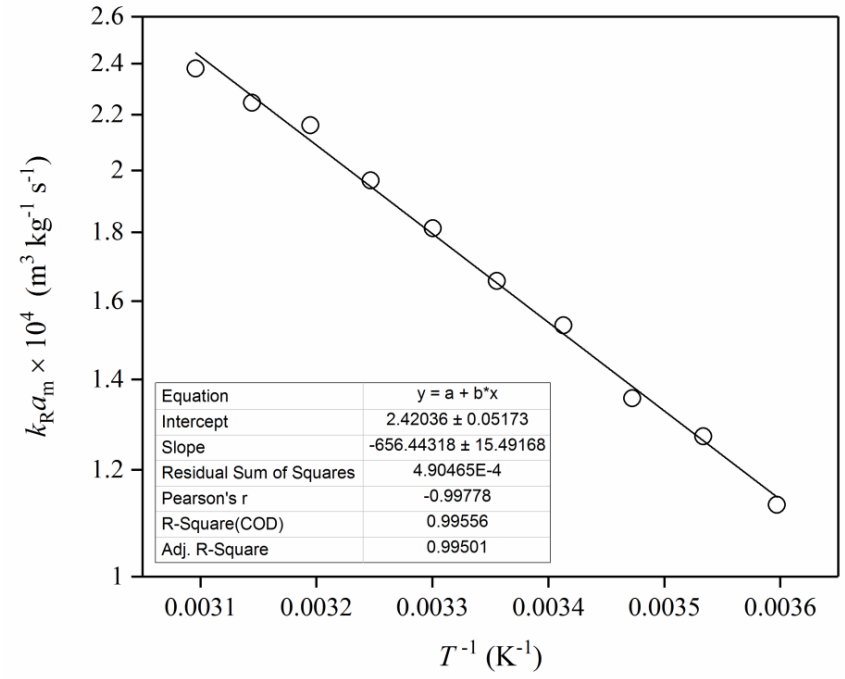

Fig. 2. Dependence of $k_R a_m$ vs. (T^{-1}) for HPD and $C_{A,In} = 85 \cdot 10^{-3}$ kg·m^{-3}

These values were used at formulation of the external mass transfer model. The kinetic parameters for deactivation of immobilized catalase were also determined but in the present analysis have been neglected.

4.3. External mass transfer model

Measurements of pseudo first-order reaction rate constants, k_P, were carried out under the process conditions for which the rate of TUC deactivation can be negligible. Such conditions correspond to low values of H_2O_2 concentration, $C_{A,In} = 85 \cdot 10^{-3}$ kg·m^{-3}, temperature in the range from 278K to 303K and $pH = 7$ (Cantemir et al., 2013). The results of these measurements are plotted in Fig. 3 in a form of a dependence $k_P = k_P(U,T)$.

It can be seen that with an increasing superficial velocity, U, values of the pseudo first-order rate constant, k_P, increase. For example, the increase of U from $4 \cdot 10^{-3}$ m·s^{-1} to $10.3 \cdot 10^{-3}$ m·s^{-1} resulted in an increase of k_P from $4.82 \cdot 10^{-5}$ m^3·kg^{-1}·s^{-1} to $6.50 \cdot 10^{-5}$ m^3·kg^{-1}·s^{-1} at $T = 278$ K and from $8.68 \cdot 10^{-5}$ m^3·kg^{-1}·s^{-1} to $11.47 \cdot 10^{-5}$ m^3·kg^{-1}·s^{-1} at $T = 303$ K. For investigation of the film diffusion effects on the HPD rate the Reynolds numbers and superficial mass velocities at the studied feed flow rates were also calculated (Table 1). Due to relatively low concentrations of H_2O_2 in the solution its density and dynamic viscosity were assumed as those for water. Only diffusivity equal to $D_f = 8.80 \cdot 10^{-10}$ m^2·s^{-1} was taken based on the data of USP Technologies Company (2017) at 293K. For others temperatures, diffusivities were calculated according to the Stokes-Einstein equation (Curcio et al., 2015).

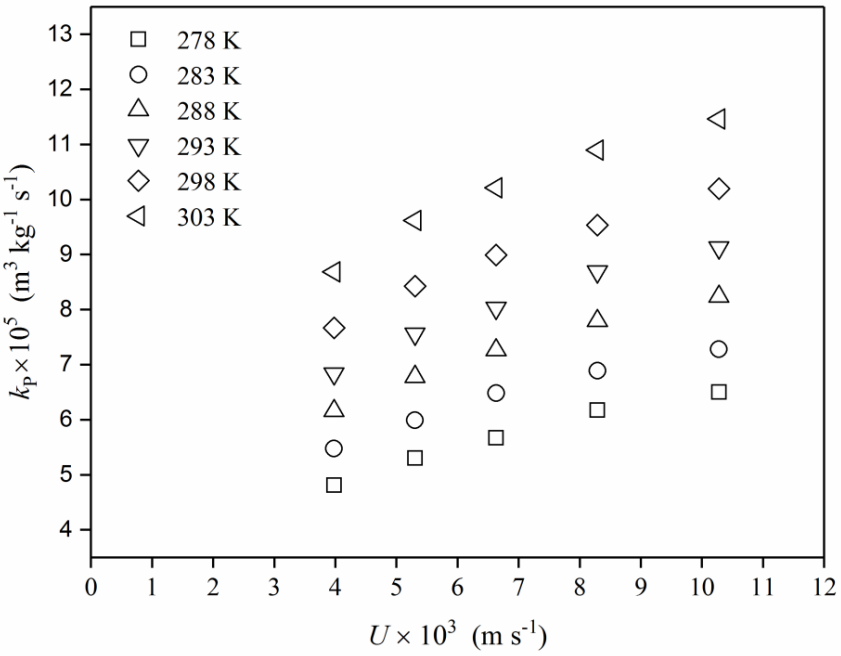

Fig. 3. Dependence of k_P vs. U for various temperatures

Having established values of the pseudo first-order rate constants, k_P, and the Reynolds numbers it is now possible to determine the values of n and K (Eq. (11)) using Eq. (15). At a fixed temperature (in a log-log plot) this equation yields a straight line with slope n and intercept $\ln[K^{-1}\mathrm{Sc}^{2/3}(\rho d_P \eta^{-1})]$. Thus, Eq. (15) was fitted to the experimental data using coordinates $(a_m k_P^{-1} - k_R^{-1})$ vs. (Re^{-1}) and non-linear least squares regression procedure with Matlab Optimization Toolbox (Mathworks Inc., Natick MA, USA) which minimizes the sum of deviation squares for all analyzed temperature values (Fig. 4). In this way the following values were obtained $n = 0.632 \pm 0.001$ and $K = 0.972 \pm 0.001$ while the

calculated values of the regression coefficient, $R^2 = 0.9986$, as well as the sum of squared error (SSE), and the root mean squared error (RMSE) were equal to SSE = $6.300 \cdot 10^{-4}$ s·m^{-1} and RMSE = $4.743 \cdot 10^{-3}$ s$^{0.5}$·m$^{-0.5}$, respectively, confirming that the developed model offers a quite good fit to the experimental data based on previously determined values of the pseudo first-order rate constants data. This conclusion is also confirmed by the statistical parameters estimated when the dependent variables, $Y = a_m k_P^{-1} - k_R^{-1}$, and, k_P^{-1}, determined experimentally have been compared with those calculated from Eqs. (15) and (14), for $n = 0.632$ and $K = 0.972$, respectively (Tables 2 and 3).

Table 1. The values of Reynolds number, Re, and superficial mass velocity, G, at studied feed flow rates, Q, and temperatures, T

$Q \cdot 10^7$ m^3·s^{-1}	$U \cdot 10^3$ m·s^{-1}	G kg·m^{-2}·s^{-1}	Re_{278}	Re_{283}	Re_{288}	Re_{293}	Re_{298}	Re_{303}
2.00	4.00	4.00	1.34	1.54	1.76	2.00	2.25	2.52
2.67	5.31	5.30	1.78	2.05	2.34	2.66	3.00	3.36
3.33	6.63	6.63	2.23	2.56	2.93	3.33	3.75	4.19
4.17	8.29	8.29	2.78	3.20	3.66	4.16	4.69	5.24
5.17	10.28	10.28	3.45	3.97	4.54	5.16	5.82	6.50

Re_T denotes the value of Reynolds number at temperature T (K)

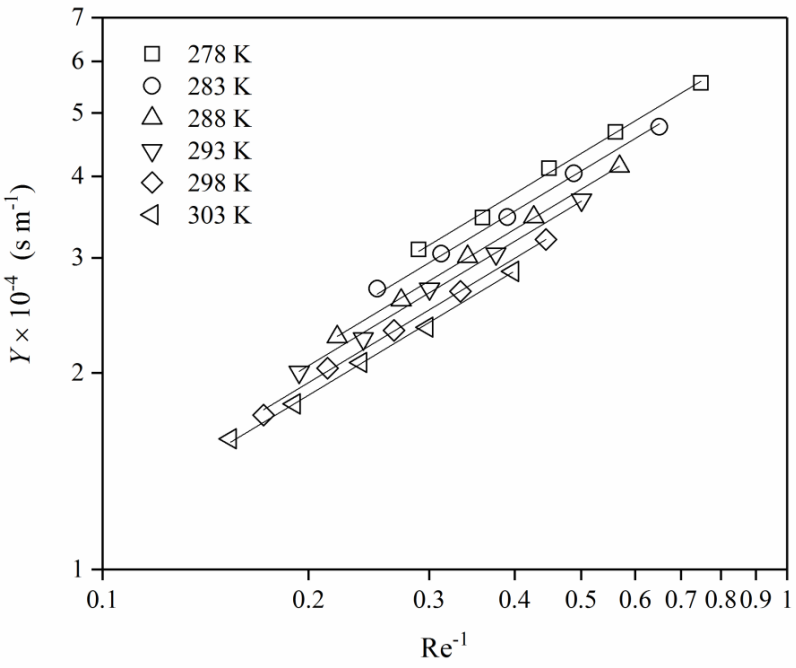

Fig. 4. Dependence of Y vs. Re^{-1} for different temperature values

It should be noticed that the relative percentage deviations of a_m and $k_R a_m$ calculated from Eq. (14) (Table 3) compared with the experimental values of $a_m = 4.57$ m^2·kg^{-1} and $k_R a_m$ did not exceed 3.72% and 4.94%, respectively. After accomplishing statistical analysis of n and K it is possible to obtain the variations of mass transfer coefficient, k_{mL}, with G or Re (Table 1) from Eq. (9). These results are illustrated in Fig. 5. From Eq. (12) n and K values were assessed again to be equal to $n = 0.632 \pm 0.007$ and $K = 0.972 \pm 0.022$ with determination coefficient of $R^2 = 0.9984$ as well as the sum of squared error (SSE) and the root mean squared error (RMSE) equal to SSE = $3.991 \cdot 10^{-4}$ m·s^{-1} and RMSE = $3.776 \cdot 10^{-3}$ m$^{0.5}$ s$^{-0.5}$, respectively. They confirm that the present mathematical analysis is self-consistent.

Table 2. The comparison of the values Y obtained from experimental data with those calculated from Eq. (15) for $n = 0.632$ and $K = 0.972$

T K	R^2	SSE $\cdot 10^4$ $s \cdot m^{-1}$	RMSE $\cdot 10^3$ $s^{0.5} \cdot m^{-0.5}$
278	0.9975	1.313	6.615
283	0.9975	1.105	6.068
288	0.9996	0.833	5.271
293	0.9976	1.327	6.652
298	0.9988	1.045	5.902
303	0.9986	0.676	4.748

Table 3. Statistical parameters of estimates for Eq. (14) at various temperatures

i	T K	$A \cdot 10^5$ $kg^{-0.632} \cdot m^{2.264} \cdot s^{-0.368}$	a_m, $m^2\ kg^{-1}$	$k_R a_m \cdot 10^4$ $m^3\ kg^{-1}\ s^{-1}$	R^2	SSE $\cdot 10^{-4}$ kg s m^{-3}	RMSE $\cdot 10^{-2}$ $kg^{0.5}\ s^{0.5}\ m^{-1.5}$
1	278	0.750	4.60 ± 0.38	1.148 ± 0.122	0.9976	4.418	1.213
2	283	0.869	4.74 ± 0.27	1.228 ± 0.067	0.9995	1.386	0.680
3	288	1.002	4.58 ± 0.16	1.402 ± 0.043	0.9980	0.326	0.330
4	293	1.147	4.46 ± 0.40	1.551 ± 0.114	0.9974	1.660	0.744
5	298	1.304	4.54 ± 0.30	1.671 ± 0.087	0.9989	0.688	0.479
6	303	1.471	4.62 ± 0.31	1.881 ± 0.092	0.9984	0.559	0.432

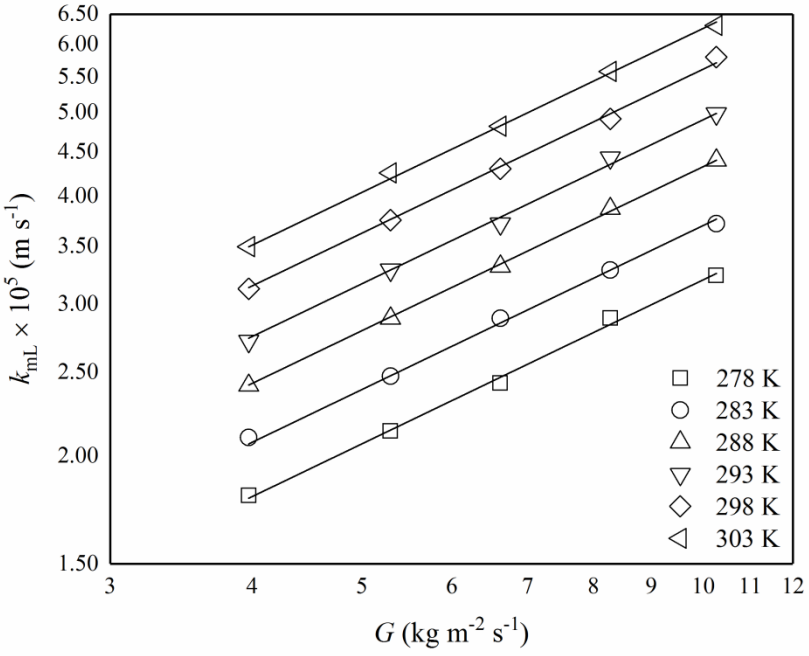

Fig. 5. Dependence of calculated values of the mass transfer coefficient, k_{mL}, on superficial mass velocity, G, for different temperatures

In view of above presented results it can be stated that the external mass transfer correlation of the form

$$J_D = 0.972\,\mathrm{Re}^{-0.378} \tag{20}$$

predicts the experimental data for hydrogen peroxide decomposition by Terminox Ultra catalase in a packed-bed reactor with the normalized deviation lower than 3.6 % (Fig. 6). It should be mentioned that mass transfer coefficients calculated with Eq. (20) are lower by about 30% than those obtained from external mass transfer model developed by Traher and Kittrell (1974) for beef liver catalase. Thus, the external mass transfer model developed in this work (Eq. (20)) may be useful in the process of hydrogen peroxide decomposition by catalase originating from various sources.

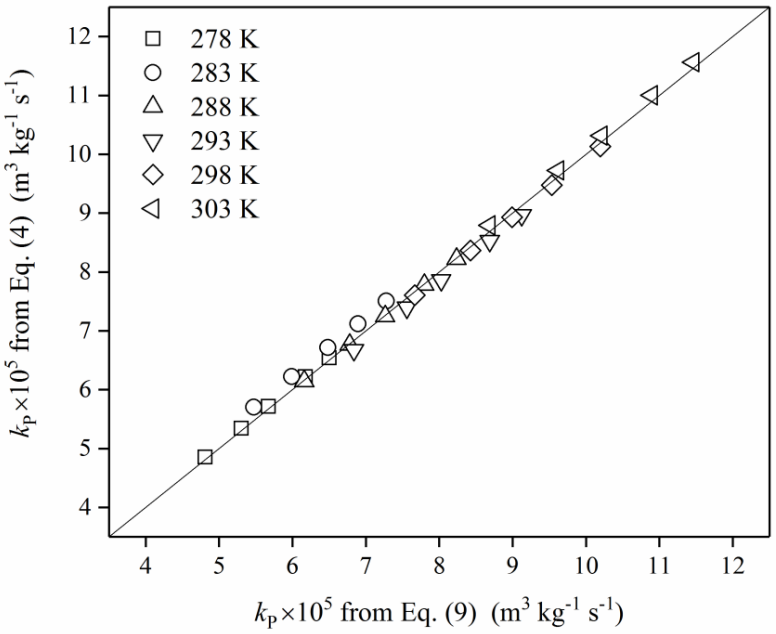

Fig. 6. The comparison of the observed first-order HPD rate constant, k_P, calculated from Eq. (4) with those calculated from Eq. (9) found for all superficial velocities, U, and temperature values

Table 4. Effects of external mass transfer, $k_{mL}a_m$, and intrinsic reaction rate, $k_R a_m$, on pseudo first-order reaction rate, k_P, for selected temperatures.

T, K	$U \cdot 10^3$ m·s^{-1}	$(k_P \cdot 10^3)^{-1}$ kg·s·m^{-3}	$(k_R a_m \cdot 10^3)^{-1}$ kg·s·m^{-3}	% Contribution of $k_R a_m$	$(k_{mL} a_m)^{-1}$ kg·s·m^{-3}	% Contribution of $k_{mL} a_m$
278	4.00	20.78	8.71	41.92	12.07	58.08
	5.31	18.86		46.18	10.15	53.82
	6.63	17.63		49.40	8.92	50.60
	8.29	16.19		53.80	7.48	46.20
	10.28	15.38		56.63	6.67	43.37
298	4.00	13.02	5.99	46.01	7.03	53.99
	5.31	11.88		50.42	5.89	49.58
	6.63	11.10		53.96	5.11	46.04
	8.29	10.50		57.05	4.51	42.95
	10.28	9.78		61.25	3.79	38.75

The combined effects of the intrinsic reaction rate constants, $k_R a_m$, and the mass transfer coefficients, $k_{mL}a_m$, on the apparent reaction rate constants, k_P, for $n = 0.632$ and $K = 0.972$ are compared in Table 4. It can be seen that the apparent reaction rate is affected by both the external film diffusion of H_2O_2 and the biochemical reaction rate. Both steps have significant contributions. At a low superficial velocity ($U = 4.0 \cdot 10^{-3}$ m·s^{-1}) and 278 K the external mass transfer dominates with contribution of 58%. At higher values of U the contribution of mass transfer decreases while the contribution of the reaction rate rises.

For example, at a superficial velocity of $U = 10.3 \cdot 10^{-3}$ m s^{-1} the external mass transfer and biochemical reaction rate contribute with 43.4% and 56.6%, respectively. Additionally, temperature increase makes the biochemical reaction rate contribution larger. Namely, temperature increase from 278 K to 298 K results in the contribution increase of reaction rate from 41.9% to 46.0% for $U = 4.0 \cdot 10^{-3}$ m s^{-1} and from 56.6% to 61.3% for $Q = 10.3 \cdot 10^{-3}$ m s^{-1}.

5. CONCLUSIONS

Based on the results of this study the following conclusions can be drawn:

- The observed apparent reaction rate constant, k_P, increases when the superficial velocity, U, of the hydrogen peroxide solution and temperature increase. This is due to reduction in the film thickness at high superficial velocities and also temperature effects on kinetics of the enzyme catalysed reaction.
- Both external film diffusion, $k_{mL}a_m$, and overall hydrogen peroxide decomposition rate, $k_R a_m$, influence the apparent reaction rate constant, k_P. However, the effects of film diffusion are significant at low superficial velocities as well as low temperatures and should not be ignored when a proper behaviour of immobilized Terminox Ultra catalase under EDR is evaluated.
- The external mass transfer model $J_D = 0.972 \mathrm{Re}^{-0.378}$ offers quite good fit to the experimental data of the pseudo first-order rate constants. This model is valid for low Reynolds numbers in the range of 0.17 - 10. It can be used to quantify the external film diffusion effects for H_2O_2 decomposed by Terminox Ultra catalase in a fixed-bed reactor.
- The approach demonstrated in this work allows to predict the effect of external film diffusion on the observed reaction rates in any operational conditions and will be useful for simulation and optimization of hydrogen peroxide decomposition process in the presence of immobilized Terminox Ultra catalase.

SYMBOLS

A	constant defined by Eq. (13), m^{2n+1} s^{n-1}/kg^n
a_m	surface area per unit weight, m^2/kg
C_A	bulk stream substrate concentration, kg/m^3
C_{As}	surface concentration of hydrogen peroxide, kg/m^3
dC_A/dh	the H_2O_2 concentration gradient along the reactor length, kg/(m^3·m)
D_f	hydrogen peroxide diffusion coefficient, m^2/s
d_P	biocatalyst particle diameter, m
G	superficial mass velocity related to the superficial velocity averaged over the entire cross section of the bed, kg/(m^2·s)
H	bed depth, m
h	distance from reactor inlet, m

z	dimensionless axial distance along the bioreactor ($=h/H$)
J_D	Colburn factor defined by Eq. (10)
K	constant in Eq. (11) related to different mass transfer conditions
k_D	rate constant for deactivation, $m^3/(kg \cdot s)$
k_{mL}	mass transfer coefficient, m/s
k_P	apparent first-order reaction rate constant, $m^3/(kg \cdot s)$
k_R	intrinsic first-order rate constant, m/s
M, N	dimensions of position and time vectors, respectively
n	constant in Eq. (11) related to different mass transfer conditions
Q	volumetric superficial velocity, m^3/s
Re	Reynolds number ($=d_p G/\eta$)
r_A	H_2O_2 consumption rate, kg/(kg·s)
r_m	mass transfer rate, kg/(kg s)
Sc	Schmidt number ($=\eta/\rho D_f$)
St_D	Stanton number for mass transfer ($=k_{mL}\rho/G$)
t	time, s
U	superficial velocity averaged over the entire cross section of the bed, m/s
W	amount of immobilized Terminox Ultra catalase, kg
Y	dependent variable ($=a_m k_P^{-1} - k_R^{-1}$), s/m

Greek symbols

α	conversion at the reactor outlet ($=1-C_{A,Out}/C_{A,In}$) calculated from Eq. (16)
β_i	dimensionless coefficients expressed by Eq. (18) ($i=1$) and Eq. (19) ($i=2$)
ε	porosity
η	fluid viscosity, kg/(m·s)
ρ	fluid density, kg/m^3
ρ_U	bulk density, kg/m^3
τ	dimensionless time ($=tQ\rho_U/W$)

Subscripts

In	inlet
Out	outlet

REFERENCES

Alptekin Ö., Seyhan Tükel S., Yildirim D., Alagöz D., 2011. Covalent immobilization of catalase onto spacer-arm attached modified florisil: Characterization and application to batch and plug-flow type reactor systems. *Enzyme Microb. Technol.*, 49, 547-554. DOI: 10.1016/j.enzmictec.2011.09.002.

Altomare R. E., Kohler J., Greenfield P. F., Kittrell J. R., 1974. Deactivation of immobilized beef liver catalase by hydrogen peroxide. *Biotechnol. Bioeng.*, 16, 1659-1673. DOI: 10.1002/bit.260161208.

Betancor L., Hidalgo A., Fernández-Lorente G., Mateo C., Fernández-Lafuente R., Guisan J. M., 2003. Preparation of a stable biocatalyst of bovine liver catalase using immobilization and postimmobilization techniques. *Biotechnol. Progres*, 19, 763-767. DOI: 10.1021/bp025785m.

Burghardt A., Bartelmus G. (Eds.), 2001. Models of Heterogeneous Fixed-Bed Catalitic Reactors, In: *Chemical Reactors Engineering. Part II. Heterogeneous Reactors*. Scientific Publishing Company, Warsaw, 170-277.

Costa S. A., Tzanov T., Carneiro F., Gubitz G. M., Cavaco-Paulo A., 2002a. Recycling of textile bleaching effluents for dyeing using immobilized catalase. *Biotechnol. Lett.*, 24, 173-176. DOI: 10.1023/a:1014136703369.

Costa S. A., Tzanov T., Filipa Carneiro A., Paar A., Gübitz G. M., Cavaco-Paulo A., 2002b. Studies of stabilization of native catalase using additives. *Enzyme Microb. Technol.*, 30, 387-391. DOI: 10.1016/S0141-0229(01)00505-1.

Curcio S., Ricca E., Saraceno A., Iorio G., Calabrò V., 2015. A mass transport/kinetic model for the description of inulin hydrolysis by immobilized inulinase. *J. Chem. Technol. Biotechnol.*, 90, 1782-1792. DOI: 10.1002/jctb.4485.

Deluca D. C., Dennis R., Smith W. G., 1995. Inactivation of an animal and a fungal catalase by hydrogen peroxide. *Arch. Biochem. Biophys.*, 320, 129-134. DOI: 10.1006/abbi.1995.1350.

Dizge N., Tansel B., 2010. External mass transfer analysis for simultaneous removal of carbohydrate and protein by immobilized activated sludge culture in a packed bed batch bioreactor. *J. Hazard. Mater.*, 184, 671-677. DOI: 10.1016/j.jhazmat.2010.08.090.

Eberhardt A. M., Pedroni V., Volpe M., Ferreira M. L., 2004. Immobilization of catalase from Aspergillus niger on inorganic and biopolymeric supports for H2O2 decomposition. *Appl. Catal. B: Environ.*, 47, 153-163. DOI: 10.1016/j.apcatb.2003.08.007.

Farkye N. Y., 2004. Cheese technology. *Int. J. Dairy Technol.*, 57, 91-98. DOI: 10.1111/j.1471-0307.2004.00146.x.

Fernández-Lafuente R., Rodriguez V., Guisán J. M., 1998. The coimmobilization of d-amino acid oxidase and catalase enables the quantitative transformation of d-amino acids (d-phenylalanine) into α-keto acids (phenylpyruvic acid). *Enzyme Microb. Technol.*, 23, 28-33. DOI: 10.1016/S0141-0229(98)00028-3.

Greenfield P. F., Kinzler D. D., Laurence R. L., 1975. Film diffusion and Michaelis-Menten kinetics in a packed-bed reactor. *Biotechnol. Bioeng.*, 17, 1555-1559. DOI: 10.1002/bit.260171014.

Illanes A., Wilson L., Vera C. (Eds.), 2014. Enzyme kinetics in a heterogeneous system, In: *Problem solving in enzyme biocatalysis*. John Wiley and Sons Ltd., Chichester, United Kingdom, 87-140.

Kalaga D. V., Dhar A., Dalvi S. V., Joshi J. B., 2014. Particle-liquid mass transfer in solid–liquid fluidized beds. *Chem. Eng. J.*, 245, 323-341. DOI: 10.1002/bit.260171014.

Mudliar S., Banerjee S., Vaidya A., Devotta S., 2008. Steady state model for evaluation of external and internal mass transfer effects in an immobilized biofilm. *Bioresource Technol.*, 99, 3468-3474. DOI: 10.1016/j.biortech.2007.08.001.

Rovito B. J., Kittrell J. R., 1973. Film and pore diffusion studies with immobilized glucose oxidase. *Biotechnol. Bioeng.*, 15, 143-161. DOI: 10.1002/bit.260150111.

Schoevaart R., Kieboom T., 2001. Combined catalytic reactions—Nature's way. *Chemical Innovation*, 31(12), 33-39.

Tarhan L., Telefoncu A., 1990. Characterization of immobilized glucose oxidase—catalase and their deactivation in a fluid-bed reactor. *Appl. Biochem. Biotechnol.*, 26, 45-57. DOI: 10.1007/BF02798392.

Tarhan L., Uslan A. H., 1990. Characterization and operational stability of immobilized catalase. *Process Biochem.*, 25(1), 14-18.

Tarhan L., 1995. Use of immobilised catalase to remove H_2O_2 used in the sterilisation of milk. *Process Biochem.*, 30, 623-628. DOI: 10.1016/0032-9592(94)00066-2.

Traher A. D., Kittrell J. R., 1974. Film diffusion studies of immobilized catalase in tubular flow reactors. *Biotechnol. Bioeng.*, 16, 419-422. DOI: 10.1002/bit.260160311.

USP Technologies Company, http://www.h2o2.com/, April 24, 2017.

Vasudevan P. T., Weiland R. H., 1990. Deactivation of catalase by hydrogen peroxide. *Biotechnol. Bioeng.*, 36, 783-789. DOI: 10.1002/bit.260360805.

Vasudeven P. T., Weiland R. H., 1993. Immobilized catalase: Deactivation and reactor stability. *Biotechnol. Bioeng.*, 41, 231-236. DOI: 10.1002/bit.260410209.

Vera-Avila L. E., Morales-Zamudio E., Garcia-Camacho M. P., 2004. Activity and reusability of sol-gel encapsulated α-amylase and catalase. Performance in flow-through systems. *J. Sol-Gel Sci. Technol.*, 30, 197-204. DOI: 10.1023/B:JSST.0000039505.49588.5d.

Zámocký M., Koller F., 1999. Understanding the structure and function of catalases: clues from molecular evolution and in vitro mutagenesis. *Prog. Biophys. Mol. Biol.*, 72, 19-66. DOI: 10.1016/S0079-6107(98)00058-3.

Received 10 October 2016
Received in revised form 9 May 2017
Accepted 23 May 2017

DE GRUYTER OPEN
www.czasopisma.pan.pl PAN POLSKA AKADEMIA NAUK www.journals.pan.pl
Chemical and Process Engineering 2017, 38 (2), 321-330
DOI: 10.1515/cpe-2017-0025
PAN

ENHANCED CHONDROCYTE PROLIFERATION IN A PROTOTYPED CULTURE SYSTEM WITH WAVE-INDUCED AGITATION

Maciej Pilarek*, Klaudia Godlewska, Aleksandra Kuźmińska, Michał Wojasiński, Katarzyna Dąbkowska

Warsaw University of Technology, Faculty of Chemical and Process Engineering, Waryńskiego 1, 00-645 Warsaw, Poland

One of the actual challenges in tissue engineering applications is to efficiently produce as high of number of cells as it is only possible, in the shortest time. In static cultures, the production of animal cell biomass in integrated forms (i.e. aggregates, inoculated scaffolds) is limited due to inefficient diffusion of culture medium components observed in such non-mixed culture systems, especially in the case of cell-inoculated fiber-based dense 3D scaffolds, inside which the intensification of mass transfer is particularly important. The applicability of a prototyped, small-scale, continuously wave-induced agitated system for intensification of anchorage-dependent CP5 chondrocytes proliferation outside and inside three-dimensional poly(lactic acid) (PLA) scaffolds has been discussed. Fibrous PLA-based constructs have been inoculated with CP5 cells and then maintained in two independent incubation systems: (i) non-agitated conditions and (ii) culture with wave-induced agitation. Significantly higher values of the volumetric glucose consumption rate have been noted for the system with the wave-induced agitation. The advantage of the presented wave-induced agitation culture system has been confirmed by lower activity of lactate dehydrogenase (LDH) released from the cells in the samples of culture medium harvested from the agitated cultures, in contrast to rather high values of LDH activity measured for static conditions. Results of the proceeded experiments and their analysis clearly exhibited the feasibility of the culture system supported with continuously wave-induced agitation for robust proliferation of the CP5 chondrocytes on PLA-based structures. Aside from the practicability of the prototyped system, we believe that it could also be applied as a standard method offering advantages for all types of the daily routine laboratory-scale animal cell cultures utilizing various fiber-based biomaterials, with the use of only regular laboratory devices.

Keywords: wave-induced agitation, small-scale animal cell culture, CP5 chondrocytes, fibrous-based scaffold, single-use bioreactor

1. INTRODUCTION

Enhancement of adherent cell proliferation inside biomaterial-based three-dimensional structures is one of the current research issues in modern bioengineering focused on development and scale-up of mammalian cell cultures. Typically applied static, i.e. non-agitated, culture conditions generally limit inoculation and proliferation efficiency due to obvious limitation of mass transfer inside biomaterial constructs (Dunn et al., 2006). Each bioprocess development improving cell proliferation in the three-dimensional inner structure of scaffolds is strongly invited to overcome these limitations.

One of the actual challenges in applications of bioengineering focused on tissue engineering is to efficiently produce as many cells as it is only possible, in the shortest time. In the static cultures the production of animal cell biomass in integrated forms (i.e. aggregates, inoculated scaffolds) is limited due to inefficient diffusion of culture medium components observed in such non-mixed culture

*Corresponding authors, e-mail: Maciej.Pilarek@pw.edu.pl

systems, especially in the case of cell-inoculated fiber-based dense 3D scaffolds, inside which the intensification of mass transfer is particularly important (Chung and Burdick, 2008; Marx, 2012). Instead of commonly applied rotating or tumbling stirrers used to induce fluid flow in classical bioreactor systems, continuously oscillating devices can be utilized for gently obtained homogeneous conditions in the systems for *in vitro* culture of fragile animal cells. In such approaches an agitation is achieved by horizontal/vertical oscillations of the culture vessel which is fixed in a rocker unit. The rocking motion is very efficient in generating waves, and the wave-induced motion in the culture container causes agitation of large volumes of culture medium (Fig. 1), and facilitates dispersion of components of a culture microenvironment (i.e. gases, nutrients, extracellularly secreted waste bioproducts) (Eibl et al., 2009).

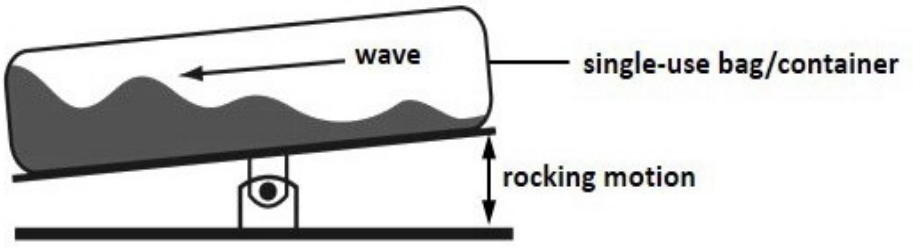

Fig. 1. An idea of a wave-induced agitation by continuous rocking motion of a disposable bag/container (i.e. a single-use bioreactor) fixed in a rocker unit

Presently, such continuously agitated bioreactor systems which utilize effectiveness of waves for culture medium mixing are readily and successfully applied in the wide types of bioprocesses not only focused on animal or insect cells (Eibl and Eibl, 2011) but also cultures of microorganisms (Junne et al., 2013), especially microalgae (Hillig et al., 2014) as well as plant (Georgiev et al., 2008) cells.

The aim of this work was to discuss the applicability of a continuous wave-induced agitation system for intensification of proliferation of chondrocytes (as an example of anchorage-dependent type of animal cells) outside and inside three-dimensional (3D) poly(lactic acid) (PLA) scaffolds. Fibrous PLA-based constructs have been inoculated with CP5 mammalian chondrocytes and then maintained in two independent incubation systems: (i) non-agitated conditions and (ii) culture system with wave-induced agitation. The volumetric glucose consumption rate (r_G) has been analyzed to recognize the metabolic activity of the CP5 cells overgrew the biomaterial structures. The death rate of the CP5 cells has been estimated based on the activity of lactate dehydrogenase (a_{LDH}) released from the cells into culture medium. SEM micrographs of the biomaterials have been used to spot distribution of the cells on the outer surface of the PLA-based constructs maintained in both examined systems.

2. MATERIALS AND METHODS

2.1. CP5 cells and culture medium

The CP5 cell line constituted by the anchorage-dependent, articular cartilage progenitor cells isolated from *Bos taurus* (Holstein-Friesian breed), was used in this work. The CP5 cells have been purchased from European Collection of Authenticated Cell Cultures (ECACC)/Health Protection Agency Culture Collection (Salisbury, UK). The CP5 chondrocytes were maintained in Dulbecco's modified Eagle medium (DMEM; Life Technologies, USA) with high glucose concentration (4.5 g L^{-1}), supplemented with GlutaMAX® (4.0 mM L-glutamine), 10 % fetal calf serum (FCS), 50 µL mL^{-1} ascorbate, 0.1 M 4-(2-hydroxyethyl)-1-piperazineethanesulfonic acid (HEPES), i.e. zwitterionic buffering agent, and antibiotics (0.05 µL mL^{-1} penicillin, 0.05 µL mL^{-1} streptomycin) at 37 °C, and 5 % of CO_2 according to

procedure applied previously (Pilarek et al., 2014). DMEM, FCS and all used chemicals were obtained from Life Technologies (USA) and were of animal cell culture certified.

2.2. PLA-based fibrous constructs

The PLA-based scaffolds (16 mm diameter, 2 - 3 mm thickness), made of 1.0-2.0 µm thin fibres electrospun in electro-hydro-dynamic atomization (EHDA) process from granulated 20 - 30 kDa PLA (Polysciences, Inc., USA) dissolved in dichloromethane:N,N-dimethylformamide (9:1, v/v) at 7 % according to procedure reported previously by Wojasiński et al. (2014). Prior to using them in culture systems, PLA scaffolds were washed and sterilized by immersion in 70 % ethanol and next dried in aseptic air for 1 h at room temperature.

2.3. Prototyped wave-induced agitation system

A prototyped wave-induced agitation system has been presented in Fig. 2. The thermostatic chamber, made with stainless-steel double walls, with inner sizes suitable for standardized multiwell-plates or flasks typically used for small-scale animal cell cultures, has been fixed on a rocking unit (Rocking Platform Shaker KL-942; JW Electronic, Poland). The constant temperature (37.0 ± 0.05 °C) inside the chamber has been obtained according to continuously flow of heated water from thermostat (Immersion Thermostat E5; Medingen, Germany) through inner space between two walls of the chamber. The rocking unit provided the possibility of smooth rocking-angle regulation from -1°/1° to -10°/10° with rocking-frequency range of 2 - 60 cpm.

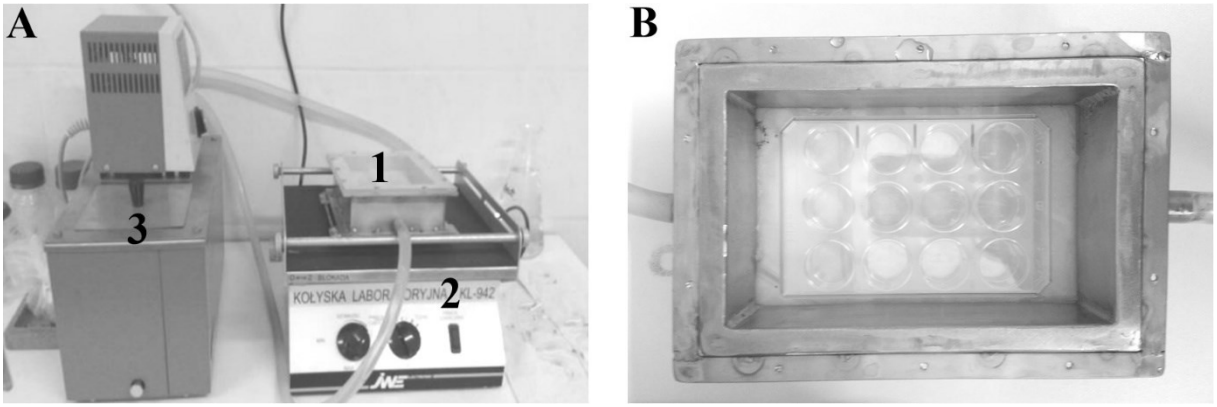

Fig. 2. The prototyped wave-induced agitation system for milliliter-scale cultures of CP5 chondrocytes on PLA-based scaffolds: A - the experimental setup including the thermostatic chamber for incubation of standardized culture multiwell-plates/flask (1), the rocking unit providing the wave-induced agitation (2) and the water thermostat (3); B - the standardized culture multiwell-plate fixed inside the double walls thermostatic chamber

2.4. Experimental procedure

The CP5 cells were cultured on PLA-based fibrous scaffolds immersed in 1.0 mL of DMEM in 24-deepwell-plates (Becton-Dickinson, USA) used as milliliter-scale culture vessels. Two independent culture systems have been maintained: (i) non-agitated conditions and (ii) culture with wave-induced agitation (rocking angle: -5° / 5°, rocking-frequency: 20 cpm). Both of compared culture systems were triplicated to obtain statistically credible values of quantitative parameters characterizing the proliferation of cells. Inoculum of CP5 cell line was prepared from standard nearly, i.e. 75 - 80 %, confluence cultures, passaged every 4 - 5 days. Briefly, cells were washed with PBS (Life

Technologies, USA), incubated in 0.05 % trypsin (Life Technologies, USA) for ca. 3 min at 37 °C, the number of cells was estimated using Malassez hemocytometer (Brand, Germany), then cells were suspended in DMEM and finally pipetted into the 24-deepwell-plates with scaffolds to obtain initial density of $5.0 \cdot 10^5$ cells mL^{-1}. The samples of culture medium have been harvested every 24 hours from both of studied culture systems containing proliferating CP5 cells for determination of the glucose concentration and the lactate dehydrogenase activity. Then additionally, to prevent cultured CP5 cells from detrimental effects caused by low concentrations of nutrients and/or high levels of extracellular secreted toxic metabolites, or cell-lysis products soluble in culture medium, the DMEM-based medium was fully exchanged for the fresh culture medium after every 24 hours of the experiment in all inoculated wells of the multiwell-plates.

2.5. Analytical procedures

Glucose concentration has been determined according to the enzymatic BioMaxima glucose-determination kit (BM-G; BioMaxima, Poland) procedure. The analytical method which has been applied in the studies is based on the results of two subsequently proceeded enzymatic reactions catalyzed by glucose oxidase (first step) and peroxidase (second step of the procedure). In the first step of the reaction, glucose is oxidizing into gluconic acid with release of hydrogen peroxide. In the second step, hydrogen peroxide molecules are selectively reacting with phenol and 4-aminoantypirine which finally results in colored chinonoimine appearance in the samples. The absorbance of chinonoimine has been measured at 500 nm vs. reference absorbance of pure BioMaxima reagent sample (i.e. without chinonoimine). Glucose concentration in the samples of culture medium (C_G) was calculated based on known values of absorbance measured for: the sample of culture medium (A_{CM}), as well as the standard (1.0 $mg \cdot mL^{-1}$) solution of glucose (A_G), with the following equation:

$$C_G = \frac{A_{CM}}{A_G}\left[mg \cdot mL^{-1}\right] \tag{1}$$

Based on the results of the C_G, the volumetric glucose consumption rate (r_G) can be easily determined as follows:

$$r_G = \frac{C_G}{t}\left[\frac{mg \cdot mL^{-1}}{day}\right] \tag{2}$$

where t represents culture period (i.e. day).

Activity of lactate dehydrogenase (a_{LDH}) has been determined according to the BioMaxima lactate dehydrogenase activity determination kit (BM-LDH; BioMaxima, Poland) procedure. The analytical method is based on the results of the reduction of pyruvic acid catalyzed by lactate dehydrogenase (LDH) released from damaged cells, in the presence of NADH. LDH released from cells reduces pyruvic acid. The changes of absorbance in time (i.e. 1 min) measured at 340 nm are related to a_{LDH} in a sample of the culture medium as following:

$$a_{LDH} = \frac{V_T \cdot 10^5}{\varepsilon_{NADH}^{340nm} l V_S} \cdot \frac{\Delta A}{t} = 267.2 \frac{\Delta A}{t}\left[\mu kat \cdot L^{-1}\right] \tag{3}$$

where:

V_T - total volume of reaction mixture (V_T = 1.01 mL), $\varepsilon_{NADH}^{340nm}$ - molar absorbance coefficient for NADH at 340 nm ($\varepsilon_{NADH}^{340nm}$ = $6.3 \cdot 10^2$ m^2 mol^{-1}), l - light path length (i.e. thickness of the measuring cuvette; l = 1 cm), V_S - volume of sample (V_S = 0.01 mL), ΔA - change of absorbance, t - time (t = 60 s).

2.6. SEM-imaging procedure

The fibrous PLA-based scaffolds were analyzed with the Phenom (FEI, USA) scanning electron microscope (SEM) supported with producer's image software. The samples selected for SEM analysis firstly were incubated in 0.5 % OsO_4 for 1 h at 4°C, then dehydrated/desiccated with anhydrous ethanol, next automatically dried (Leica EM CPD300, Germany), and finally coated with 15-nm layer of gold (K550 Emitech, USA).

3. RESULTS

To show the feasibility of the wave-inducing agitation for metabolic activity of CP5 cells overgrowing the PLA-scaffolds, we have analyzed r_G and a_{LDH} in samples of the culture medium maintained in both compared, i.e. non-agitated and wave-agitated culture systems. r_G may be recognized as the parameter which quantitatively characterizes metabolic activity of the maintained cells. LDH is an enzyme found in all kinds of animal cells. Because it is released during cell or tissue damage, it may be recognized as a marker of cell destruction or damage. Due to this, a_{LDH}, i.e. the activity of intracellular LDH released from cells into the culture medium, may be identified as quantitative parameter for identification of the culture system which negatively or detrimentally influences cells which are incubated in defined culture system, with an effect of extracellularly leaking of such enzyme-based indicator.

The values of r_G determined for both compared culture systems have been presented in Fig. 3. Significantly higher values of r_G have been observed for CP5 cells maintained within PLA-scaffolds in the culture system with wave-induced agitation when compared to rather moderate values of r_G values noted for the same cells cultured in static, i.e. non-agitated, conditions. In the case of 4 - 5 days of culture the values of r_G measured for the system with wave mixing (i.e. 1.8, 2.1 and 2.2 mg·mL^{-1}·day^{-1} in consecutive days of culture) were up to 3× higher than the r_G values noted for the static system (i.e. 0.67, 0.71 and 0.83 mg·mL^{-1}·day^{-1} in consecutive days of culture).

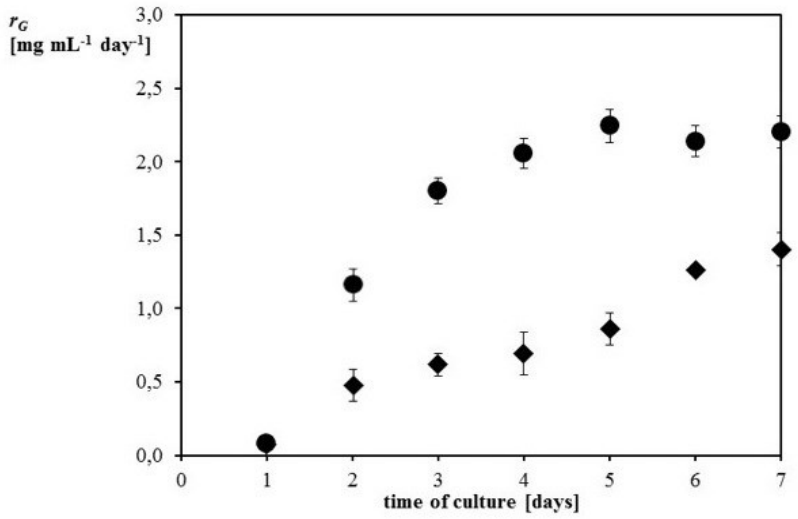

Fig. 3. Values of r_G determined for CP5 cells cultures within PLA-based scaffolds in two compared systems: non-agitated culture (◆) and culture with wave-induced agitation (●)

The values of a_{LDH} determined in culture medium from two compared culture systems have been presented in Fig. 4. The level of a_{LDH} determined in samples from the wave-agitated culture system was significantly lower for the whole time-range of compared cultures. In the case of 4 - 6 days of culture the values of a_{LDH} measured for the static culture system (i.e. 6.8, 6.9 and 7.3 µkat·L^{-1} in consecutive

days of culture) were at least twice higher than the a_{LDH} values noted for the wave-mixed system (i.e. 3.2, 3.4 and 3.4 μkat·L^{-1} in consecutive days of culture).

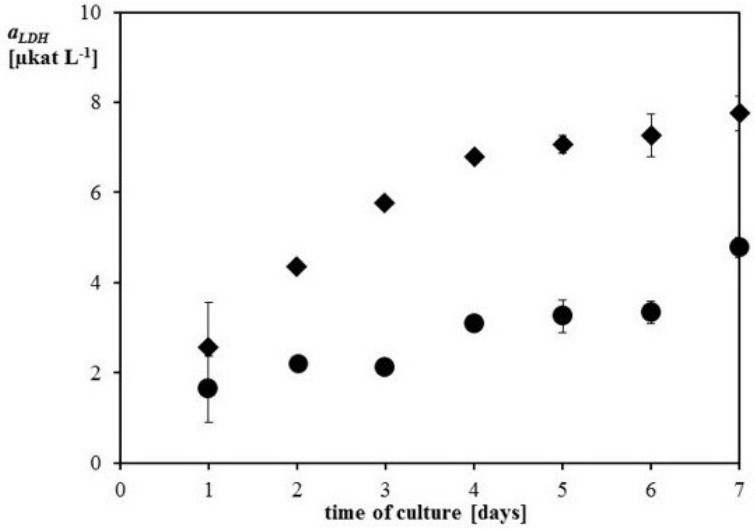

Fig. 4. Values of a_{LDH} determined in samples of culture medium harvested in parallel from two compared systems: non-agitated culture (◆) and culture with wave-induced agitation (●), which have been used for CP5 cells maintaining within PLA-based scaffolds

The SEM micrographs of the biomaterials have been used to spot distribution of the cells on the outer surface of the PLA-based constructs maintained in both examined systems. In the case of culture conditions characterizing our experiments, CP5 chondrocytes adhered to fibres of PLA on the outer surface of used biomaterial constructs after 7 days of cultures in both compared culture systems have been presented in Fig. 5. It can be clearly seen that CP5 cells have proliferated more intensively on the outer surface of the biomaterial maintained in the culture system with wave-induced agitation (Fig. 5B) when compared to rather limited distribution of the cells in the case of constructs incubated in the non-agitated culture system (Fig. 5A). Robust and intensive proliferation of CP5 chondrocytes on the PLA-based biomaterial observed in the wave-agitated system resulted in progressive invasion of the outer area, i.e. as overgrew of the constructs by the cells and formation of the large cell-clusters on the surface of the fibrous biomaterial.

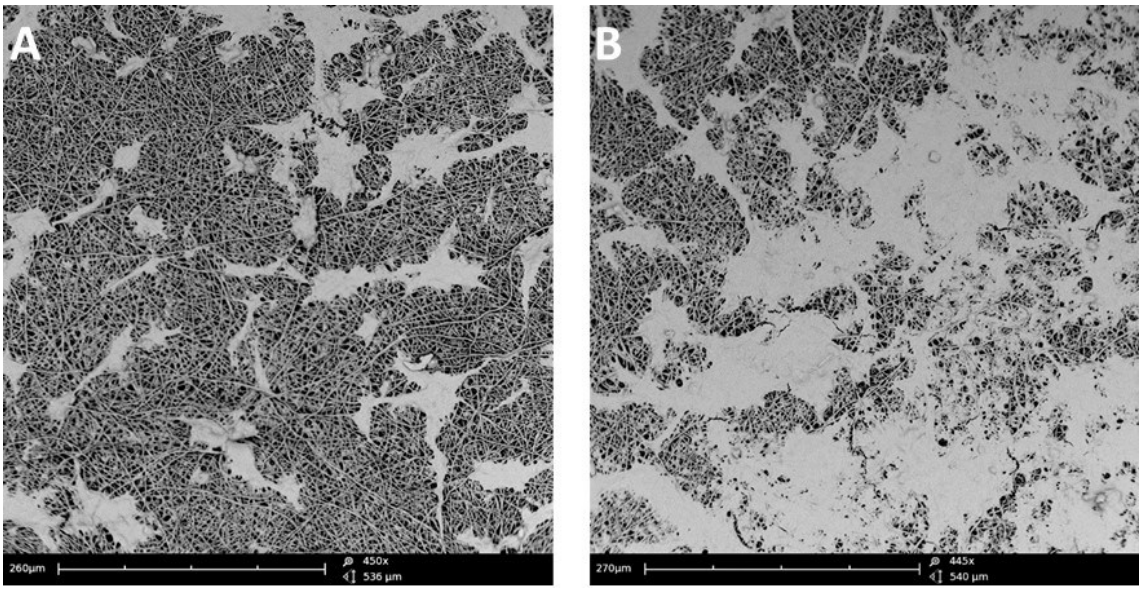

Fig. 5. SEM micrographs of the PLA-based scaffolds inoculated with CP5 chondrocytes and maintained in two compared systems (7th day of cultures): non-agitated culture (A) and culture with wave-induced agitation (B)

4. DISCUSSION

Due to fragility of animal cells resulting from lack of cell walls, which triggers extreme sensitivity of animal cells to shear stress forces generated in typical (i.e. mechanically agitated) cultures, the culture systems providing low-grade forces are needed as proper environment for animal cells *in vitro* propagation. The wave-induced culture system should be taken into consideration as the suitable solution for cells cultured within biomaterial-based constructs, in which gradients of ingredients of culture medium, extracellularly secreted waste metabolites as well as O_2 and CO_2, are usually observed inside the biomaterial and in its vicinity. Mass transfer limitations are identified as substantial problems in static (i.e. non-agitated) conditions typically applied in small-scale (i.e. mililiter-scale) cultures of adherent mammalian cells (Marx, 2012; Matsuura, 2006). Bearing all this in mind, we propose the prototyped continuously agitated mililiter-scale system which utilizes effectiveness of waves for culture medium mixing as the system which can intensify the yield of various types of bioprocesses proceeded with animal cells, especially those which are prepared with application of biomaterial-based 3D scaffolds.

Chondrocytes, as the CP5 cells, have been chosen to perform experiments because they are usually *in vitro* cultured within 3D scaffolds in high density of extracellular matrix. A 3D environment of the culture system is necessary for the maintenance of the native phenotype by isolated chondrocytes cultured *in vitro*, as chondrocytes maintained in typical monolayered form tend to dedifferentiate into fibroblast form (Noriega et al., 2013). Previously, the 3D scaffolds made of micrometre-scale diameters PLA fibres produced by electrospinning process were successfully investigated (e.g. Kwon et al., 2013; Li et al., 2006; Pilarek et al., 2014; Wojasiński et al., 2014) as a synthetic polymeric biomaterial for chondrocyte implant development, whose properties, such as mechanical strength, degradation rate and dimensions can all be easily controlled. There is a distinct need to develop alternative techniques of mass transfer intensification within such 3D dense biomaterial-based constructs/implants to prevent the expansion of detrimental effects caused by progressive necrosis of the cells (Keeney et al., 2011; Pilarek et al., 2014).

High rates of r_G, which occurred in the case of CP5 chondrocytes cultured in the prototyped system with wave-induced agitation, during almost the whole time span (i.e. from 2nd day until end) of the experiment (see Fig. 3) may be the result of high metabolic activity of the cells in culture conditions provided by the wave-induced agitation in contrast to rather moderate levels of r_G values noted for the same cells but maintained in the reference non-agitated conditions. The exception to this are similar values of r_G estimated for both compared systems on 1st day of cultures, which probably resulted from the effects of the adaptation of cells to the culture conditions after passaging during lag-phase.

The determination of intracellular LDH activity, i.e. a_{LDH}, in a culture medium may be recognized as the quantitative method of the death rate of CP5 cell determination because LDH is only leaked from damaged cells (Chan et al., 2013). Significantly lower values of a_{LDH} determined in the samples of culture medium harvested from the system with wave-induced agitation, compared to up to three-times higher values of a_{LDH} in the samples of medium from non-agitated system (see Fig. 4) prove the lack of negative or detrimental influences of culture conditions on maintained cells provided by the wave-induced agitation applied in our prototyped system. We are also hypothesizing that the wave-induced agitation results in intensification of the flow of culture medium through spaces between fibres inside the 3D structure of PLA-based constructs used as scaffolds for proliferating CP5 cells. Therefore more homogenous culture conditions have been probably obtained in the studied culture system if related to the static, i.e. non-mixed, conditions applied in the reference culture system. Accordingly, the mass transfer limitations inside the used biomaterial constructs, e.g. inefficient diffusion of nutrients to cells, have been overcome in the presented culture system mixed by the wave-induced agitation.

As was presented in the results section, the growth of CP5 cells maintained in non-mixed conditions has been rather limited (see Fig. 5A). Robust and intensive proliferation of CP5 chondrocytes, as well as enhanced cell-cluster formation on the fibrous PLA-based scaffolds, have been achieved in the wave-induced culture system (see Fig. 5B). The phenotype of the CP5 chondrocytes on the PLA scaffolds shown by SEM is rather not typical for the native morphology in cartilage extracellular matrix. But the morphology of cells cultured under experimental conditions is in accordance with the results of previously published studies focused on proliferation of cartilage cells on fibrous scaffolds (Hogrebe et al., 2017; McCullen et al., 2012; Pilarek et al., 2014). Such phenotype differences were probably caused by two factors. One of them is the progenitor-nature of the cells applied as inoculum (Dowthwaite et al., 2004). The second reason can be interpreted as the mechanical influence of culture conditions on proliferating biomass in the presented *in vitro* system with gentle wave-type mixing. The flow of culture medium forced by continuous wave-induced agitation intensifies the mass transfer inside 3D constructs but also can additionally influence chondrocyte morphology according to possible mechanical stimulation of proliferating cells. Such hypothetical effects are consistent with conclusions considered previously by other authors (e.g. Chung and Burdick, 2008; Noriega et al., 2013; Vunjak-Novakovic et al., 1999), that *in vitro* cultured isolated chondrocytes should be maintained under culture conditions supporting mechanical stimulation of the cells because mechanical stimuli (e.g. hydrodynamic effects caused by mixing of culture medium) have been recognized as one of the key factors which stabilizes morphology of the cells and influences positively the mechanical properties of cartilage implants. Summarizing, the results of enhanced CP5 cell proliferation outside and inside 3D fibrous-based PLA-constructs when incubated in the proposed prototyped simple small-scale system with the wave-type mixing are proving hypothetic applicability of such a culture system for a range of animal/human cells (e.g. fibroblasts, osteoblasts, vascular cells, etc.) which are *in vitro* cultured within various porous polymeric bioresorbable scaffolds utilized in tissue engineering.

5. CONCLUSIONS AND OUTLOOK

Summarizing, the following conclusions can be drawn based on the results of the experiments presented and discussed above:

- significantly higher values of r_G, denoting high metabolic activity of cells, have been determined for CP5 chondrocytes cultured in the prototyped system with wave-induced agitation than for the same cells cultured in the reference non-mixed conditions;
- up to three-times lower values of a_{LDH} (i.e. intracellular enzyme marker) have been determined in the samples of culture medium harvested from the system with wave-induced agitation, compared to values of the parameter obtained for the samples of medium from non-agitated system;
- higher metabolic activity (represented by values of r_G) and lower level of activity of intracellular enzymatic marker (i.e. a_{LDH}) determined in samples of culture medium harvested from the cultures of CP5 chondrocytes proceeded in the system with wave-induced agitation unambiguously indicate that such a system can be recognized as the suitable environment for 3D cultures of CP5 chondrocytes;
- maintaining of CP5 chondrocyte-seeded fibrous PLA-based 3D scaffolds under conditions provided by the low-shear culture system with wave-induced agitation results in enhanced proliferation of cells on the surface of the biomaterial constructs.

Aside from the practicability of the prototyped system, further studies on quantitative characteristic of mass transfer in the presented prototyped milliliter-scale culture system with wave-induced agitation must be performed to fully recognize and identify in detail the advantages of the system. Nevertheless we believe that the developed culture system could also be applied as a standard method offering

advantages for all types of the daily routine laboratory-scale animal cell cultures utilizing various fibre-based biomaterials, with the use of only regular, and typically available in laboratory, devices.

This work has been supported by the budget sources for The National Centre for Science, Poland, Grant no. DEC-2015/17/B/ST8/00631.

SYMBOLS

A_{CM}	absorbance of culture medium
A_G	absorbance of standard solution of glucose
C_G	glucose concentration in the samples of culture medium, mg·mL^{-1}
l	light path length, cm
r_G	volumetric glucose consumption rate, mg·mL^{-1}·day^{-1}
t	time, s
V_S	volume of sample, mL
V_T	total volume of reaction mixture, mL

Greek symbols

a_{LDH}	activity of lactate dehydrogenase, µkat·L^{-1}
ΔA	change of absorbance
$\varepsilon_{NADH}^{340nm}$	molar absorbance coefficient for NADH at 340 nm, m^2·mol^{-1}

Superscripts

340nm	wavelenght of peak absorption of NADH

Subscripts

CM	culture medium
G	glucose
LDH	lactate dehydrogenase
NADH	reduced form of nicotinamide adenine dinucleotide
S	sample
T	total (e.g. total volume)

Abbreviations

3D	three-dimensional
BM-G	BioMaxima glucose concentration determination kit
BM-LDH	BioMaxima lactate dehydrogenase activity determination kit
CP5	mammalian (*Bos taurus*) chondrocyte progenitor cell line
DMEM	Dulbecco's modified Eagle medium
EHDA	electro-hydro-dynamic atomization
FCS	fetal calf serum
HEPES	4-(2-hydroxyethyl)-1-piperazineethanesulfonic acid (zwitterionic-based buffering agent)
LDH	lactate dehydrogenase
NADH	reduced form of nicotinamide adenine dinucleotide
PBS	phosphate-buffered saline buffer
PLA	poly(lactic)acid
SEM	scanning electron microscopy

REFERENCES

Chan F.K.-M., Moriwaki K., de Rosa J.M., 2013. Detection of necrosis by release of lactate dehydrogenase activity. *Methods Mol. Biol.*, 979, 65-70. DOI: 10.1007/978-1-62703-290-2_7.

Chung C., Burdick J.A., 2008. Engineering cartilage tissue. *Adv. Drug Deliv. Rev.*, 60, 243-262. DOI: 10.1016/j.addr.2007.08.027.

Dowthwaite G.P., Bishop J.C., Redman S.N., Khan I.M., Rooney P., Evans D.J.R., Haughton L., Bayram Z., Boyer S., Thomson B., Wolfe M. S., Archer C. W., 2004. The surface of articular cartilage contains a progenitor cell population. *J. Cell. Sci.*, 117, 889-897. DOI: 10.1242/jcs.00912.

Dunn J.C.Y., Chan W.Y., Christini V., Kim J.S., Lowengrub J., Singh S., Wu B.M., 2006. Analysis of cell growth in three-dimensional scaffolds. *Tissue Eng.*, 12, 705-716. DOI: 10.1089/ten.2006.12.705.

Eibl R., Eibl D. (Eds.) *Single-use technology in biopharmaceutical manufacture*. Wiley, Hoboken 2011.

Eibl R., Werner S., Eibl D., 2009. Bag bioreactor based on wave-induced motion: characteristics and applications. *Adv. Biochem. Eng. Biotechnol.*, 115, 55-87. DOI: 10.1007/10_2008_15.

Georgiev M., Weber J., Maciuk A., 2009. Bioprocessing of plant cell cultures for mass production of targeted compounds. *Appl. Microbiol. Biotechnol.*, 83, 809-823. DOI: 10.1007/s00253-009-2049-x.

Hillig F., Pilarek M., Junne S., Neubauer P., 2014. Cultivation of marine microorganisms in single-use systems. *Adv. Biochem. Eng. Biotechnol.*, 138, 179-206. DOI: 10.1007/10_2013_219.

Hogrebe N.J., Reinhardt J.W., Gooch K.J., 2017. Biomaterial microarchitecture: A potent regulator of individual cell behavior and multicellular organization. *J. Biomed. Mater. Res. A.*, 105, 640-661. DOI: 10.1002/jbm.a.35914.

Junne S., Solymosi T., Oosterhuis N., Neubauer P., 2013. Cultivation of cells and microorganisms in wave-mixed disposable bag bioreactors at different scales. *Chem. Ing. Tech.*, 85, 57-66. DOI: 10.1002/cite.201200149.

Keeney M., Lai J.H., Yang F., 2011. Recent progress in cartilage tissue engineering. *Curr. Opin. Biotechnol.*, 22, 734-740. DOI: 10.1016/j.copbio.2011.04.003.

Kwon H., Sun L., Cairns D.M., Rainbow R.S., Preda R.C., Kaplan D.L., Zeng L., 2013. The influence of scaffold material on chondrocytes under inflammatory conditions. *Acta Biomater.*, 9, 6563-6575. DOI: 10.1016/j.actbio.2013.01.004.

Li W.J, Cooper J.A, Mauck R.L., Tuan R., 2006. Fabrication and characterization of six electrospun poly(alpha-hydroxy ester)-based fibrous scaffolds for tissue engineering applications. *Acta Biomater.*, 4, 377-385. DOI: 10.1016/j.actbio.2006.02.005.

McCullen S.D., Autefage H., Callanan A., Gentleman E., Stevens M.M., 2012. Anisotropic fibrous scaffolds for articular cartilage regeneration. *Tissue Eng. Part A.*, 18, 2073-2083. DOI: 10.1089/ten.tea.2011.0606.

Marx U., 2012. Trends in cell culture technology. *Adv. Exp. Med. Biol.*, 745, 26-46. DOI: 10.1007/978-1-4614-3055-1_3.

Matsuura T., 2006. Bioreactors for 3-dimensional high-density culture of human cells. *Human Cell.*, 19, 11-16. DOI: 10.1111/j.1749-0774.2005.00002.x.

Noriega S., Mamedov T., Turner J.A., Subramanian A., 2007. Intermittent applications of continuous ultrasound on the viability, proliferation, morphology, and matrix production of chondrocytes in 3D matrices. *Tissue Eng.*, 13, 611-618. DOI: 10.1089/ten.2006.0130.

Pilarek M., Grabowska I., Senderek I., Wojasiński M., Janicka J., Janczyk-Ilach K., Ciach T., 2014. Liquid perfluorochemical-supported hybrid cell culture system for proliferation of chondrocytes on fibrous polylactide scaffolds. *Bioprocess Biosyst. Eng.*, 37, 1707-1715. DOI: 10.1007/s00449-014-1143-3.

Vunjak-Novakovic G., Martin I., Obradovic B., Treppo S., Grodzinsky A.J., Langer R., Freed L.E., 1999. Bioreactor cultivation conditions modulate the composition and mechanical properties of tissue-engineered cartilage. *J. Orthop. Res.*, 17, 130-138. DOI: 10.1002/jor.1100170119.

Wojasiński M., Pilarek M., Ciach T., 2014. Comparative studies of electrospinning and solution blow spinning processes for the production of nanofibrous poly(L-lactic acid) materials for biomedical engineering. *Polish J. Chem. Technol.*, 16, 43-50. DOI: 10.2478/pjct-2014-0028.

Received 06 October 2016
Received in revised form 08 May 2017
Accepted 24 May 2017

www.czasopisma.pan.pl PAN www.journals.pan.pl
Chemical and Process Engineering 2017, 38 (2), 331-342
DOI: 10.1515/cpe-2017-0026

THE EFFECT OF WETTING ON THE COURSE OF THE DRUM GRANULATION

Michał Błaszczyk[1], Andrzej Heim[2], Tomasz P. Olejnik[*3]

[1]Lodz University of Technology, The Institute of Turbomachinery, ul. Wólczańska 219/223, 90-924 Łódź, Poland

[2]Lodz University of Technology, Department of Process Equipment, ul. Wólczańska 213, 90-924 Łódź, Poland

[3]Lodz University of Technology, The Institute of Food Technology and Analysis, ul. Stefanowskiego 4/10, 90-924 Łódź, Poland

This paper presents the results of experimental drum granulation of silica flour with the use of wetting liquids with different values of surface tension. Additionally, different liquid jet breakup and different residual moisture of the bed were applied in the tests. The process was conducted periodically in two stages: wetting and proper granulation, during which no liquid was supplied to the bed. The condition of the granulated material after the period of wetting (particle size distribution and moisture of separate fractions) and a change in the particle size distribution during the further conduct of the process (granulation kinetics) were determined.

Keywords: drum granulation, surface tension, particle size distribution

1. INTRODUCTION

The agglomerative non-pressure granulation of powders in the flowing layer of material despite some imperfections (the product is polydisperse (Obraniak and Gluba, 2008), and the mechanical strength of granules is lower in comparison to the granulation obtained in the pressure), is widely applied at the industrial scale. Its advantages include simplicity of the device design and low energy expenditures for conducting the process. Drum granulation is one of the ways to realize this granulation (Obraniak and Gluba, 2011; Obraniak and Gluba, 2012a). An important element of this way of agglomeration is wetting the bed by means of liquid which by creating the so-called liquid bridges enables to create bonds between the raw material particles (Hapgood et al. 2002; Nguyen et al. 2009). This phenomenon which has a significant effect on granulation and its course depends on the amount of the wetting liquid (Marín Rivera et al. 2017; Ramachandran Rohit et al. 2008; Smirani-Khayati et al. 2009) and its properties, i.e. viscosity and surface tension (Hotta et al., 1974; Opaliński, 2001; Pepin et al., 2000; Rajniak et al., 2007; Willet et al., 2003). However, previous theoretical analyses and experimental studies do not enable the unambiguous evaluation of the effect of the bed wetting conditions on the granulation process course.

During the selection of a binding agent, forces occurring during the collision of two spherical particles were analyzed theoretically (Ennis et al., 1990; Ennis et al., 1991). The authors introduced the Stokes number, the value of which is inversely proportional to the binding liquid viscosity and which does not depend on its surface tension, to describe the phenomenon. This theory was modified by Nienow (Nienow, 1995), demonstrating the need to take also surface tension of the liquid phase into account.

*Corresponding authors, e-mail: tomasz.olejnik@p.lodz.pl

He stated, based on experiments, that the surface tension has a greater effect on the granulation process than the liquid viscosity. Conclusions in both cases are more of qualitative than quantitative nature. Also the effect of non-ionic surfactants on the shape, size and strength of granules was examined (Junnila, 1988). A mixture of cellulose and corn starch was used as the study material, while aqueous solutions of polysorbate 80 were used to wet the bed. It was found that the addition of a surfactant causes a decrease in the number of fine granules with the simultaneous formation of excessively large granules. The meagerness of results of works concerning particularly the effect of liquid surface tension on the course of flow granulation justifies conducting further studies concerning this question.

2. AIM OF THE STUDY

The aim of the study was to examine the effect of the bed wetting conditions on the course of drum granulation, and in particular:

- surface tension of the wetting liquid,
- the diameter of drops of the wetting liquid,
- the residual moisture of the bed.

2.1. Description of the research methodology

Granulation trials were conducted in a drum granulator with the diameter of 0.6 m and length of 0.4 m. The drum had 8 lengthwise dividers attached to its internal wall. The drum rotations in all trials were the same and were equal to 15 s^{-1}. It corresponded to 0.275 n_{critical}. Adopting such a value of the drum rotational speed enabled to obtain the desired, cascade motion of the material during the whole cycle of the process. The degree to which the drum was filled was also constant and was equal to 15%.

Silica flour, whose granulometric composition is shown in Fig. 1, was used as the granulated material. The average dimension of flour particles was equal to $d_{32}^{(m)} = 0.024$ mm, while density of loosely heaped bed $\rho_l = 951$ kg/m^3, and concentrated $\rho_z = 1525$ kg/m^3.

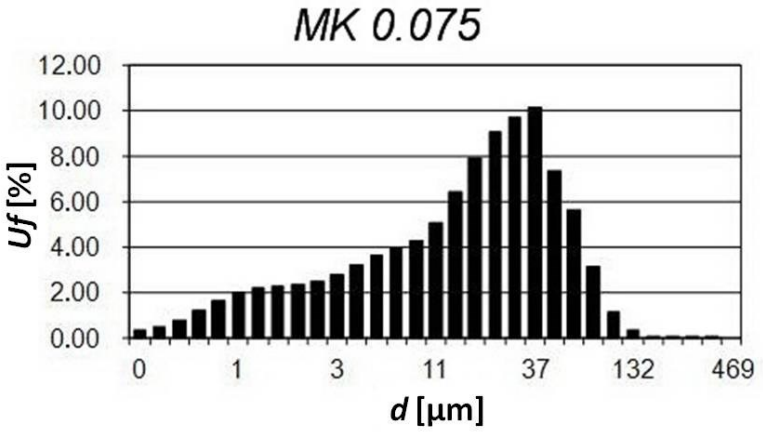

Fig. 1. Granulometric composition of silica flour used in the tests

Distilled water and aqueous solutions of polyoxyalkene glycol ether of lauryl alcohol, under the trade name of Rokanol L4P5, were used to wet the bed. The Rokanol concentration in separate trials was from 0.01% to 0.04%, which caused a significant decrease in the liquid surface tension, and at the same time small changes in viscosity. Properties of solutions used are shown in Table 1.

Table 1. Properties of used wetting liquids

	Water	0.01%	0.02%	0.03%	0.04%
Surface tension, $\gamma \times 10^3$ [N/m]	71.97	54.79	42.40	37.61	35.04
Viscosity at 25°C $\eta \times 10^3$[Pa s]	0.898	0.880	0.864	0.846	0.820

Wetting parameters were established experimentally based on the initial tests. The wetting liquid was sprayed using a Spraying System Deutschland GmbH pneumatic nozzle with 2050 head. The highest mono-dispersion of the drops jet was obtained at the liquid flow rate of 0.006 m^3/h and air flow rates between 1.25 and 2 m^3/h. Four air flow rates were used and the obtained average dimensions of drops $d_{32}^{(k)}$ are shown in Table 2.

Table 2. Sauter mean diameters of the sprayed liquid drops

Q_{air} [m^3/h]	1.25	1.50	1.75	2.00
$d_{32}^{(k)}$ [μm]	23.22	20.24	14.85	13.13

From the initial tests, it was determined that for dry silica flour, moisture enabling to conduct the granulation process is contained in the range from 0.19 to 0.21 g liquid/g dry matter of the powder. Below this limit value, granulation does not occur, forming only nuclei of nucleation in the bed, without the possibility of their growth to the size of granules. However, after exceeding the upper limit value of moisture, the over-wetted material sticks to the granulator walls. 4 values of moisture were selected for testing: 0.190; 0.195; 0.200 and 0.205 g liquid/g dry matter of the powder, respectively.

The granulation process was conducted in the periodic way in two stages: wetting of the bed and the proper granulation, without supplying the liquid to the granulated material. This imitated the continuous process, during which, in the initial section of the drum, flowing and moving material is wetted, while in the next section only shaping of the product occurs. At the constant liquid flow rate, times of the first stage (wetting) differed from each other and in boundary cases were equal to 841 s and 974 s, respectively.

Following the end of wetting, a sample was taken and its particle size distribution and values of moisture of separate fractions were determined. During the second stage of the process, in which the liquid was not supplied to the bed, samples of the granulated material were taken after 240, 480,960, 1440 and 1920 s, respectively when the process was interrupted, because the phenomenon of sticking the granulated material to the drum occurred. For separate times of granulation, particle size distribution of the granulated material was determined.

3. RESULTS

3.1. The wetting stage

Based on the sieve analysis results of the material samples taken following the wetting, a significant share of the non-granulated material was determined in all granulation samples. The material which passed through a sieve with a mesh size of 1 mm was considered the non-granulated material. The share of this non-granulated part of the material as well as the particle size distribution of the granules obtained after the wetting, depended significantly on the bed wetting conditions. Examples of this are shown in Figs. 2, 3 and 4. The dependence character for different parameter sets is similar in all cases.

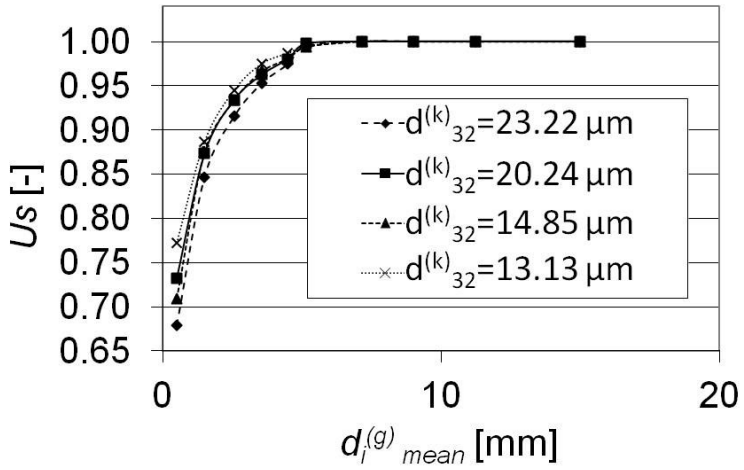

Fig. 2. The exemplary comparison of granulometric compositions of the bed after the wetting stage obtained for different degrees of the wetting liquid jet breakup, for $\gamma = 35.04 \cdot 10^{-3}$ N/m and $w = 0.2$ g liquid/g dry matter

The effect of wetting liquid drops size is shown in Fig. 2. It indicates that along with the increase in the dimension of drops, the share of the non-granulated material decreases. The increase in the wetting liquid drop diameter, which results in the increase in the weight of the liquid, enhanced the probability of local overwetting in the bed, which in turn meant creating kernel of granule. The wetting liquid surface tension has a significantly smaller effect (Fig. 3). In this case, the amount of the non-granulated material increases along with a decrease in the value of this parameter, which is probably the result of lowering of the mechanical durability of granules and their disintegration during circular movement.

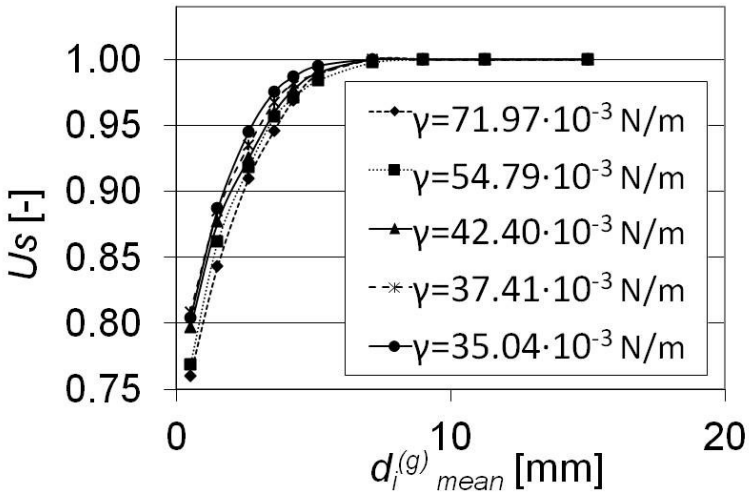

Fig. 3. The exemplary comparison of granulometric compositions of the bed after the wetting stage obtained using liquids with different values of surface tension, for diameters of drops $d_{32}^{(k)} = 20.24$ µm and moisture content $w = 0.19$ g liquid/g dry matter

However, the amount of the non-granulated material after the period of wetting depends essentially on the residual moisture of the bed (Fig. 4). An increase in this moisture means better kernel yielding and an increase in the number of liquid bonds between the material grains, which in consequence significantly decreases the amount of the non-granulated material. For the most beneficial set of parameters in this regard ($d_{32}^{(k)} = 23.22$ µm, $\gamma = 71.97 \cdot 10^{-3}$ N/m and $w = 0.205$ g liquid/g dry matter), the smallest amount of the non-granulated material equal to 62 % by weight was obtained after the period of wetting.

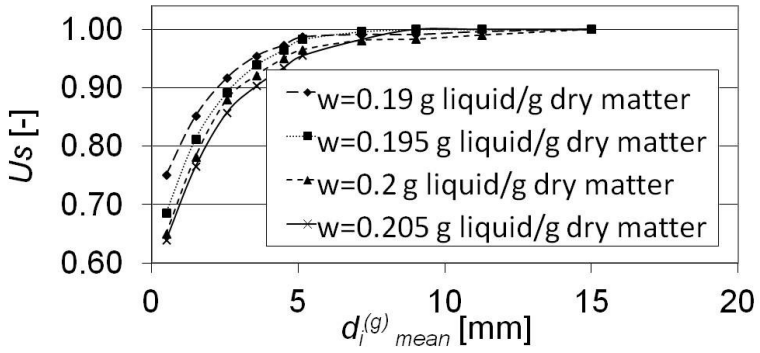

Fig. 4. The exemplary comparison of the granulometric compositions of the bed after the wetting stage obtained for different values of residual moisture, at $d_{32}^{(k)}$ = 23.22 μm and $\gamma = 54.79 \cdot 10^{-3}$ N/m

Also the moisture distribution in granules from separate size fractions was examined and it was determined that this distribution is different during the application of the wetting liquid with a different value of surface tension. In all cases in the smallest granules (up to about 5 mm) along with an increase in the granules dimensions, their moisture increased, while for large granules (over 5 mm), this dependence was different during the application of liquids differing in the value of surface tension. For clear water, a further increase in moisture with an increase in granules dimensions occurred, while for the solution with the lowest value of surface tension, a clear decrease in moisture in granules with larger dimensions was observed. During the application of liquid with intermediate values of surface tension, results within these boundaries were obtained. Exemplary results for one of the trials are shown in Fig. 5.

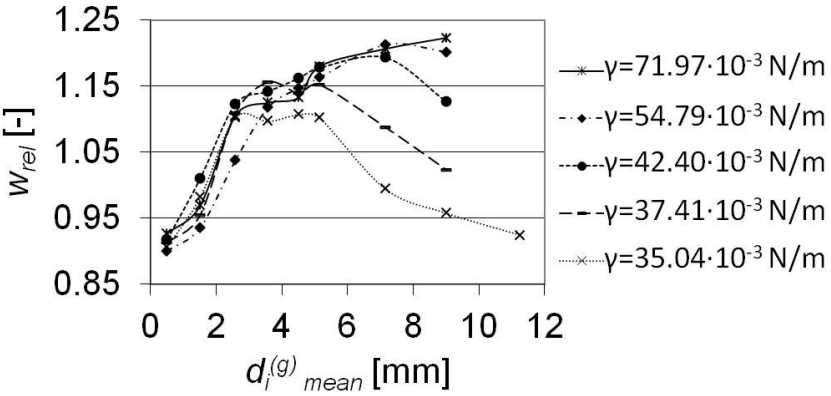

Fig. 5. The comparison of relative moisture values of separate fractions of the bed for different values of the wetting liquid surface tension ($d_{32}^{(k)}$= 13.13 μm; w = 0.2 g liquid/g dry matter)

The presented results indicate that a decrease in the wetting liquid surface tension facilitates its penetration to the layer of the granulated material, which intensifies the initial agglomeration process. At the lowest value of the liquid surface tension, particles of the primary material are attached to larger agglomerates more intensively, which causes a decrease in the relative moisture of these large granules.

3.2. The stage of proper granulation

During the second stage, the following phenomena occur simultaneously (Heim et al., 2000; Iveson et al. 2001; Obraniak and Gluba, 2012b; Sastry and Fuerstenu, 1973):

- multiple layers of the non-granulated material on the granules formed in the first stage,
- smaller granules' bonding,

- wearing of the primary material particles (separating from the granules' surface),
- breakup of granules with the insufficient strength,
- increase in the granule strength as a result of their consolidation.

However, it is assumed that due to the lack of wetting the bed from the primary material (single particles), new nuclei of granules are not formed, and thus the mechanism of enucleation does not occur. The mechanisms enumerated above cause a change in the particle size distribution of the processed material and an increase in the average dimension of particles. As was determined, three wetting parameters changed in tests have a different effect on the process kinetics. This is shown in exemplary Figs. 6, 7 and 8. It follows from them that this kinetics in terms of time used in the tests can be approximated by a straight line obtaining high values of correlation coefficient R^2. It must be underlined once more that limiting this time resulted from the phenomenon of sticking the material to the granulator walls (liquid was squeezed from the inside of granules to their surface). Consequently, the granulation kinetics in its second stage is described by the equation

$$d_{avg}^{(g)} = A \cdot t + B \tag{1}$$

in which constant value B is characteristic of the bed condition after wetting, while constant A indicates the rate of the average granule dimension increase during the proper granulation.

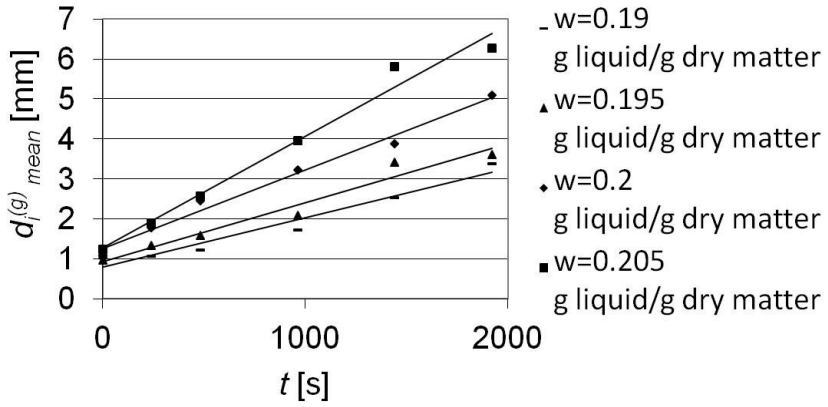

Fig. 6. The exemplary comparison of the rate of the average granule diameter increase for different values of residual moisture of the bed ($d_{32}^{(k)}$=13.13μm; γ=71.97·10^{-3} N/m)

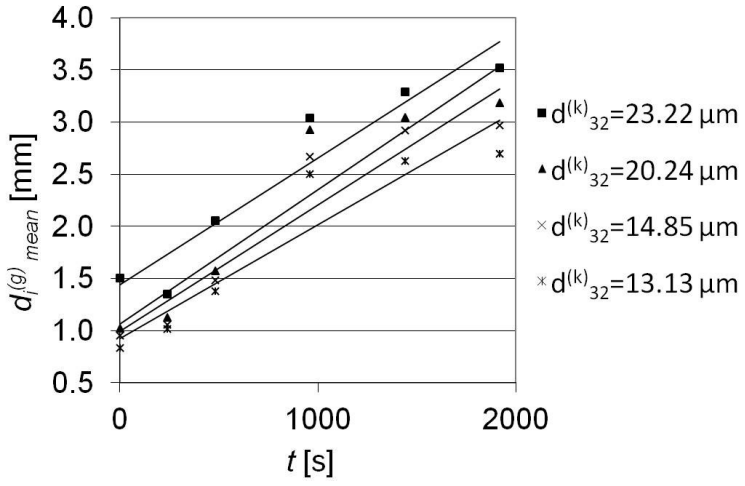

Fig. 7. The exemplary comparison of the average granule diameter increase rate for different degrees of the liquid jet breakup (w = 0.19 g liquid/g dry matter; γ = 35.04·10^{-3} N/m)

The increase in the bed moisture as indicated in Fig. 6, makes the average dimension of particles after wetting (at the beginning of the proper granulation stage) be greater (a higher degree of the material agglomeration). The granulation rate in this second period is also greater. However, the degree of partitioning of the liquid jet, that is the size of drops, has a very small effect on the process kinetics during the proper granulation (Fig. 7). And although the final product differs in separate trials performed at different liquid partitioning, it is the result of the previous formation of particles during wetting.

A change in the wetting liquid surface tension from about $72 \cdot 10^{-3}$ N/m, to about $55 \cdot 10^{-3}$ N/m, causes significant changes in the granulation rate (Fig. 8). The value of constant A decreases then from 0.002 to 0.0013, but further decreasing the liquid surface tension does not cause practically any change in this rate.

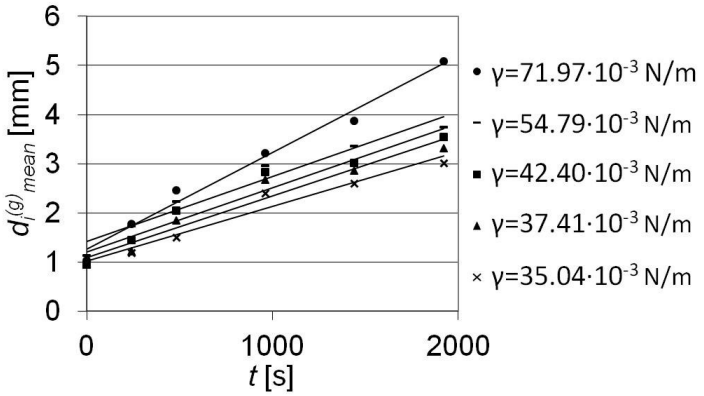

Fig. 8. The exemplary comparison of the average granule diameter increase for different values of the wetting liquid surface tension (w = 0.2 g liquid/g dry matter; $d_{32}^{(k)}$ = 13.13 μm)

3.3. The description of granulation product particle size distribution

Equation (1), in which coefficients A and B are dependent on bed wetting conditions, is used to describe granulated material particle size distribution. The results of tests enabled to determine the detailed form of these dependencies.

$$A = \left(\frac{\Delta d_{32}^{(g)}}{t}\right)_{\mathrm{o}} \left[10^{-2.8}\left(\frac{w}{w_{\mathrm{o}}}\right)^{0.68}\left(\frac{\gamma}{\gamma_{\mathrm{o}}}\right)^{0.29}\left(\frac{d_{32}^{(k)}}{d_{32\,\mathrm{o}}^{(k)}}\right)^{0.34}\right] \tag{2}$$

$$B = d_{32}^{(m)}\left[10^{1.82}\left(\frac{w}{w_{\mathrm{o}}}\right)^{0.89}\left(\frac{\gamma}{\gamma_{\mathrm{o}}}\right)^{0.29}\left(\frac{d_{32}^{(k)}}{d_{32\,\mathrm{o}}^{(k)}}\right)^{0.34}\right] \tag{3}$$

where $(\Delta d_{32}^{(g)}/t)_{\mathrm{o}}$ is the rate of the average granule dimension increase using basic parameters which were equal to: w_o = 0.19 g liquid/ g dry matter; $d_{32o}^{(k)}$ = 13.13 μm; γ_o = $35.04 \cdot 10^{-3}$ N/m.

As follows from Eqs. (2) and (3), the values of power exponents in expressions related to the size of the wetting liquid drops and surface tension of this liquid are in both cases the same, the final form of the dependence describing the process kinetics can be presented by the equation:

$$d_{32}^{(g)} = \left[10^{-2.8}\left(\frac{d_{32}^{(g)}}{t}\right)_{\mathrm{o}}\left(\frac{w}{w_{\mathrm{o}}}\right)^{0.68} \cdot t + 10^{1.82} d_{32}^{(m)}\left(\frac{w}{w_{\mathrm{o}}}\right)^{0.89}\right]\left[\left(\frac{\gamma}{\gamma_{\mathrm{o}}}\right)^{0.29}\left(\frac{d_{32}^{(k)}}{d_{32\,\mathrm{o}}^{(k)}}\right)^{0.34}\right] \tag{4}$$

Correlation coefficient of the obtained dependence is R^2 = 0.91.

From the practical point of view, not only the average dimension of particles, but also the dispersion of the granule size in the final product is of interest. They are different at different wetting conditions, as shown in Figs. 9, 10 and 11.

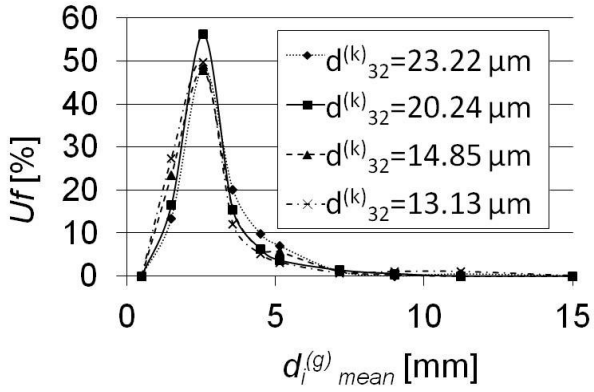

Fig. 9. The exemplary comparison of shares of separate particle sizes in the final product at different diameters of the wetting liquid drops (w = 0.19 g liquid/g dry matter; $\gamma = 71.97 \cdot 10^{-3}$ N/m)

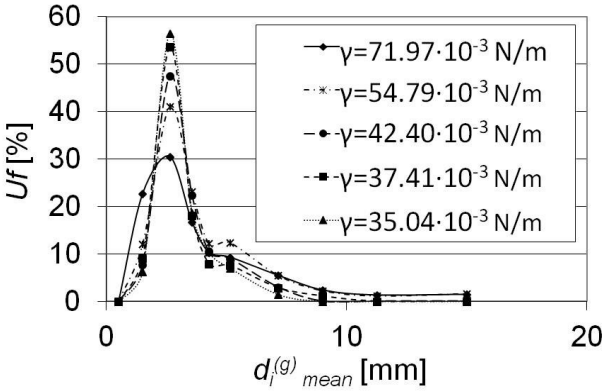

Fig. 10. The exemplary comparison of shares of separate particle sizes in the final product for different values of the liquid surface tension ($d_{32}^{(k)}$ = 20.24 µm; w = 0.19 g liquid/g dry matter)

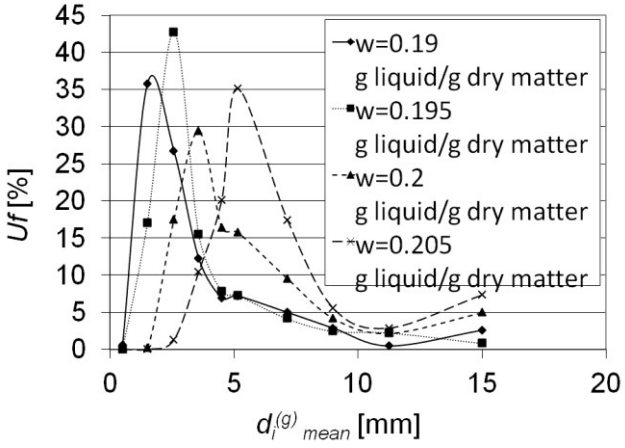

Fig. 11. The exemplary comparison of shares of separate particle sizes in the final product for different values of residual moisture of the bed ($d_{32}^{(k)}$ = 13.13 µm; $\gamma = 71.97 \times 10^{-3}$ N/m)

For the mathematical description of these compositions, modified asymmetry coefficient K_1 and flattening coefficient K_2 calculated from the equations were used

$$K_1 = \frac{M_4 - (M_2)^2}{M_4} \tag{5}$$

$$K_2 = \frac{M_3}{M_2^{3/2} + |M_3|} \tag{6}$$

where the central moment of order k is determined by the formula

$$m_1 = \sum_{i=1}^{n} x_i^{(g)} d_i^{(g)}$$

$$M_k = \sum_{i=1}^{n} \left(x_i^{(g)} - m_i \right)^k d_i^{(g)} \tag{7}$$

and the zero moment of the first order

$$m_1 = \sum_{i=1}^{n} x_i^{(g)} d_i^{(g)} \tag{8}$$

While analyzing the obtained results, a virtual absence of the effect of the liquid drop diameter and its surface tension on the asymmetry coefficient value was determined. In boundary cases, values differing by less than 10% were obtained. A change in the dimension of drops had also a very small effect on the flattening coefficient (a maximum of about 2%). However, a significant effect of the liquid surface tension and the residual moisture of the bed on the value of the flattening coefficient were determined. It is shown as an example in Figs. 12 and 13.

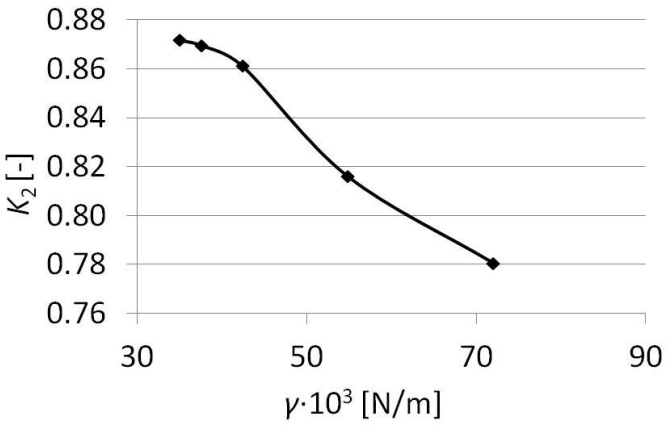

Fig. 12. The exemplary comparison of changes in flattening coefficient K_2 obtained for different values of the liquid surface tension ($d_{32}^{(k)}$ = 20.24μm; w = 0.19 g liquid/g dry matter)

Also the residual moisture of the bed affects significantly the value of the asymmetry coefficient (Fig. 14). In the case of the liquid surface tension, as indicated by Fig. 12, its decrease causes an increase in the value of the coefficient, which indicates greater dimensional homogeneity of the granulation product. Granules created in these conditions are less mechanically durable, which in turn means a rise in the contribution of smaller granules. However, the effect of the residual moisture of the bed is more complex. An increase in this moisture from 0.19 to 0.195 g liquid/g dry matter results in an increase in the value of both the flattening coefficient and the asymmetry coefficient. Higher values of these coefficients indicate that the product is more monodisperse. However, further increasing the bed moisture leads to greater dispersion of the obtained granule size. This is caused by the fact that more moisturized granules which also achieve bigger final diameter are less prone to destructive mechanisms. Moreover, the excess moisture that is squeezed outside in the later stage of granulation causes binding of granules and building up of not yet granulated material creating big agglomerates.

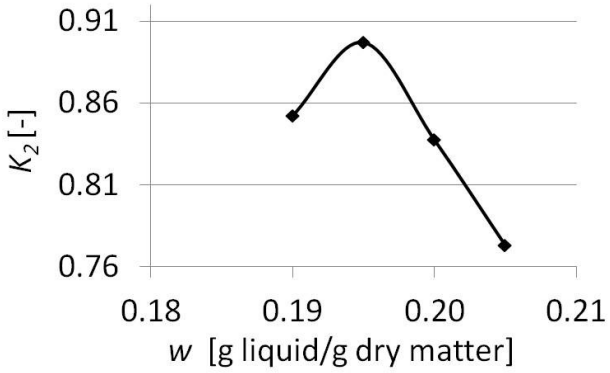

Fig. 13. The exemplary comparison of changes in flattening coefficient K_2 obtained for different values of the residual moisture of the product ($d_{32}^{(k)}$= 13.13μm; γ = 71.97·10^{-3} N/m)

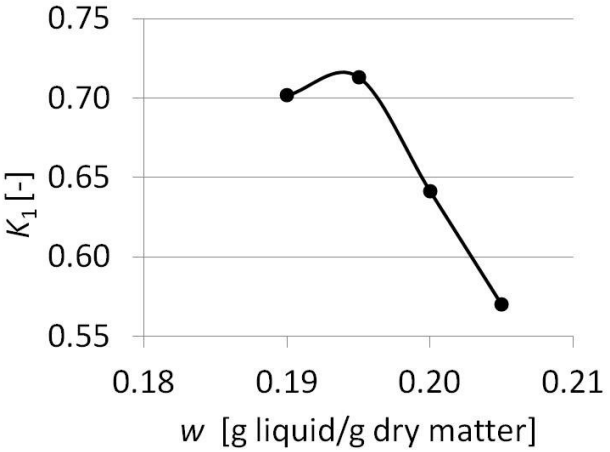

Fig. 14. The exemplary comparison of values of asymmetry coefficient K_1 for different values of the product moisture ($d_{32}^{(k)}$ = 13.13 μm; γ = 71.97·10^{-3} N/m)

4. CONCLUSIONS

- The flow granulation process of silica flour is possible from the practical point of view using wetted beds within boundaries from 0.190 to 0.205 g of liquid/g dry matter. A similar limitation is set by the granulation time. When its critical value is exceeded, the material sticks to the drum walls.
- The process course both in the wetting stage and during the proper granulation is affected mostly by the bed moisture. The wetting liquid surface tension and the degree of its partitioning during wetting have a smaller effect and in both cases it is on the same level.
- The size composition of the final granulation product depends on the wetting conditions. It is affected to a different extent by the residual moisture, a degree of bonding liquid partitioning and its surface tension.

SYMBOLS

A,B	constants, -
K_1	modified asymmetry coefficient, -
K_2	modified flattening coefficient, -

M	central moment, -
R^2	correlation coefficient, -
Uf	shares of separate particle sizes, %
Us	shares of total particle sizes, %
Q	flow rate, m^3/h
$d^{(g)}$	the average dimension of granules, mm
$d^{(k)}$	the average dimension of drops, µm
$d^{(m)}$	the average dimension of flour particles, µm
t	time, s
m	zero moment, -
w	moisture, g liquid/g dry matter
x	the weight share in the product, -
γ	surface tension, N/m
η	viscosity, Pa s
ρ	density, kg/m^3

Subscripts

avg	average
i	i-th fraction
k	order k
l	loosely heaped
o	basic
mean	arithmetic mean
rel	relative
z	concentrated
1	first order
32	Sauter mean diameter

Superscript

(g)	granules
(k)	drops
(m)	flour

REFERENCES

Charles-Williams H.R., Wengeler R., Flore K., Feise H., Hounslow M.J., Salman A.D., 2011. Granule nucleation and growth: Competing drop spreading and infiltration processes. *Powder Technol*. 206, 63-71, DOI: 10.1016/j.powtec.2010.06.013.

Ennis B.B., Li J., Tardos G.I., Pfeffer R., 1990. The influence of viscosity on the strength of an axially strained pendular liquid bridge. *Chem. Eng. Sci*., 45, 3071-3088. DOI: 10.1016/0009-2509(90)80054-I.

Ennis B.B., Li J., Tardos G.I., Pfeffer R., 1991. A microlevel – based characterization of granulation phenomena. *Powder Technol.*, 65, 257-272. DOI: 10.1016/0032-5910(91)80189-P.

Gluba T., Obraniak A., 2008. Ocena jednorodności produktu mokrej granulacji bębnowej. *Przemysł Chemiczny*, 87 (2), 125-128.

Hapgood K.P., Litster J.D., Biggs S.R., Howes T., 2002. Drop penetration into porous powder beds. *J. Colloid Interface Sci.*, 253, 353-366. DOI: 10.1006/jcis.2002.8527.

Heim A., Gluba T., Obraniak A., 2000. The effect of process and equipment parameters on the drum granulation kinetics. *Physicochemical Problems of Mineral Processing*, 34, 67-76.

Hotta K., Takeda K., Iinoya K., 1974. The capillary bonding force of a liquid bridge. *Powder Technol.*, 10, 231 - 236. DOI: 10.1016/0032-5910(74)85047-3.

Iveson S.M., Litster J.D., Hapgood K., Ennis B.J., 2001. Nucleation, growth and breakage phenomena in agitated wet granulation processes. *Powder Technol.*, 117, 3-39. DOI: 10.1016/S0032-5910(01)00313-8.

Junnila R., Heinamaki J., Yliruusi J., 1998. Effect of surface – active agent on the size, shape and hardness of micro – crystalline cellulose /maize starch pellets prepared by an extrusion – spheronization technique. *S.T.P. Pharma Sciences*, 8 (4), 221-226.

Nguyen T., Shen W., Hapgood K., 2009. Drop penetration time in heterogeneous powder beds. *Chem. Eng. Sci.*, 64, 5210-5221. DOI: 10.1016/j.ces.2009.08.038.

Nienow A.W., 1995. Fluidised bed granulation and coating application to materials agriculture and biotechnology. *Chem. Eng. Comm.,* 139, 233-253. DOI: 10.1080/00986449508936406.

Obraniak A., Gluba T., 2011. A model of granule porosity changes during drum granulation. *Physicochemical Problems of Mineral Processing*, 46, 219-228.

Obraniak A.. Gluba T., 2012a. A model of agglomerate formation during disc granulation process. *Chem. Process Eng.,* 33,1,153-165. DOI: 10.2478/v10176-012-0014-1.

Obraniak A., Gluba T., 2012b. Model of energy consumption in the range of nucleation and granule growth in drum granulation bentonite. *Physicochemical Problems of Mineral Processing,* 48, 1, 121-128.

Opaliński I., 2001. Siły adhezji kapilarnej w materiałach rozdrobnionych. Mechanizm oddziaływania i modelowanie. *Inż. Chem. Proc.,* 22, 99-108.

Pepin X., Sossetti D., Simons S.J.R., 2000. Modeling pendular liquid bridges with a reducing solid liquid interface. *J. Coll. Int. Sci.,* 232, 298-308. DOI: 10.1016/S0032-5910(02)00235-8.

Rajniak P., Mancinelli C., Chern R.T., Stepanek F., Farber L., Hill B.T., 2007. Experimental study of wet granulation in fluidized bed: Impact of the binder properties on the granule morphology. *Int. J. Pharm.*, 334, 92-102. DOI: 10.1016/j.ijpharm.2006.10.040.

Ramachandran R.P., Sanders J.M.-H., Constantijn F.W., Glaser Th., Immanuel Ch.D., Doyle III F.J.; Litster J.D., Stepanek F., Wang Fu-Yang, Cameron I.T., 2008. Experimental studies on distributions of granule size, binder content and porosity in batch drum granulation: Inferences on process modelling requirements and process sensitivities. *Powder Technol.* 188, 89-101. DOI: 10.1016/j.powtec.2008.04.013.

Rivera M.R., Koltsov A., Araya Lazcano B., Douce J.-F., 2017. Wettability in water/iron ore powder systems: To the universality of the Cassie model. *Int. J. Miner. Process.*, 162, 36-47. DOI: 10.1016/j.minpro.2017.02.016.

Sastry K.V.S., Fuerstenu D.W., 1973. Mechanism of agglomerate growth in green palletization. *Powder Technol.,* 7, 97-105.

Smirani-Khayati N., Falk V., Bardin-Monnier N., Marchal-Heussler L., 2009. Binder liquid distribution during granulation process and its relationship to granule size distribution. *Powder Technol*. 195, 105-112. DOI: 10.1016/j.powtec.2009.05.020.

Willett C.D., Adams M.J., Johnson S.A., Seville J.P.K., 2003. Effect of wetting hysteresis on pendular liquid bridges between rigid spheres. *Powder Technol.,* 130, 63-71. DOI: 10.1016/S0032-5910(02)00235-8.

Received 20 October 2016
Received in revised form 23 May 2017
Accepted 10 June 2017

Instructions for Authors

All manuscripts submitted for publication in Chemical and Process Engineering must comprise a description of original research that has neither been published nor submitted for publication elsewhere.

The content, aim and scope of the proposals should comply with the main subject of the journal, i.e. they should deal with mathematical modelling and/or experimental investigations on momentum, heat and mass transfer, unit processes and operations, integrated processes, biochemical engineering, statics and kinetics of chemical reactions. The experiments and modelling may cover different scales and processes ranging from the molecular phenomena up to production systems. The journal language is grammatically correct British English.

Chemical and Process Engineering publishes: i) full text research articles, ii) invited reviews, iii) letters to the editor and iv) short communications, aiming at important new results and/or applications. Each of the publication form is peer-reviewed by at least two independent referees.

Submission of materials for publication

The manuscripts are submitted for publication via email address *A.Bin@ichip.pw.edu.pl*. When writing the manuscript, authors should preferably use the template for articles, which is available on the *www.degruyter.com/view/j/cpe*.

Proposals of a paper should be uploaded using the Internet site of the journal and should contain:

- a manuscript file in Word format (*.doc, *.docx),
- the manuscript mirror in PDF format,
- all graphical figures in separate graphics files.

In the following paragraph the general guidelines for the manuscript preparation are presented.

Manuscript outline

1. Header details

a. Title of paper
b. Names (first name and further initials) and surnames of authors
c. Institution(s) (affiliation)
d. Address(es) of authors
e. Information about the corresponding author; academic title, name and surname, email address, address for correspondence

2. Abstract – should contain a short summary of the proposed paper. In the maximum of 200 words the authors should present the main assumptions, results and conclusions drawn from the presented study.

3. Keywords – Up to 5 characteristic keyword items should be provided.

4. Text

a. Introduction. In this part, description of motivation for the study and formulation of the scientific problem should be included and supported by a concise review of recent literature.
b. Main text. It should contain all important elements of the scientific investigations, such as presentation of experimental rigs, mathematical models, results and their discussion. This part may be divided into subchapters.
c. Conclusions. The major conclusions can be put forward in concise style in a separate chapter. Presentation of conclusions from the reported research work accompanied by a short commentary is also acceptable.

Figures: drawings, diagrams and photographs should be located in appropriate places in the manuscript text according to the template. Their graphical form should be of vector or raster type with the minimum resolution of 900 dpi. In addition, separate files containing each of the drawings, graphs and photos should be uploaded onto the journal Web site in one of the following formats: bmp, gif, tiff, jpg, eps. Due to rigid editorial reasons, graphical elements created within MS Word and Excel are not acceptable. The final length of figures should be intended typically for 8 cm (single column) or 16 cm in special cases of rich-detail figures. The basic font size of letters in figures should be at least 10 pts after adjusting graphs to the final length.

Figures: drawings, diagrams and photographs should be in gray scale. In case of coloured graphs or photo an additional payment of 300 PLN (72 €) per 1 page containing coloured figures on both sides, or 150 PLN (36 €) per page containing coloured figures on one side will be required.

Tables should be made according to the format shown in the template.

All figures and tables should be numbered and provided with appropriate title and legend, if necessary. They have to be properly referenced to and commented in the text of the manuscript.

5. List of symbols should be accompanied by their units

6. Acknowledgements may be included before the list of literature references

7. Literature citations

The method of quoting literature source in the manuscript depends on the number of its authors:

- single author – their surname and year of publication should be given, e.g. Marquardt (1996) or (Marquardt, 1996),
- two authors – the two surnames separated by the conjunction "and" with the publication year should be given, e.g. Charpentier and McKenna (2004) or (Charpentier and McKenna, 2004),
- three and more authors – the surname of the first author followed by the abbreviation "et al." and year of publication should be given, e.g. Bird et al. (1960) or (Bird et al., 1960).

In the case of citing more sources in one bracket, they should be listed in alphabetical order using semicolon for separation, e.g. (Bird et al., 1960; Charpentier and McKenna, 2004; Marquardt, 1996). Should more citations of the same author(s) and year appear in the manuscript then letters "a, b, c, ..." should be successively applied after the publication year.

Bibliographic data of the quoted literature should be arranged at the end of the manuscript text in alphabetic order of surnames of the first author. It is obligatory to indicate the DOI number of those literature items, which have the numbers already assigned. Journal titles should be specified by typing their right abbreviations or, in case of doubts, according to the List of Title Word Abbreviations available at http://www.issn.org/2-22661-LTWA-online.php.

Examples of citation for:

Articles

Charpentier J. C., McKenna T. F., 2004. Managing complex systems: some trends for the future of chemical and process engineering. *Chem. Eng. Sci.*, 59, 1617-1640. DOI: 10.1016/j.ces.2004.01.044.

Information from books (we suggest adding the page numbers where the quoted information can be found)

Bird R. B., Stewart W.E., Lightfood E.N., 2002. *Transport Phenomena*. 2nd edition, Wiley, New York, 415-421.

Chapters in books

Hanjalić K., Jakirlić S., 2002. Second-moment turbulence closure modelling, In: Launder B.E., Sandham N.D. (Eds.), *Closure strategies for turbulent and transitional flows*. Cambridge University Press, Cambridge, 47-101.

Conferences

ten Cate A., Bermingham S.K., Derksen J.J., Kramer H.M.J., 2000. Compartmental modeling of an 1100L DTB crystallizer based on Large Eddy flow simulation. *10th European Conference on Mixing*. Delft, the Netherlands, 2-5 July 2000, 255-264.

8. Payments

Starting from 2014 a principle of publishing articles against payment is introduced, assuming non-profit making editorial office. According to the principle authors or institutions employing them, will have to cover the expenses amounting to 40 PLN (or 10 €) per printed page. The above amount will be used to supplement the limited financial means received from the Polish Academy of Sciences for the editorial and publishing; and in particular to increase the capacity of the next CPE volumes and to proofread the linguistic correctness of the articles. The method of payment will be indicated in an invoice sent to the authors or institutions after acceptance of their manuscripts to be published. In justifiable cases presented in writing, the editorial staff may decide to relieve authors from basic payment, either partially or fully.

All correspondence should be sent to Editor-in-Chief, Prof. Andrzej K. Biń, email address *A.Bin@ichip.pw.edu.pl*.

The Azoty Group is a future-oriented project. But this has always been the case. When in 1927 President Ignacy Mościcki decided to build the State-owned Nitrogenous Compounds Factory it was a vision of the future. A vision of Poland's grand chemical industry.

This vision, and the history of all the companies the Group put together give us the picture of one of the key capital groups in the European fertiliser-chemical sector.

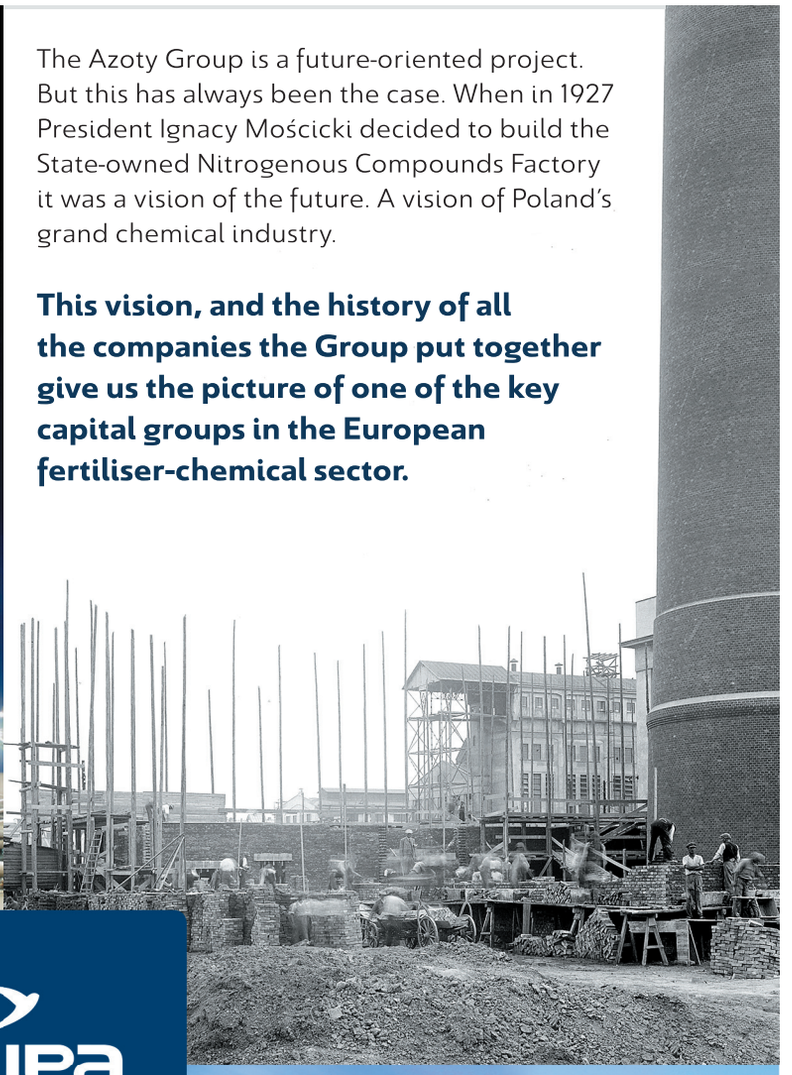

GRUPA AZOTY

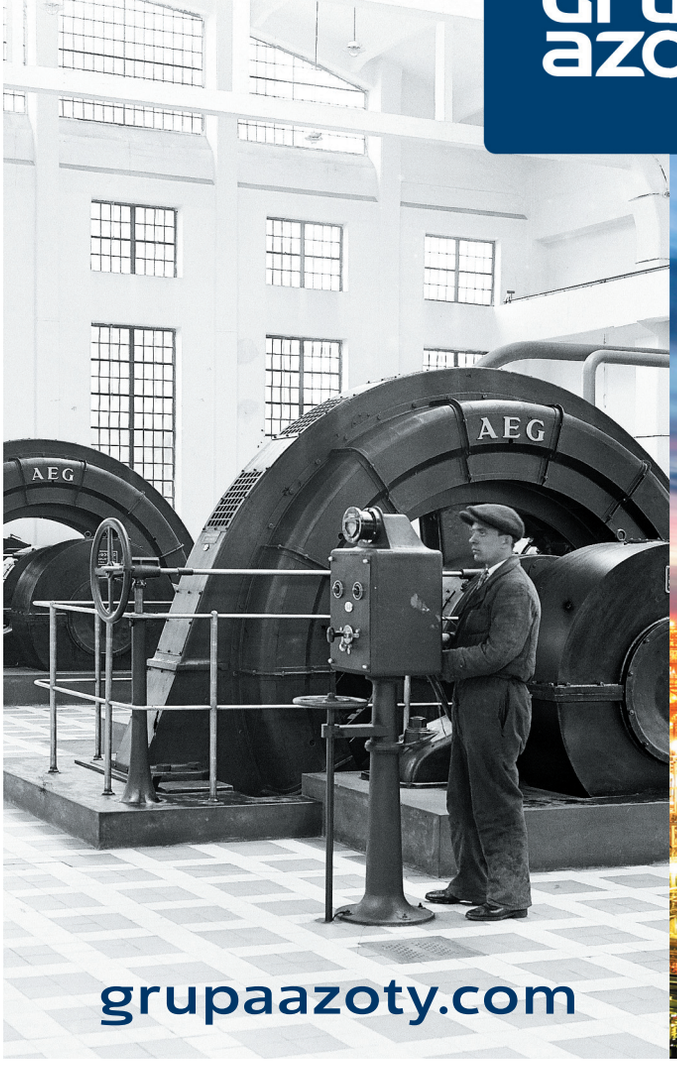

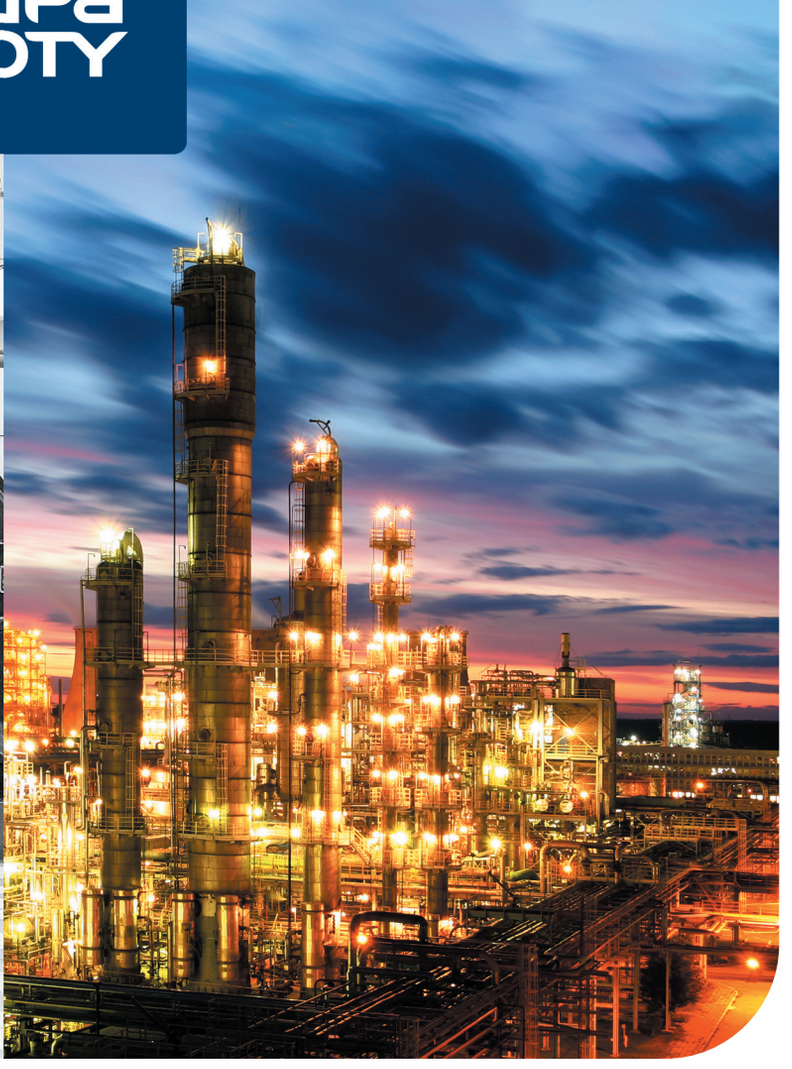

grupaazoty.com